Characterization of Optical Properties of Mandovi and Zuari Estuarine Waters

A thesis submitted to **Goa University** for the award of the Degree of

Doctor of Philosophy

In

Physics

by

Thayapurath Suresh

Under the guidance of

Prof. J.A.E. Desa

Department of Physics

Goa University, Goa 403206

January 2020

DECLARATION

As required under the University Ordinance OB.9A, I state that the present thesis entitled, "**Characterization of Optical Properties of Mandovi and Zuari Estuarine Waters**", submitted to Goa University for the award of the degree of Doctor of Philosophy in Physics is a record of original and independent work carried out by me during the period January 2014 – January 2020, under the supervision of **Prof. J.A.E. Desa**, Department of Physics, Goa University, and that it has not formed the basis for the award of any Degree or Diploma to me or to any other candidate of this or any other University.

Date : January 2020

Place : Goa University, Goa

Thayapurath Suresh

CERTIFICATE

It is hereby certified that this thesis entitled, "**Characterization of Optical Properties of Mandovi and Zuari Estuarine Waters**" submitted to Goa University for the award of the degree of Doctor of Philosophy in Physics is a record of original and independent work carried out by **Mr. Thayapurath Suresh** during the period January 2014 – January 2020, and that it has not formed the basis for the award of any Degree or Diploma to any candidate of this or any other University.

Place : Goa University

Date : January 2020

Prof. J.A.E. Desa

(Guide)

Department of Physics

Goa University

Prof. K. R. Shenvi Priolkar

(Co-Guide)

Department of Physics

Goa University

I would like to dedicate this thesis to my Amma and Achan, my children Adi, and Nami, and Ettan and Echi ... and to all my colleagues

ACKNOWLEDGEMENTS

I would like express my gratitude to Dr. Elgar Desa my mentor and Guru, who introduced me to this exciting, and fascinating world of marine optics and ocean color remote sensing without which I would not have engaged myself in this field. Thank you for the knowledge imparted in this subject, time you spent with me educating me, for the encouragement and also being there whenever required. Thank you, Dr. Ehrlich Desa for your support.

Dr. Erwin Desa my guide, thank you for accepting me as your student. He has always been supportive, encouraging and was optimistic of my completing the PhD. Thank him for his helping nature and calm unperturbed approach towards all his students. Thank you, Dr. Kaustubh Priolkar, my co-guide for your support.

Some people in your life matters a lot and always there to render help at all times and it was my staff Miss Albertina Dias who was the shining photon, without whom I would have never registered, continued and reached to this stage. She was there with me all through with a magic wand in her hand.

Dr. Madhubala Talaulikar helped me during the early days of studies when we were new to this subject, setting up the laboratory, organizing and participating in the field measurements and analyzing the data with her sound knowledge of programming and engaging in fruitful discussions.

I am indebted to the duo, Ashvesh Gimonkar and Mithilesh Mane whose sincere, sustained efforts facilitated in the field measurements, calibration and upkeep of the instruments. Thanks are also due to the Reshmitha, Shreya, Nupoor and others who helped me with the field measurements and analysis. I shall always cherish the moments of field measurements on boats, birthday celebrations, fishing, and picnics. With you all being there, working was so pleasant, enjoyable and fruitful.

I am grateful to Space Application Centre (ISRO), Ahmedabad, National Remote Sensing Centre (ISRO), Hyderabad, ESSO-INCOIS and Naval Research Board, New Delhi for the support and interactions with the staff. Thank you Dr. Shanmugham, IIT Madras for the discussions, suggestions, encouragement and help. I am thankful to the Directors of CSIR-National Institute of Oceanography, where I was employed, who always encouraged and supported me to undertake projects in ocean color applications. Thank you all at my division of Marine Instrumentation Division for your continued support and encouragements. Thank you Dr. Mithun of lbrary, staff of ship cell, ITG and others at NIO who always helped me whenever required.

ABSTRACT

The research topic was in the field of marine optics and ocean color applications. The focuses of the studies were to understand the light properties of the optically complex waters of Goa, which included the two estuaries Mandovi and Zuari and the coastal waters off Goa (Latitude 15.35 to 15.55° N, Longitude 73.65 to 74.047° E). This study was carried-out using large data of measured spectral optical, physical, biological and ancillary parameters of these waters to understand the spatial and temporal variations optical properties and their associations with other parameters, physical and biological features and also the development of new algorithms to derive optical parameters that could be used for ocean color satellite applications.

There were three types of data used for the studies, which included measured, derived from the radiative transfer simulations and satellite data. There were measured data from 500 field measurements, and these were from 27 regular time-series stations which included, Mandovi(12), Zuari(8), and coastal (9) where measurements carried-out all through the year at periodic intervals.

There were distinct spatial and temporal variations of optical, biological, physical, and ancillary parameters of coastal and estuarine waters.

Two parameters that have been used to indicate the penetration of light in water were first optical depth or penetration depth Z_{90} (m) and Secchi depth, Zsd. There was sufficient light available in these waters till the bottom during all seasons, and average %PAR at was about 22%. The values of Z_{90} and Z_{sd} show that light penetrates the deepest in coastal waters, and among estuaries, the light penetrations in Mandovi were deeper than Zuari. The wavelength at maximum $Z_{90}(\lambda)$ was about 577 nm in the estuaries and was higher compared to the coastal waters, which was at about 545 nm. The bulk refractive index was higher in the estuaries, indicating more mineral particles. The particle sizes were relatively smaller in the estuaries.

Monsoons play an important role in modulating the physical, biological, and optical parameters of these estuaries. However, during monsoon, despite the availability of nutrients and sufficient light, the chlorophyll was low and high discharge, and flow rates were presumed to be responsible for it. Contributions of CDOM and detritus were significant in the estuaries, with the highest values observed during monsoon. A new method developed to determine the iso layers could identify the MLD and ILD of these estuaries and the studies of the physical features such as MLD, ILD, thermal inversions, and bottom heating and their association with optical and biological parameters attempted for the first time in these waters provided encouraging results. The time-series observations at a station could show the variations of optical parameters with the tides.

Cluster analysis of these large measured data of complex coastal and estuarine waters could identify distinct classes with each class having similar optical, biological, and physical properties, and the classes differed from each other in all these aspects. These classes were mostly season invariant but spatially apart.

There were spatial and temporal variations of Secchi depths or transparencies of waters of the estuaries and coastal waters of Goa, and the study provided an understanding of the parameters that control the transparency, visibility, or light penetrations in these waters. The transparencies of coastal waters increased during algal blooms such as *Noctiluca* and *Trichodesmium*. The transparencies of water decreased by a large factor during the monsoon season due to the increase in optical properties that control the transparencies of water. The amount of rainfall was inversely proportional to the transparencies. Transparency of light given by Secchi depth, Z_{sd} was found to be close to Z_{90}. The wavelength of the deepest penetrating light in water varied inversely with the transparency, Zsd.

Algorithms were developed to derive optical parameters from optically complex waters which were slope of the spectral CDM, $a_{dg}(\lambda)$, absorption of CDM, adg(412), spectral total absorption $a_t(\lambda)$, volume scattering function (VSF) or phase function and underwater vertical and horizontal visibilities. The new algorithms derived were also validated with satellite data.

CONTENTS

LIST OF FIGURES

LIST OF TABLES

LIST OF SYSMBOLS AND ACRONYMS

Symbols

Symbol	Description	Unit
γ	Spectral slope of c(λ)	nm^{-1}
a	Absorption excluding pure water	m^{-1}
a_d	Absorption due to detritus or NAP	m^{-1}
a_{dg}	Absorption due to CDM (ag +ad)	m^{-1}
a_g	Absorption due to CDOM	m^{-1}
a_{ph}	Absorption due to phytoplankton	m^{-1}
a_t	Total absorption coefficient	m^{-1}
a_w	Absorption due to pure water	m^{-1}
b_w	Scattering of pure water	m^{-1}
b	Scattering excluding pure water	m^{-1}
b_{bp}	Particulate backscattering	m^{-1}
b_{bt}	Total backscattering	m^{-1}
b_t	Total scattering coefficient	m^{-1}
c	Beam attenuation without pure water	m^{-1}
c(v)	Photopic beam attenuation coefficient	
c_t	Total beam attenuation coefficient	m^{-1}
E_d	Downwelling plane irradiance	$Wm^{-2}nm^{-1}/\mu wcm^{-2}nm^{-1}$
E_o	Scalar irradiance	$Wm^{-2}nm^{-1}/\mu wcm^{-2}nm^{-1}$
E_s	Surface solar irradiance	$Wm^{-2}nm^{-1}/\mu wcm^{-2}nm^{-1}$
E_u	Upwelling plane irradiance	$Wm^{-2}nm^{-1}/\mu wcm^{-2}nm^{-1}$
HV	Horizontal visibility	m
ILD	Isothermal Layer depth	M
K_d	Diffuse attenuation coefficient of downwelling irradiance	m^{-1}
Kd(v)	Photopic vertical diffuse attenuation coefficient	
K_E	Attenuation coefficient of vector irradiance	m^{-1}
L_w	Water leaving radiance at the surface	$Wm^{-2}sr^{-1}$
MLD	Mixed Layer Depth	m
n_p	Bulk refractive index with respect to water	
Q	Bi-directionality factor	
R	Irradiance reflectance just below surface of water	
R_{rs}	Remote sensing reflectance at the surface of water	sr^{-1}
Sdg	Slope of $a_{dg}(\lambda)$	nm^{-1}
TSM	Total Suspended Matter	g/m^3
VV	Vertical visibility	m

z	Depth	m
z	Depth	m
Z_{90}	Penetration or first optical depth	m
Z_{eu}	Euphotic depth	m
Zmax	Maximum depth	m
Z_{sd}	Secchi depth or transparency	m
β	Volume scattering function	$m^{-1}sr^{-1}$
Γ	Coupling coefficient	
θ	Viewing angle	Degree/radiance
λ	Wavelength	nm
μ or $\bar{\mu}$	Average underwater cosine	
ξ	PSD slope or Junge exponent	
ρ_b	Bottom reflectance	
ω_o	Single scattering albedo	

Acronyms

Acronym	**Full form**
AOP	Apparent Optical Properties
AWS	Automatic Weather Station
CaTS	Candolim Time Series
CDM	Colored Detritus Matter ,CDOM + NAP(detritus)
CDOM	Colored Dissolved Organic Matter
CTD	Conductivity Temperature Depth
ECV	Essential Climate Variables
IOP	Inherent Optical properties
ISRO	Indian Space Research Organization
MODIS	Moderate Resolution Imaging Spectrometer
NAP	Non Algal Particles
NIO	National Institute of Oceanography
NOMAD	NASA bio-Optical Marine Algorithm Dataset
OCM	Ocean Color Monitor
PAR	Photosynthetically Available Radiation
PSD	Particle Size Distribution
RTE	Radiative Transfer Equation
SeaBASS	SeaWiFS Bio-Optical Archive and Storage System
SeaDAS	SeaWiFS Data Analysis System
SeaWiFS	Sea-viewing Wide Field-of-view Sensor
UV	Ultra Violet

CHAPTER 1. INTRODUCTION

Life on earth depends on solar light. The results of the research carried out here were in the field of marine optics and ocean color applications. The studies carried-out here were limited to the two estuaries of Goa, Mandovi and Zuari and the coastal waters over a short distance from the mouth of the estuaries. The objectives were to understand the underwater light, variations of the optical properties of water, developments of new algorithms to derive parameters from ocean color satellite data and other studies related to ocean color applications for these waters.

These coastal and estuarine waters are complex, and the optically active substances that interact with underwater light may not co-vary with the phytoplankton or chlorophyll. These waters were categorized as Case 2 waters from an earlier scheme of classifications of water types for optical studies (Morel & Prieur, 1977). The studies of underwater light and ocean color applications of such waters are important (IOCCG, 2000). The coastal waters selected here were also different from other coastal waters as these coastal waters were off the mouth of estuaries and would have the influence of estuaries. Monsoon and tides play an important role in these monsoonal estuaries, which modulate the physical, biological, chemical, and other environmental parameters (Shetye, Kumar, & Shankar, 2007; Vijith, 2014).

The two estuaries Mandovi and Zuari have been explored and studied in-depth in all aspects, and most disciplines of marine science by CSIR-National Institute of Oceanography, Goa since its inception in 1966 and then with the establishment of Goa University in 1985, many Ph.D. studies have been undertaken. Three disciplines that explored Mandovi and Zuari estuaries in-depth of various parameter variations were biology, physics, and chemistry. Numerous publications of earlier investigations were reported in two Indian journals, the Indian Journal of Marine Sciences and Mahasagar, and as technical reports at CSIR-NIO. There were publications during 1970 that related to the studies in biology (Bhargava & Dwivedi, 1976; Dehadrai & Bhargava, 1972; Dehadrai, 1970), physical oceanography (Das, Murty, & Varadachari, 1972), chemistry (Singbal, 1973) and geology (Rao, 1974). The studies carried-out here could not have been complete without the results, information, and insights provided by earlier in-depth studies carried-out by many researchers of these waters.

One of the earliest methods that could relate to the underwater light field was using the Secchi depth using the Secchi disk. In simple terms, the higher the value of Secchi depth was indicative of deeper depths of light penetration, while smaller values suggested that light got attenuated and penetrated to a shallow depth. This simple tool provided ample information about the transparencies of water and underwater light. The measurements of Secchi depths were first reported for the waters off the east coast of India about a half century ago (Prasad, 1952; La Fond & Sastry, 1957; Rao, 1957). The earliest record of spectral light transmission measurements in Indian water was carried out by Rangarajan (Rangarajan, 1959), and in the estuary, the spectral light transmission and Secchi depths were studied by Bhatnagar and Purushothaman (Bhatnagar & Purushothaman, 1974). One of the earliest studies of light measurements carried-out in the waters off west India was in the estuarine waters of Kochi, Kerala, by S. Z. Qasim (1968). One of the earliest reports of Secchi depths in the Zuari estuary, Goa was in 1970 (Dehadrai, 1970) and in the Mandovi and Cumburjua canal of Goa was reported in 1976 (Bhattathiri, Devassy, & Bhargava, 1976). Studies related to theoretical aspects of light attenuations in water were carried out in 1969 (Murty, 1969).

Though work on marine optics in the coastal waters of Goa was reported in 1982 (Sathyendranath & Varadachari, 1982), it was only in 2000 that theoretical work to understand the transparencies of the coastal waters was attempted (Levin et al., 2000). In 2005, inherent optical properties (IOPs) and apparent optical properties (AOPs) measurements were carried-out in the estuaries of Goa to understand the seasonal variations of optical parameters (Menon, Lotliker, & Nayak, 2005). It continued thereafter with radiative transfer models, hyperspectral measurements of inherent optical properties (IOPs) and apparent optical properties (AOPs), bio-optical studies and ocean color remote sensing (Suresh et al., 1998; Suresh, Naik, Bandishte, et al., 2006; Talaulikar, Suresh, Desa, & Inamdar, 2014a,2014b; Thayapurath, Talaulikar, Desa, & Lotlikar, 2016).

There were no detailed studies carried out to understand the variations of the optical properties of these complex coastal and estuarine waters of Mandovi and Zuari. There were also requirements for new algorithms to derive various optical properties of these complex waters.

Global warming has been estimated from various studies to have caused approximately 1.0°C of warming above pre-industrial levels and with a likely increase reaching 1.5°C

between 2030 and 2052. Various scientific groups have hypothesized concerning the probable outcomes of a temperature increase of between 1.5°C and 2 °C (IPCC, 2018). Global warming and climate change will impact the estuaries with regards to the sea level height, temperature, and salinity changes (Glamore, Rayner, & Rahman, 2016). Considering the importance of ocean color, the updated sets of 54 Essential Climate Variables (ECV) now include ocean color parameters (https://gcos.wmo.int/en/essential-climate-variables/table). Indian Space Research Organisation (ISRO) and other space agencies over the world, has plans to launch better ocean color satellite sensors, together with other sensors to fulfill various objectives and goals. ISRO will continue with its mission on Oceansat with the next of the series OCM-3 sensor to be launched soon. These studies will find applications in the utilizations of OCM-3 and other ocean color sensors.

1.1 Overview of the structure of the thesis

Chapter 1 (the present chapter) informs in brief about the scope, relevance, earlier studies carried-out in this subject and the objectives.

Chapter 2 A few optical parameters are introduced which are relevant to the studies carried-out in this work such as the measured optical, biological and ancillary parameters.

Chapter 3 is about the methodology, which includes information on the geographical areas of studies, station details, and data acquisition methodologies.

Chapter 4 is about the variations of the optical, biological and physical parameters.

Chapter 5 discusses about the physical features of stratifications such as mixed layer depth, iso thermal layer, thermal inversion, bottom heating and tides and the optical parameters associated with them

Chapter 6 provides results of the classification using cluster analysis.

Chapter 7 examines the underwater light availability and transparencies of waters

Chapter 8 describes the algorithms used to derive optical parameters

Chapter 9 contains the summary of the studies and the conclusions of the work undertaken.

Appendix A List of the publications

CHAPTER 2. OPTICAL PROPERTIES

A brief overview of the ocean color parameters is presented in the context of the present studies. The definitions and other details of ocean optics are available in the Ocean Optics web book http://www.oceanopticsbook.info/, book entitled 'Light and Water: Radiative Transfer in Natural Waters' (Mobley, 1994) as well as in 'Light and Photosynthesis in Aquatic Ecosystems' (Kirk, 2010).

Marine optics, ocean optics, optical oceanography, and ocean color studies are synonymous as all are focused on the interaction of light and the optically active constituents in water. Earlier, there used to be a lack of good commercial optical instruments, and hence studies in marine optics tended to focus on theoretical studies to understand the underwater light field, optical properties, and interactions of light with constituents of water. With the advent of advanced in-situ measuring optical instruments and the launch of ocean color satellites, marine optics has been taken over by studies of ocean color. One of the earliest reference to 'ocean color' remote sensing began with measurements from aircraft of backscattered light to map chlorophyll (Clarke, Ewing & Lorenzen, 1970;Mueller, 1973).

When light enters the water, there are two processes - absorption and scattering of light. The constituents inside the water will absorb the photons or scatter them. These absorption and scattering components vary spectrally depending on the constituents. Dissolved material such as CDOM (Colored Dissolved Organic Matter) may not scatter but will absorb, while phytoplankton will scatter, and the pigments in phytoplankton will absorb light spectrally. Hence the spectral light which enters the water will be modified by the optically active constituents, and when they exit from the surface of the water, they will be spectrally altered. Hence the "color" of the water will be determined by the interactions of incident light with optically active substances present in the water. This forms the basis for changes in the color of the water as well as the satellite ocean color remote sensing. Hence, analyzing the spectral properties that exit the surface of the water will yield information about the constituents.

2.1 Solar radiation

The sun is the primary source of light energy on earth. A brief summary of the central importance that sun played in various cultures worldwide follows:

According to the Upanishads, light is life itself. Surya (also known as Aditya) is the Hindu god of the Sun. He is considered the creator of the universe and the source of all life. Surya first appears in the *Rigveda*, the oldest of the Vedas composed between 1500 and 1000 BCE. In the Bible with reference to the creation of Earth, - God said, "Let there be light," and there was light, which is another testament of the prerequisite and fundamental requirements of light as a source of life on Earth. In every mythology, Sun has an important status and has the position as the creator, source of energy, protector, health, such as Aztec (Nanahuatzin), Buddhist (Marici), Chinese (Doumu), Egyptian (Ra), Hindu (Aditya, Surya), Japanese (Amaterasu) and Roman (Sol).

The simple and important relation $E = h\frac{c}{\lambda}$ that relates light energy to its wavelength implies that light with shorter wavelength (blue) has more energy and will be able to penetrate deeper in water, and those in longer wavelengths (red) will have relatively less energy and find it difficult to go deeper.

This electromagnetic radiation received from sun is spectrally distributed as shown in Table 2.1 (Iqbal, 1983). The studies carried-out here have been limited to the range 350 to 800 nm.

Table 2.1 Spectral distribution of solar irradiance at the top of the atmosphere (TOA), $E_s(\lambda)$

Band	Wavelength Interval (nm)	Solar Irradiance Wm^{-2}	% of total E_s
Ultraviolet And Beyond	< 350	62	4.5
Near Ultraviolet	350-400	57	4.2
Visible	400-700	522	38.2
Near Infrared	700-1000	309	22.6
Infrared and beyond	>1000	417	30.5
Total		1367	100.0

Of the total solar energy near the sun of 6.33×10^7 Wm^{-2}, the amount of total solar energy available just above the atmosphere is 1367 Wm^{-2} and is known as the solar constant.

The solar irradiance measured during different seasons at a station in the coastal and estuarine waters of Goa is given in Figure 2.1. It can be observed that during summer, the solar irradiance was the highest, and during monsoon, the solar irradiance was the lowest. Very low solar irradiance during monsoons was because of the clouds. The solar radiation from 350-400 will be part of the UV-A spectrum (UVA 315-400 nm), 400-700 will be PAR region, and 700-800 will form part of infrared radiation. The focus here will be on the visible region of 400 to 700 nm. The studies were also carried-out for light in the UV region of these waters (Talaulikar, Suresh, Silveira, & Matondkar, 2011). The longer wavelengths are important for the ocean color satellite atmospheric corrections.

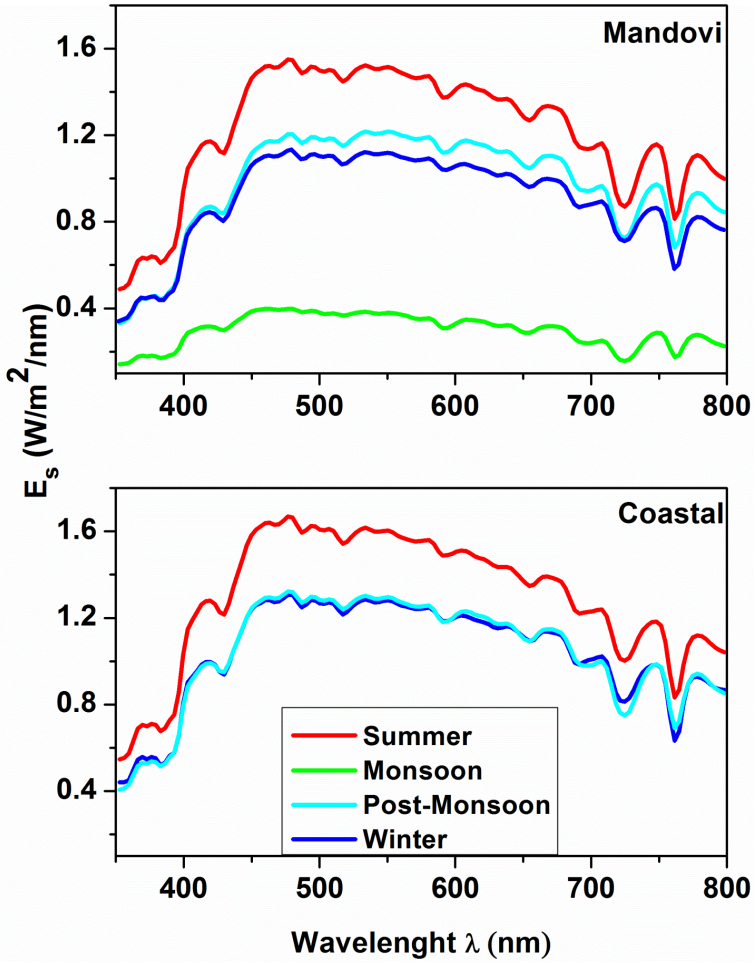

Figure 2.1 Seasonal variations of solar irradiance over the coastal waters and Mandovi estuary

The spectrum of solar irradiance is not smooth, and the dips in the spectrum are the Fraunhofer lines, caused by the absorption of chemical elements in the atmosphere.

2.1.1 Photosynthetically Available Radiation (PAR)

The solar light in the spectral range of 400 to 700 nm, known as Photosynthetically Available Radiation PAR, is an important parameter for the photoautotrophs like terrestrial plants and aquatic beings that use this solar energy for photosynthesis to produce biomass with the help of chlorophyll pigment. Photosynthetic yield per quantum for the algae in water decrease beyond the range of PAR. PAR is also a visible range for the human eye.

Since photosynthesis is a quantum process and the interest is in the number of photons rather than the energy that will be required for photosynthesis, PAR is also expressed in terms of Photosynthetic Photon Flux Density (PPFD, μmol m^{-2} s^{-1}). There is a simple conversion factor between these two units of PAR, 1Wm^{-2} = 4.52 μmol m^{-2} s^{-1} (Suresh et al., 1996).

2.2 IOP

Some of the IOPs are absorption, scattering, beam attenuation, underwater average cosine, and single scattering albedo. IOPs were obtained from measurements using AC-9 and backscattering instruments and from the Radiative Transfer Equation (RTE) simulations with Hydrolight software (Chapter 3).

2.2.1 Absorption, scattering and beam attenuation

Absorption is the loss of a photon resulting in the energy of absorbed photon being converted to heat, chemical, vibration, or rotational energy. Scattering changes the direction of the photon. These are known as Inherent Optical Properties of the water, as they do not depend on the ambient light field, and if the constituents of the water do not change, the IOPs of the water will not change irrespective of time and place. IOPs are difficult to measure with good accuracy, and not all IOPs can be measured in-situ, due to non-availability of commercial and proven instruments. Absorption and scattering or volume scattering function is the prime parameters that can describe the underwater light fields. IOPs are additive and the total loss of photons will be given in optical properties as:

$$\text{Beam attenuation} = \text{Absorption} + \text{Scattering} \quad (1)$$

Hence the spectral beam attenuation coefficient $c_t(\lambda)$ (m^{-1}) = $a_t(\lambda)$ + $b_t(\lambda)$, where $a_t(\lambda)$ and $b_t(\lambda)$ are spectral absorption and scattering coefficients respectively. For brevity, at times, the spectral (λ) and depth (z) parts may be omitted, and unless mentioned at a particular wavelength, most optical parameters are spectral. The total absorption of water was measured using in-situ measuring instruments at the site and in the laboratory. The AC-9 is a spectral profiling instrument that measured in-situ absorption and beam attenuation at 9 wavelengths, 412, 440, 488, 510, 532, 555, 650, 676, and 715nm. The absorption $a(\lambda)$ and $c(\lambda)$ measured with AC-9 does not include the contributions from water (Chang & Dickey, 1999).

$$a(\lambda) = a_t(\lambda) - a_w(\lambda) \tag{2}$$

The absorptions were also measured in the laboratory using a spectrophotometer. Water samples were collected at discrete depths from the station, transported to the laboratory, and analyzed following the standard protocols. The absorptions include contributions from various constituents in the water. Since the inherent optical property of absorption is additive, the total absorption coefficient of water is given as the sum total of the absorption coefficients of the partitioned components (Mobley, 1994).

$$a_t(\lambda) = a_w(\lambda) + a_{ph}(\lambda) + a_d(\lambda) + a_g(\lambda) \tag{3}$$

$$a(\lambda) = a_{ph}(\lambda) + a_d(\lambda) + a_g(\lambda) \tag{4}$$

Where the subscripts w, ph, d, and g represent pure water, phytoplankton, non-algal particles (NAP) or detritus, and colored dissolved organic matter (CDOM), respectively. The nomenclatures for the absorption of various components have been retained as was used for open ocean or Case 1 waters. Since non-algal particles were dominated by detritus in Case 1 water, it was referred as a_d, which has continued for estuaries or Case 2 waters which refer to absorption due to de-pigmented particles or NAP, and CDOM was earlier referred as “yellow substance”, gilvin, or Gelbstoff (German), and since Gelbstoff is still retained, CDOM is given as a_g. Most of the particulate matter will absorb and scatter light, while CDOM will only absorb light. The spectral absorption due to CDOM and NAP have similar absorption spectral variations, and the combined absorption due to CDOM and NAP is often referred to as colored detrital matter (CDM = CDOM + NAP) (Siegel, 2002).

The CDOM, NAP, and CDM vary spectrally in a similar manner, exponentially decaying with increasing wavelength. The slopes of CDOM in the different spectral segments are important parameters and have been used to understand the CDOM of these waters (Dias, Thayapurath, Sahay, & Chauhan, 2017). As a part of this study, a new algorithm has been developed to find the slope of spectral variation of CDM for these waters (Thayapurath, Dias, Desa, & Sahay, 2018). All the components of absorptions due to phytoplankton, CDOM, and NAP are important. Apart from the peaks at Soret band, 440 nm, and at 676 nm of the $a_{ph}(\lambda)$ which are attributed to chlorophyll a pigment, there are other peaks that indicate the presence of other pigments (Bidigare et al., 1990; Hoepffner & Sathyendranath, 1991). The contributions by water $a_w(\lambda)$ are low till 500 nm and very significant in the longer wavelengths. With the exception of constant $a_w(\lambda)$, spectral variations of other components differ for the coastal and estuaries of Goa (Figure 2.2, top). The contributions of each component to the total absorption were contrasting for these waters (Figure 2.2, bottom). The contributions of $a_d(\lambda)$ peak around 550 nm and then decrease (Shi et al., 2013). In the coastal waters, $a_{ph}(\lambda)$ was much higher than CDM, while in the estuaries, CDM dominates over $a_{ph}(\lambda)$. The contribution of CDM at 412 nm in the coastal waters was about 34%, while in the estuaries, it was about 90%. These levels of contributions affect the underwater light field and optical properties of interest like remote sensing reflectance $R_{rs}(\lambda)$ and water leaving radiance $L_w(\lambda)$, whose spectral shape gets modified. The contribution of CDOM was lower in the coastal waters as compared to the estuaries (Dias, Thayapurath, Sahay, & Chauhan, 2017). One of the first spectral IOPs measured using AC-9 in the Arabian Sea showed $a(\lambda)$ and $c(\lambda)$ much lower than coastal waters (Suresh et al., 1998).

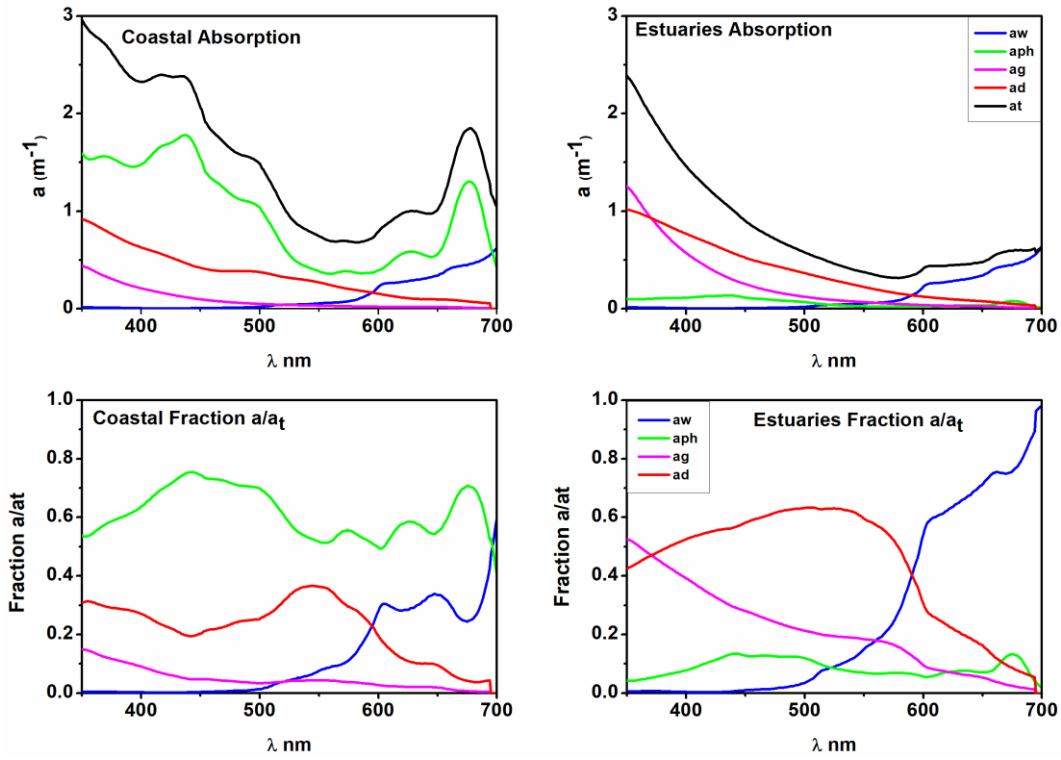

Figure 2.2 The absorptions of various components $a_w(\lambda)$, $a_{ph}(\lambda)$, $a_g(\lambda)$ and $a_d(\lambda)$ for the coastal water and estuaries (top left for coastal, top right for estuaries) and the contributions of the components given as fraction of the total absorption (bottom left for coastal and bottom right for estuaries)

Beam attenuation measured by AC-9 will be

$$c(\lambda) = c_t(\lambda) - c_w(\lambda) \tag{5}$$

The scattering will be

$$b(\lambda) = c(\lambda) - a(\lambda) \tag{6}$$

The $b(\lambda)$ and $c(\lambda)$ are also commonly referred to as particulate contributions and given as $b_p(\lambda)$ and $c_p(\lambda)$ (Huot et al., 2008).

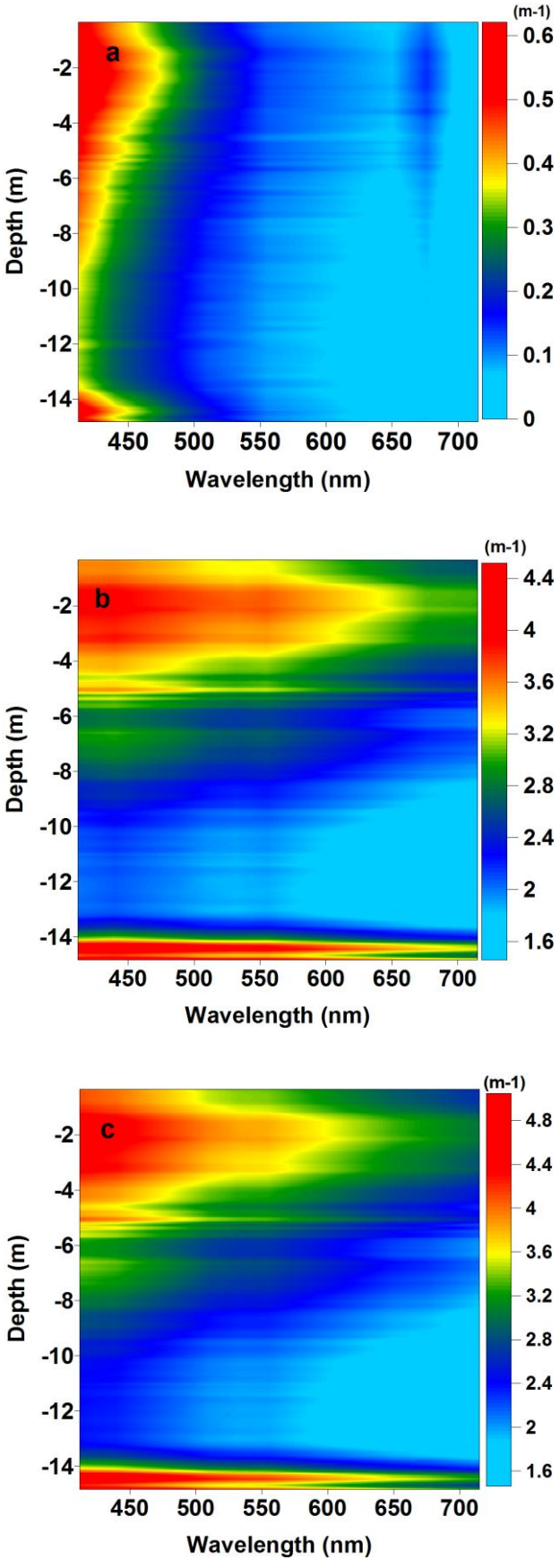

Figure 2.3 The a(λ) (a- top) and c(λ) (c- bottom) measured using AC-9 in the coastal waters (17/12/2013) and b(λ) derived from and c(λ) - a(λ) (b - middle).

The a(λ), b(λ) and c(λ) measured by AC-9 for a station in the coastal waters shows a typical variation of these parameters in these waters, with large particulate matter in the sub-surface at about 3 to 4 m depth and also at the bottom (Figure 2.3). The particulate matters at 3 to 4 m are due to more chlorophyllous materials like phytoplankton, indicated by the relatively higher absorption at 676 nm, which is due to the absorption of chlorophyll a. The high values of a(λ) at the bottom in lower wavelength below 440 nm indicate the presence of more CDM, and the high in the b(λ) and c(λ) at the bottom indicate an abundance of suspended sediment. There is much less chlorophyll beyond the depth of 9 m, as indicated by low values of a(676). The average a(λ), b(λ) and c(λ) show the contributions of a(λ) to be far lower than b(λ) and c(λ). (Figure 2.4)

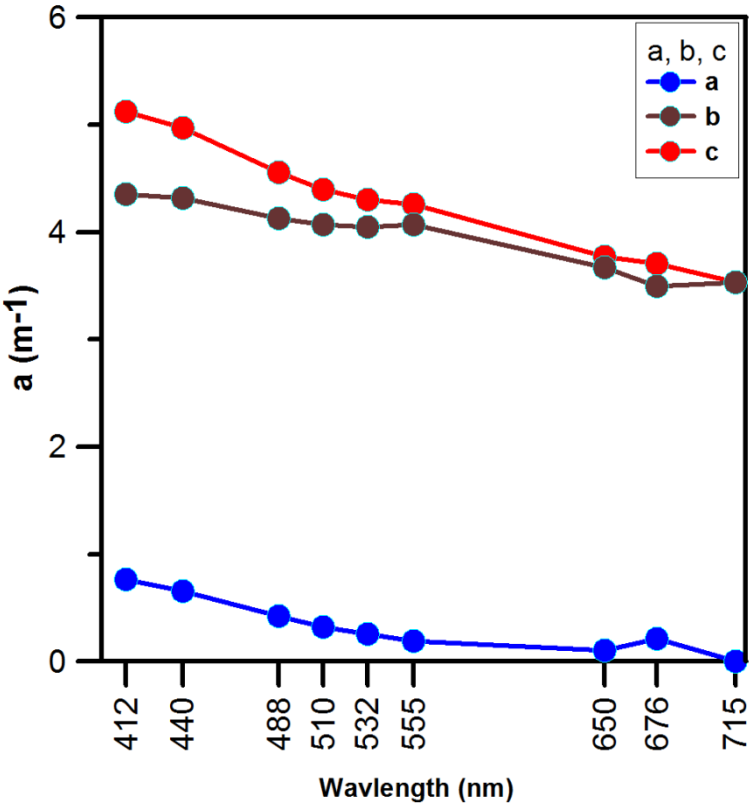

Figure 2.4 The average of a,b and c measured by AC-9 at nine wavelengths

Scattering from a particle (0 to π) can be either forward scattered (0 to π/2) or backscattered (π/2 to π). Large particles enhance forward scattering, and backscattering is more sensitive to smaller particle sizes (Boss et al., 2004). In marine optics and ocean color studies there is more emphasis on backscattering coefficient, $b_b(\lambda)$, particulate backscattering $b_{bp}(\lambda) = b_b(\lambda) - b_{bw}(\lambda)$, where $b_{bw}(\lambda)$ is the contribution due to pure water and fraction of particulate backscattering $Bp = b_p/b_{bp}$. Wherever there is particulate matter,

b_b (Figure 2.5), b, and c will be high (Figure 2.3). From these optical parameters, the importance of IOPs can be appreciated in understanding the optically active constituents of water.

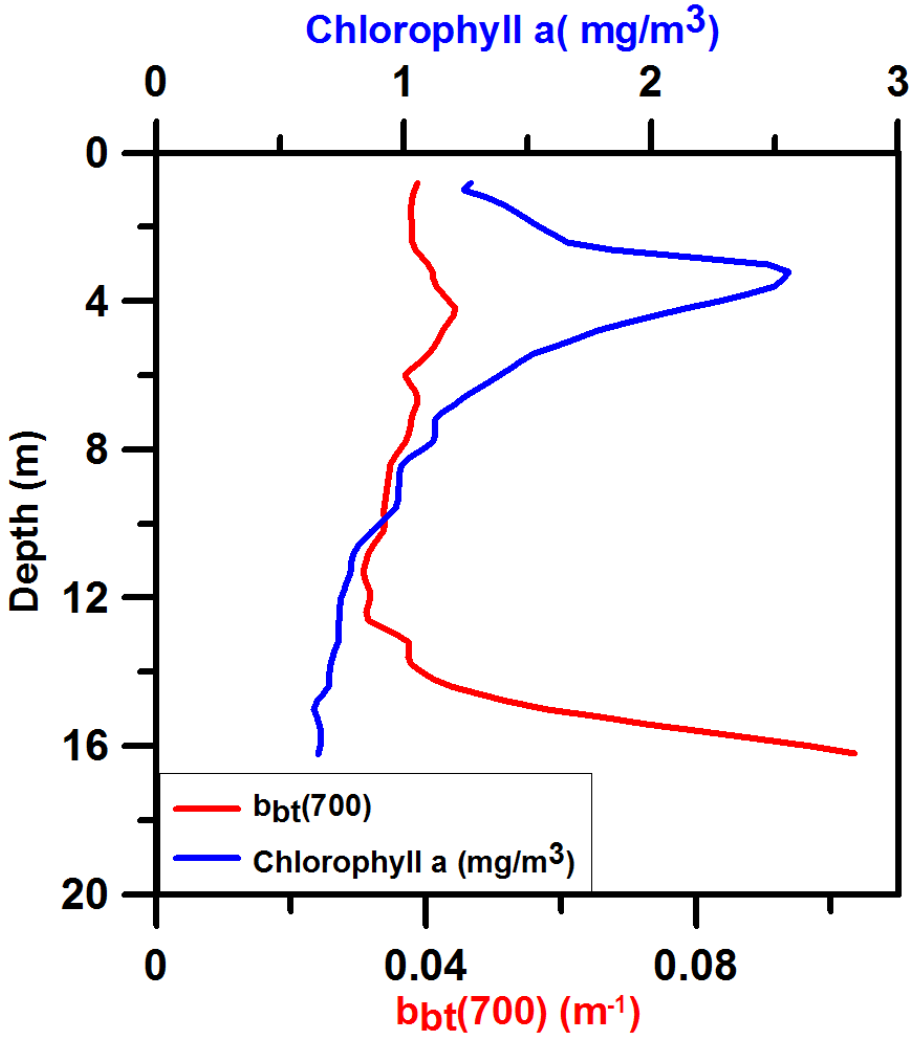

Figure 2.5 The depth profiles of $b_{bt}(700)$ and chlorophyll from sensor

2.2.2 PSD slope ξ, bulk refractive index, and single scattering albedo ω_o.

The particle size distribution (number of particles per unit volume per unit particle size) and the refractive index are parameters that influence the scattering of light in water (Boss & Pegau, 2001; Boss, Twardowski, & Herring, 2001; Buonassissi & Dierssen, 2010). PSD for the oceanic, estuarine, and coastal waters are best given by a hyperbolic power-law function or "Junge type" with the power index or differential slope ξ that decreases with an increase in particle size. The slope ξ usually ranges from around 2.5 to 5, and the measurements from various water types confirm it to lie between 2.7 to 4.7 (Buonassissi &

Dierssen, 2010). The index of power-law PSD ξ can be derived from the spectral particle beam attenuation coefficient $c(\lambda)$ measured by AC-9 as, $c \alpha \lambda^{-\gamma}$ and $\xi = \gamma + 3$. The slope ξ has been found to deviate from the linear relation, and the new relation was given as $\xi = \gamma + 3\text{-}0.5e^{-6\gamma}$ (Boss, Twardowski, & Herring, 2001).

The refractive index of water is the lower limit for biological materials, and it is assumed that the water of the algae has the same density and refractive index as seawater and its value is taken as 1.339 at a density of 1.025 g/cm3, which corresponds to a salinity 35.0 psu, at a temperature 20.0°C and a wavelength of 589 nm. For most of the marine biological applications, the refractive index is taken relative to the seawater. Thus, it will be observed that the living organic materials have lower refractive indices close to unity, which is due to their high water content. The bulk indices of relative refraction for phytoplankton are in the range of 1.02 to 1.07 and for inorganic particles such as quartz and aragonite within 1.15 and 1.24 (Carder, Tomlinson, & Beardsley, 1972). The bulk refractive index (relative to water) n_p, has been modeled as a function of particulate backscattering ratio $\tilde{b}_{bp}$ ($\tilde{b}_{bp}$ = particulate backscattering, b_{bp}/particulate scattering b_p) and ξ (Twardowski et al., 2001). An algorithm to derive a refractive index was developed, and the same was used to show the variations of n_p of the coastal waters off Goa (Suresh, Desa, Mascaranahas, et al., 2006).

The single scattering albedo is the probability that the photon may be scattered before it is absorbed, $\omega_0 = b/c$ also plays an important role. An algorithm to derive single scattering albedo and backscattering ratio were derived for the waters of the Arabian Sea (Suresh, Desa, Matondkar, et al., 2006).

For the data in Figure 2.4 the values were $\gamma = 0.9163$, $\xi = 3.9142$ and $n_p = 1.105$.

2.2.3 Underwater average cosine

The underwater average cosine of the entire light field can also be defined as the average cosine of zenith angles of all the photons at a particular point. Since the average cosine gives directional information about the radiance distribution, it varies between 0 and 1. When the value of $\bar{\mu}(\lambda) = 0$, it indicates that light is uniformly distributed in the water while when $\bar{\mu}(\lambda) = 1$ all the light propagates vertically down. The value of $\bar{\mu}(\lambda)$ depends

on the absorption and scattering properties of the medium, and it is higher in absorption-dominated waters such as open ocean than in the coastal waters. The value of $\bar{\mu}(\lambda)$ decreases with depth, and the rate of change with depth for most waters are strongly dependent on scattering, while the influence of absorption is only seen in clear waters. Robust algorithms were developed to derive spectral underwater average cosine for these waters at 490 nm (Talaulikar, Thayapurath, & Desa, et.al., 2012) and spectral $\bar{\mu}(\lambda)$ (Talaulikar, Suresh, Desa, & Inamdar, 2014a). It is an important parameter that can be used to derive spectral absorption $a_t(\lambda)$ with the formulation of Gershun (Gershun, 1939) that relates the IOP with AOP (Thayapurath, Talaulikar, Desa, & Lotlikar, 2016).

2.3 AOP

Apparent Optical Properties (AOPs) were obtained from the in-situ measurements using hyperspectral profiling radiometer, Hyper-OCR, and derived from RTE simulations using Hydrolight software.

2.3.1 Downwelling irradiance, $E_d(\lambda)$

Solar light is a prime parameter and source that determines the underwater light. The spectral solar irradiance just beneath the surface of water $E_d(0,\lambda)$ decrease exponentially with depth, z (meters) following the Lambert-Beer law and the solar irradiance at any depth z, $E_d(z,\lambda)$ is given as

$$E_d(z,\lambda) = E_d(0,\lambda)e^{-K_d(\lambda)z} \tag{7}$$

where $K_d(\lambda)$ is the average diffuse attenuation of downwelling irradiance. The shape of $E_d(\lambda)$ is similar to $E_s(\lambda)$. The solar irradiance will be attenuated spectrally with depth, and the spectral shape of the $K_d(\lambda)$ will determine the penetration of light. The spectral downwelling irradiance $E_d(\lambda)$ in the coastal and estuaries are not the same (Figure 2.6). The wavelength of the light that penetrates the deepest in the estuaries shift to a longer wavelength compared to the coastal waters. (See the band in Figure 2.6).

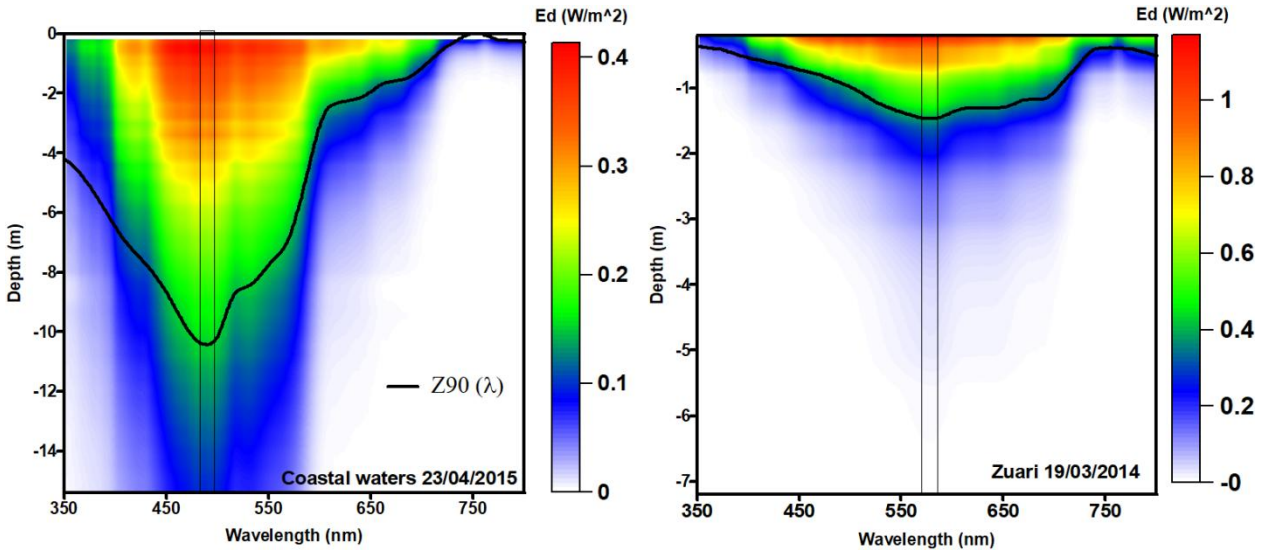

Figure 2.6 $E_d(z,\lambda)$ in the coastal waters (left) and estuary (right). The band shown is the $E_d(z,\lambda)$ that penetrate the deepest.

2.3.2 Remote sensing reflectance, $R_{rs}(\lambda)$

Remote sensing reflectance $R_{rs}(\lambda)$ is an important AOP which has gained importance since the 1990s and has been of use since then in the developments of algorithms to derive parameters from ocean color satellite such as SeaWiFS. This is the most often sought after optical parameter for the ocean color related studies. In simple terms, it is the amount of radiance that exits the surface of the water for the amount of solar irradiance that enters the water.

The earlier optical models were based on reflectance, $R(\lambda)$ just below the surface of the water, and $R(\lambda)$ primarily depended on the ratio of backscattering to the absorption of water, $b_{bt}(\lambda)/a_t(\lambda)$. This model was proposed by Russian scientists Gamburstev, Kozlyianinov in 1922, and thereafter by S.Q Duntley at MIT, USA, in 1942, 1974 (Morel and Prieur, 1977). Since Δ is limited to a small value of 0.05, the model as per Equation (8) became one of the much referred to models in marine optics and was also used to derive various products using empirical models (Equation (9)) (Morel and Prieur, 1977).

$$R(\lambda) = 0.33\frac{b_{bt}(\lambda)}{a_t(\lambda)}(1+\Delta) \tag{8}$$

$$R(\lambda) = 0.33 \frac{b_{bt}(\lambda)}{a_t(\lambda)} \tag{9}$$

With the advent of new and refined methods in satellite remote sensing applications, the reflectance R(λ) was replaced with remote sensing reflectance, $R_{rs}(\lambda)$ and the model used now is given as (Lee et al., 1994)

$$R_{rs}(\lambda) = \frac{f}{Q(\lambda)} \frac{t^2}{n^2} \frac{b_{bt}(\lambda)}{a_t(\lambda) + b_{bt}(\lambda)} \tag{10}$$

Though f is a function of solar zenith angle,(Gordon et al., 1988) f/Q≈0.0949 is found to be nearly independent of solar zenith angle and, f ≈ 0.33 (Morel and Prieur, 1977), t is the transmittance across air to sea and n is the real part of the refractive index of sea water, $t^2/n^2 = 0.54$ (Austin, 1974).

The above model was derived for optically deep waters. For shallow waters, the bottom reflectance also needs to be considered. The measured bottom reflectances for various bottom types for these waters of estuaries are given in Chapter 4. The model for $R_{rs}(\lambda)$ in shallow waters will be a function of spectral absorption a(λ), scattering or VSF β, bottom reflectance ρ, subsurface viewing geometry, solar zenith angle θ_w, viewing angle from nadir θ, and azimuth angle from solar plane φ. (Lee et al.,1999).

$$R_{rs}(\lambda) = f[a_t(\lambda), \beta(\lambda), \rho(\lambda), Z, \theta_w, \theta, \varphi] \tag{11}$$

The above model has been parameterized with the above mentioned parameters using analytical models (Albert & Mobley, 2003) and semi-analytical methods with coefficients derived from Hydrolight simulations (Lee et al., 1999).

2.3.3 Diffuse attenuation coefficient $K_d(\lambda)$

As mentioned earlier, $K_d(\lambda)$ determines how the underwater downwelling irradiance $E_d(\lambda)$ is attenuated in the water.

$$K_d(z, \lambda) = \frac{-1}{E_d(z, \lambda)} \frac{dE_d(z, \lambda)}{dz} \tag{12}$$

This is a local property of water at a particular depth z. In the open ocean, $K_d(\lambda)$ will be very low, and in coastal waters, $K_d(\lambda)$ will be lower than the waters of estuaries. A little ambiguity in the definitions need to be clarified (Gordon, 1989a; Lee, Du, & Arnone, 2005). The $K_d(\lambda)$ given in Equation (12) is the average $K_d(z,\lambda)$ over the depth 0 to z (m), while the $K_d(z,\lambda)$ obtained from the measured values of $E_d(z,\lambda)$ is computed between two close depths, z_1 and z_2 (Mueller et al., 2003). This will give the depth variations of $K_d(z,\lambda)$ (Equation (13).

$$K_d(z_2 - z_1) = \frac{1}{z_2 - z_1} \ln\left[\frac{E_d(z_1)}{E_d(z_2)}\right] \tag{13}$$

Since $K_{d(}\lambda)$ have been modeled in terms of IOPS $a(\lambda)$ and $b_b(\lambda)$, similar to $Rrs(\lambda)$ it has been included in the list of 'quasi inherent property' (Baker & Smith, 1980). There are many algorithms to determine $K_d(\lambda)$ and Kd(490), and they have been evaluated (Brewin et al., 2015; Suresh et al., 2007; Thayapurath & Talaulikar, 2011). The mean spectral $K_d(\lambda)$ for the coastal and estuaries show large differences in the blue region (Figure 2.7).

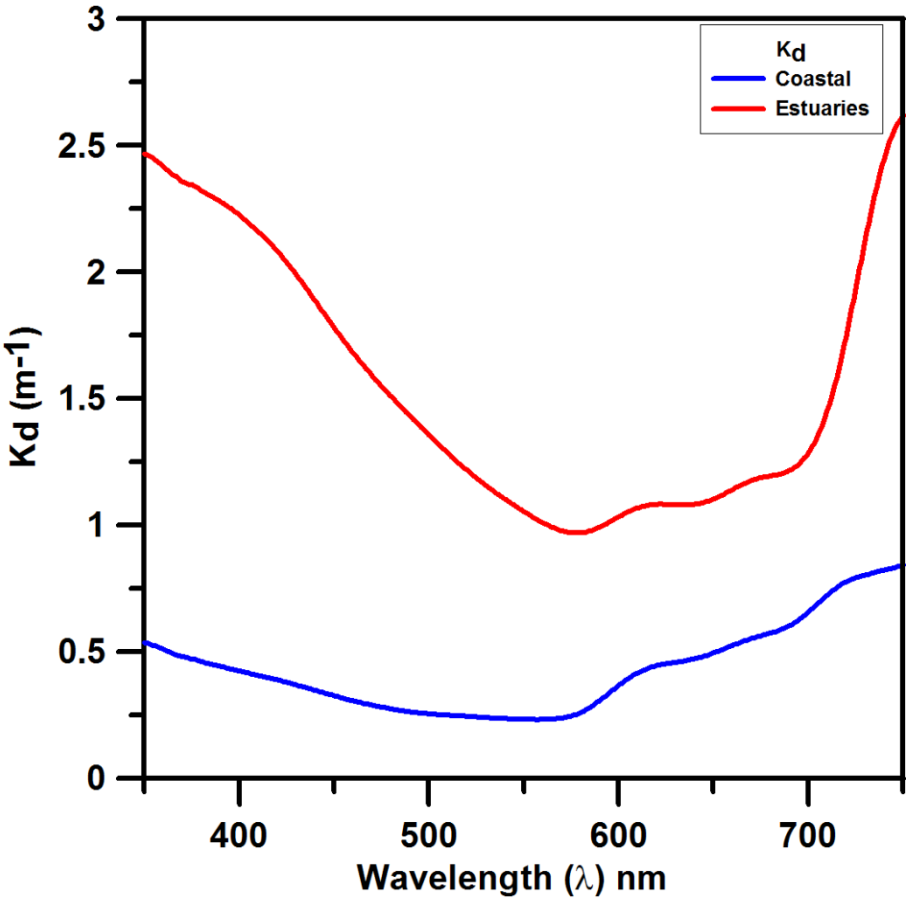

Figure 2.7 Average $K_d(\lambda)$ for the coastal water and estuary

2.3.4 Depths, Z_{90}, Z_{eu}, Z_{sd}

There are few depths defined in these studies which need elaboration. There is a depth that is often used with regards to satellite remote sensing applications known as Z90. Most optical and biological data are available as depth profiles, while the ocean color satellite will provide a value of any parameter, which is an average of the depth profile values. The critical issue is about the 'average value' and depth within which the average is considered. The satellite provides the radiance that exits from the surface of the water, and this radiance carries information about the constituents within the water. Derived from the quasi-single scattering approximation, it was shown for a homogeneous ocean that about 90% of the diffusely reflected irradiance (excluding specular reflectance) originates from the first optical depth, Z_{90} (Gordon & McCluney, 1975).

$$Z_{90}(\lambda) = \frac{1}{K_d(\lambda)} \tag{14}$$

Hence optical parameters and optically active constituents are averaged within Z_{90} when algorithms are developed or validated with ocean color satellite data. This 'penetration depth' Z_{90} is at a depth where Photosynthetically Available Radiation, PAR, reduces to 1/e of its value at the surface or at 36.8% of PAR. This depth is only 0.217 of the euphotic layer. This is a spectral quantity, and the singular value of Z_{90} is given here as the maximum of $Z_{90}(\lambda)$ and the wavelength of a maximum of $Z_{90}(\lambda)$ (Figure 2.8).

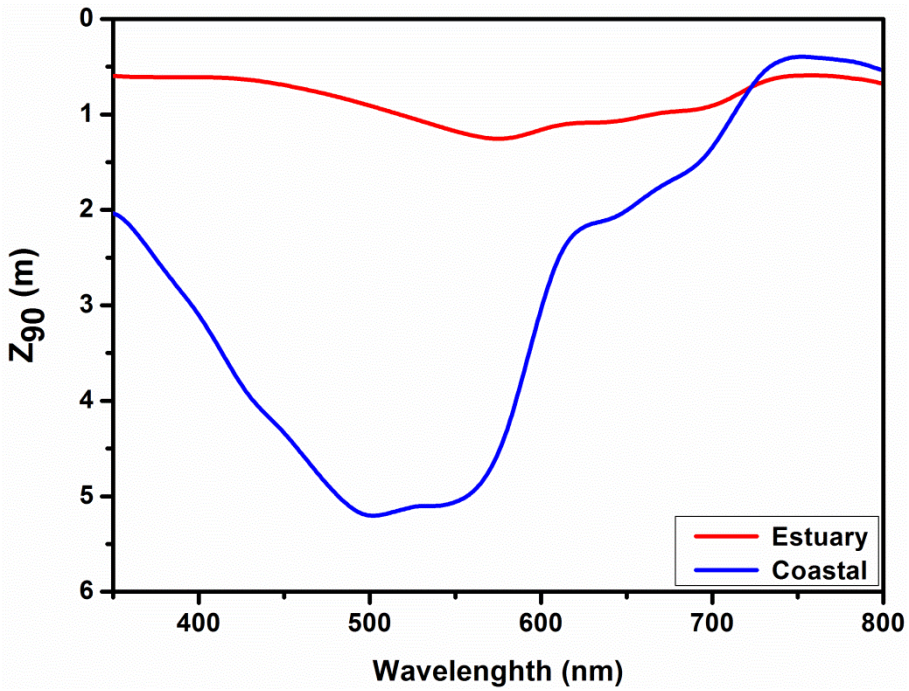

Figure 2.8 Average $Z_{90}(\lambda)$ for coastal water and estuary

Euphotic depth Z_{eu} (m) is another important parameter. Light energy in photosynthesis used by phytoplankton in the water help to generate organic compounds. The production of organic carbon from inorganic carbon during photosynthesis is defined as primary productivity (PP) (Lee, Marra, Perry, & Kahru, 2015). Euphotic depth defines a depth region where this primary production by phytoplankton is valid. It is defined as the depth where PAR is 1% of its value at the surface (Lee et al., 2007). All organisms in water will respire, converting the organic matter to carbon dioxide. There is a critical depth where respiration and photosynthesis equal, and this is often just below the euphotic zone, also known as 'compensating depth' as defined by Sverdrup. Below this depth is the aphotic zone where respiration exceeds photosynthesis. Most primary productions are calculated within this depth. The average nominal compensation depth is the euphotic depth Z_{eu}. Earlier measurements were restricted to 10% due to the constraints on the sensitivity of the

instruments measuring underwater light. The average value of Z_{eu} of 1% light depth in the ocean is about 65 m, which is about ten times the value in the estuaries of Mandovi and Zuari. The euphotic zone being defined within Z_{eu}, and limited to 1% light level has been contested with regards to photosynthesis by the phytoplankton and their energy demand (Banse, 2004). Considering the contribution of phytoplankton to photosynthesis, up to 1% light level would not make a large difference in the open ocean for integrated values unless there was a deep chlorophyll maximum within this depth. However, as the coastal and estuaries are shallow and with the availability of phytoplankton of various species at very low of light, there will be contributions from phytoplankton even up to Z_{eu} (Ramakrishnan, Thayapurath, Manguesh, & Dias, 2018).

Secchi depth, Z_{sd}(m) is the depth where the Secchi disk first disappears from sight when lowered in the water. It is discussed in Chapter 7. This basic and required parameter is estimated without any sensors to measure either the depth or any optical parameter. This Z_{sd} is a measure of the transparency of water and studies carried out in the coastal waters and estuaries of Z_{sd} have resulted in models, empirical relations with constituents and optical parameters(Levin et al., 2000; Suresh et al., 1998; Suresh, Naik, Bandishte, et al., 2006; Thayapurath, Joshi, Talaulikar, & Desa, 2016).

2.4 Radiative Transfer Equation (RTE)

The Radiative Transfer Equation (RTE) describes mathematically what happens to the light traveling inside the medium, such as water. A beam of light having unpolarized spectral radiance $L(z,\mu,\varphi,\lambda)$, traveling through the medium in a direction θ, ϕ may undergo different processes during its journey through the medium in which there may be gains and losses of photons, The gains are from inelastic scattering, emissions from bioluminescence while losses are from scattering and absorption (Mobley, 1994).

This is given as

$$\mu \frac{dL(z,\mu,\phi,\lambda)}{dz} = -c_t L(z,\mu,\phi,\lambda) + S_e(z,\mu_0,\mu,\phi,\lambda) + S_i(z,\mu_0,\mu,\phi,\lambda) \quad (15)$$

where z- depth, λ- wavelength, $\mu_0 = \cos(\theta_s)$, $\mu = \cos(\theta_v)$, θ_s - solar zenith angle, θ_v – viewing angle, ϕ - viewing azimuth angle, c_t – beam attenuation coefficient, the sum of absorption + scattering, S_e – elastic source contribution and S_i – inelastic source

contribution. Inelastic contributions S_i can be found from Raman scattering during fluorescence from the fluorescence of dissolved organic matter (FDOM) and chlorophyll fluorescence. The internal sources may be from bioluminescence.

The solar light entering water is usually unpolarized; however, the underwater light is partially polarized. The vector RTE considers polarization of light, making computation and validation difficult. Considering the practical applications which do not generally utilize polarization either in the developments of optical algorithms, utilization of the light by phytoplankton, or measurements, it is thought prudent to use scalar RTE without polarization. There are radiative transfer models available, and the results of their comparisons showed that the Monte Carlo method and Discrete Ordinate method could compute all quantities with better accuracy compared to others (Mobley, Gentili, & Gordon, 1993).

The software Hydrolight from Sequoia Inc. is based on the invariant imbedding techniques to solve the radiative transfer equation (Mobley, 1994). Since the objectives of the studies required understanding the underwater light field, simulations were carried-out using Hydrolight (Version 5.2). Hydrolight simulations were fast and could use the measured optical parameters as inputs to provide the complete information of the underwater light field (Chapter 3). It also had the advantage of providing optical parameters that could not be measured due to the non-availability of instruments to measure in-situ, which include parameters as underwater average cosine. These simulations carried-out using Hydrolight for these waters allowed to study various parameters and also develop for the first time an algorithm to derive spectral underwater average cosine and use it for ocean color remote sensing (Talaulikar, Suresh, Desa, & Inamdar, 2014a; Talaulikar, Suresh et al., 2012).

2.5 Ocean Color Remote Sensing

Here a brief overview of the radiance observed by the ocean color satellite sensor and atmospheric correction is presented (Figure 2.9). At the satellite altitude, the sensor-measured radiance at a given wavelength for the ocean-atmosphere system can be written as a linear sum from various contributions (IOCCG, 2010)

$$L_t(\lambda) = L_r(\lambda) + L_a(\lambda) + t(\lambda)L_{wc}(\lambda) + T(\lambda)L_g(\lambda) + t(\lambda)L_w(\lambda) \quad (16)$$

where the radiance contributions are from

$L_t(\lambda)$ - Total Radiance received by the satellite sensor.

$L_r(\lambda)$ - Rayleigh scattering from air molecules

$L_a(\lambda)$ - Aerosol scattering

$L_{wc}(\lambda)$ - white caps on the surface of the water

$L_g(\lambda)$ - sunglint reflection

$L_w(\lambda)$ - water leaving radiance from the surface of water

$T(\lambda)$ - direct transmittance

$t(\lambda)$ - diffuse transmittance

The water-leaving radiance $L_w(\lambda)$, which can be related to the ocean near-surface physical and bio-optical properties, is the desired quantity to be retrieved after the atmospheric correction for the ocean color remote sensing applications. This quantity $L_w(\lambda)$, which contains the information about the constituents, is only about 10% of the total radiance received by satellite, and the remaining contributions are mainly from Rayleigh and aerosol scattering. The procedure for removing the atmospheric and other contributions to obtain $L_w(\lambda)$ is known as the atmospheric correction method. The atmospheric correction procedure uses the bands in the red and infrared channels, based on the assumption that signals from the ocean are nil or very minimum at these bands, and the ocean appears as a black target at these wavelengths. This is known as "dark pixel assumption". The contributions of the atmosphere at the other visible channels are then determined by extrapolations of the contributions from two or more bands in the red region to the equivalent atmospheric path radiance in the lower visible bands. Having determined the atmospheric path radiance, the contribution of water leaving radiance is obtained by subtracting the path radiance from the total radiance observed by the sensor, $L_t(\lambda)$. For further reading on satellite remote sensing, it is available at https://ioccg.org/what-we-do/training-and-education/educational-links-and-resources/.

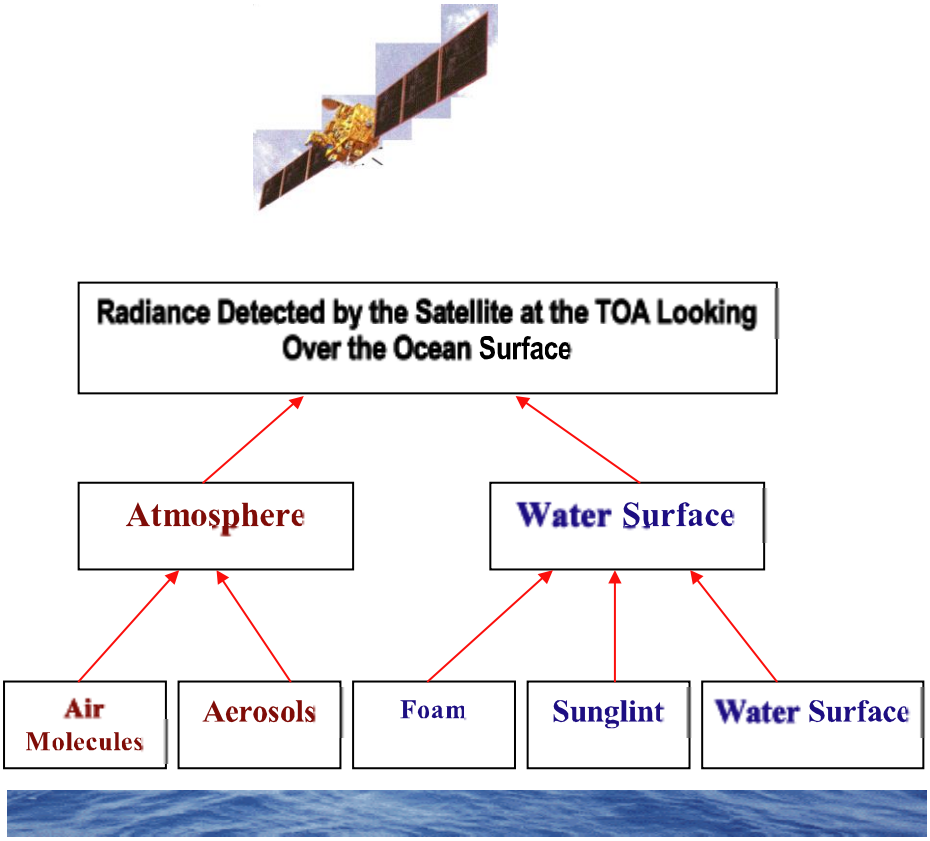

Figure 2.9 Contributions of radiance detected by the ocean color satellite sensor.

The ocean color satellite data were processed using a free software SeaDAS (Version 7.5) available from Ocean Color group of NASA (https://seadas.gsfc.nasa.gov/).

CHAPTER 3. METHODOLOGY

3.1 Study area

The bio-optical properties of coastal and estuarine waters will be affected by the constituents in the water. These constituents that affect the optical parameters will be controlled by the season, physical, biological, chemical phenomenon and processes in these waters.

In the coastal waters there were seasonal algal blooms such as *Trichodesmium* spp during summer (D'Silva, et al., 2012; Desa et al., 2005a; Devassy, Bhattathiri, & Qasim, 1979; Dias, Suresh, & Kurian, 2019; Tholkapiyan, Shanmugam, & Suresh, 2014) and bloom of *Noctiluca* were often observed during the February-March period (Devassy & Nair, 1987; D'Silva et al., 2012; Do Rosário Gomes et al., 2014; Mishra & Gould, 2016). A phenomenon of oxygen minimum is observed in these coastal waters (Naqvi, 2009). Thermal inversions were also observed during winter (Thadathil, 1992).

The constituents of Mandovi and Zuari estuaries will be affected by physical processes such as tides during non-monsoon seasons, run-off during monsoon and anthropogenic activities. Physical processes have been studied (Manoj, Unnikrishnan and Sundar, 2009; Sundar et al., 2015; Vijith, Sundar, & Shetye, 2009). These physical processes will influence biological (Gonsalves et al., 2009; Patil & Anil, 2015; Pednekar et al., 2018; Pednekar, et al., 2014; Rajaneesh & Mitbavkar, 2013), chemical (DeSousa & SenGupta, 1986; Anand et al., 2014), and geological (Kessarkar et al., 2010) parameters. Hence it is presumed that these processes will modify and alter the optical parameters of these waters.

The waters of Goa, India for this study include the two estuaries Mandovi and Zuari and the coastal waters off Goa (Latitude 15.35 to 15.55° N, Longitude 73.65 to 74.047° E) (Figure 3.1). Mandovi and Zuari are the largest rivers of the eleven major rivers of Goa (Pradhan, 2016). These two rivers drain into the eastern Arabian Sea and become the two major estuaries of Goa. The two estuaries are Mandovi in the north and Zuari in the south, with the Kumbharjua canal interconnecting the two estuaries upstream at a distance of about 16 Km. The two coastal sites were INCOIS, which forms the extension of the Mandovi and the CaTS (CAndolim Time Series) which was off Candolim and north of INCOIS site.

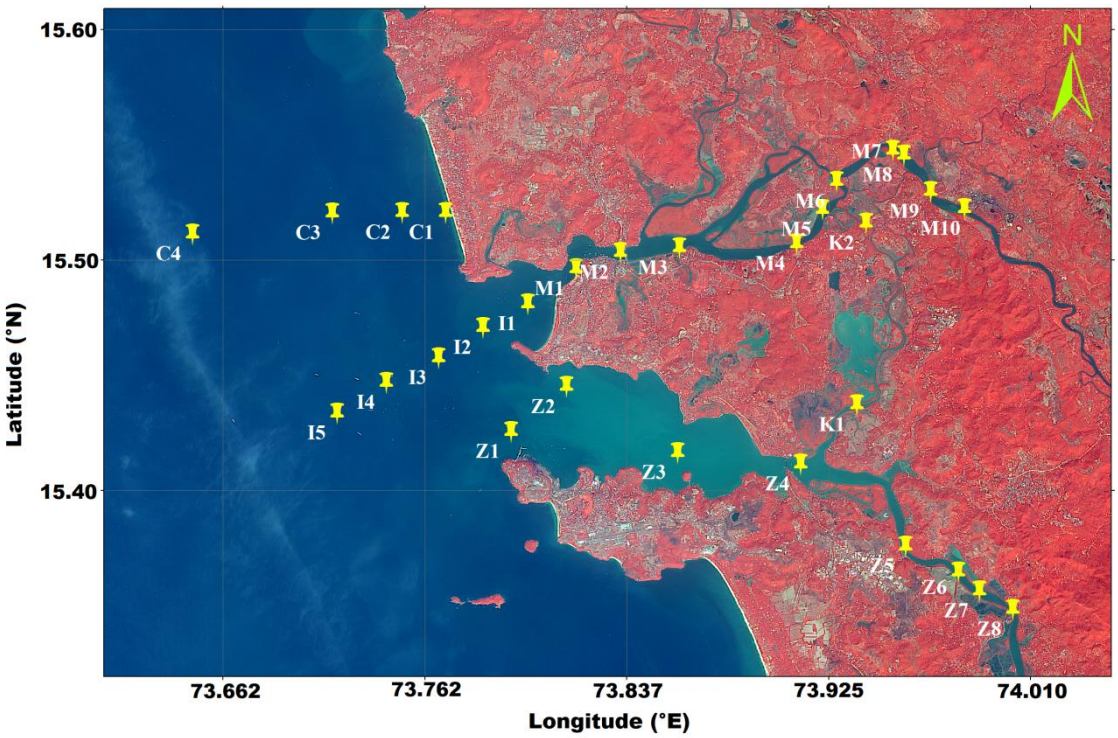

Figure 3.1 Study area with time-series stations in the coastal waters off Goa (C1 –C4 and I1 – I5) and the two estuaries of Goa, Mandovi (M1 –M10) and Zuari (Z1 – Z8), and the Kumbharjua canal (K1 and K2).

The sampling sites for time-series measurements were selected considering the variations of physical, biological and chemical parameters from various studies undertaken earlier. The stations at the coastal sites were transects at regular distances from the shore. On-going biogeochemical studies have been continuing at the CaTS sampling stations for more than a decade (Naqvi et al., 2006,2009; Shenoy et al., 2012). The summary of the field measurements is given in Table 3.1.

Table 3.1 Summary of the measurement sites

Site	Latitude (°N)		Longitude (°E)		Depth (m) (Minimum and Maximum)		Depth (m)	Distance (Km)	n
	From	To	From	To	Min	Max	Mean		
CaTS	15.5092	15.5223	73.6484	73.7696	4.3	30.0	17.0	12.38	60
INCOIS	15.4204	15.4813	73.6617	73.7972	4.4	27.9	14.8	12.19	123
Kumbarjua	15.4367	15.5157	73.9372	73.9417	3.0	5.0	4.2	19.58	6
Mandovi	15.4955	15.5500	73.8145	73.9840	1.0	14.0	6.2	28.80	197
Zuari	15.3479	15.4481	73.7874	74.0051	2.0	15.0	7.1	28.48	130

The mean depths of the sites Mandovi, Zuari, Kumbharjua, CaTS and INCOIS were 6.24m, 7.08m, 4.16m, 14.8 and 17.0 respectively. The information on the regular stations is given in Table 3.2. There were also stations which were not part of these regular stations and carried-out measurements during studies related to algal blooms, bottom reflectance, bathymetry, CDOM, bioluminescence and others. The distance was given with reference to the coastline, being positive with increasing longitude or moving to the right in the estuaries and negative towards the left from the coastline or with decreasing longitude. Thus, the distances of most stations of estuaries were positive while those in coastal waters were negative. The depths increased moving away from coast in the coastal waters. The depths given in Table 3.2 were the mean depths of the stations and these depths could vary with tides and during the monsoon. There were no noticeable linear variations of depths with distance in the estuaries. However there was a decrease in depths moving upstream until about 15 Km, at the rate of 0.5 m per Km. The physical description of the two estuaries and their characteristics have been studied (Vijith, 2014). The Mandovi and Zuari estuaries are classified as monsoonal and mesotidal estuaries (Manoj,Unnikrishnan and Sundar, 2009).

Mandovi - M1 is the closest sampling station to the mouth of the estuary and it will have the influence of the coastal waters. On the southern side, there is the St Inez creek that meanders through the various locations inside the Panjim city and empties close to this site. On the north side there is also a small river, Nerul that joins Mandovi close to this site. M2 is largely influenced by the capital city of Goa, Panjim and various anthropogenic

activities. There is a creek Rua de Ourem that also empties near this station. Moving upstream, there is a region of shallow water off Ribander patto, where a green patch of grass is often visible during low tide. This is the sampling station, M3. Very close to this station is the ferry route of Ribander to Chorao. Thereafter there is M4 with relatively deeper water depths, off Old Goa, close to the Old Goa ferry route and the banks have barge, and ship repair yard. The next is a shallow water station, just below the Konkan railway bridge of Divar and is also close to the entrance of the man-made Kumbharjua canal that links Mandovi and Zuari rivers. The M6 is at the confluence of the anabranches of Mandovi River coming around the Divar Island from the north and the south. This is the deepest station in the Mandovi. Frequent and regular sand mining operations were carried-out using boats in these and in regions upstream. This station M7 was at the meander and had shallow region on the inside with plenty of mangroves. The station M8 was close to the Saramanas-Tonka ferry route and an ore loading point. Station M9 was below the Amona Bridge and was a busy area with small canoes. The last sampling point, M10 was of interest as it was an ore loading point with high traffic of barges. The estuary narrows after the region M7 and being a mining area, the transportations of ores creates moderate traffic of barges. Moving upstream after M2 dominant mangroves were observed mostly on the left side of the bank.

The phenomenon and factors in the estuaries that affect the properties of water could be natural and anthropogenic. The properties that affect these water could be due to tides during dry or non-monsoon seasons, river runoff during monsoon, rains, tributaries and rivers that join them, discharges from adjoining fields, khazans, salt pans, broken dyes or ‘bunds’ and the outcome of anthropogenic activities.

Zuari - The sampling stations in the Zuari begin with Z1, from the mouth off Mormugao port. This station has all the characteristics of the coastal waters. Moving ahead towards upstream, the station Z2 is off Siridao. The next station Z3 is off St. Jacinto Island was chosen as some distinct and atypical features observed from earlier studies. Further up was the Z4 station close to the entrance of the Kumbharjua canal that linked Zuari and Mandovi and was on the earlier ferry route of Agassaim to Cortalim and the present route of Cortalim to Madkai ferry. This is close to the Cortalim fishing jetty. The station Z5 was narrower and had ship repair yards and boatyards on the right side of the bank with thick mangroves and rivulets on the left side. It was close to the ferry routes of Adpal and

Durbhat. The next station Z6 and Z7 had plenty of fields and enclosed water logged regions or khazans. The last sampling station,Z8 was below the Borim bridge.

Coastal - There were two coastal sites, Coastal-1 and Coastal-2. Coastal-1 was a transect from the mouth of Mandovi and had 5 stations. These stations were nearly 2.5 Km apart, beginning from the station I1 off Miramar beach in the Mandovi. This was known as INCOIS. The depth of water column in these waters increased at the rate of 1.1 m per Km of distance. The other coastal site, Coastal-2 was a transect just north of Coastal-1 and the stations are same as CaTS (Candolim Time Series). This site was adopted as various biogeochemical studies have been carried-out at CaTS for over a decade (Naqvi et al., 2006, 2009; Shenoy et al., 2012). There were 4 stations (C1-C4) in this transect and the water depth increased at 1.7m per Km.

Kumbharjua – Kumbharjua or Cumbarjua is a narrow 15 Km canal that interconnects Mandovi and Zuari. Though it is a narrow canal with shallow depths, the empty barges often operate in these waters. Tourist boats are often seen in these waters for sighting crocodiles.

Table 3.2 Details of the measurement stations

Station Id	Latitude (°N)	Longitude (°E)	Maximum depth (m)	Distance (Km)
Coastal Waters				
CaTS				
C1	15.52015	73.75911	6.1	-0.56
C2	15.52016	73.74017	13.2	-2.54
C3	15.51997	73.70995	17.8	-5.77
C4	15.51089	73.64941	28.1	-12.33
INCOIS				
I1	15.48055	73.79462	5.95	2.52
I2	15.47037	73.77521	11.2	-0.0012
I3	15.45714	73.75595	15.2	-2.39
I4	15.44648	73.7334	17.8	-5.07
I5	15.43322	73.7121	19.5	-7.79
Estuaries				
Kumbharjua				
K1	15.43673	73.93721	3.8	16.47
K2	15.51556	73.94131	4.4	19.58
Mandovi				
I2	15.47037	73.77521	11.2	0
I1	15.48055	73.79462	5.95	2.52
M1	15.49581	73.81557	5.9	5.33
M2	15.50286	73.83474	8.0	7.92
M3	15.50502	73.86023	3.6	10.65
M4	15.50661	73.91121	6.5	16.36
M5	15.52151	73.92229	3.5	18.44
M6	15.5337	73.92854	14.0	20.56
M7	15.54726	73.95281	6.3	24.02
M8	15.54505	73.9576	6	24.62
M9	15.52934	73.96926	7.6	26.88
M10	15.52188	73.98386	4.9	28.80
Zuari				
Z1	15.42523	73.78746	9.9	1.142
Z2	15.44471	73.81146	5.9	3.49
Z3	15.41604	73.85949	3.8	9.19
Z4	15.41105	73.9129	6.4	14.90
Z5	15.37546	73.95833	7.2	22.16
Z6	15.3642	73.98113	3.7	25.22
Z7	15.35603	73.99043	5.3	26.62
Z8	15.34806	74.00475	8.9	28.42

3.2 Data

There were three types of data used for the studies. They were measured from the region of study, measured data of various other waters obtained from external source, derived from Hydrolight simulations and satellite data (Figure 3.2). The measured data comprised those measured from the coastal waters and two estuaries of Goa, Mandovi and Zuari.

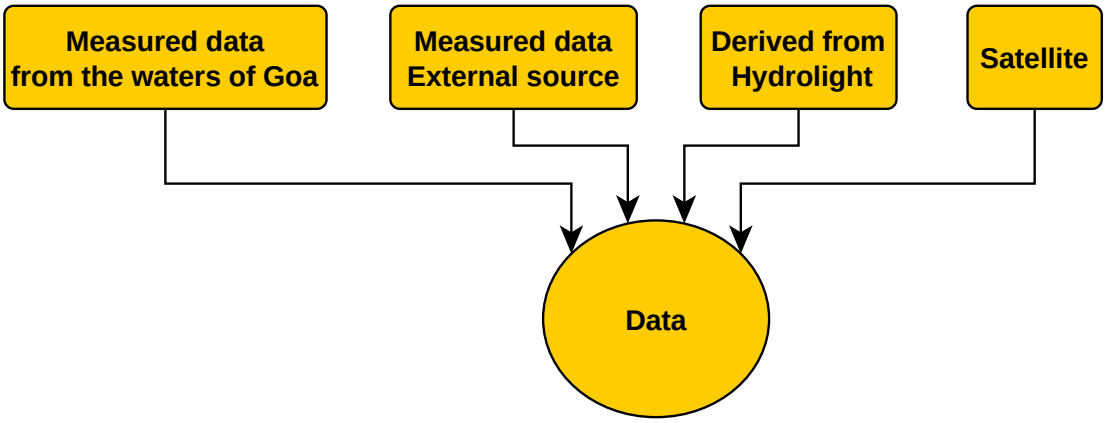

Figure 3.2 Sources of data

3.2.1 Measured data

The apparent and inherent optical parameters were measured using in-situ profiling instruments and sensors at various stations from the boats. The measurements would begin in the morning and finish by evening. The mean solar zenith angles during the measurements were 36° (± 15°).

3.2.1.1 In-situ optical parameters and the instruments

The AOPs and IOPs were measured in-situ using profiling instruments.Parameters	**Wavelength**	**Instrument**	**Make**	**Mode of operation**
AOPS (Downwelling irradiance, upwelling radiance)	Hyper 350-800 nm	Hyper-OCR Radiometer,	Satlantic Inc, Canada	Float and profiling
IOPs (Absorption, beam attenuation and scattering coefficients)	9 (Discrete) 412, 440, 488, 510, 532, 555, 650, 676, 715 nm	AC-9	WetLabs, US	Profiling
IOP (Backscattering coefficient)	3 488, 532, 630 nm	BB3	WetLabs	Profiling Mounted on AC-9 instrument cage
IOP (Backscattering coefficient)	1 650/700 nm	ECOBB (Part of Hyper-OCR radiometer)	WetLabs	Profiling Available with Hyper-OCR radiometer

3.2.1.2 Ancillary parameters and instruments

Parameter	Model	Make	Mode of Operation
Secchi depth	-	In house	Hand operated
CTD Density σ_t = (ρ - 1000) kg m^{-3}	Satlantic	Satlantic (This sensor was part of radiometer)	In-situ profile

3.2.1.3 Biological parameters

The biological parameters were measured with the water samples collected at discrete depths in the laboratory.

Parameters	**Model**	**Make**
Chlorophyll	Fluorometer, Trilogy	Turner https://www.turnerdesigns.com/
Pigments (including chlorophyll)	HPLC, 1100	Agilent http:// www.agilent.com
Total suspended sediment (TSM)	Weighing balance, MA 150	Sartorius
Chlorophyll (sensor)	ECOBB	WetLabs (This sensor is part of radiometer)
Spectral absorption (phytoplankton, CDOM and detritus)	UV-Visible spectrophotometer, UV2600	Shimadzu http://www.shimadzu.com

3.2.2 External data

The NASA bio-Optical Marine Algorithm Data set (NOMAD) is a high quality global dataset of optical parameters compiled by the NASA OBPG at the Goddard Space Flight Center, which is available free to the users from https://seabass.gsfc.nasa.gov/wiki/NOMAD. The last updated data of version 2, 18 July 2008 were used for the developments and validation of algorithms developed. This is a compiled data of in-situ measured optical data from various waters over the globe. These data have been used by others for the various ocean-colour algorithm developments and satellite-data product-validation activities (Werdell & Bailey, 2005). Apart from NOMAD, a larger dataset has been compiled under ESA Ocean Colour Climate Change Initiative (OC-CCI) (Valente et al., 2016). Such data sets of various waters have helped in validating algorithms and determining their robustness.

3.2.2.1 Hydrolight Data

In order to understand the underwater light field there is a theoretical framework, known as the Radiative Transfer Equation (RTE). One of the popular code that is used by many researchers in the field of ocean optics is Hydrolight (Mobley, 1994). It is available from Sequoia Scientific Inc (http://www.sequoiasci.com/product/hydrolight/).HydroLight solves the 1D time-independent radiative transfer equation to compute the radiance distribution within and leaving any plane-parallel water body with much less time than Monte Carlo methods. The objectives of using Hydrolight (Version 5.0) were to understand the underwater light fields, derive some of the optical parameters that could not be measured for the lack of any proven and commercial instruments, and use those parameters for the developments of algorithms to derive products. The parameters required for the execution of Hydrolight are provided in Figure 3.3.

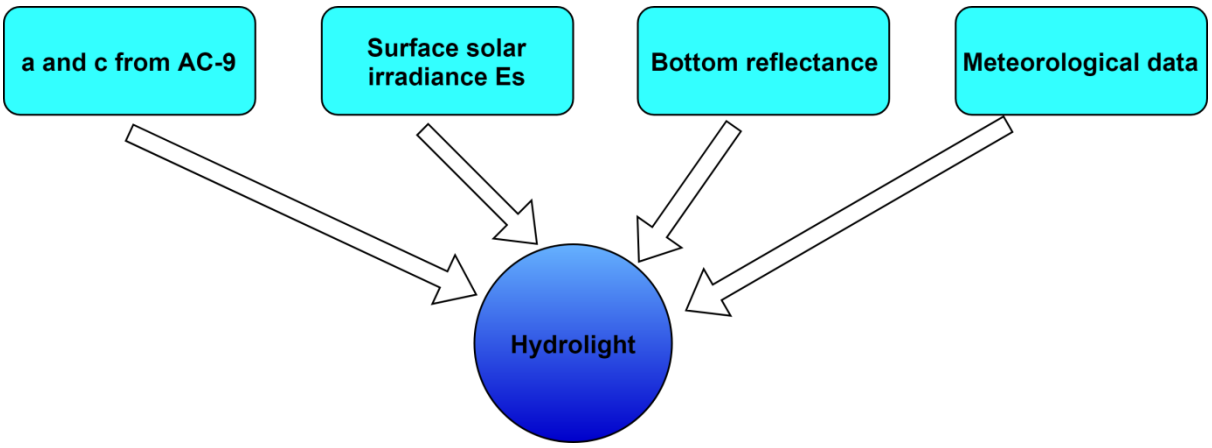

Figure 3.3 Parameters required for Hydrolight simulations

All Hydrolight simulations were carried out neglecting the effect of chlorophyll fluorescence, CDOM fluorescence, Raman scattering and bioluminescence. To understand the underwater light parameters at a station, the Hydrolight were run with the following four parameters which were obtained from the measured IOPS, AOPs and meteorological data at the station and phase function available in Hydrolight.

a. Depth profile spectral $a(\lambda)$ and $c(\lambda)$ from the AC-9 at nine wavelengths.
b. Surface solar irradiance $E_s(\lambda)$ was obtained from the reference sensor of the hyperspectral radiometer, mounted above water at a clear height on the mast of the boat.

c. Bottom reflectance $\rho_b(\lambda)$ was obtained using a Rrs(λ) model for shallow waters (a Albert & Mobley, 2003; Z Lee et al., 1999).
d. The meteorological parameters such as wind speed and relative humidity required for the Hydrolight inputs were obtained from the automatic weather station installed at CSIR-National Institute of Oceanography, Dona-Paula as meteorological data were not measured on the boat during optical measurements at the stations. These data were presumed to be valid since the stations of measurements were not far from the Automatic Weather Station (AWS) locations and the variations of AWS and station location would not yield any large errors in the simulated outputs.
e. Phase function is an important IOP that defines the scattering of the media. The "average particle" Petzold phase function (with b_{bp}/b_p= 0.018) (Petzold, 1972) is the default VSF or phase function in Hydrolight. Since the values of b_{bp}/b_p differs from 0.018 for the coastal and estuarine waters and the VSF is not measured, it was necessary to identify the appropriate phase function agreeing with the waters of which the simulations were being carried-out. Hydrolight provides phase functions based on Fournier-Forand with b_{bp}/b_p varying from 0.0001 to 0.50 and one of these phase functions is used during a run of the Hydrolight simulations.

The Hydrolight simulations were executed for all available phase functions, keeping all other parameters (a-d) given above without change. The spectral remote sensing reflectance and water leaving radiances generated using all types of phase functions available from simulations were compared with the in situ measured remote sensing reflectance and water leaving radiance. The $R_{rs}(\lambda)$ from simulations were compared with the measured $R_{rs}(\lambda)$ using radiometer and the phase function for which the $R_{rs}(\lambda)$ scored minimum deviation over the spectral range was then selected as an optimum phase function for that station (Figure 3.4) (Talaulikar et al., 2014a, 2014b; Talaulikar, Thayapurath, Desa, et al., 2012; Thayapurath, Talaulikar, Desa, & Lotlikar, 2016).

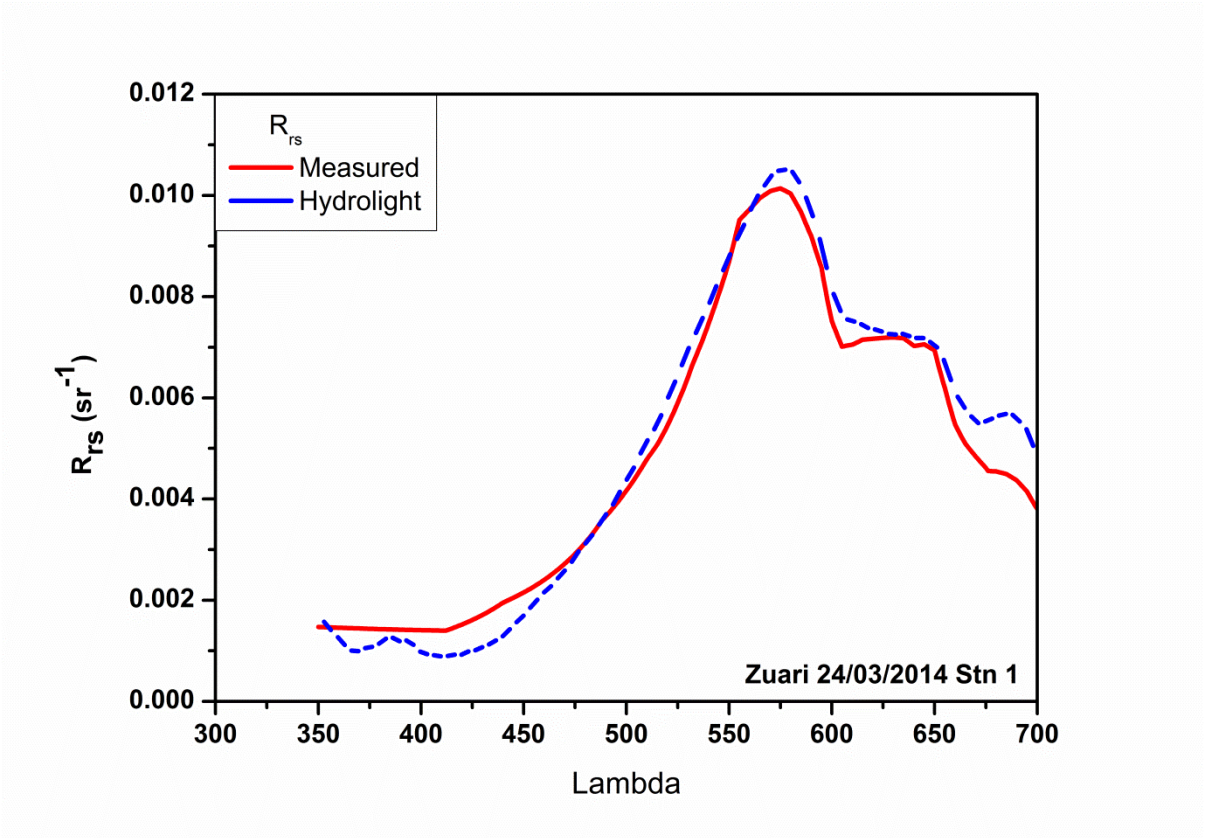

Figure 3.4 Comparison of selected $R_{rs}(\lambda)$ (blue dash) from simulations and the measured $R_{rs}(\lambda)$ (red straight continuous).

The output optical and other parameters generated from the simulation are listed in Table 3.3

Table 3.3 Optical properties generated by Hydrolight simulations

Optical Property	Units		Optical Property	Units
PAR(z)	µmol pho/m^2 s		KPAR(z)	µmol pho/m^2 s
$K_{Lu}(\lambda,z)$	m^{-1}		$K_u(\lambda,z)$	m^{-1}
$K_d(\lambda,z)$	m^{-1}		Eo_Quantum(λ,z)	microEinst/(m^2 s)
$R_{rs}(\lambda)$	Sr^{-1}		R(λ,z)	-
$L_u/E_d(\lambda,z)$	Sr^{-1}		$E_u(\lambda,z)$	W/m^2 nm
$E_d(\lambda,z)$	W/m^2 nm		$E_o(\lambda,z)$	W/m^2 nm
$E_{ou}(\lambda,z)$	W/m^2 nm		$E_{od}(\lambda,z)$	W/m^2 nm
$L_u(\lambda,z)$	W/m^2 nm sr		$E_d(\lambda)$ in air	W/m^2 nm
$b_b/b(\lambda,z)$_Total			$b_b/b(\lambda,z)$_Component1	
$b_b/b(\lambda,z)$_Component2			$b(\lambda,z)$_Total	m^{-1}
$b(\lambda,z)$_Component1	m^{-1}		$b(\lambda,z)$_Component2	m^{-1}
$a(\lambda,z)$_Total			$a(\lambda,z)$_Component1	
$a(\lambda,z)$_Component2			Solar zenith angle	Degree
Solar azimuth angle	Degree		Secchi depth	m

Here Component 1 is the pure water and Component 2 is everything else

3.2.2.2 Satellite Data

The satellite data were obtained from two sources, National Remote Sensing Centre (ISRO), Hyderabad and internet sites. NRSC is the nodal agency to acquire Indian and other satellite data in India (http://www.nrsc.gov.in). Data from Indian Ocean color satellites, OCM-1 and OCM-2 were obtained from NRSC. MODIS and SeaWiFS data were downloaded from the ocean color portal that provide free satellite data from most ocean color satellite sensors, CZCS, SeaWiFS, MODIS,HICO, MERIS,GOCI, VIIRS and Sentinel 3 (https://oceancolor.gsfc.nasa.gov/). The L1B data were processed using SeaDAS (Present Version 7.53) (https://seadas.gsfc.nasa.gov/). SeaDAS is free software from Ocean Color Group of NASA to process, display, analyse ocean color satellite data.

3.2.3 Protocols for measurements, calibrations and analysis

Standard protocols were followed for the calibrations, measurements, processing and analysis of the data. These protocols followed are available at https://oceancolor.gsfc.nasa.gov/docs/technical/. These protocols are also being updated and the same is available at https://ioccg.org/what-we-do/ioccg-publications/ocean-optics-protocols-satellite-ocean-colour-sensor-validation/

The optical data were checked with various criteria and the data which were filtered and screened were used for the studies (Silveira et al., 2014). The profiling radiometer was operated in two modes, profiling and float and in each mode multiple casts were take in quick succession. This was to obtain good data as the radiometer had inherent flaws in its design and it was difficult to obtain good data near the surface in the profile mode(Suresh et al., 2012). For the AC-9, the instrument was calibrated before every field measurements with pure water (Pegau et al., 2002). The measurements using a hyper-spectral profiling radiometer were carefully carried-out in profile and float mode (Morrow, et al., 2010; Mueller et al., 2003; Silveira et al., 2014).

The water samples at discrete depths were collected with high-grade silicon tubing attached to the AC-9 instrument and water was drawn using a DC pump on the deck. One of the depths was always at the surface. The water samples were usually collected from depths where some significant features were observed in the AC-9 profile. This method of collecting water samples was found to be purposeful, logical and also convincing about

fulfilling the objectives of various studies to be carried-out. Since AC-9 had a good depth sensor, water samples were collected at precise required depths, which was not possible using a bottle sampler. Water samples were collected, stored and analysed in the laboratory following the standard protocols (Boss et al., 2018).

3.2.3.1 Data for the development and validation of algorithms for ocean color satellite

The average values of an optically active substance such as chlorophyll or parameter as observed by the ocean color satellite sensor is given in Equation (1) (Gordon & Clark, 1980; Smith, 1981).

$$P_{sat} = \frac{\int_0^{Z_{90}} P(z)g(z)dz}{\int_0^{Z_{90}} g(z)dz} \tag{1}$$

where

$$g(z) = -\exp\left[-2\int_0^{Z_{90}} K_d(z)dz\right] \tag{2}$$

This method is adopted for the optical parameters used here for the development of various optical algorithms. A refined analytically method was derived to find the weighted average for remote sensing application (Sokoletsky & Yacobi, 2011). However since there were small differences in the average values calculated from the two methods, the method by Gordon was chosen for its simplicity and for the fact that the average values available from others sources used this method.

This average value may not always depict the true variations within the water column. The chlorophyll variations within water may be non-uniform with depth. There is chlorophyll maximum occurring in water and the contributions may not be considered if the same is below Z_{90}. In the waters of this study the Z_{90} were often shallow (Chapter 4) and the sub-surface chlorophyll maximum were analysed to show their impact on satellite derived chlorophyll values (Dias, Suresh, Talaulikar & Lotlikar, 2013).

This method of finding weighted average was not adopted to find the mean values of physical parameters and they were the arithmetic mean of values within Z_{90}.

CHAPTER 4. VARIATIONS OF PARAMETERS

4.1 Introduction

Here the variations of the optical parameters and associated physical and biological parameter variations are presented of the two estuaries, Mandovi and Zuari, and the coastal waters off Goa. These variations are described in three parts; the first part describes the variations of parameters at gross and seasonal scales; the second part describes the spatial variations of parameters in the estuaries, and the third part characterizes the optical parameters associated with *Trichodesmium spp.*

4.2 Results

4.2.1 Gross variations of parameters

The gross variations of the bio-optical parameters of the three regions, two estuaries of Mandovi and Zuari and the coastal waters, are given in Table 4.1 - 4.6. There were distinct variations in the parameters among these three sites. *It may be noted that these variations are listed in tabular form in the interests of summarizing the data without loss of numerical detail and effective reduction of graphical representation i.e., minimizing the number of Figures.*

The physical parameters temperature, salinity, and density agree with those reported earlier for these waters (Manoj, 2008; Pednekar et al., 2014; Vijith, 2014).

Solar radiation, as indicated by $E_S(490)$ and PAR, was found to be lower over the estuaries and higher over the coastal waters.

Two parameters that have been used to indicate the penetration of light in water were Z_{90} (m) and Z_{sd} (m). The values of Z_{90} light show that light penetrates the deepest in coastal waters, and among estuaries, the light penetrations in Mondovi were deeper than Zuari. Similar was the case observed of the transparencies of water, Z_{sd} (Suresh et al, 2018; Suresh, Dias, and Desa, 2019). Since $Z_{90}(\lambda)$ was spectral, the value of Z_{90} given here was the maximum values of $Z_{90}(\lambda)$. The euphotic depths, Z_{eu} also follow a similar pattern of variations. The wavelength at maximum $Z_{90}(\lambda)$ was about 577 nm in the estuaries and was higher compared to the coastal waters, which was at about 545 nm. The values of $E_d(\lambda)$ at

$Z_{90}(\lambda)$ also followed the same patterns of variations for these waters. The % PAR at Z_{eu} and Z_{sd} were comparable for similar water types (Table 4.1- 4.3).

The values of IOPs, namely absorption $a(\lambda)$, beam attenuation $c(\lambda)$, scattering $b(\lambda)$, backscattering $b_b(700)$, coefficients and the AOP, $K_d(\lambda)$, were much higher in the estuarine waters compared to the coastal waters. The bulk refractive index, n_p in the estuaries were relatively higher than coastal waters. The exponent of the particle size distribution (PSD), ξ was relatively higher in the estuarine waters as compared to coastal waters. The shape of $R_{rs}(\lambda)$ in the estuaries, resembled typical spectral variations observed in turbid waters (Lubac & Loisel, 2007).

The chlorophyll was higher in the estuaries, and it was higher in the Zuari compared to Mandovi. TSM values were comparable in the estuaries and lower in the coastal waters. Though CDOM was marginally higher in the Zuari, detritus contribution was higher in the Mandovi. In the estuaries, the contributions from detritus were the highest, while in the coastal waters absorptions due to phytoplankton were highest. In coastal waters, CDOM was more than detritus, and in the estuaries, detritus was more than CDOM.

Light availability at Z_{90} was the same in the estuaries, marginally higher in coastal waters. %PAR was nearly similar. The wavelength of maximum light decreased in coastal waters.

Table 4.1 Mean parameter values of Mandovi

Parameter	Mean	σ	Minimum	Maximum
Physical				
Temperature (°C)	29.1	1.66	25.06	33.17
Salinity	25.03	10.07	0.05	36.28
Density σ (Kg/m^3)	15.67	6.11	0.05	22.82
Solar radiation at surface				
$E_S(350)$ ($W/m^2/nm$)	0.3142	0.1251	0.0285	1.05
$E_S(490)$ ($W/m^2/nm$)	0.9862	0.3657	0.0721	1.7289
PAR E_S (W/m^2)	275.3638	102.6299	19.0796	478.6248
Light penetration				
Z_{Max} (m)	6.3	2.27	1.2	12.33
λ (of maximum Z_{90}) (nm)	571	11	481	599
Z_{90} (m)	1.31	0.77	0.41	5.01
Z_{SD} (m)	1.64	0.99	0.41	7
Z_{eu} (m)	6.03	3.53	1.89	23.07
PAR at Z_{90}(μmole/m^2/s)	305.12	140.72	0.01	784.73
%PAR at Z_{90}	24.3	5.13	3.92	45.31
PAR at Z_{SD}(μmole/m^2/s)	183.69	181.97	6.17	1017.4
%PAR at Z_{SD}	18.72	10.22	0.46	74.56

λ (of Maximum E_d) (nm)	575	10	479	611
E_d at Z_{90}($W/m^2/nm$)	0.4617	0.1923	0.0001	1.0098
λ (at Maximum E_{SD}) (nm)	575	10	479	584
E_d at Z_{SD}($W/m^2/nm$)	0.318	0.2386	0.0164	1.3137
IOP				
$b_b(700)$ (m^{-1})	0.08287	0.07126	0.01096	0.49437
a(412) (m^{-1})	1.424	0.6832	0.0006	4.5887
a(440) (m^{-1})	1.0809	0.4965	0.3722	3.4193
a(488) (m^{-1})	0.6451	0.3444	0.1772	2.2677
a(490) (m^{-1})	0.6315	0.3445	0.1857	2.4162
a(510) (m^{-1})	0.4947	0.2815	0.0837	2.2382
a(532) (m^{-1})	0.3855	0.324	0.1461	3.3364
a(555) (m^{-1})	0.2677	0.3389	0.091	3.8052
a(650) (m^{-1})	0.1048	0.1588	0.0187	1.5148
a(676) (m^{-1})	0.137	0.1082	0.0166	1.0002
a(715) (m^{-1})	0	0	0	0
c(412) (m^{-1})	5.6143	5.5007	0.0006	61.3425
c(440) (m^{-1})	5.3922	5.5546	0.718	63.0754
c(488) (m^{-1})	4.9457	6.2143	1.0008	73.9259
c(490) (m^{-1})	4.9295	6.2668	0.9939	74.6913
c(510) (m^{-1})	4.6929	6.805	0.476	82.3452
c(532) (m^{-1})	4.6842	5.6729	0.9044	66.7399
c(555) (m^{-1})	4.4384	2.8049	0.5943	17.7681
c(650) (m^{-1})	3.8171	4.7881	0.0703	56.1165
c(676) (m^{-1})	3.6727	2.4714	0.0166	17.0104
c(715) (m^{-1})	3.4282	5.9881	0.3052	56.8263
γ	1.08	0.35	0.11	3.56
ξ	4.06	0.4	2.19	6.56
n_p	1.1078	0.0422	1	1.2174
AOP				
$K_d(350)$ (m^{-1})	1.2866	1.4997	0.0003	8.6982
$K_d(412)$ (m^{-1})	1.7779	1.0682	0.0014	7.96
$K_d(443)$ (m^{-1})	1.5409	0.8811	0.0027	6.4523
$K_d(490)$ (m^{-1})	1.1724	0.6762	0.0014	5.5066
$K_d(510)$ (m^{-1})	1.0591	0.5863	0.0154	4.7507
$K_d(532)$ (m^{-1})	0.9531	0.4962	0.015	4.0595
$K_d(555)$ (m^{-1})	0.8661	0.4383	0.0117	3.2474
$K_d(566)$ (m^{-1})	0.8286	0.448	0.0004	5.7426
$K_d(620)$ (m^{-1})	0.9957	0.371	0.0068	2.6201
$K_d(650)$ (m^{-1})	0.9957	0.3565	0.0061	2.2766
$K_d(670)$ (m^{-1})	1.0923	0.3717	0.0057	2.4624
$K_d(676)$ (m^{-1})	1.1004	0.3735	0.0056	2.2115
$K_d(681)$ (m^{-1})	1.0988	0.3749	0.0053	2.183
$K_d(700)$ (m^{-1})	1.164	0.403	0.0126	2.8292
$R_{rs}(350)$ (sr^{-1})	0.000592	0.0022	1E-006	0.026466
$R_{rs}(412)$ (sr^{-1})	0.001294	0.051691	6E-006	0.928595
$R_{rs}(443)$ (sr^{-1})	0.002095	0.040963	3.8E-005	0.997833
$R_{rs}(490)$ (sr^{-1})	0.004027	0.005703	1E-006	0.082804
$R_{rs}(510)$ (sr^{-1})	0.005036	0.00534	5.7E-005	0.075802
$R_{rs}(532)$ (sr^{-1})	0.006513	0.005354	0.000203	0.071124
$R_{rs}(555)$ (sr^{-1})	0.008285	0.005536	0.000455	0.070594
$R_{rs}(566)$ (sr^{-1})	0.009132	0.006241	0.000604	0.073313
$R_{rs}(620)$ (sr^{-1})	0.005884	0.005292	0.00035	0.05958

$R_{rs}(650)$ (sr^{-1})	0.005367	0.005129	0.000303	0.056105
$R_{rs}(670)$ (sr^{-1})	0.00441	0.004947	5.1E-005	0.053719
$R_{rs}(676)$ (sr^{-1})	0.004377	0.004896	0.000146	0.053014
$R_{rs}(681)$ (sr^{-1})	0.004409	0.00483	0.000134	0.051862
$R_{rs}(700)$ (sr^{-1})	0.003347	0.006367	2.8E-005	0.119225
Biological				
Chlorophyll (mg/m^3)	2.18	3.05	0.13	16.14
Chlorophyll(mg/m^3)-Sensor	1.72	1.45	0.13	7.4
TSM (g/m^3)	8.01	16.5	0.02	160
pH	7.72	0.32	6.97	8.16
λ (FLH R_{rs})	693	3	685	698
$R_{rs}(\lambda)$ FLH (sr^{-1})	0.00143	0.00075	0.00016	0.00446
λ (FLH L_w) nm	687	8	678	698
$L_w(\lambda)$ FLH ($\mu Wcm^{-2}sr^{-1}$)	0.03933	0.03754	0.00591	0.24399
$a_{ph}(412)$ (m^{-1})	0.0677	0.0935	0.0096	0.5426
$a_{ph}(440)$ (m^{-1})	0.0657	0.0727	0.0068	0.4422
$a_{ph}(488)$ (m^{-1})	0.0628	0.0529	0.0041	0.3151
$a_{ph}(490)$ (m^{-1})	0.0471	0.0369	0.0002	0.2081
$a_{ph}(510)$ (m^{-1})	0.0316	0.0304	0.0002	0.1708
$a_{ph}(532)$ (m^{-1})	0.0189	0.0195	0.001	0.1051
$a_{ph}(555)$ (m^{-1})	0.0114	0.014	0.0002	0.0628
$a_{ph}(650)$ (m^{-1})	0.0327	0.027	0.001	0.1206
$a_{ph}(676)$ (m^{-1})	0.0305	0.0267	0.0014	0.1194
$a_{ph}(715)$ (m^{-1})	0.0141	0.0103	0.0007	0.0476
$a_g(412)$ (m^{-1})	0.3654	0.1656	0.0483	0.7771
$a_g(440)$ (m^{-1})	0.2368	0.1172	0.0064	0.5673
$a_g(488)$ (m^{-1})	0.1186	0.0738	0.0259	0.3642
$a_g(490)$ (m^{-1})	0.0756	0.0586	0.0126	0.2894
$a_g(510)$ (m^{-1})	0.0699	0.0541	0.008	0.2644
$a_g(532)$ (m^{-1})	0.0512	0.0443	0.0041	0.2112
$a_g(555)$ (m^{-1})	0.0379	0.0321	0.0025	0.1462
$a_g(650)$ (m^{-1})	0.0187	0.0256	0.0029	0.1028
$a_g(676)$ (m^{-1})	0.0009	0.0014	0.0001	0.0061
$a_g(715)$ (m^{-1})	0.0002	0.0004	0.0002	0.0009
$a_d(412)$ (m^{-1})	0.5351	0.3359	0.0916	2.1825
$a_d(440)$ (m^{-1})	0.4394	0.282	0.0745	1.9047
$a_d(488)$ (m^{-1})	0.3551	0.2305	0.0571	1.6273
$a_d(490)$ (m^{-1})	0.303	0.2046	0.0474	1.4726
$a_d(510)$ (m^{-1})	0.2752	0.1874	0.0424	1.3573
$a_d(532)$ (m^{-1})	0.2263	0.159	0.0321	1.1665
$a_d(555)$ (m^{-1})	0.1535	0.1096	0.0161	0.8092
$a_d(650)$ (m^{-1})	0.0848	0.0622	0.0024	0.4566
$a_d(676)$ (m^{-1})	0.0257	0.0214	0.0026	0.1521
$a_d(715)$ (m^{-1})	0.0092	0.0076	0.0011	0.0546

Table 4.2 Mean parameter values of Zuari

Parameter	**Mean**	**σ**	**Minimum**	**Maximum**
Physical				
Temperature (°C)	29.71	1.84	26.47	33.08
Salinity	24.63	9.68	0.15	35.15
Density (Kg/m^3)	15.27	5.94	0.31	22.57

Solar radiation at surface				
$E_S(350)$ ($W/m^2/nm$)	0.311	0.1178	0.0061	0.5413
$E_S(490)$ ($W/m^2/nm$)	0.9636	0.3651	0.0196	1.6048
PAR E_S (W/m^2)	268.5979	101.9028	4.5553	444.6871
Light penetration				
Z_{Max} (m)	7.68	2.2	2.5	11.12
λ (of maximum Z_{90}) (nm)	569	15	481	597
Z_{90} (m)	1.19	0.92	0.32	5.1
Z_{SD} (m)	1.32	0.85	0.42	4.65
Z_{eu} (m)	5.48	4.26	1.47	23.49
PAR at Z_{90}($\mu mole/m^2/s$)	306.52	136.03	1.19	630.82
%PAR at Z_{90}	24.27	5.45	3.62	41.06
PAR at Z_{SD}($\mu mole/m^2/s$)	226.09	198.78	0.07	1028.97
%PAR at Z_{SD}	21.27	11.06	0.01	64.16
λ (of Maximum E_d) (nm)	572	28	350	641
E_d at Z_{90}($W/m^2/nm$)	0.468	0.2109	0.006	1.6468
λ (at Maximum E_{SD}) (nm)	576	17	480	641
E_d at Z_{SD}($W/m^2/nm$)	0.4088	0.2855	0.006	1.7418
IOP				
$b_b(700)$ (m^{-1})	0.07902	0.15288	0.00898	0.94901
a(412)	1.5636	1.5665	0.3136	8.1592
a(440)	1.156	1.071	0.2376	6.1354
a(488)	0.6702	0.6805	0.1752	4.0704
a(490)	0.6553	0.6679	0.1739	3.9978
a(510)	0.4976	0.5509	0.147	3.2724
a(532)	0.3583	0.4282	0.115	2.5679
a(555)	0.2471	0.3052	0.0886	1.9258
a(650)	0.1091	0.0748	0.0088	0.5926
a(676)	0.1557	0.0873	0.0479	0.535
a(715)	0	0	0	0
c(412)	7.263	13.0164	1.1912	90.3878
c(440)	6.6177	13.2313	0.9914	93.9163
c(488)	5.713	13.9795	0.601	88.0719
c(490)	5.6907	13.7622	0.5942	86.3662
c(510)	5.4676	11.9739	0.5264	87.0369
c(532)	5.3182	12.1892	0.5615	87.7747
c(555)	5.074	11.4187	0.5969	92.952
c(650)	4.5594	11.7138	1.1321	87.6738
c(676)	4.3874	11.3484	1.1081	86.6148
c(715)	4.1077	11.0491	0.8617	85.8137
γ	1.09	0.38	0.11	2.26
ξ	4.05	0.46	2.49	5.26
n_p	1.0931	0.0477	1	1.1996
AOP				
$K_d(350)$	1.1551	1.6501	0.0204	7.9599
$K_d(412)$	1.9033	1.3645	0.0011	7.4171
$K_d(443)$	1.6536	1.1723	0.0011	8.9725
$K_d(490)$	1.1683	0.9193	0.0029	6.5051
$K_d(510)$	1.0231	0.8913	0.0389	6.6501
$K_d(532)$	0.9209	0.7912	0.0039	5.68
$K_d(555)$	0.8301	0.7759	0.0176	6.5023
$K_d(566)$	0.7859	0.6859	0.0314	5.2542
$K_d(620)$	0.983	0.6503	0.0345	7.2615

$K_d(650)$	1.0159	0.6306	0.086	6.4544
$K_d(670)$	1.1179	0.6471	0.051	6.2507
$K_d(676)$	1.1356	0.5604	0.0526	4.1552
$K_d(681)$	1.1256	0.6896	0.0163	7.8948
$K_d(700)$	1.2134	0.6608	0.0573	7.6665
$R_{rs}(350)$	0.000613	0.001895	8E-006	0.015133
$R_{rs}(412)$	0.001624	0.005378	1.6E-005	0.08132
$R_{rs}(443)$	0.002586	0.004215	8.4E-005	0.06275
$R_{rs}(490)$	0.004697	0.002933	5.3E-005	0.027518
$R_{rs}(510)$	0.006176	0.021855	0.000306	0.389835
$R_{rs}(532)$	0.007953	0.016769	0.000749	0.298861
$R_{rs}(555)$	0.009905	0.012975	0.000176	0.228967
$R_{rs}(566)$	0.010702	0.011481	4.3E-005	0.200007
$R_{rs}(620)$	0.006856	0.008813	0.000458	0.143418
$R_{rs}(650)$	0.006286	0.008062	0.000384	0.12767
$R_{rs}(670)$	0.004873	0.007732	0.000141	0.122574
$R_{rs}(676)$	0.004857	0.007421	0.000145	0.11604
$R_{rs}(681)$	0.004931	0.007545	0.000182	0.118978
$R_{rs}(700)$	0.003522	0.007004	0.000158	0.111533
Biological				
Chlorophyll (mg/m^3)	4.28	2.88	0.02	11.62
Chlorophyll(mg/m^3)-Sensor	2.28	1.44	0.71	8.49
TSM (g/m^3)	8.05	12.16	2	130
pH	7.6	0.24	7.09	8.13
$\lambda 1$ FLH R_{rs}	693	4	671	698
$R_{rs}(\lambda 1)$ FLH	0.0014	0.00079	0.00045	0.00384
$\lambda 1$ FLH L_w	689	9	671	698
$L_w(\lambda 1)$ FLH	0.03834	0.05313	0.00291	0.33339
$a_{ph}(412)$	0.0757	0.1449	0.0016	0.8483
$a_{ph}(440)$	0.069	0.1199	0.0015	0.672
$a_{ph}(488)$	0.0568	0.0903	0.0013	0.4959
$a_{ph}(490)$	0.0424	0.0659	0.0012	0.4084
$a_{ph}(510)$	0.0338	0.055	0.0003	0.3615
$a_{ph}(532)$	0.0246	0.0398	0.0007	0.278
$a_{ph}(555)$	0.0158	0.0261	0.0004	0.1802
$a_{ph}(650)$	0.0352	0.0351	0.0002	0.1831
$a_{ph}(676)$	0.0328	0.0338	0	0.1823
$a_{ph}(715)$	0.0158	0.0126	0.0057	0.0743
$a_g(412)$	0.4068	0.2245	0.0001	1.3856
$a_g(440)$	0.2742	0.1599	0.0001	1.04
$a_g(488)$	0.1512	0.1018	0.0001	0.702
$a_g(490)$	0.1107	0.0812	0.0001	0.5644
$a_g(510)$	0.0995	0.0736	0.0041	0.5147
$a_g(532)$	0.0787	0.06	0.0004	0.4181
$a_g(555)$	0.053	0.0407	0.0008	0.285
$a_g(650)$	0.0346	0.0268	0.0008	0.1785
$a_g(676)$	0.0011	0.0059	0.0003	0.0337
$a_g(715)$	0	0	0	0
$a_d(412)$	0.4707	0.577	0.0817	2.742
$a_d(440)$	0.3848	0.4767	0.0626	2.2336
$a_d(488)$	0.2976	0.3811	0.0436	1.7349
$a_d(490)$	0.2568	0.335	0.0343	1.4969

$a_d(510)$	0.2316	0.3043	0.0285	1.3488
$a_d(532)$	0.1869	0.2528	0.0207	1.0965
$a_d(555)$	0.1246	0.1712	0.0112	0.739
$a_d(650)$	0.0703	0.0958	0.0034	0.4291
$a_d(676)$	0.0199	0.0327	0.0029	0.1693
$a_d(715)$	0.0077	0.0119	0.0011	0.0604

Table 4.3 Mean parameters values of coastal waters

Parameter	**Mean**	**ρ**	**Minimum**	**Maximum**
Physical				
Temperature (°C)	29.04	1.37	26.47	32.13
Salinity	34.77	0.72	32.21	36.44
Density σ (Kg/m^3)	21.88	0.63	19.8	23.32
Solar radiation at surface				
$E_S(350)$ ($W/m^2/nm$)	0.3677	0.0937	0.0873	0.6169
$E_S(490)$ ($W/m^2/nm$)	1.1574	0.2743	0.245	1.5977
PAR E_S (W/m^2)	322.7538	76.3252	67.5449	440.6275
Light penetration				
Z_{Max} (m)	17.12	5.88	4.3	30
λ (of maximum Z_{90}) (nm)	545	26	482	573
Z_{90} (m)	4.28	3.02	1.58	16.29
Z_{SD} (m)	4.04	2.24	1.29	13.5
Z_{eu} (m)	19.73	13.92	7.28	75.02
PAR at Z_{90}(μmole/m^2/s)	313.85	81.33	93.13	529.07
%PAR at Z_{90}	21.43	3.58	8.52	37.99
PAR at Z_{SD}(μmole/m^2/s)	365.35	159.87	113.18	948.27
%PAR at Z_{SD}	24.77	7.93	9.5	52.15
λ (of Maximum E_d) (nm)	545	24	479	576
E_d at Z_{90}($W/m^2/nm$)	0.4891	0.1144	0.1369	0.8191
λ (at Maximum E_{SD}) (nm)	544	25	479	580
E_d at Z_{SD}($W/m^2/nm$)	0.5546	0.2102	0.2028	1.3513
IOP				
$b_b(700)$ (m^{-1})	0.00993	0.01586	0.002	0.07025
a(412) (m^{-1})	0.3992	0.2731	0.0006	2.4675
a(440) (m^{-1})	0.2957	0.1885	0.0012	0.9396
a(488) (m^{-1})	0.2061	0.1887	0.0012	2.3954
a(490) (m^{-1})	0.2023	0.1773	0.0011	2.2152
a(510) (m^{-1})	0.1718	0.0869	0	0.4379
a(532) (m^{-1})	0.146	0.0699	0.0012	0.4877
a(555) (m^{-1})	0.1112	0.0493	0.0012	0.3177
a(650) (m^{-1})	0.069	0.027	0.0003	0.1442
a(676) (m^{-1})	0.0904	0.0682	0.001	0.7385
a(715) (m^{-1})	0	0	0	0
c(412) (m^{-1})	1.631	2.2848	0.0006	17.3559
c(440) (m^{-1})	1.5436	2.2093	0.0012	17.3937
c(488) (m^{-1})	1.3045	1.3526	0.0012	6.2211
c(490) (m^{-1})	1.2993	1.3474	0.0011	6.1916
c(510) (m^{-1})	1.2603	1.2999	0	5.8967
c(532) (m^{-1})	1.2268	1.2766	0.0012	5.7375
c(555) (m^{-1})	1.1716	1.2627	0.0012	5.621
c(650) (m^{-1})	1.0634	1.7664	0.0003	17.0363

c(676) (m^{-1})	1.0215	2.13	0.0023	18.1733
c(715) (m^{-1})	0.9291	7.6567	0.0054	90.9966
γ	0.99	0.33	0.16	1.91
ξ	3.91	0.53	0.52	4.91
n_p	1.0778	0.0494	1	1.2221
AOP				
K_d(350) (m^{-1})	0.5161	0.4481	0.0146	3.9393
K_d(412) (m^{-1})	0.3979	0.3321	0.0243	1.8967
K_d(443) (m^{-1})	0.3447	0.281	0.0033	1.65
K_d(490) (m^{-1})	0.2584	0.2184	0	1.2515
K_d(510) (m^{-1})	0.2525	0.197	0	1.1424
K_d(532) (m^{-1})	0.2522	0.1776	0	1.0497
K_d(555) (m^{-1})	0.2513	0.1606	0	0.9757
K_d(566) (m^{-1})	0.2505	0.1538	0.0081	0.9438
K_d(620) (m^{-1})	0.4953	0.1564	0.0227	1.1455
K_d(650) (m^{-1})	0.5325	0.1679	0.0116	1.3517
K_d(670) (m^{-1})	0.6173	0.2077	0.0161	1.8103
K_d(676) (m^{-1})	0.6244	0.2156	0.0036	2.2225
K_d(681) (m^{-1})	0.618	0.205	0.0061	1.3717
K_d(700) (m^{-1})	0.6877	0.2616	0.0197	2.4331
R_{rs}(350) (sr^{-1})	0.002019	0.115458	1E-006	2.459452
R_{rs}(412) (sr^{-1})	0.003095	0.001614	0.000215	0.012657
R_{rs}(443) (sr^{-1})	0.003779	0.001932	0.000238	0.015313
R_{rs}(490) (sr^{-1})	0.005557	0.00243	0.000513	0.017729
R_{rs}(510) (sr^{-1})	0.005847	0.002653	0.000631	0.018092
R_{rs}(532) (sr^{-1})	0.006173	0.002999	0.00076	0.01916
R_{rs}(555) (sr^{-1})	0.005903	0.003317	0.000832	0.01943
R_{rs}(566) (sr^{-1})	0.005667	0.003465	0.00087	0.019555
R_{rs}(620) (sr^{-1})	0.001501	0.002062	7.1E-005	0.013871
R_{rs}(650) (sr^{-1})	0.001233	0.001866	4.2E-005	0.013121
R_{rs}(670) (sr^{-1})	0.000974	0.001473	5.1E-005	0.010945
R_{rs}(676) (sr^{-1})	0.001017	0.001462	5.2E-005	0.011274
R_{rs}(681) (sr^{-1})	0.001031	0.001453	4E-006	0.010957
R_{rs}(700) (sr^{-1})	0.000649	0.006554	3E-006	0.128804
Biological				
Chlorophyll (mg/m^3)	1.16	25.42	0.15	247.2
Chlorophyll(mg/m^3)-Sensor	0.98	1.02	0.17	6.81
TSM (g/m^3)	6.2	15.38	2	134.5
pH	7.99	0.17	7.27	8.16
λ (FLH R_{rs})	688	4	681	698
$R_{rs}(\lambda)$ FLH (sr^{-1})	0.00046	0.00035	2E-005	0.00184
λ (FLH L_w) nm	683	5	678	708
$L_w(\lambda)$ FLH ($\mu Wcm^{-2}sr^{-1}$)	0.02653	0.02564	0.00216	0.16376
a_{ph}(412) (m^{-1})	0.0492	9.4502	0.0089	55.0764
a_{ph}(440) (m^{-1})	0.0487	8.4761	0.0099	48.8126
a_{ph}(488) (m^{-1})	0.044	7.05	0.0093	40.2027
a_{ph}(490) (m^{-1})	0.0331	5.5805	0.0046	31.9769
a_{ph}(510) (m^{-1})	0.0262	4.5638	0.0022	26.0304
a_{ph}(532) (m^{-1})	0.0163	2.9377	0.0033	16.7079
a_{ph}(555) (m^{-1})	0.0102	1.9484	0.0013	10.8445
a_{ph}(650) (m^{-1})	0.0169	4.2281	0.0011	23.4327
a_{ph}(676) (m^{-1})	0.0151	4.0694	0.0006	22.4182

$a_{ph}(715)$ (m^{-1})	0.0071	2.0196	0.0011	11.3249
$a_g(412)$ (m^{-1})	0.1385	4.7074	0.0271	24.6247
$a_g(440)$ (m^{-1})	0.0878	4.3584	0.0127	25.2086
$a_g(488)$ (m^{-1})	0.0408	5.0287	0	31.8148
$a_g(490)$ (m^{-1})	0.0248	6.4517	0.001	41.8861
$a_g(510)$ (m^{-1})	0.0208	6.0002	0	39.543
$a_g(532)$ (m^{-1})	0.0172	6.8161	0	41.85
$a_g(555)$ (m^{-1})	0.0137	5.3625	0.0004	31.9666
$a_g(650)$ (m^{-1})	0.0114	2.5632	0.0003	15.4531
$a_g(676)$ (m^{-1})	0.0022	0.1746	0.0002	0.9171
$a_g(715)$ (m^{-1})	0.0003	0.0001	0.0001	0.0004
$a_d(412)$ (m^{-1})	0.0738	2.2551	0.0093	13.2128
$a_d(440)$ (m^{-1})	0.0572	2.0804	0.0059	12.5151
$a_d(488)$ (m^{-1})	0.0419	2.0788	0.0027	13.0169
$a_d(490)$ (m^{-1})	0.0347	2.224	0.0001	14.2135
$a_d(510)$ (m^{-1})	0.0334	2.127	0.0007	13.5052
$a_d(532)$ (m^{-1})	0.0288	2.0927	0.0004	13.2891
$a_d(555)$ (m^{-1})	0.0207	1.5606	0.0002	9.8819
$a_d(650)$ (m^{-1})	0.0119	0.8713	0.0001	5.4403
$a_d(676)$ (m^{-1})	0.0044	0.2473	0.0003	1.3946
$a_d(715)$ (m^{-1})	0.0017	0.1075	0	0.6287

4.2.2 Seasonal Variations

The seasons have been defined considering the period of monsoons analyzed for the years 1871 to 2016 (Kothawale & Rajeevan, 2017) and the data variability of these waters. Classification of data using the clustering method also helped in identifying the seasons. There were four seasons summer or pre-monsoon (March-May), monsoon (June-September), post-monsoon (October-November), and winter (December – February).

Seasonal variations were observed in both estuaries and coastal waters, which were very distinct and also significant in few parameters. The largest differences in parameters between the four seasons were found during the monsoon, and the trend was similar in all the waters. No data was available in the coastal waters during monsoon.

The Z_{90} and Z_{sd} values were the highest during the winter and lowest during the monsoon. The wavelength at which the maximum underwater spectral light energy, $E_d(\lambda)$ was available at either Z_{90} or Z_{sd} depths was relatively higher during monsoon. The wavelength of underwater light that penetrated the deepest changed with seasons and water types. Since the Z_{sd} and Z_{90} were comparable, the % PAR available at these depths were also comparable. There were seasonal variations in the IOPs and AOPs. Scattering dominated during monsoon in the estuaries. During winter in Zuari, the backscattering coefficient was relatively higher compared to summer and post monsoon, while in Mandovi, it was the

lowest. In the coastal water, the lowest backscattering was observed during post-monsoon. CDOM and detritus were dominant during monsoon in the estuaries, while in the coastal waters, CDOM and detritus were high during summer (Dias et al., 2017).

The refractive indices were highest during monsoon. The slope of PSD ξ was relatively higher during winter in the Zuari, while it was always comparatively lower in the coastal waters.

The solar radiation was the highest during summer and lowest during the monsoon.

Table 4.4 Seasonal Variations of Mandovi

Parameter	Summer	Monsoon	Post-Monsoon	Winter	Summer σ	Monsoon σ	Post-Monsoon σ	Winter σ
Physical								
Temperature (°C)	30.53	26.96	29.35	28.07	1.31	1.09	0.96	0.9
Salinity	28.95	9.79	21.93	25.29	5.52	11.65	11.51	9.14
Density (Kg/m^3)	17.04	9.28	15.58	15.12	4.2	8.32	5.75	6.88
Solar radiation at surface								
$E_S(350)$ ($W/m^2/nm$)	0.3839	0.2339	0.2611	0.2947	0.1118	0.1323	0..1003	0.1091
$E_S(490)$ ($W/m^2/nm$)	1.1973	0.7189	0.8253	0.9353	0.2815	0.4504	0.3033	0.3147
PAR E_S (W/m^2)	334.80	197.30	230.99	261.68	78.47	124.61	85.00	88.86
Light penetration								
Z_{Max} (m)	6.22	5.87	6.52	6.44	2.48	2.04	2	2.19
λ (of maximum Z_{90}) (nm)	572	579	571	567	10	4	5	14
Z_{90} (m)	1.39	1.04	1.27	1.76	0.8	0.39	0.65	0.77
Z_{SD} (m)	1.56	1.1	1.68	2.29	0.54	0.33	0.7	1.29
Z_{eu} (m)	6.39	4.78	5.83	8.09	3.68	1.82	2.98	3.52
PAR at Z_{90}(µmole/m^2/s)	390.02	209.43	260.35	282.63	119.49	132.45	100.9	135.04
%PAR at Z_{90}	24.93	24.52	24.9	23.36	4.82	3.47	2.44	6.4
PAR at Z_{SD}(µmole/m^2/s)	312.49	204.71	181.26	248.15	198.54	163.05	99.78	180.51
%PAR at Z_{SD}	19.84	23.35	18.01	19.24	11.8	7.3	8.05	9.99
λ (of Maximum E_d) (nm)	575	581	576	573	14	6	7	7
E_d at Z_{90}($W/m^2/nm$)	0.5756	0.3266	0.398	0.4409	0.1526	0.1905	0.1633	0.1839
λ (at Maximum E_{SD}) (nm)	574	580	576	573	15	1	6	8
E_d at Z_{SD}($W/m^2/nm$)	0.4747	0.3342	0.2835	0.3772	0.2333	0.2631	0.1431	0.24
IOP								
$b_b(700)$ (m^{-1})	0.10203	0.18196	0.11812	0.06672	0.0506	0.0923	0.0494	0.0339

a(412) (m^{-1})	1.6535	2.2992	1.2624	1.1769	0.5269	1.0335	0.5357	0.4499
a(440) (m^{-1})	1.26	1.6294	0.9717	0.8839	0.4084	0.7646	0.2961	0.3569
a(488) (m^{-1})	0.7496	1.0399	0.5904	0.5696	0.2454	0.4983	0.2095	0.3275
a(490) (m^{-1})	0.7332	1.01741	0.579	0.5625	0.2401	0.4891	0.2047	0.3426
a(510) (m^{-1})	0.5689	0.7928	0.4655	0.4415	0.1918	0.4041	0.1561	0.2944
a(532) (m^{-1})	0.4604	0.6578	0.3438	0.3787	0.1847	0.3629	0.1166	0.4247
a(555) (m^{-1})	0.3232	0.4354	0.2567	0.2913	0.164	0.2468	0.1084	0.5037
a(650) (m^{-1})	0.134	0.1236	0.0977	0.1311	0.1084	0.0804	0.0309	0.2313
a(676) (m^{-1})	0.1766	0.1163	0.1195	0.1513	0.079	0.0647	0.0433	0.1481
a(715) (m^{-1})	0	0	0	0	0	0	0	0
c(412) (m^{-1})	6.8094	12.8715	5.5518	4.7519	3.0293	12.442	2.5439	2.121
c(440) (m^{-1})	6.5286	12.2311	5.1671	4.57	2.9457	12.907	2.0725	2.324
c(488) (m^{-1})	5.9987	11.9438	4.8953	4.17061	2.8388	15.427	1.6606	2.0281
c(490) (m^{-1})	5.9762	11.9552	4.8857	4.1591	2.8279	15.603	1.6515	2.0308
c(510) (m^{-1})	5.7519	12.0691	4.5359	4.0541	2.7337	17.371	1.8407	2.0713
c(532) (m^{-1})	5.6744	11.2216	4.7568	3.8978	2.7392	13.878	1.3516	1.9156
c(555) (m^{-1})	5.5423	7.8095	4.2553	3.9423	2.7982	3.5993	1.6421	2.086
c(650) (m^{-1})	4.8068	8.9725	3.7901	3.3376	2.5553	11.744	1.4839	1.7102
c(676) (m^{-1})	4.65231	6.4919	3.6976	3.1909	2.5234	3.4909	1.4068	1.6423
c(715) (m^{-1})	5.1021	8.4929	4.8278	3.018	5.4437	11.996	5.4734	1.7988
γ	1.16	1.05	1.04	1.03	0.45	0.09	0.26	0.27
ξ	4.12	4.04	4.02	4.02	0.53	0.09	0.33	0.29
n_p	1.0972	1.1265	1.1178	1.1118	0.0429	0.0222	0.0433	0.0409
AOP								
K_d(350) (m^{-1})	2.4572	2.1561	2.1268	1.7187	1.6528	1.7938	1.6427	1.0799
K_d(412) (m^{-1})	2.1783	2.5751	1.8599	1.4926	1.0069	1.5104	0.9797	0.7476
K_d(443) (m^{-1})	1.8094	2.2592	1.6283	1.2575	0.8192	1.2366	0.7782	0.6196
K_d(490) (m^{-1})	1.4127	1.7327	1.2952	0.9908	0.6121	1.0008	0.5676	0.4804
K_d(510) (m^{-1})	1.2678	1.5478	1.1941	0.904	0.548	0.8023	0.5089	0.4325
K_d(532) (m^{-1})	1.1157	1.3265	1.0867	0.8155	0.4771	0.6505	0.437	0.3756
K_d(555) (m^{-1})	1.0095	1.1961	0.9892	0.7374	0.4365	0.5391	0.3843	0.3303

$K_d(566)$ (m^{-1})	0.9829	1.12831	0.948	0.7063	0.5018	0.4957	0.3717	0.315
$K_d(620)$ (m^{-1})	1.076	1.1447	1.04961	0.8458	0.3857	0.4031	0.3366	0.3028
$K_d(650)$ (m^{-1})	1.0735	1.0977	1.055	0.8624	0.3669	0.4149	0.3277	0.2907
$K_d(670)$ (m^{-1})	1.1756	1.1922	1.13621	0.9607	0.3837	0.423	0.3448	0.3097
$K_d(676)$ (m^{-1})	1.1864	1.2033	1.13841	0.9676	0.3841	0.4194	0.3426	0.3164
$K_d(681)$ (m^{-1})	1.1842	1.1723	1.1455	0.9735	0.3877	0.4264	0.3473	0.3174
$K_d(700)$ (m^{-1})	1.2246	1.2779	1.2306	1.0402	0.4049	0.5193	0.3721	0.3306
$R_{rs}(350)$ (sr^{-1})	0.00157	0.00113	0.00086	0.00114	0.0033	0.0018	0.0006	0.0012
$R_{rs}(412)$ (sr^{-1})	0.00205	0.0185	0.00208	0.00703	0.0016	0.0941	0.0021	0.0667
$R_{rs}(443)$ (sr^{-1})	0.00287	0.00689	0.00299	0.00788	0.002	0.0178	0.0023	0.0701
$R_{rs}(490)$ (sr^{-1})	0.00449	0.0081	0.00467	0.00472	0.0026	0.0119	0.0029	0.005
$R_{rs}(510)$ (sr^{-1})	0.00544	0.0093	0.00566	0.00542	0.0029	0.0107	0.0032	0.0045
$R_{rs}(532)$ (sr^{-1})	0.00682	0.01125	0.00708	0.00659	0.0033	0.0097	0.0036	0.0048
$R_{rs}(555)$ (sr^{-1})	0.00842	0.014	0.00873	0.00772	0.0037	0.0094	0.004	0.0046
$R_{rs}(566)$ (sr^{-1})	0.00917	0.01539	0.00954	0.00858	0.0039	0.0092	0.0042	0.0066
$R_{rs}(620)$ (sr^{-1})	0.00703	0.01341	0.00719	0.00537	0.0035	0.0083	0.0038	0.0041
$R_{rs}(650)$ (sr^{-1})	0.00674	0.01298	0.00687	0.005	0.0034	0.008	0.0038	0.0039
$R_{rs}(670)$ (sr^{-1})	0.00559	0.01157	0.00582	0.00416	0.0031	0.0079	0.0035	0.004
$R_{rs}(676)$ (sr^{-1})	0.00559	0.01149	0.00578	0.00414	0.0031	0.0078	0.0035	0.0039
$R_{rs}(681)$ (sr^{-1})	0.00564	0.01136	0.00578	0.00416	0.0031	0.0076	0.0035	0.0039
$R_{rs}(700)$ (sr^{-1})	0.00467	0.00896	0.00458	0.00385	0.0028	0.007	0.0031	0.0091
Biological								
Chlorophyll (mg/m^3)	4.93	2.38	4.14	3.03	3.51	1.79	2.41	2.76
Chlorophyll(mg/m^3)-Sensor	3.04	1.29	2.10	2.37	1.43	1.13	0.77	1.37
TSM (g/m^3)	14.74	9.51	14.28	8.96	24.49	8.51	8.79	4.93
pH	7.8	7.58	7.78	7.74	0.24	0.37	0.27	0.3401
λ (FLH R_{rs})	694	693	693	692	2	3	2	3
$R_{rs}(\lambda)$ FLH (sr^{-1})	0.00167	0.0023	0.0015	0.00112	0.0006	0.001	0.0006	0.0005
λ (FLH L_w) nm	691	682	685	686	8	5	7	8
$L_w(\lambda)$ FLH ($\mu Wcm^{-2}sr^{-1}$)	0.0658	0.082	0.03778	0.03312	0.039	0.0482	0.0167	0.0181

$a_{ph}(412)$ (m^{-1})	0.1294	0.0826	0.1205	0.07771	0.089	0.0409	0.1517	0.0535
$a_{ph}(440)$ (m^{-1})	0.1209	0.0769	0.0978	0.06901	0.0766	0.0373	0.0994	0.0465
$a_{ph}(488)$ (m^{-1})	0.103	0.0675	0.0711	0.0542	0.0602	0.0336	0.0511	0.0372
$a_{ph}(490)$ (m^{-1})	0.0741	0.0549	0.05	0.0407	0.0414	0.0303	0.0332	0.0247
$a_{ph}(510)$ (m^{-1})	0.0583	0.0477	0.04	0.0296	0.0319	0.0287	0.0286	0.0213
$a_{ph}(532)$ (m^{-1})	0.0344	0.0342	0.0247	0.0222	0.0188	0.0253	0.0196	0.0109
$a_{ph}(555)$ (m^{-1})	0.0233	0.0229	0.0169	0.012	0.0132	0.0178	0.0137	0.009
$a_{ph}(650)$ (m^{-1})	0.0593	0.0319	0.0341	0.0307	0.0319	0.0151	0.0203	0.0153
$a_{ph}(676)$ (m^{-1})	0.0566	0.0276	0.0331	0.0304	0.0319	0.0147	0.0196	0.0151
$a_{ph}(715)$ (m^{-1})	0.024	0.013	0.0168	0.0134	0.0116	0.007	0.0085	0.0062
$a_{g}(412)$ (m^{-1})	0.4513	0.3737	0.2774	0.3404	0.1747	0.206	0.0769	0.1191
$a_{g}(440)$ (m^{-1})	0.3061	0.28311	0.1852	0.2327	0.1196	0.1478	0.0541	0.0927
$a_{g}(488)$ (m^{-1})	0.1656	0.1861	0.0965	0.1283	0.0686	0.093	0.033	0.068
$a_{g}(490)$ (m^{-1})	0.1156	0.16	0.0667	0.0895	0.0516	0.0652	0.0258	0.0572
$a_{g}(510)$ (m^{-1})	0.1048	0.1455	0.0601	0.0804	0.0473	0.06	0.0235	0.0534
$a_{g}(532)$ (m^{-1})	0.0773	0.1202	0.0473	0.0625	0.0383	0.0472	0.0205	0.0444
$a_{g}(555)$ (m^{-1})	0.0484	0.0883	0.03281	0.0432	0.0276	0.0306	0.0162	0.0323
$a_{g}(650)$ (m^{-1})	0.0292	0.0678	0.0215	0.0314	0.0214	0.0231	0.0123	0.0251
$a_{g}(676)$ (m^{-1})	0.0016	0.002	0.0023	0.0011	0.0015	0.0014	0.0012	0.0008
$a_{g}(715)$ (m^{-1})	0.0009	0	0.0002	0	0	0	0	0
$a_{d}(412)$ (m^{-1})	0.6312	0.9584	0.5697	0.366	0.2022	0.4976	0.2453	0.1977
$a_{d}(440)$ (m^{-1})	0.5171	0.7981	0.4634	0.3019	0.164	0.4349	0.1888	0.164
$a_{d}(488)$ (m^{-1})	0.4007	0.6403	0.3567	0.2366	0.128	0.3731	0.1344	0.1309
$a_{d}(490)$ (m^{-1})	0.3404	0.5625	0.304	0.202	0.1094	0.3386	0.1099	0.1135
$a_{d}(510)$ (m^{-1})	0.30981	0.51171	0.2758	0.1832	0.0999	0.3123	0.0985	0.1039
$a_{d}(532)$ (m^{-1})	0.2549	0.4279	0.2264	0.1499	0.0829	0.2689	0.078	0.0874
$a_{d}(555)$ (m^{-1})	0.1733	0.2922	0.1538	0.1009	0.0568	0.1863	0.0514	0.0611
$a_{d}(650)$ (m^{-1})	0.0982	0.1641	0.0878	0.0562	0.0334	0.1044	0.0292	0.0364
$a_{d}(676)$ (m^{-1})	0.0338	0.0542	0.0306	0.0199	0.0136	0.0346	0.0117	0.0133
$a_{d}(715)$ (m^{-1})	0.012	0.0197	0.0111	0.0071	0.0047	0.0124	0.0039	0.0045

Table 4.5 Seasonal variations of Zuari

Parameter	Summer	Monsoon	Post-Monsoon	Winter	Summer_Std	Monsoon_Std	Post-Monsoon_Std	Winter_Std
Physical								
Temperature (°C)	31.48	28.55	29.38	28.05	1.1201	1.03	1.3601	1.13
Salinity	27.14	6.13	24.21	26.92	5.93	9.28	10.39	7.11
Density σ (Kg/m^3)	15.39	7.99	14.78	16.39	4.67	6.6	7.12	5.43
Solar radiation at surface								
$E_S(350)$ ($W/m^2/nm$)	0.3641	0.2793	0.2919	0.2743	0.116301	0.1265	0.1186	0.087101
$E_S(490)$ ($W/m^2/nm$)	1.1394	0.848	0.8762	0.8726	0.3625	0.4091	0.3593	0.2533
PAR E_S (W/m^2)	318.37	233.54	243.07	244.70	100.46	114.27	100.51	70.40
Light penetration								
Z_{Max} (m)	7.18	8.57	8.28	7.33	2.17	1.45	2.32	2.13
λ (of maximum Z_{90}) (nm)	570	581	564	568	11	9	19	17
Z_{90} (m)	1.24	0.85	2.11	1.52	0.46	0.44	1.16	0.94
Z_{SD} (m)	1.37	0.92	1.96	1.67	0.5	0.42	1.03	0.92
Z_{eu} (m)	5.69	3.91	9.7	7	2.12	2.04	5.33	4.33
PAR at Z_{90}(μmole/m^2/s)	359.6	251.84	275.86	289.61	134.45	160.29	113.38	124.94
%PAR at Z_{90}	24.5	21.83	23.75	25.61	4.54	8.14	2.5	6.69
PAR at Z_{SD}(μmole/m^2/s)	359.03	219.93	294.18	266.12	227.98	182.47	142.69	193.6
%PAR at Z_{SD}	23.53	18.	25.29	22.53	12.05	8.39	6.46	13.65
λ (of Maximum E_d) (nm)	578	583	560	573	11	9	47	18
E_d at Z_{90}($W/m^2/nm$)	0.5647	0.41	0.4071	0.4598	0.196701	0.1939	0.1523	0.2456
λ (at Maximum E_{SD}) (nm)	577	589	569	576	12	20	10	23
E_d at Z_{SD}($W/m^2/nm$)	0.5565	0.3924	0.4151	0.4194	0.366	0.1991	0.1781	0.2536
IOP								
$b_b(700)$ (m^{-1})	0.1127	0.34404	0.09583	0.16496	0.0717	0.225	0.123	0.1082
a(412) (m^{-1})	2.0107	4.1596	1.4779	1.8164	0.9027	2.4522	1.2933	0.7539
a(440) (m^{-1})	1.5456	2.8885	1.08391	1.3297	0.6485	1.5962	0.9294	0.5766

a(488) (m^{-1})	0.9512	1.8021	0.5667	0.8431	0.4487	0.9797	0.5283	0.3908
a(490) (m^{-1})	0.9299	1.7638	0.55411	0.8312	0.4416	0.9575	0.5189	0.3913
a(510) (m^{-1})	0.7175	1.3803	0.4285	0.7121	0.3764	0.7378	0.4273	0.4226
a(532) (m^{-1})	0.5757	1.0306	0.29971	0.5323	0.3731	0.5349	0.3301	0.2613
a(555) (m^{-1})	0.4061	0.6884	0.2122	0.3805	0.2773	0.3653	0.248	0.2075
a(650) (m^{-1})	0.1527	0.16121	0.0962	0.1121	0.0768	0.0609	0.0805	0.0496
a(676) (m^{-1})	0.2188	0.1665	0.15591	0.1282	0.0934	0.0368	0.1039	0.0322
a(715) (m^{-1})	0	0	0	0	0	0	0	0
c(412) (m^{-1})	13.1657	19.5754	8.14151	7.96	17.5049	11.9833	10.7377	3.0726
c(440) (m^{-1})	12.7871	18.05421	7.8347	7.6931	18.0274	10.8414	11.753	3.0925
c(488) (m^{-1})	12.6296	16.1554	7.4271	7.3091	19.3842	9.4741	13.2002	3.0667
c(490) (m^{-1})	12.4852	16.08771	7.3997	7.2905	18.9344	9.422	13.1712	3.0624
c(510) (m^{-1})	11.0411	15.4101	7.1257	7.1042	15.1764	8.901	12.8816	3.0204
c(532) (m^{-1})	11.0205	14.7594	7.0799	6.9064	15.7606	8.4123	13.0725	3.0029
c(555) (m^{-1})	11.0572	14.1368	5.8273	6.8263	16.8163	7.9434	8.5316	2.999
c(650) (m^{-1})	10.051	11.8626	6.3049	6.0294	16.002	6.6094	12.142	2.7976
c(676) (m^{-1})	9.6244	11.3212	6.1165	5.8204	15.5454	6.3077	11.7637	2.735
c(715) (m^{-1})	9.333	10.5479	6.0533	5.3532	15.4191	5.891	11.161	2.5778
γ	1.11001	1.06	0.92	1.23	0.3401	0.16	0.41	0.41
ξ	4.11001	4.06	3.79	4.23001	0.3401	0.16	0.57	0.41
n_p	1.0835	1.1133	1.1032	1.09001	0.0382	0.0445	0.0551	0.0491
AOP								
K_d(350) (m^{-1})	2.3615	1.5518	1.7231	2.2452	1.8008	1.5682	1.2569	1.7574
K_d(412) (m^{-1})	2.382	1.8057	1.605	2.2873	1.2366	1.6266	1.0594	1.55
K_d(443) (m^{-1})	2.1108	1.941	1.3531	1.8746	1.0352	1.7777	0.8295	1.1947
K_d(490) (m^{-1})	1.5859	1.7231	1.0671	1.4964	0.7817	1.3626	0.6015	1.0264
K_d(510) (m^{-1})	1.4052	1.7527	0.9799	1.4189	0.7021	1.3679	0.64	0.9662
K_d(532) (m^{-1})	1.2784	1.6301	0.8707	1.2706	0.6242	1.2331	0.5422	0.8307
K_d(555) (m^{-1})	1.1596	1.4754	0.7962	1.1568	0.7162	1.11	0.5097	0.8015
K_d(566) (m^{-1})	1.078	1.4319	0.738	1.08401	0.5304	1.1024	0.4632	0.7049
K_d(620) (m^{-1})	1.19681	1.3157	0.8809	1.1433	0.6953	0.7458	0.4203	0.6837

$K_d(650)$ (m^{-1})	1.1994	1.3198	0.9071	1.1675	0.6226	0.8736	0.4079	0.6507
$K_d(670)$ (m^{-1})	1.3221	1.4023	1.0084	1.2273	0.6184	0.8683	0.4361	0.7016
$K_d(676)$ (m^{-1})	1.2963	1.2502	1.031	1.2314	0.4584	0.7041	0.4245	0.6915
$K_d(681)$ (m^{-1})	1.3406	1.3884	1.0324	1.228	0.7204	0.9138	0.4359	0.7075
$K_d(700)$ (m^{-1})	1.3549	1.4031	1.0875	1.3166	0.6831	0.8185	0.4216	0.723
$R_{rs}(350)$ (sr^{-1})	0.00113	0.00079	0.00182	0.00093	0.0016	0.0009	0.0028	0.0007
$R_{rs}(412)$ (sr^{-1})	0.00304	0.00388	0.00227	0.00221	0.0047	0.0134	0.0011	0.0015
$R_{rs}(443)$ (sr^{-1})	0.00327	0.00494	0.00319	0.0039	0.0024	0.0105	0.0015	0.0033
$R_{rs}(490)$ (sr^{-1})	0.00518	0.00507	0.0051	0.00568	0.0029	0.0046	0.0019	0.0032
$R_{rs}(510)$ (sr^{-1})	0.00643	0.01655	0.0062	0.00677	0.0031	0.0624	0.0021	0.0035
$R_{rs}(532)$ (sr^{-1})	0.00811	0.01617	0.00774	0.00831	0.0035	0.0474	0.0024	0.0038
$R_{rs}(555)$ (sr^{-1})	0.00992	0.01732	0.00917	0.01003	0.004	0.0357	0.0028	0.0042
$R_{rs}(566)$ (sr^{-1})	0.01072	0.01793	0.00974	0.01083	0.0043	0.0309	0.003	0.0044
$R_{rs}(620)$ (sr^{-1})	0.00806	0.01601	0.00578	0.00826	0.0041	0.0222	0.0026	0.0039
$R_{rs}(650)$ (sr^{-1})	0.0077	0.01561	0.00533	0.0079	0.0039	0.0197	0.0025	0.0037
$R_{rs}(670)$ (sr^{-1})	0.00629	0.01422	0.00423	0.00674	0.0036	0.0192	0.0021	0.0033
$R_{rs}(676)$ (sr^{-1})	0.00629	0.01403	0.00422	0.0067	0.0036	0.0182	0.0021	0.0033
$R_{rs}(681)$ (sr^{-1})	0.00637	0.01408	0.00426	0.00669	0.0035	0.0186	0.0021	0.0033
$R_{rs}(700)$ (sr^{-1})	0.00535	0.01204	0.0033	0.00528	0.0032	0.0175	0.0019	0.003
Biological								
Chlorophyll (mg/m^3)	6.24	5.89	5.62	3.07	2.92	2.9901	2.45	1.97
Chlorophyll(mg/m^3)-Sensor	3.36	2.08	2.64	1.91	1.6	1.28	1.38	0.48
TSM (g/m^3)	12.66	19.67	10.11	15.15	7.33	12.2	17.58	7.17
pH	7.75	7.43	7.67	7.5	0.09	0.19	0.22	0.29
λ (FLH R_{rs})	695	695	692	692	3	2	4	3
$R_{rs}(\lambda)$ FLH (sr^{-1})	0.00207	0.002	0.00129	0.0015	0.0009	0.0011	0.0006	0.0007
λ (FLH L_w) nm	695	686	688	686	6	10	8	7
$L_w(\lambda)$ FLH ($\mu Wcm^{-2}sr^{-1}$)	0.07663	0.12622	0.05054	0.04184	0.0469	0.0679	0.0507	0.0172
$a_{ph}(412)$ (m^{-1})	0.1636	0.2418	0.1082	0.0634	0.1067	0.2294	0.1208	0.0246
$a_{ph}(440)$ (m^{-1})	0.1502	0.2049	0.1007	0.056	0.0919	0.1812	0.104	0.0247

$a_{ph}(488)$ (m^{-1})	0.1243	0.1604	0.084	0.0446	0.0707	0.1321	0.0779	0.0242
$a_{ph}(490)$ (m^{-1})	0.0862	0.1232	0.0572	0.0356	0.0467	0.1067	0.0477	0.0178
$a_{ph}(510)$ (m^{-1})	0.0677	0.1046	0.0432	0.0266	0.0352	0.0944	0.0335	0.0162
$a_{ph}(532)$ (m^{-1})	0.0376	0.0728	0.0219	0.01931	0.0203	0.0751	0.0144	0.0091
$a_{ph}(555)$ (m^{-1})	0.0264	0.0481	0.0165	0.0131	0.0159	0.0486	0.0108	0.0067
$a_{ph}(650)$ (m^{-1})	0.0684	0.0572	0.046	0.028	0.0404	0.0306	0.0311	0.0104
$a_{ph}(676)$ (m^{-1})	0.0669	0.0464	0.0444	0.0273	0.04	0.0259	0.0298	0.0101
$a_{ph}(715)$ (m^{-1})	0.0286	0.023	0.0188	0.0134	0.0153	0.0098	0.0093	0.0046
$a_{g}(412)$ (m^{-1})	0.4322	0.5042	0.3555	0.4455	0.2239	0.3396	0.1587	0.1307
$a_{g}(440)$ (m^{-1})	0.3031	0.3603	0.2404	0.307	0.1447	0.2576	0.1109	0.087
$a_{g}(488)$ (m^{-1})	0.1635	0.2213	0.1301	0.1737	0.076	0.1781	0.0658	0.0464
$a_{g}(490)$ (m^{-1})	0.1087	0.1703	0.0923	0.1271	0.0567	0.1449	0.0502	0.0327
$a_{g}(510)$ (m^{-1})	0.0968	0.1534	0.0879	0.116	0.0518	0.1329	0.0424	0.029
$a_{g}(532)$ (m^{-1})	0.0693	0.122	0.06511	0.09	0.0395	0.108	0.0371	0.0228
$a_{g}(555)$ (m^{-1})	0.042	0.0834	0.0455	0.0641	0.024	0.0728	0.0256	0.0166
$a_{g}(650)$ (m^{-1})	0.0212	0.0544	0.032	0.0454	0.0125	0.0443	0.0189	0.0146
$a_{g}(676)$ (m^{-1})	0.0016	0.003	0.0025	0.0046	0.001	0.0014	0.0022	0.0095
$a_{g}(715)$ (m^{-1})	0	0	0	0	0	0	0	0
$a_{d}(412)$ (m^{-1})	0.6146	1.5304	0.5821	0.3857	0.2535	0.7632	0.4302	0.1883
$a_{d}(440)$ (m^{-1})	0.4967	1.2605	0.4629	0.3174	0.2013	0.6432	0.3411	0.1564
$a_{d}(488)$ (m^{-1})	0.3783	0.9952	0.3449	0.2487	0.1522	0.529	0.2586	0.1243
$a_{d}(490)$ (m^{-1})	0.3197	0.8667	0.29011	0.2137	0.13	0.4705	0.221	0.1077
$a_{d}(510)$ (m^{-1})	0.2887	0.7859	0.26191	0.1935	0.1179	0.4274	0.2009	0.0992
$a_{d}(532)$ (m^{-1})	0.2334	0.6481	0.212	0.1592	0.0966	0.357	0.1654	0.0831
$a_{d}(555)$ (m^{-1})	0.1546	0.436	0.1434	0.108	0.0663	0.2409	0.1146	0.0583
$a_{d}(650)$ (m^{-1})	0.0831	0.2403	0.0829	0.0615	0.0403	0.1316	0.0696	0.0353
$a_{d}(676)$ (m^{-1})	0.026	0.0783	0.0299	0.0243	0.017	0.0419	0.0277	0.012
$a_{d}(715)$ (m^{-1})	0.0095	0.0288	0.0108	0.0087	0.0062	0.0154	0.0098	0.0041

Table 4.6 Seasonal variations of coastal waters

Parameter	Summer	Monsoon	Post-Monsoon	Winter	Summer_Std	Monsoon_Std	Post-Monsoon_Std	Winter_Std
Physical								
Temperature (°C)	30.34	0	29.04	27.77	0.87	0	0.79	0.6801
Salinity	35.23	0	34.13	34.71	0.57	0	0.8	0.4
Density (Kg/m^3)	21.79	0	21.41	22.26	0.53	0	0.78	0.31
Solar radiation at surface								
$E_S(350)$ ($W/m^2/nm$)	0.4336	0	0.3345	0.3233	0.0804	0	0.077	0.0772
$E_S(490)$ ($W/m^2/nm$)	1.3403	0	1.0741	1.0284	0.2134	0	0.252	0.2416
PAR E_S (W/m^2)	372.99	0	299.25	287.72	59.36	0	70.27	67.98
Light penetration								
Z_{Max} (m)	17.57	0	17.21	16.60001	5.55	0	6.1901	5.9801
λ (of maximum Z_{90}) (nm)	535	0	549	551	30	0	24	19
Z_{90} (m)	6.57	0	4.97	3.73	3.98	0	1.83	1.49
Z_{SD} (m)	5.38	0	4.73	3.79	2.68	0	1.83	1.6201
Z_{eu} (m)	30.24	0	22.9	17.16	18.31	0	8.43	6.88
PAR at Z_{90}(µmole/m^2/s)	353.84	0	277.7	298.13	81.66	0	63.98	74.72
%PAR at Z_{90}	20.94	0	20.11	22.74	3.9	0	1.9	3.65
PAR at Z_{SD}(µmole/m^2/s)	468.62	0	321.78	314.04001	176.96	0	133.15	101.25
%PAR at Z_{SD}	27.34	0	22.88	23.32	9.48	0	7.27	5.56
λ (of Maximum E_d) (nm)	535	0	552	552	29	0	19	16
E_d at Z_{90}($W/m^2/nm$)	0.5591	0	0.4485	0.4472	0.0983	0	0.1056	0.1008
λ (at Maximum E_{SD}) (nm)	533	0	553	551	30	0	21	15
E_d at Z_{SD}($W/m^2/nm$)	0.6890	0	0.4903	0.4573	0.2277	0	0.1774	0.1181
IOP								
$b_b(700)$ (m^{-1})	0.01587	0	0.00882	0.02611	0.0163	0	0.0055	0.0145
a(412) (m^{-1})	0.4322	0	0.4937	0.4768	0.3358	0	0.3002	0.1719
a(440) (m^{-1})	0.3131	0	0.3726	0.3659	0.198	0	0.2307	0.1397

a(488) (m^{-1})	0.2331	0	0.2347	0.2386	0.2859	0	0.1285	0.0817
a(490) (m^{-1})	0.2266	0	0.2305	0.2343	0.266	0	0.1258	0.0799
a(510) (m^{-1})	0.1623	0	0.189	0.191	0.0972	0	0.0993	0.0633
a(532) (m^{-1})	0.1457	0	0.1492	0.16271	0.0866	0	0.0721	0.0474
a(555) (m^{-1})	0.1076	0	0.1113	0.1231	0.0598	0	0.0497	0.0359
a(650) (m^{-1})	0.0606	0	0.073	0.0738	0.0281	0	0.0292	0.0224
a(676) (m^{-1})	0.0869	0	0.11	0.1011	0.089	0	0.0614	0.0461
a(715) (m^{-1})	0	0	0	0	0	0	0	0
c(412) (m^{-1})	2.4234	0	2.2508	2.8489	3.3001	0	1.61	1.286
c(440) (m^{-1})	2.2994	0	2.1349	2.7621	3.1802	0	1.5542	1.2581
c(488) (m^{-1})	1.5656	0	1.9236	2.5368	1.3101	0	1.4165	1.1725
c(490) (m^{-1})	1.5571	0	1.9175	2.5274	1.3019	0	1.4128	1.1686
c(510) (m^{-1})	1.472	0	1.8568	2.4328	1.233	0	1.3777	1.1303
c(532) (m^{-1})	1.4869	0	1.7985	2.3475	1.2592	0	1.3227	1.1157
c(555) (m^{-1})	1.4278	0	1.7666	2.3305	1.2365	0	1.3011	1.0989
c(650) (m^{-1})	1.6126	0	1.5948	2.0138	2.6231	0	1.1153	0.9474
c(676) (m^{-1})	1.7981	0	1.548	1.9416	3.3108	0	1.0931	0.9217
c(715) (m^{-1})	3.4397	0	2.3742	1.7604	11.7575	0	5.9388	0.9212
γ	0.89	0	1.12001	1.01	0.27	0	0.33	0.3401
ξ	3.69	0	4.12	4	0.69	0	0.33	0.36
n_p	1.08801	0	1.0464	1.0854	0.0536	0	0.0381	0.0439
AOP								
K_d(350) (m^{-1})	0.5771	0	0.6573	0.7521	0.5235	0	0.3469	0.4079
K_d(412) (m^{-1})	0.4246	0	0.5028	0.6137	0.3742	0	0.2676	0.2975
K_d(443) (m^{-1})	0.3567	0	0.4339	0.5375	0.3114	0	0.2428	0.2412
K_d(490) (m^{-1})	0.2717	0	0.3358	0.4171	0.2418	0	0.2011	0.1775
K_d(510) (m^{-1})	0.2566	0	0.3086	0.3929	0.2188	0	0.1808	0.157
K_d(532) (m^{-1})	0.246	0	0.2927	0.3666	0.1958	0	0.1686	0.1406
K_d(555) (m^{-1})	0.2377	0	0.2809	0.3506	0.174	0	0.1533	0.1286
K_d(566) (m^{-1})	0.2359	0	0.2749	0.3428	0.1696	0	0.1431	0.1226
K_d(620) (m^{-1})	0.4559	0	0.4847	0.5413	0.1732	0	0.1345	0.1396

$K_d(650)$ (m^{-1})	0.4965	0	0.5219	0.5749	0.1875	0	0.1278	0.161
$K_d(670)$ (m^{-1})	0.5748	0	0.6153	0.6607	0.2227	0	0.1691	0.2067
$K_d(676)$ (m^{-1})	0.5867	0	0.6255	0.6612	0.242	0	0.1633	0.2118
$K_d(681)$ (m^{-1})	0.58321	0	0.619	0.65181	0.2219	0	0.1581	0.2092
$K_d(700)$ (m^{-1})	0.6505	0	0.6977	0.7182	0.2586	0	0.1897	0.2982
$R_{rs}(350)$ (sr^{-1})	0.00241	0	0.02614	0.0024	0.0018	0	0.2446	0.0015
$R_{rs}(412)$ (sr^{-1})	0.00334	0	0.00237	0.00384	0.0015	0	0.0013	0.0017
$R_{rs}(443)$ (sr^{-1})	0.00394	0	0.00275	0.00485	0.0016	0	0.0016	0.0021
$R_{rs}(490)$ (sr^{-1})	0.00542	0	0.00394	0.00684	0.002	0	0.0021	0.0025
$R_{rs}(510)$ (sr^{-1})	0.00562	0	0.00434	0.00739	0.0023	0	0.0023	0.0026
$R_{rs}(532)$ (sr^{-1})	0.00604	0	0.00489	0.00805	0.0028	0	0.0026	0.0028
$R_{rs}(555)$ (sr^{-1})	0.00599	0	0.00523	0.00832	0.0032	0	0.003	0.003
$R_{rs}(566)$ (sr^{-1})	0.006	0	0.00538	0.00843	0.0035	0	0.0032	0.0031
$R_{rs}(620)$ (sr^{-1})	0.0022	0	0.00203	0.00323	0.0021	0	0.0022	0.0019
$R_{rs}(650)$ (sr^{-1})	0.00188	0	0.00177	0.00274	0.0019	0	0.0021	0.0017
$R_{rs}(670)$ (sr^{-1})	0.00141	0	0.00148	0.00214	0.0015	0	0.0017	0.0014
$R_{rs}(676)$ (sr^{-1})	0.00142	0	0.00156	0.00216	0.0015	0	0.0017	0.0014
$R_{rs}(681)$ (sr^{-1})	0.00143	0	0.00162	0.00216	0.0014	0	0.0017	0.0013
$R_{rs}(700)$ (sr^{-1})	0.00209	0	0.00119	0.00149	0.0108	0	0.0017	0.0011
Biological								
Chlorophyll (mg/m^3)	10.26	0	2.74	2.3	44.45	0	2.2	2.57
Chlorophyll(mg/m^3)-Sensor	0.91	0.00	1.20	1.92	0.61	0.00	0.42	1.07
TSM (g/m^3)	14.99	0	8.08	10.54	23	0	9.82	6.32
pH	7.99	0	7.97	8.02	0.25	0	0.06	0.09
λ (FLH R_{rs})	688	0	686	688	5	0	3	2
$R_{rs}(\lambda)$ FLH (sr^{-1})	0.00047	0	0.00055	0.00063	0.0004	0	0.0004	0.0004
λ (FLH L_w) nm	684	0	682	682	6	0	3	4
$L_w(\lambda)$ FLH ($\mu Wcm^{-2}sr^{-1}$)	0.03584	0	0.04203	0.03546	0.03	0	0.0262	0.0199
$a_{ph}(412)$ (m^{-1})	5.3792	0	0.1384	0.062	13.1277	0	0.1347	0.0377
$a_{ph}(440)$ (m^{-1})	4.8468	0	0.1202	0.0587	11.7699	0	0.1016	0.0341

$a_{ph}(488)$ (m^{-1})	4.0392	0	0.0972	0.0516	9.788	0	0.0711	0.0297
$a_{ph}(490)$ (m^{-1})	3.156	0	0.07431	0.03961	7.756	0	0.0549	0.0235
$a_{ph}(510)$ (m^{-1})	2.5724	0	0.061	0.0332	6.3448	0	0.0461	0.0207
$a_{ph}(532)$ (m^{-1})	1.7241	0	0.04	0.0232	4.1459	0	0.0314	0.0157
$a_{ph}(555)$ (m^{-1})	1.159	0	0.0242	0.0149	2.7459	0	0.02	0.0104
$a_{ph}(650)$ (m^{-1})	2.4506	0	0.0401	0.0233	5.8614	0	0.0285	0.0178
$a_{ph}(676)$ (m^{-1})	2.3714	0	0.03671	0.0203	5.6381	0	0.0257	0.0162
$a_{ph}(715)$ (m^{-1})	1.19271	0	0.0184	0.0092	2.8199	0	0.0131	0.0072
$a_{g}(412)$ (m^{-1})	3.2018	0	0.1416	0.1398	6.6407	0	0.062	0.0432
$a_{g}(440)$ (m^{-1})	2.9022	0	0.0893	0.0943	6.1545	0	0.0465	0.0342
$a_{g}(488)$ (m^{-1})	3.1029	0	0.0417	0.05	7.0852	0	0.0309	0.025
$a_{g}(490)$ (m^{-1})	3.6177	0	0.0298	0.0343	9.0608	0	0.0248	0.021
$a_{g}(510)$ (m^{-1})	3.415	0	0.0224	0.0321	8.641	0	0.0248	0.02
$a_{g}(532)$ (m^{-1})	3.9272	0	0.0202	0.0266	9.6226	0	0.0239	0.0171
$a_{g}(555)$ (m^{-1})	3.1121	0	0.0147	0.0206	7.421	0	0.0183	0.0129
$a_{g}(650)$ (m^{-1})	1.5507	0	0.0132	0.0151	3.5274	0	0.0141	0.0126
$a_{g}(676)$ (m^{-1})	0.0628	0	0.0027	0.0034	0.2282	0	0.0036	0.002
$a_{g}(715)$ (m^{-1})	0.0004	0	0	0.0001	0	0	0	0
$a_{d}(412)$ (m^{-1})	1.3184	0	0.1524	0.1382	3.0604	0	0.1871	0.081
$a_{d}(440)$ (m^{-1})	1.1734	0	0.1222	0.1089	2.8286	0	0.1515	0.0638
$a_{d}(488)$ (m^{-1})	1.1012	0	0.0915	0.0796	2.835	0	0.1156	0.0467
$a_{d}(490)$ (m^{-1})	1.1285	0	0.07631	0.0659	3.0387	0	0.0977	0.0388
$a_{d}(510)$ (m^{-1})	1.0619	0	0.0696	0.0642	2.8843	0	0.0892	0.0324
$a_{d}(532)$ (m^{-1})	1.0186	0	0.0629	0.0524	2.8253	0	0.0749	0.0263
$a_{d}(555)$ (m^{-1})	0.7744	0	0.0439	0.0365	2.1255	0	0.0535	0.0185
$a_{d}(650)$ (m^{-1})	0.4457	0	0.0269	0.0228	1.1847	0	0.0347	0.012
$a_{d}(676)$ (m^{-1})	0.1485	0	0.0106	0.0094	0.3386	0	0.0152	0.0052
$a_{d}(715)$ (m^{-1})	0.0618	0	0.0038	0.0034	0.1462	0	0.0053	0.0018

4.2.3 Spatial and temporal variations

There were spatial and temporal variations of bio-optical parameters observed in these waters.

The $b_b(700)$ was high upstream during all dry seasons in the Mandovi and low during monsoon (Figure 4.1). During monsoon, it was high in the bottom waters near the mouth of the Mandovi. Similar patterns were observed of chlorophyll indicating, a good correlation between $b_b(700)$ and chlorophyll. In the Zuari, the lowest values were observed in the water column during winter. There was a region from 15 to 20 Km stretch where notable high $b_b(700)$ values were observed (Figure 4.2).

Bulk refractive index values, n_p were higher upstream in both the estuaries (Figure 4.3 and 4.4). There were regions where low values of n_p were observed at the bottom, indicating high absorbing materials like phytoplankton. Bottom waters near the mouth had low n_p.

The particle size distributions also showed spatial and temporal variations, as indicated by the slope ξ of PSD (Figure 4.5 and 4.6). Low values of ξ indicate relatively large particles and vice versa. The lowest values were observed in Zuari during post-monsoon and relatively lower during monsoon. The mid region had higher values of ξ (Figure 4.6).

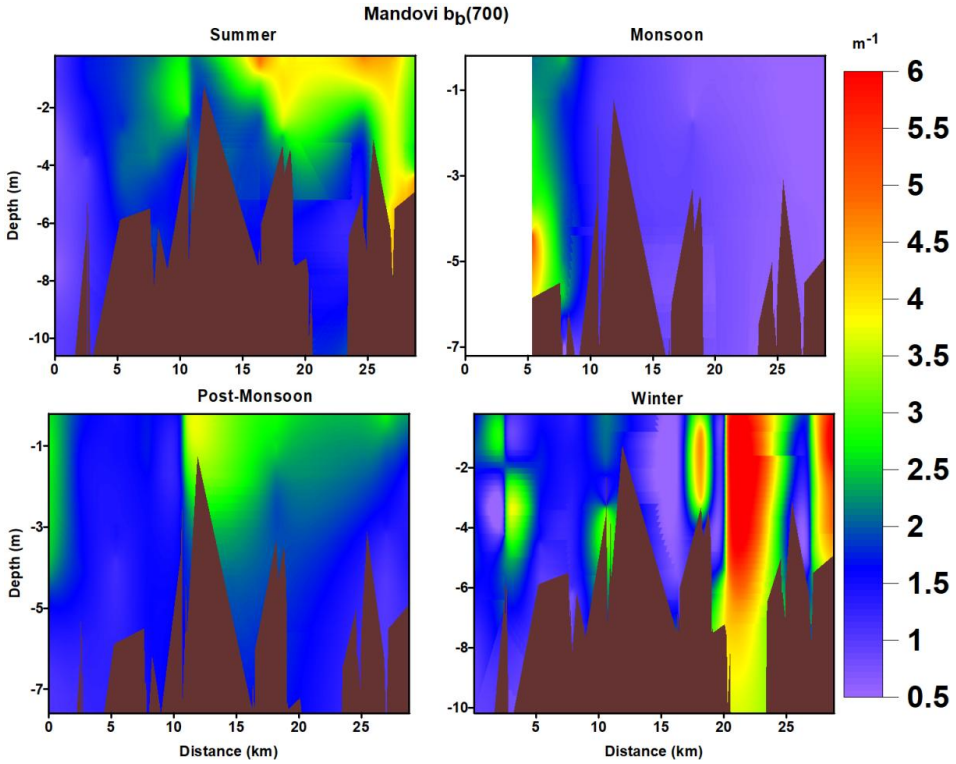

Figure 4.1 Spatial and seasonal variations of b_b(700) (m^{-1}) in the Mandovi

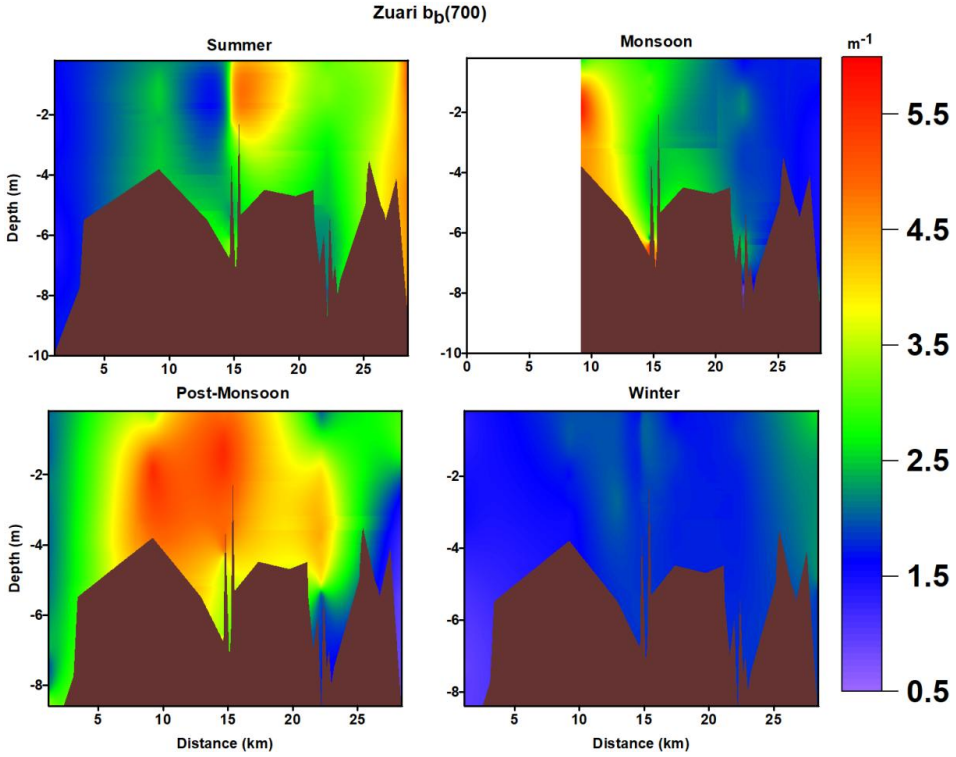

Figure 4.2 Spatial and seasonal variations of b_b(700) (m^{-1}) in the Zuari

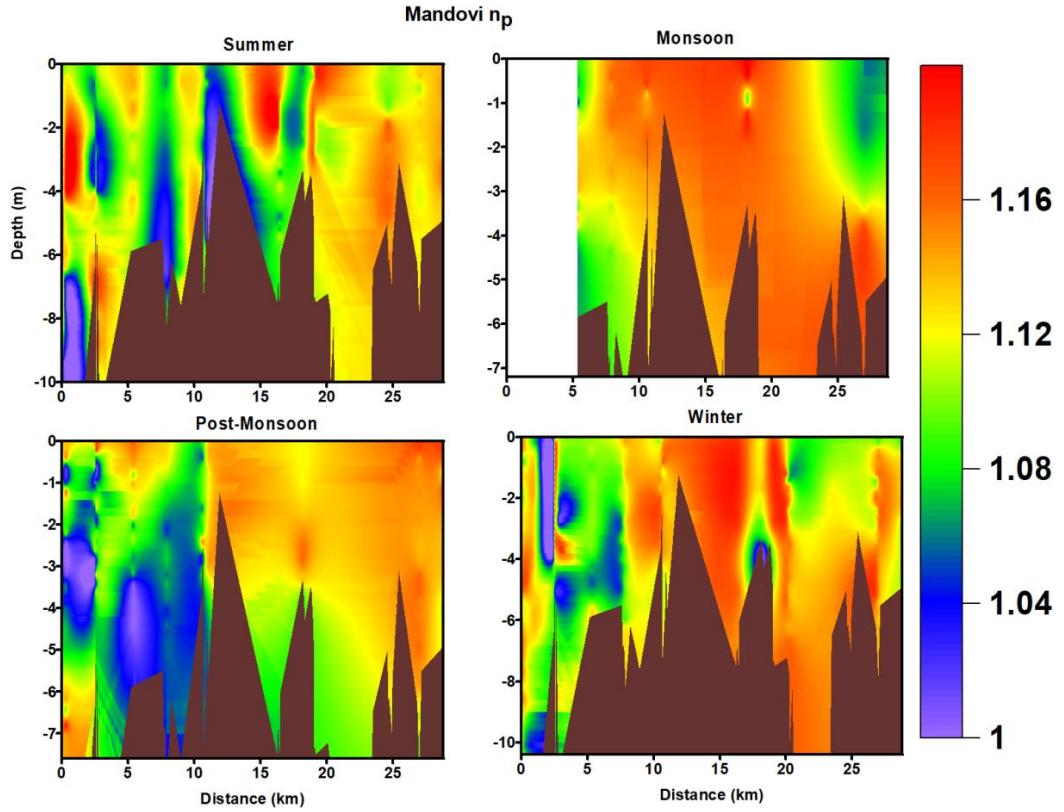

Figure 4.3 Spatial and seasonal variations of n_p in the Mandovi

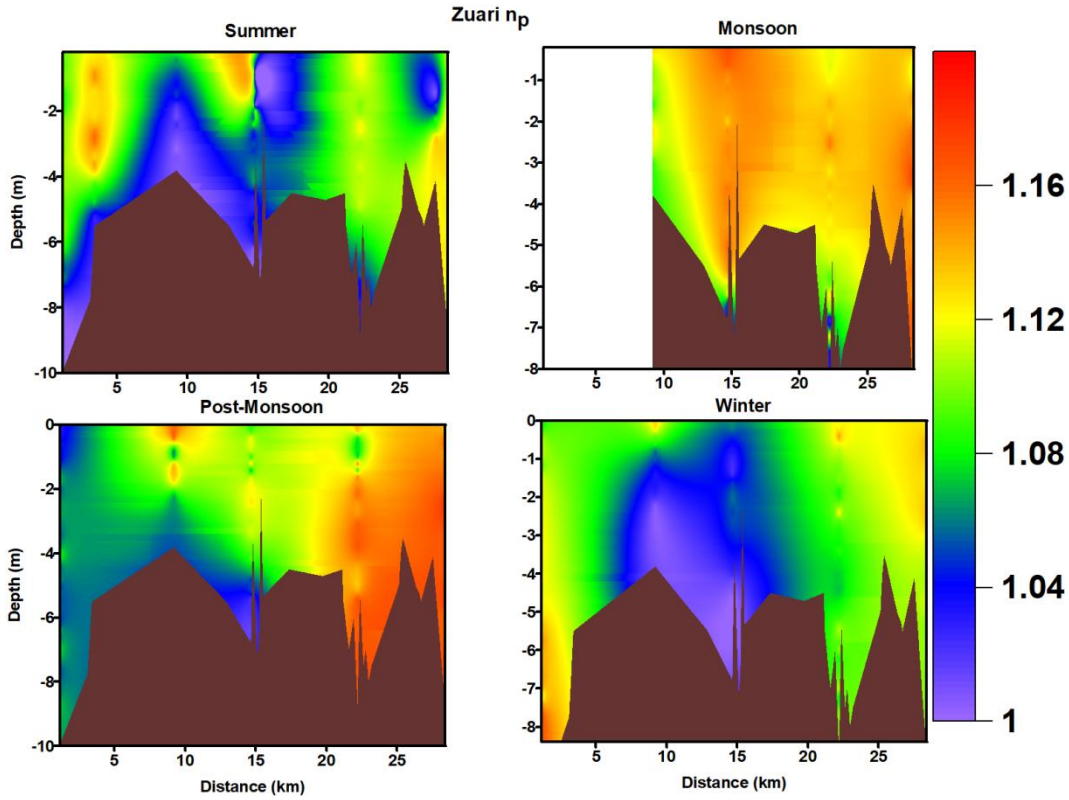

Figure 4.4 Spatial and seasonal variations of n_p in the Zuari

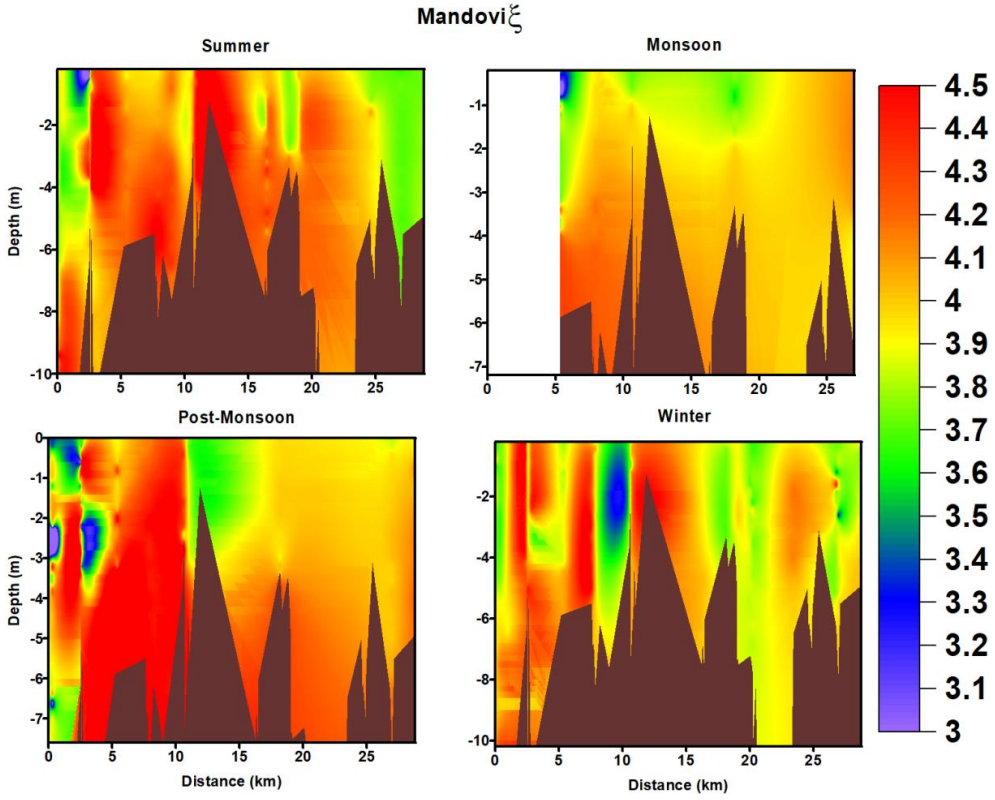

Figure 4.5 Spatial and seasonal variations of ξ in the Mandovi.

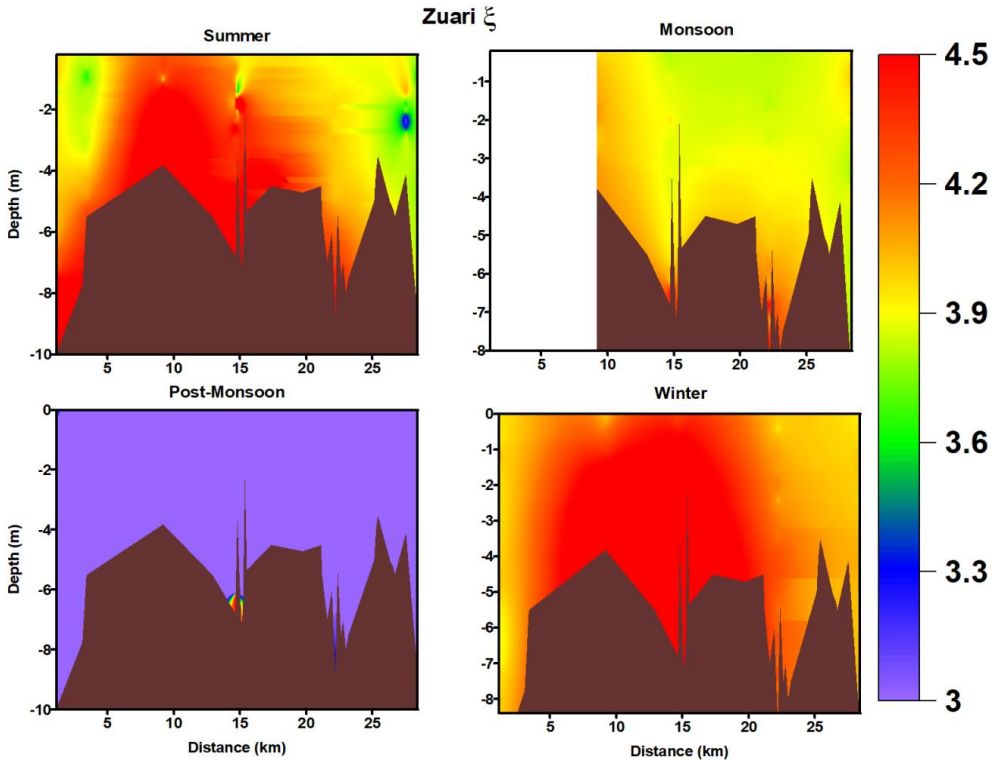

Figure 4.6 Spatial and seasonal variations of ξ in the Zuari.

One of the notable features of variations was observed during monsoon when the density σ was correlated well with the $b_b(700)$ (Figure4.7).

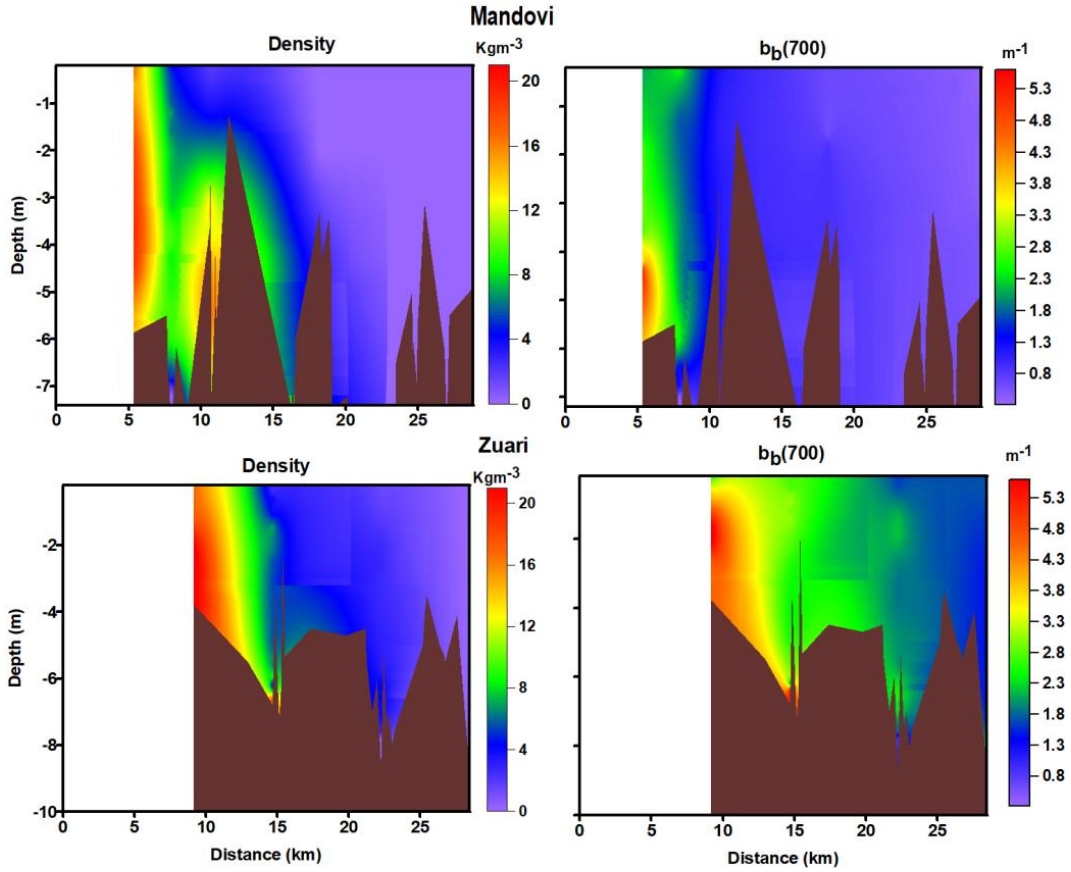

Figure 4.7 Density σ (Kgm^{-3}) and $b_b(700)$ (m^{-1}) during monsoon in the estuaries

4.2.3.1 Parameter variations during *Trichodesmium spp* blooms

There are annual recurring *Trichodesmium spp* blooms observed during summer in these coastal waters of Goa (D'Silva, et al., 2012; Desa et al., 2005a; Devassy, Bhattathiri, & Qasim, 1979; Dias, Kurian, & Suresh, 2019; Tholkapiyan, Shanmugam, & Suresh, 2014) (See Figure 4.8). These blooms result in the surface layers being very productive, with very high values of chlorophyll being observed. The biological and optical properties show very uncommon characteristics during the *Trichodesmium spp* blooms. The variations of various parameters during such blooms are given in Table 4.7. The objective of this study was to identify signatures in $R_{rs}(\lambda)$ during the blooms.

Figure 4.8 *Trichodesmium* blooms in the coastal waters of Goa on 24 April 2014

Table 4.7 Mean parameters during *Trichodesmium* spp. bloom

Parameter	Mean	Std	Minimum	Maximum
Physical				
Temperature (°C)	31.12	0.22	30.68	31.53
Salinity	35.27	0.58	33.41	35.88
Density (Kg/m^3)	21.55	0.50	20.01	22.15
Solar				
$E_S(350)$ ($\mu W/cm^2$)	44.28	5.67	34.40	52.31
$E_S(490)$ ($\mu W/cm^2$)	136.77	14.01	114.25	155.79
PAR E_S ($\mu W/cm^2$)	38110.57	3863.00	32062.97	43202.84
Light at depth				
λ (of maximum Z_{90}) (nm)	545	21	497	573
Z_{Max} (m)	17.41	3.71	14.00	25.80
Z_{90} (m)	5.79	1.94	2.01	8.97
Z_{SD} (m)	6.86	3.00	1.40	13.50
Z_{eu} (m)	26.65	8.93	9.26	41.31
PAR at Z_{90} ($\mu mole/m^2$)	351.43	64.79	251.84	484.21
%PAR at Z_{90}	19.91	1.86	17.14	24.42
PAR at Z_{SD} ($\mu mole/cm^2$)	357.35	155.29	152.12	681.44
%PAR at Z_{SD}	20.53	8.38	10.35	35.78
λ (at Maximum E_d) (nm)	540.	8	497.	553.
E_d at Z_{90}($W/m^2/nm$)	0.569	0.07	0.454	0.69
λ (at Maximum E_{SD}) (nm)	536.	24.	494.	560.
E_d at Z_{SD}($W/m^2/nm$)	0.565	0.168	0.318	0.842
IOP				

$b_b(700)$ (m^{-1})	0.01182	0.01000	0.00625	0.04442
a(412) (m^{-1})	0.3384	0.1616	0.1421	0.5108
a(440) (m^{-1})	0.2668	0.1263	0.0972	0.3925
a(488) (m^{-1})	0.3523	0.6098	0.1017	2.3954
a(490) (m^{-1})	0.3352	0.5615	0.0986	2.2152
a(510) (m^{-1})	0.1643	0.0890	0.0676	0.4132
a(532) (m^{-1})	0.1352	0.0314	0.0870	0.1683
a(555) (m^{-1})	0.1053	0.0449	0.0470	0.2250
a(650) (m^{-1})	0.0608	0.0230	0.0280	0.1183
a(676) (m^{-1})	0.1242	0.1868	0.0012	0.7385
a(715) (m^{-1})	0.	0.	0.	0.
c(412) (m^{-1})	4.6719	6.5849	0.5433	17.3559
c(440) (m^{-1})	4.4831	6.3962	0.5096	17.3937
c(488) (m^{-1})	1.2504	0.7093	0.4515	3.1868
c(490) (m^{-1})	1.2346	0.6742	0.4495	3.0284
c(510) (m^{-1})	1.0767	0.4097	0.4289	1.4538
c(532) (m^{-1})	1.1371	0.4510	0.4285	1.6938
c(555) (m^{-1})	1.0526	0.4103	0.4373	1.6812
c(650) (m^{-1})	3.1328	5.5139	0.4131	17.0363
c(676) (m^{-1})	4.4201	6.9823	0.4060	18.1733
c(715) (m^{-1})	12.8748	25.5588	0.3618	90.9966
AOP				
$K_d(350)$ (m^{-1})	0.3693	0.2777	0.0146	1.4232
$K_d(412)$ (m^{-1})	0.3073	0.0759	0.1907	0.4869
$K_d(443)$ (m^{-1})	0.2818	0.1144	0.1558	0.7723
$K_d(490)$ (m^{-1})	0.1907	0.0519	0.1030	0.3074
$K_d(510)$ (m^{-1})	0.1760	0.0570	0.0180	0.2892
$K_d(532)$ (m^{-1})	0.1733	0.0442	0.0717	0.2576
$K_d(555)$ (m^{-1})	0.1712	0.0387	0.0857	0.2409
$K_d(566)$ (m^{-1})	0.1685	0.0407	0.0695	0.2402
$K_d(620)$ (m^{-1})	0.4007	0.0535	0.3103	0.5341
$K_d(650)$ (m^{-1})	0.4404	0.0830	0.2677	0.7136
$K_d(670)$ (m^{-1})	0.5015	0.1473	0.0600	0.8991
$K_d(676)$ (m^{-1})	0.5161	0.1600	0.0554	0.9690
$K_d(681)$ (m^{-1})	0.5158	0.1673	0.0317	0.9470
$K_d(700)$ (m^{-1})	0.5351	0.2696	0.0387	0.9201
$R_{rs}(350)$ (sr^{-1})	0.001779	0.000699	0.000616	0.002851
$R_{rs}(412)$ (sr^{-1})	0.002681	0.001131	0.000670	0.004687
$R_{rs}(443)$ (sr^{-1})	0.002887	0.001291	0.000734	0.004846
$R_{rs}(490)$ (sr^{-1})	0.004029	0.001663	0.001241	0.006493
$R_{rs}(510)$ (sr^{-1})	0.004307	0.001656	0.001532	0.007207
$R_{rs}(532)$ (sr^{-1})	0.004668	0.001692	0.001845	0.008154
$R_{rs}(555)$ (sr^{-1})	0.004519	0.001509	0.001945	0.007891
$R_{rs}(566)$ (sr^{-1})	0.004405	0.001448	0.001982	0.007578
$R_{rs}(620)$ (sr^{-1})	0.001626	0.000847	0.000722	0.004223
$R_{rs}(650)$ (sr^{-1})	0.001418	0.000731	0.000572	0.003594
$R_{rs}(670)$ (sr^{-1})	0.000906	0.000348	0.000443	0.001769
$R_{rs}(676)$ (sr^{-1})	0.000904	0.000324	0.000321	0.001655
$R_{rs}(681)$ (sr^{-1})	0.000930	0.000353	0.000326	0.001771
$R_{rs}(700)$ (sr^{-1})	0.000996	0.000631	0.000331	0.002491
γ	1.05	0.18	0.82	1.40
ξ	3.60	0.77	2.31	4.40
n_p	1.0598	0.0464	1.0206	1.1967

Biology				
Chlorophyll (mg/m^3)	84.76	113.37	1.52	247.20
Chlorophyll (mg/m^3) Sensor	2.00	1.68	0.44	6.81
TSM (g/m^3)	78.68	58.84	22.85	134.50
pH	7.27	0.00	7.27	7.27
λ FLH R_{rs}	693.	5.	684.	698.
$R_{rs}(\lambda)$ FLH	0.00050	0.00050	0.00003	0.00158
λ FLH L_w	690.	9.	681.	708.
$L_w(\lambda)$ FLH	0.03604	0.04285	0.00216	0.16376
$a_{ph}(440)$ (m^{-1})	22.3617	16.3666	2.6080	48.8126
$a_{ph}(488)$ (m^{-1})	18.6186	13.5911	2.2737	40.2027
$a_{ph}(490)$ (m^{-1})	14.5372	11.0046	1.1063	31.9769
$a_{ph}(510)$ (m^{-1})	11.8368	9.0621	0.5034	26.0304
$a_{ph}(532)$ (m^{-1})	8.7533	5.3778	0.9410	16.7079
$a_{ph}(555)$ (m^{-1})	4.9578	3.8344	0.2741	10.8445
$a_{ph}(650)$ (m^{-1})	11.3155	7.9435	1.3238	23.4327
$a_{ph}(676)$ (m^{-1})	10.9658	7.5435	1.2634	22.4182
$a_{ph}(715)$ (m^{-1})	5.3316	3.8087	0.5754	11.3249
$a_g(412)$ (m^{-1})	12.1429	8.7753	1.1934	24.6247
$a_g(440)$ (m^{-1})	11.2356	8.1637	1.1118	25.2086
$a_g(488)$ (m^{-1})	12.2926	10.0149	1.2124	31.8148
$a_g(490)$ (m^{-1})	14.0558	13.9660	1.3500	41.8861
$a_g(510)$ (m^{-1})	13.2451	13.4386	1.3108	39.5430
$a_g(532)$ (m^{-1})	17.0947	14.2921	1.3182	41.8500
$a_g(555)$ (m^{-1})	11.4957	10.9200	0.9894	31.9666
$a_g(650)$ (m^{-1})	5.7259	4.9836	0.4517	15.4531
$a_g(676)$ (m^{-1})	0.4185	0.4774	0.0029	0.9171
$a_g(715)$ (m^{-1})	0.	0	0	0
$a_d(412)$ (m^{-1})	5.7660	4.3958	0.6939	13.2128
$a_d(440)$ (m^{-1})	5.1872	4.1909	0.5985	12.5151
$a_d(488)$ (m^{-1})	4.9510	4.4105	0.5305	13.0169
$a_d(490)$ (m^{-1})	5.1265	4.8710	0.4820	14.2135
$a_d(510)$ (m^{-1})	4.8318	4.6506	0.3356	13.5052
$a_d(532)$ (m^{-1})	4.5675	4.6107	0.1615	13.2891
$a_d(555)$ (m^{-1})	3.3414	3.4300	0.1329	9.8819
$a_d(650)$ (m^{-1})	1.9252	1.8619	0.1862	5.4403
$a_d(676)$ (m^{-1})	0.5950	0.4613	0.0954	1.3946
$a_d(715)$ (m^{-1})	0.2576	0.2054	0.0429	0.6287

4.2.4 Characteristics of $R_{rs}(\lambda)$ at *Trichodesmium* bloom

The $a_{ph}(\lambda)$ of *Trichodesmium* bears some unique signatures due to pigments and could be used as diagnostic absorptions peaks to identify *Trichodesmium* (McKinna, Furnas, & Ridd, 2011; McKinna, 2015). The $R_{rs}(\lambda)$ model show that $R_{rs}(\lambda)$ α $b_b(\lambda)/a(\lambda)$ and since $b_b(\lambda)$ usually follow a definite nonlinear spectral variation, $a(\lambda)$ will singularly determine the spectral shape of $R_{rs}(\lambda)$ as compared to $b_b(\lambda)$. The $R_{rs}(\lambda)$ of the bloom will have peaks and troughs. The troughs were attributed to the absorptions. The objectives of this study

were to identify the peaks and troughs in the $R_{rs}(\lambda)$ at the *Trichodesmium* spp. blooms from the coastal waters off Goa.

The earlier studies had studied the spectra of optical properties and used the characteristic features of the spectra to develop algorithms to detect *Trichodesmium* blooms from ocean color satellite data (Subramaniam, Carpenter, & Falkowski, 1999; Subramaniam, Brown, Hood, Carpenter, & Capone, 2001; Westberry, Siegel, & Subramaniam, 2005). *Trichodesmium* spp in the coastal waters off Goa were detected from OCM-1(Desa et al., 2005a; Suresh et al., 2005). Measurements of $R_{rs}(\lambda)$ at the bloom occurring in various waters found distinct and pronounced peaks and troughs in the $R_{rs}(\lambda)$ at specific spectral locations (McKinna, Furnas, & Ridd, 2011; McKinna, 2015). One of the commonly followed methods to identify peaks was using a derivative method, which was effectively used to identify absorption peaks of phytoplankton pigments (Bidigare et al., 1990). Since the spectral absorption due to phytoplankton $a_{ph}(\lambda)$ could be approximated as a convolution of many Gaussian spectra of varying widths and height, this method of Gaussian deconvolution had been used to identify absorption peaks due to pigments in the $a_{ph}(\lambda)$ (Hoepffner & Sathyendranath, 1991). Similar to Gaussian, Lorentzian deconvolution was also applied to $a_{ph}(\lambda)$ (Bricaud & Morel, 1986). A combination of Gaussian and Lorentzian spectral curves, known as Gaussian- Lorentzian or Voigt was found to be better to describe the $a_{ph}(\lambda)$ and hence the deconvolution method using Gaussian- Lorentzian curve function has been used to identify the absorption peaks of the pigments in $a_{ph}(\lambda)$ (Aguirre-Gómez, Weeks, & Boxall, 2001).

4.2.5 Detections of peaks in $R_{rs}(\lambda)$

The peaks detected using the deconvolution method with Gaussian-Lorentzian functions for the Rrs(λ) measured during the blooms on 24/4/2014 and 18/5/2015 off Goa are given in Figure 4.9 and 4.10.

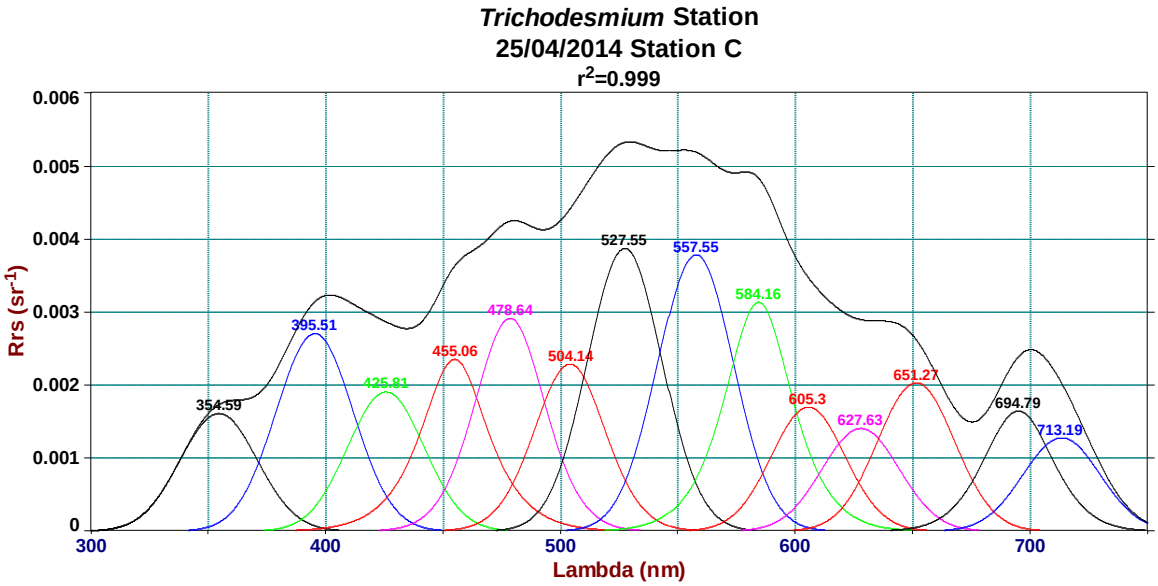

Figure 4.9 Peaks in the $R_{rs}(\lambda)$ at the *Trichodesmium* bloom (24/4/2014 Station C), at 355,396,426,455,479,504,528, 558, 584, 605, 628, 651, 695 and 713 nm

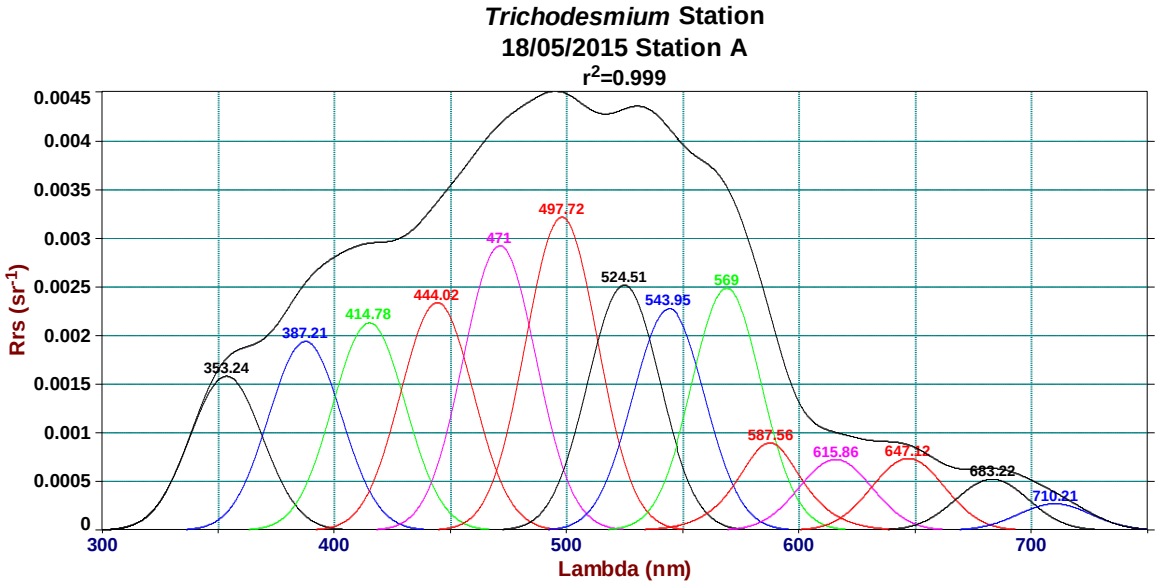

Figure 4.10 Peaks in the $R_{rs}(\lambda)$ at the *Trichodesmium* bloom (18/5/2015 Station A) blooms, at 353, 387, 415, 444, 471, 498, 525, 544, 588, 616, 647, 683 and 710 nm.

The multiple peaks observed in $R_{rs}(\lambda)$ from earlier studies were usually observed around 460, 527, 561, 593, and 647 nm (McKinna et al., 2011; McKinna, 2015). From these analyses of multiple $R_{rs}(\lambda)$ measured during the *Trichodesmium* spp blooms during April and May in the coastal waters of Goa, peaks in $R_{rs}(\lambda)$ were observed around 356, 398, 425, 464, 480, 497, 524, 563, 639, 685 and 696 nm. Peaks in $R_{rs}(\lambda)$ below 400 nm were also observed, which have not been found to be published or reported earlier from $R_{rs}(\lambda)$. These

peaks and troughs in the lower wavelengths below 400 nm are important as they bear a characteristic signature of $R_{rs}(\lambda)$ during *Trichodesmium* spp blooms and could be used to identify *Trichodesmium* spp blooms. Though the spectral shapes were not similar, the spectral components in the blue, green, and red regions were similar (Figure 4.9 and 4.10).

4.2.6 Detections of pigments from $R_{rs}(\lambda)$

The troughs in the $R_{rs}(\lambda)$ revealed much more information than the peaks. The spectral troughs are created by the absorptions by pigments. These spectral signatures of $a_{ph}(\lambda)$ can be used to identify pigments available in the phytoplankton, and further combinations of available pigments can be used to classify phytoplankton, depending on their function such as nitrogen fixers (*Trichodesmium* spp), silicifiers, pico-autotrophs, calcifiers or DMS producers under phytoplankton functional type (PFT) (Nair et al., 2008; IOCCG, 2014; Uitz et al., 2015) and also under different classes depending on the size of phytoplankton, PSC (phytoplankton size class) (Vidussi et al., 2001; Alvain et al., 2005). The specific spectral regions of these pigments have been identified, and the details of few *in-vivo* analyzed pigments were chlorophyll a (440,675), chlorophyll b (450,630 nm), carotenoids(475 – 540 nm), Phycocyanin (580 – 600 nm) and Phycoerythrin (540 – 565 nm) (Bidigare et al., 1990). Carotenoids can be photoprotective or photosynthetic. The *Trichodesmium* spp will have specific pigments, which are a general characteristic signature of such cyanobacteria, which include, PUB (phycourobilin), PEB (phycoerythrobilin), and PC (phycocyanin) (Subramaniam et al., 1999).

Since $R_{rs}(\lambda)$ α $b_{bt}(\lambda)/a_t(\lambda)$, inverting the spectra of $R_{rs}(\lambda)$ should convert the troughs to peaks. Since these troughs were due to the absorptions of pigments, these peaks in the inverted $R_{rs}(\lambda)$ should correspond to absorptions of pigments. Based on this conjecture, peaks were detected in the inverted $R_{rs}(\lambda)$. The inverted normalized $R_{rs}(\lambda) = 1 - [R_{rs}(\lambda)/(\text{Max } R_{rs}(\lambda))]*0.98$. The scaling factor 0.98 was used to avoid data with zero values. A similar procedure of deconvolution method with Gaussian- Lorentzian functions were adopted to identify peaks in this normalized inverse $R_{rs}(\lambda)$, where $R_{rs}(\lambda)$ were only from the *Trichodesmium* blooms. The peaks identified in these inverted normalized $R_{rs}(\lambda)$ corresponding to the measured $R_{rs}(\lambda)$ of Figures 4.9 and 4.10 are given in Figures 4.11 and 4.12. The peaks did correspond to the phytoplankton pigments found during *Trichodesmium* spp blooms reported earlier (McKinna et al., 2011; McKinna, 2015). From

the analysis of various spectra, peaks were observed at 350, 377, 408, 410, 438, 465, 492, 504, 514, 545, 552, 574, 584, 604, 633, 685, 691 and 719 nm.

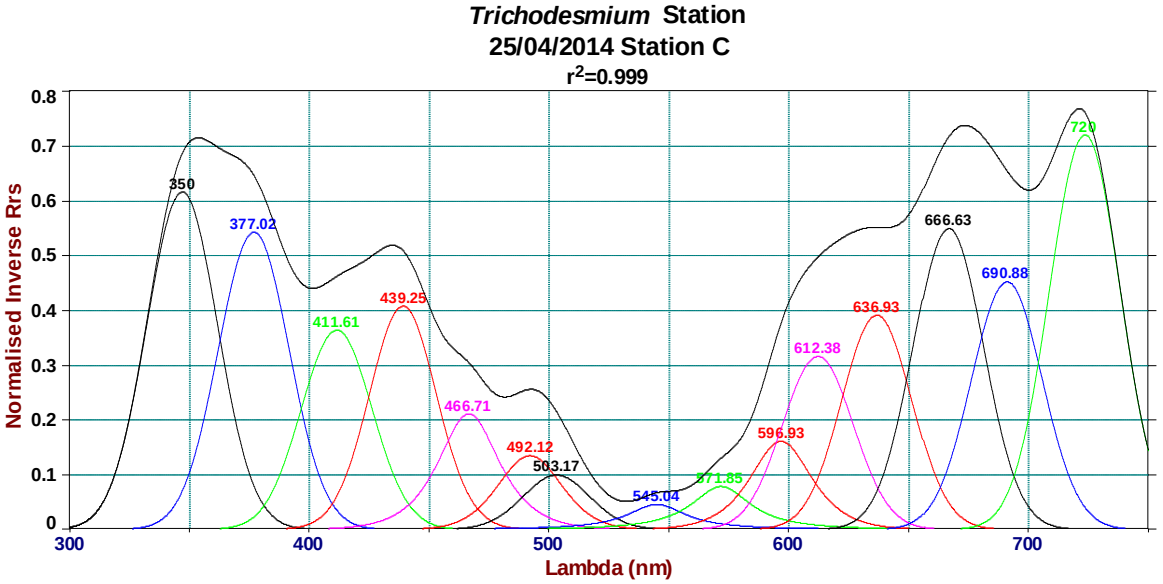

Figure 4.11 Peaks in the normalised inverse $R_{rs}(\lambda)$ at the *Trichodesmium* bloom (25/4/2014 Station C) at 350,377,412,439,467, 492, 504, 545, 572, 597, 612, 637, 667, 691 and 720 nm.

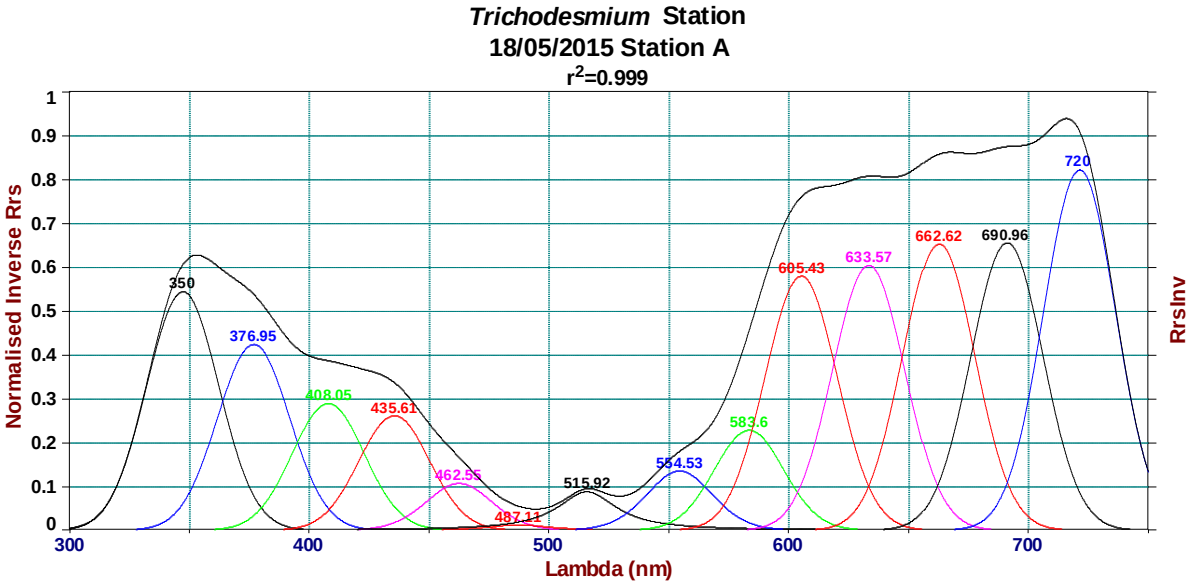

Figure 4.12 Peaks in the normalised inverse $R_{rs}(\lambda)$ at the *Trichodesmium* bloom (18/5/2015 Station A) at 350, 377, 408, 436, 463, 487, 516, 555, 584, 605, 634, 663, 691 and 720 nm.

The peaks detected from these analyses of the troughs in $R_{rs}(\lambda)$ are given in Table 4.8. These peaks did correspond to the peaks identified due to pigments, which were usually

observed during *Trichodesmium* blooms. Apart from these pigments, which were often observed in absorption during *Trichodesmium* blooms, the peaks were also detected at other pigments like MAA and chlorophyll c. Similar results were observed for the *Trichodesmium* observed on 8/5/2018.

Table 4.8 Peaks identified from inverted and normalized $R_{rs}(\lambda)$

Wavelength (nm)	**Pigment**
350 -377	MAA
408 - 440	Chlorophyll a
465	Chlorophyll b/ c
492	PPC (photoprotective Carotenoids)
504 - 514	Carotenoids
545 - 552	PEB
574	PEC
584	Chlorophyll c
604	PC
633 – 690	Chlorophyll a

4.2.6.1 CDOM during *Trichodesmium* bloom

Among the components of absorption, $a(\lambda)$, only $a_{ph}(\lambda)$ exhibit absorption selectively at specific regions or bands of spectra due to pigments, such as chlorophyll, which may absorb in the blue at 440 and red at 676 nm. The $a_g(\lambda)$ and $a_d(\lambda)$ decay exponentially with increasing wavelength. However, there are departures in these types of spectral variations for CDOM, $a_g(\lambda)$ for $\lambda < 400$ nm, around the region of 350 nm. High absorption peaks were observed in $a_g(\lambda)$ around 350 nm due to mycosporine-like amino acids (MAAs), which are photoprotective agents, to protect species from high UV solar radiation (Dias, Suresh, Sahay, & Chauhan, 2017; Dias, Kurian, & Suresh, 2019) (Figure 4.13).

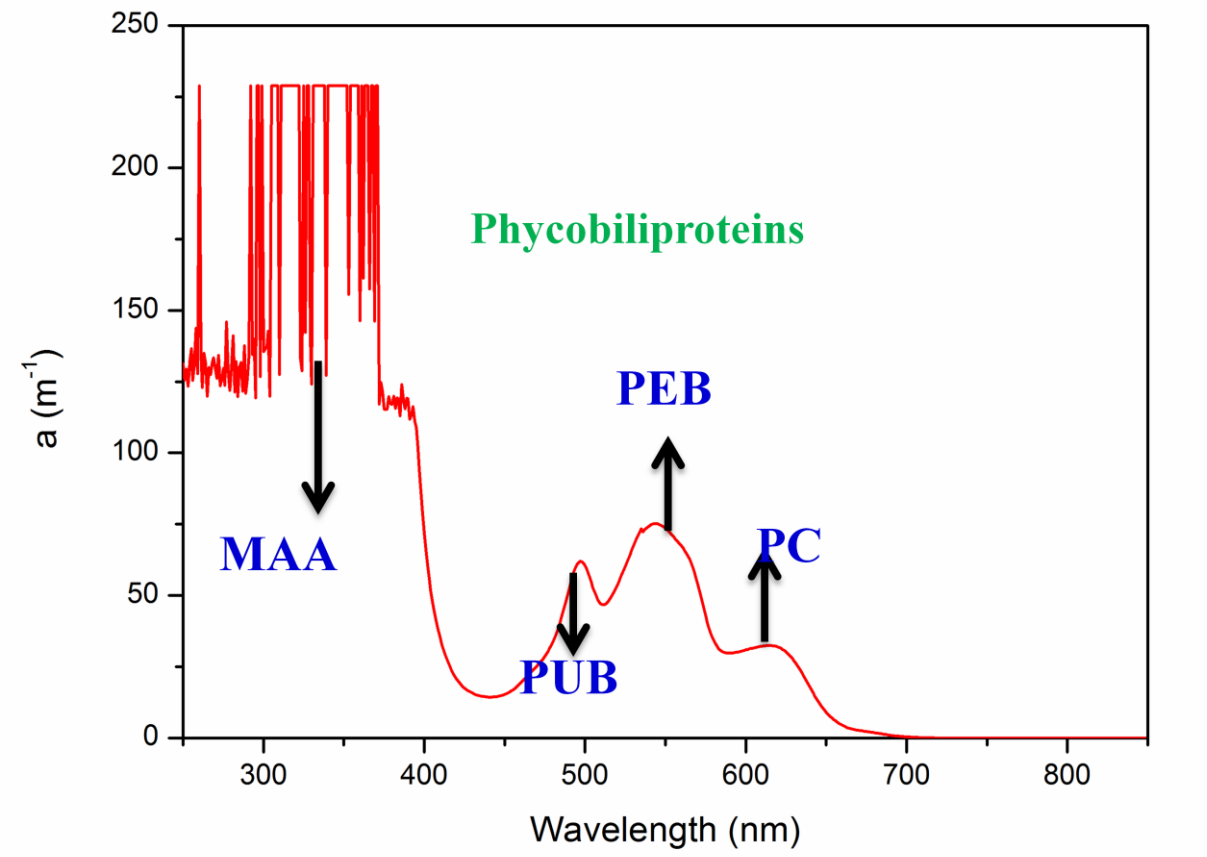

Figure 4.13 Absorption spectra of CDOM of *Trichodesmium* bloom, showing absorptions due to MAA in the UV and other pigments, PUB, PEB and PC

4.2.6.2 Bottom reflectance

Bottom reflectance was measured with the radiometer at various locations in the estuaries for bottom types sandy clay, rocky, mangrove, rocky, and seagrass, at coastal waters near the mouth of Mandovi for sandy, at Ilha Grande island of Goa for the coral bottom (Figure 4.14).

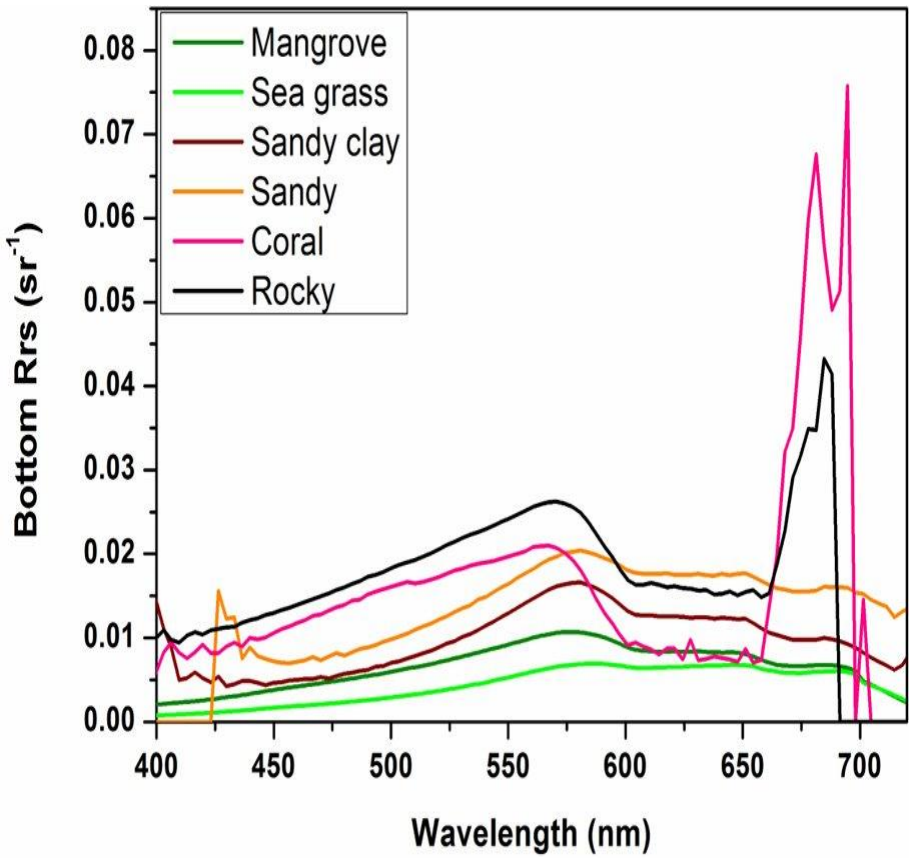

Figure 4.14 Measured bottom reflectance of various bottom types

4.3 Discussion

There were very contrasting features in the physical, optical, and biological parameters observed in these estuarine and coastal waters of Goa with locations and seasons. The parameters listed for these waters here show the gross variations for the two water types, which were two estuaries, Mandovi and Zuari and the coastal waters, and also their seasonal behavior. There were distinct variations of all parameters observed in the coastal and estuarine waters. The seasonal variations of all parameters also differed in these waters. The variations of parameters were examined and reasoned to understand the variability of water quality parameters in general, such as light availability in water, productivity, CDOM, and particulate matter. Detailed studies on light penetration and transparencies of these waters are given in Chapter 7. Results of detailed studies on the variations of CDOM in these waters are given by Dias (2015, 2017, 2019).

4.3.1 Light penetration

Solar radiations over the estuaries were less than over the coastal waters. This was probably due to the aerosol in the atmosphere, and this atmospheric turbidity could be due to various factors such as fine particles from mines, due to heavy vehicles that generate particles from emission and their traffic in the mining areas and also from other anthropogenic origins. Seasonal variations of aerosol were observed over Goa, and hence it would affect the solar radiation (Suresh & Desa, 2005).

The light availability in water was defined here by two parameters, Z_{90} and Z_{sd}, which often show similar variations; hence, either of them could be used as an indicator of light availability in water. Light availability in water depends on the absorptions and scattering properties of water (See Chapter 7 for detailed explanation). Monsoon plays a vital role in the estuaries, and the optical parameters exhibit extreme values during monsoon compared to other seasons. In Mandovi and Zuari, Z_{90} and Z_{sd} were the lowest during monsoon, and the total absorption and scattering were much greater. Contributions to total absorption come from detritus, CDOM, and phytoplankton, apart from water. During monsoon in the Mandovi, the absorption due to detritus during was about 70% compared to 25% of CDOM. The backscattering was also the highest during monsoon. The enhanced scattering and absorption resulted in high K_d and c, which was the reason for the reduced transparency and penetration of underwater light. During monsoon, particulate matters play an important role, and the particulate load was the highest, as observed from the TSM seen here and also reported by others (Fernandes, Rao, Kessarkar, & Suresh, 2018; Suja et al., 2016; Varma, Rao, & Cherian, 1975). In the Mandovi, the lowest transparencies were during winter, and the values of associated optical parameters supported the same.

In Zuari, the lowest transparencies were observed during monsoon, but unlike Mandovi, the highest values of transparencies were during post-monsoon and not during winter. The absorption, beam attenuation c, backscattering b_b, diffuse attenuation, K_d were relatively much lower during post-monsoon and winter than summer and monsoon. These resulted in the high values of Z_{sd} and Z_{90} being observed during post-monsoon. The amount of light available at Z_{90} and Z_{sd} was higher than in Mandovi, at 24% and 18%, respectively.

The transparencies Z_{sd} and penetration of light, Z_{90} in the coastal waters were higher than estuaries, as there were fewer particles to scatter, and the absorption was also lower. The

CDOM sources in the coastal waters were mostly from autochthonous sources, and hence the $a_g(412)$ was relatively lower (Dias et al., 2015) and the absorption by detritus and phytoplankton were also low.

In the estuaries since Z_{sd} and Z_{90} were at very shallow depths, the PAR% at these depths were relatively higher (23%). There was always plenty of light available in the bottom layer, and even during monsoon when the solar light at the surface was low, there was no dearth of light as the 1% light level was available just above bottom (~80% of total depth).

The wavelength of the maximum light penetration and availability in water depends on the absorption and backscattering properties. In the estuaries, the wavelength of underwater light moved towards higher wavelengths, 570 nm during non-monsoon and 580 nm during monsoon, since the waters have abundant CDOM and detritus which absorb lights in the blue. While in the coastal waters since the absorptions due to CDOM and detritus were less, the maximum penetration of light moved to lower wavelengths closer to 540 nm.

In the coastal waters, since the absorptions and scattering were lower than estuaries, the transparencies and light penetration were higher. There were two contrasting and dissimilar features observed of the coastal waters as compared to the estuaries, one of them related to the highest chlorophyll observed during summer and the high penetration of light.

The sequel and aftereffects of this *Trichodesmium* spp bloom were the scavenging effects or washout of the water column, with transparencies and penetration of light often increasing and the optical parameters of K_d and c were low in the water column.

A second periodic bloom was of *Noctiluca*, often observed during the February-March period (Devassy & Nair, 1987; D'Silva et al., 2012; Do Rosário Gomes et al., 2014; Mishra & Gould, 2016). These blooms could also affect the water column, increase the K_d and c, and reduce the transparency Z_{sd} and Z_{90}.

4.3.2 Chlorophyll

Chlorophyll measured from water samples and in-situ from chlorophyll sensor exhibit the same pattern as having been reported by others, with high during summer and low during monsoon (Kumari, Bhattathiri, & John, 2002). Even the zooplanktons were reported to show similar seasonal patterns (Padmavati, 1996; Selvakumar, Nair, & Madhupratap, 1980). This pattern of chlorophyll agreed well with the other proxies, such as phytoplankton absorption a_{ph} at the Soret band of 440nm and red band of 676 nm, absorption from AC-9 at 676 nm a(676) and FLH from R_{rs} and L_w. The a(676) of AC-9 is a good proxy for the chlorophyll as it was found to correlate well with chlorophyll for the waters of the Arabian Sea (Suresh et al., 1998). The low bulk refractive index n_p values during summer also indicate higher biological matter in the water.

In Zuari, the lowest values of chlorophyll were observed during winter and highest during summer, and these were also confirmed from the values of chlorophyll from the in-situ chlorophyll sensor, a(676) and $a_{ph}(440)$, $a_{ph}(676)$, FLH from R_{rs} and L_w. During monsoon and post-monsoon, chlorophyll did not show large variations. In Zuari during monsoon, chlorophyll was higher than Mandovi and comparable to other seasons, while in Mandovi, it was the lowest during monsoon, and these agreed with others (Bhargava & Dwivedi, 1976; Pradeep Ram, Nair, & Chandramohan, 2007). In both the estuaries, the chlorophyll values during winter were similar. Three sources of nutrients in these estuaries were sediments, mangroves, mining rejects, spillages, and fertilizers. (Sardessai & Sundar, 2007). The mangrove coverage of Zuari was higher (9 ha) than Mandovi (7 ha) (Untawale, 1982, Dhargalkar, 2014). The surface and catchment areas of Zuari are larger than Mandovi (Vijith, 2014). In Zuari, inorganic nutrients were highest during monsoon, and even during the recovery period of post-monsoon, the nutrient levels were high. During summer, the nutrients were the lowest (Subha Anand et al., 2014).

Chlorophyll was relatively lower in the coastal waters compared to the estuaries. Though there was enough light available till the bottom during all seasons of measurements, the nutrients were probably relatively lower. Most nutrients show a positive gradient moving from the mouth upstream, with low observed near the mouth of the estuaries and high moving upstream (Pednekar et al., 2018; Subha Anand et al., 2014). During the *Trichodesmium* blooms in summer, chlorophyll values were high, exceeding 100mg/m^3 at times (Desa et al., 2005a).

4.3.2.1 Chlorophyll during monsoon in the estuaries

Phytoplankton requires light and nutrients as primary factors for its growth and suitable environmental conditions for its sustenance. Though these factors were favorable during monsoon in the estuaries, the chlorophyll levels were low during monsoon.

One of the plausible reasons has often been attributed to turbidity and limitations of light in water. In the Mandovi, during summer and winter, more than 1% of lights were available at the bottom, and during monsoon 1% light was available till 80% of maximum depth. However, it has been shown in laboratory studies that the minimum light level required by phytoplankton was about 2 µmol/m^2/s (Overmann & Garcia-Pichel, 2013) and which was equivalent to about 0.5W/m^2 (Suresh et al., 1996). Some studies have shown even lower light levels, such as for O_2-evolving marine photolithotrophs to grow the minimum photon flux density of photosynthetically active radiation required was about 0.01 µmol/m^2/s, while marine non-O_2-evolvers it was even lower at about 0.004 µmol/m^2/s (Raven, Kübler, & Beardall, 2000). Phytoplanktons were also observed at very low light in the coastal and estuaries of Goa during all seasons, and of the 93 phytoplankton genera observed the most abundant were *Skeletonema spp., Leptocylindrus spp., Thalassiosira spp., Cerataulina sp*. and *Fragilariopsis sp.*(Ramakrishnan, Thayapurath, Gauns, & Dias, 2018).

However, not all days, you find clouds in the sky during monsoon, and on a clear sky day during monsoon season, the solar irradiance was much higher (Figure 4.15). Hence, it would not be a valid statement that during monsoons, there was always a limitation of solar irradiance over these waters. During such a period, solar irradiance was high as on sunny days, there were no clouds, and the aerosol content in the atmosphere could be low as they would have been washed-out during rain.

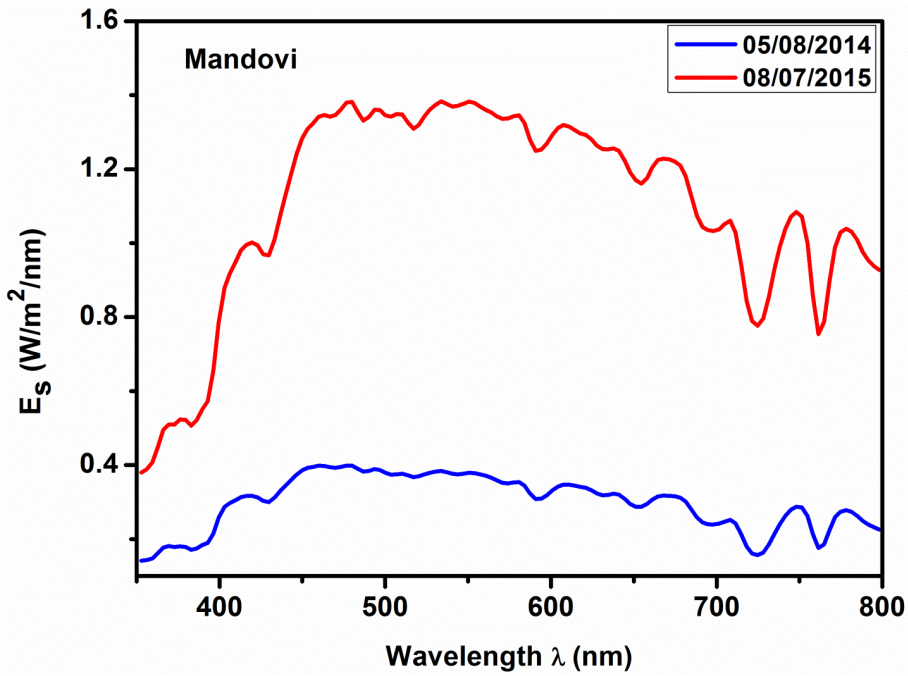

Figure 4.15 Solar irradiance over Mandovi during monsoons

The nutrients were reported to be plenty during monsoon in these estuaries (Kumari et al., 2002; Pednekar et al., 2018; Subha Anand et al., 2014).

Apart from high turbidity, there was high turbulence in the waters during monsoon. Studies have shown that there was a threshold limit of the flow rate of water for the growth of phytoplankton, and when the flow rate increased beyond this threshold, there was a reduction in chlorophyll concentration and phytoplankton biomass (Mitrovic et al., 2003). Controlling flow rates and with higher discharge rates above a limit in the turbid river, they have been able to mitigate algal blooms (Mitrovic, Lorrainehardwick, & Forughdorani, 2011) and such a practice has been adopted by many to control harmful algal blooms. Apart from the vital parameters required for the phytoplankton, the water flow rate, and resident time of waters in these estuaries could also play an important role in modulating the variations of chlorophyll. Chlorophyll and metabolic rates were found to be related to discharge rates in the Godavari estuary, with very low chlorophyll being observed during peak discharge rates (Sarma et al., 2009). The water flow in these estuaries during non-monsoon periods is controlled by tides, and the currents were about 0.8/1.0 m/sec during spring tide and 0.4/0.6 m/sec during neap tide (Manoj, 2008) and the flow rate would be higher during monsoon. These flow rates beyond the critical flow rates would inhibit the growth and sustenance of phytoplankton (Zhang et al.,2015). The vegetation such as grass

and mangroves on the tidal flats could also restrict the flow of water, and since the mangrove covers in the Zuari were higher than Mandovi, this could be one of the plausible reasons that the chlorophyll was higher in Zuari during monsoon and other seasons. During monsoon, the zooplankton was the lowest in these estuaries (Padmavati, 1996). Light availability in the water column would depend on varying absorption and scattering depending on the phytoplankton, particulate matter, and CDOM. The distributions of nutrients in the water column would depend on the availability and turbulence factors that control the mixing**.** Hence the plausible reasons for low chlorophyll during monsoon seems to be the river run-off and discharge rates that control the water residence times and light availability (Fernandes, Kessarkar, Suja, Ray, & Bhat, 2018; Patil & Anil, 2015; Vijith, Sundar, & Shetye, 2009).

4.3.3 CDOM and detritus

The CDOM was found to be highest during summer in the Mandovi, as indicated by the absorption of CDOM $a_g(412)$ and $K_d(350)$. Absorption at 412, a(412), cannot be a proxy for CDOM alone but for CDM, i.e. CDOM + detritus, as the contributions of detritus were much higher at 412 nm than CDOM. The contribution due to phytoplankton $a_{ph}(412)$ was relatively low. That was the reason a(412) is reported to be highest during monsoon (Dias et al., 2015).

One of the notable observations regarding CDOM and detritus in these estuaries was that during summer and monsoon, the contributions of CDOM and detritus were the same, though the actual values differed. The contribution of CDOM was 37% and detritus 52% during summer, and CDOM was 24% and detritus 68% during monsoon.

The mangroves were one of the major contributors to particulate organic matters in these estuaries. The mangrove litters were high during monsoon, and they degrade faster than phytoplankton debris and get converted to detritus by bacterial degradation (Sardessai, 1993). The tidal flats have vegetations that contribute to humic acids, and thus river runoff also increases humification. From these optical data, it can be hypothesized that though freshwater discharges were high during monsoon, they do not contribute to the absorption by CDOM as compared to the detritus, which were also the observations regarding humic acids of these estuaries (Sardessai, 1993). During monsoon, the run-off and resuspension of suspended sediments were high due to high winds, and these suspended sediments also

contribute to the particulate matter and detritus (Jagtap, 1987). Since the coverage of mangroves of Mandovi was relatively less (7 sqKm) than Zuari (9 sqKm) (Untawale, 1982), the same was also reflected in the values of $a_d(412)$, as the contributions by detritus during monsoon in Mandovi were less than Zuari. CDOM was relatively higher in Zuari during most parts of the year. Urbanization and industrializations close to the banks have increased, and they too could contribute to CDOM and detritus. Apart from the natural sources, the contributions to CDOM from various anthropogenic sources could be large. It was assessed nearly 4 decades ago that Mandovi receives about 5.21×10^6 m^3 of sewage and effluents per year (Qasim and Sengupta 1981). Other sources during monsoon could be from khazans and agriculture fields.

In the coastal waters, CDOM and detritus were the lowest compared to both estuaries. High CDM values during summer in the coastal waters could be attributed to the algal blooms.

4.3.4 Spatial and temporal variations

The upstream regions were always under the influence of mining during non-monsoon, and the same was manifested in the high values of n_p observed upstream. In the Zuari Estuary, there was a region from 5 to 20 km, which had very contrasting characteristics with very low n_p, high values of $b_b(700)$, and ξ and the region was very productive indicated by high chlorophyll. Chlorophyll values were higher in Zuari and high biomass of zooplankton observed in the Zuari Estuary (Gauns et al., 2015). The depth variations of $b_b(700)$ and n_p suggest chlorophyll maxima in the bottom waters.

Relatively lower values ξ were observed during monsoon, indicating the dominance of large particles while smaller particles, high ξ dominates the estuary during the non-monsoon season. The smaller particles were abundant in the estuaries.

The density of water followed a similar pattern, as reported earlier (Vijith, 2014). In general, density decreased from the mouth to the upstream of both the estuaries. Density and $b_b(700)$ were observed to co-vary inversely in both the estuaries and positively correlate during monsoon suggest that the fresh water upstream had relatively less particulate and phytoplankton and the particulate matter were being transported and deposited at the mouth of the estuaries.

These observations of $b_b(700)$, n_p, and ξ were also in agreement with earlier studies (Fernandes, Kessarkar, Suja et al., 2018; Suja et al., 2016). In the estuaries, b_b could be a good proxy for chlorophyll.

4.4 Conclusion

A summary of the conclusions of this Chapter are listed below:

There were distinct spatial and temporal variations of optical, biological, physical, and ancillary parameters of both coastal and estuarine waters.

The solar radiation was maximum during summer and lowest during monsoon. However, during clear sunny days of monsoon, the solar lights were also much higher. The solar light decreased moving from coastal waters to upstream of the estuary, which indicated the increase of atmospheric turbidity or aerosols in the interiors of Goa.

There was sufficient light available in these waters till the bottom during all seasons, and average %PAR at Secchi depth, Zsd was about 22%.

The bulk refractive index was higher in the estuaries, indicating more mineral particles. The particle sizes were relatively smaller in the estuaries.

Monsoons play an important role in modulating the physical, biological, and optical parameters of these estuaries. Monsoons were observed to promote CDOM, detritus, and sediment and restrict the light availability in water. During monsoon, low chlorophyll, despite the availability of nutrients and sufficient light, was attributed to high discharge and flow rates. The low transparencies during monsoon were due to high optical properties. The penetration depth, Z_{90}, and Z_{sd} values were the highest during the winter and lowest during the monsoon. Contributions of CDOM and detritus were significant in the estuaries, with the highest during monsoon.

Since Z_{90} and Z_{sd} were comparable, and Z_{sd} which could be measured with ease and could be used to provide a rough estimate of Z_{90} and Z_{eu}.

The chlorophyll and CDOM were higher in the Zuari and the highest detritus were observed in the Mandovi.

CHAPTER 5. PHYSICAL AND OPTICAL PARAMETERS

5.1 Introduction

An estuary is a dynamic system with various physical processes that influence its spatial and temporal variations of parameters. These processes could be hydrodynamic that influence the movement of water mass in the estuaries such as tides, vertical mixing of top fresh and bottom dense saline water due to gravitational forces, river run-off from rains, wind forces that create the turbulence and mixing. These processes affect the biology, chemistry and influence the water quality parameters such as transparency or light availability, pH, temperature, salinity, density, nutrients, dissolved oxygen, suspended sediment, chlorophyll, and productivity (Glamore, Rayner and Rehman, 2016).

Most of the studies in the Mandovi and Zuari estuaries have focused on the salinity as the sole parameter that controls various processes, which include physical (Manoj, Unnikrishnan and Sundar, 2009; Sundar et al., 2015; Vijith, Sundar, & Shetye, 2009), biological (Gonsalves et al., 2009; Patil & Anil, 2015; Pednekar et al., 2018; Pednekar, et al., 2014; Rajaneesh & Mitbavkar, 2013), chemical (DeSousa & SenGupta, 1986), and geological (Kessarkar et al., 2010) processes. Some studies concluded minimal role of temperature in the variations of nutrients and dissolved oxygen in the Zuari (Subha Anand et al., 2014).

There has not been any study relating to the physical processes and parameters and their effects on the optical parameters of Mandovi and Zuari estuaries.

Though much of the studies in these estuaries have focused on salinity, the temperature is also an important parameter. Since phytoplankton are ectotherms, they require optimum temperature for their sustenance. For the growth of phytoplankton, apart from light and nutrients, the temperature influences the metabolic rates (Eppley, 1972; Raven and Geider, 1988; Grimaud et al., 2015). Temperature seems to be associated with some physical processes that help in the growth of phytoplankton, such as coastal upwelling, mixed layer depths, thermal inversions, stratification and mixing of water masses. These physical processes which are related to temperature also govern and control the availability of nutrients in the upper water column. One of the national programs that provide the fisherman the information about the probable grounds for fish abundance, Potential Fishing

Zone advisory (PFZ), is based on sea surface temperature (https://incois.gov.in/MarineFisheries/PfzAdvisory). Phytoplankton structure and taxonomic composition are affected by changes in the temperature. Phytoplankton species are comfortable in a specific range of temperatures, such as cyanobacteria prefer warm waters and can tolerate heat, while diatoms would prefer relatively lower temperature (Johnson, 2015; Paerl & Huisman, 2008).

Global warming is a certainty and undisputed truth. It is estimated from various studies to have caused approximately 1.0°C of global warming above pre-industrial levels and the trend shows to likely reach 1.5°C between 2030 and 2052. The scientific groups and others concerned have postulated and hypothesized the probable outcomes from the temperature increase to 1.5°C and 2 °C (IPCC, 2018). As compared to photosynthesis rates or primary production, the grazing by heterotrophic organisms is more sensitive to temperatures and hence affect the phytoplankton stock. Since higher temperatures are favorable for the growth of cyanobacteria (often above 25°C) than other species of diatoms and green algae, this will lead to frequent HAB (Harmful Algal Blooms) (Paerl & Huisman, 2008). Warming of waters will affect vertical thermal stratification and mixing and consequently the availability of resources for the phytoplankton growth, light, and nutrients (Winder & Sommer, 2012). The rise in temperature will affect the coastal and estuarine waters. Increasing temperature will also affect the sea-level rise and thereafter the salinity of the estuaries and have implications on the phytoplankton taxa, dissolved oxygen, and biochemistry.

The objective to carry out these studies relating to the physical phenomena of stratification and the optical properties were based on the presumption that the variability of phytoplankton, productivity, chlorophyll, suspended sediments, and water quality were related not only to the physical parameters but also the optical parameters. This was the first attempt at examining the physical parameters of the coastal and estuarine waters of Goa along with the optical properties. Here, the variations of optical parameters were examined under different physical conditions of waters such as iso or mixed layers of temperature and density, thermal inversion, bottom heating, and tides.

5.2 New method to determine iso layer

There are usually two constraints when a study of the estuaries is undertaken about variations of the physical parameters and they are data and the methods.

Since the depths are shallow compared to coastal waters or open sea, not exceeding 7m on an average, the variations of depth profiles of parameters were limited to a small range. Hence, an instrument with high accuracy, better precisions was required for the measurements to show the small variations. The sensors in the instrument such as CTD must discern and resolve small variations.

The second concern is regarding the method adopted to identify iso layers such as MLD and ILD.

There are methods available to quantify the depth or extent of the mixed layer of the open ocean. These available methods can be classified as "threshold" and "mathematical model" (de Boyer et al., 2004; Kara, Rochford, & Hurlburt, 2000). The simple threshold method is the most commonly used method to determine 'iso' depths of temperature (ILD), salinity or density (MLD). Most of the earlier MLDs were determined using temperature (Kara et al., 2000; Rao, Molinari, & Festa, 1989). Since the isothermal layer and isopycnal layer could differ, so the MLD layer was determined using density (de Boyer et al., 2007).

The methods to derive MLD using mathematical models include, the gradient of temperature or density with depth and this method was similar to threshold method, finding the maximum gradient, which was assumed to be located at the base of the mixed layer (Lukas & Lindstrom, 1991), combinations of straight line and polynomial fits (Lavender, Davis, & Owens, 2002), ‘‘split and merge’’ of multiple line segments (Thomson, Richard, 2003) and “curvature” or shape of the temperature profile (Holte & Talley, 2009; Lorbacher et al., 2006). There is a refined gradient method that uses the angle between two vectors derived from the profile data, one of them from the surface and the other from the end of the first vector (Chu & Fan, 2011). Most of these methods have been used for the data available for the regions of studies and at times, they have failed when applied to other regions. The method of Lavender (Lavender et al., 2002) was found to work well in North Atlantic but had partial success for the Southern Ocean (Holte & Talley, 2009). The threshold and gradient were subjective, often region-specific and also depended on the types of sensors used for the measurements. A sensitivity study with varying thresholds of

either temperature or density yielded MLD of varying values (Dong, et al., 2008; Lorbacher et al., 2006). The threshold method often tends to overestimate MLD (Holte & Talley, 2009) and it is also misrepresented due to salinity barrier layers (Lukas & Lindstrom, 1991). To overcome various problems encountered in defining MLD using temperature, the density was adopted, which also had all shortcomings of threshold and gradient methods. Using density too was also reported to have problems in identifying MLD due to density-compensating layers (Lukas & Lindstrom, 1991).

Most of the methods mentioned above have been applied to the deep waters. Though there were objective and subjective methods available to determine the iso-layer of water, these methods would not have qualified to determine the iso-layers of the coastal and estuarine waters as summarized below.

- The threshold methods were not universal and any change in the threshold and reference could provide erroneous values of MLDs (Holte & Talley, 2009; Lorbacher et al., 2006). Presently there are no recommended threshold values of any study in the shallow waters that could be used to determine the MLD by threshold method.
- The threshold criteria for the identifications of ' íso' depth avoids the layer close to the surface, as these regions have large randomness in the values of temperature, salinity or density due to various factors. The data from the surface layers are often discarded and the data beyond the reference depth about 5 m are considered to avoid the "skin effects" from the surface until the parameter variations are within the threshold value (Kara et al., 2000). For most methods used for defining 'iso' or MLD, there was often a reference depth chosen from the surface. The selections of this threshold and reference reported were arbitrary, subjective and varied from the region, season, and types of data from sensors or instruments (de Boyer Montégut et al., 2004). For the open ocean data, surface reference of 10 m was often adopted (Kara et al., 2000). The observed iso-layers in the surface waters of this study usually did not exceed 5 meters and the maximum depths were less than 20 m. Hence, the method used for open ocean waters would not be suitable for such shallow waters where a very small value or even zero may have to be used as reference depth. The average depths of these estuaries were less than 7 m and 17m in the coastal waters of the study.
- The ranges of threshold values to determine MLD using temperature varied from a low value of 0.1 °C (Sprintall & Roemmich, 1999) to 1°C (Rao et al., 1989). The

temperature variations and the gradient in the coastal and estuarine waters were relatively small (less than 0.1°C) compared to the open ocean. The variations observed in the temperature, salinity, and density for the coastal and estuarine waters varied with season. Hence, the threshold values of any parameter in these waters that have to be used to identify MLD could not be static.

Since the available threshold methods were subjective, they would be unsuitable for the coastal waters for the reasons given above and it was thought prudent to opt for an objective method. One of the objective methods that are based on the angle between two vectors was a novel mathematical algorithm based on the shape of the profile to determine the MLD. This method was suited with an adequate amount of data and may not work in shallow waters or with a coarse resolution of depths (Chen, 2015). The gradient or derivative methods have the disadvantages with data measured with better depth resolution sensors, noise and near the surface. These types of data will provide false MLD and hence data will have to be pre-processed with careful smoothing and filtering.

Considering the need to identify the shallow iso-layers of coastal and estuarine waters, a simple method was developed which could evaluate the iso-layers with better accuracy. For most of the data, no significant barrier or compensating layer was observed due to the differences in depths of isothermal or isohaline. For the study here, the iso-layer of temperature was synonymously designated as Mixed Layer Depth (MLD) or ILD.

Here a simple linear line fitting method was used to find the iso-layer. The two parameters used were 1) Chi-square (χ^2) that determines the goodness of fit and 2) the slope or gradient 'm', which was the slope of the linear fit.

A brief explanation of the method is given here and the exact procedure with steps is given thereafter in the following section. Let P be the parameter (temperature or density) whose 'iso' characteristic was required to be determined within the upper surface layer. The P_0 is the value of the parameter, temperature or density at the surface, Z_0. There is no reference depth and consider Z_0 as the minimum depth of the profile. Thus, Z_0 is often zero, as most profiles begin from the surface. Beginning from the deepest depth the linear fit of all the data pairs from that depth to the surface is determined. (Here x = depths and y = corresponding parameter and the linear fit has the form, y= mx + c). The goodness of fit given by chi-square (χ^2) and the slope m was evaluated for this fit. The next fit uses the

data pairs of the profile, whose depth was lower than previous depth and all data pairs till the surface. Assuming a depth interval of 1 m for the profile data and with the maximum depth Z_{max}, the first data set will include Z_0 to Z_{max} and the successive data profiles will be from Z_0 to Z_{max}-1, then Z_0 to Z_{max}-2 and the same continues till there is a profile close to the surface with only 3 pairs of data i.e from Z_0 +3 to Z_0. The linear fits of type y = mx + c were evaluated for all data profiles. The values of $\chi 2$ and slope m reduce rapidly as the MLD approach closer and these values are lower in this vicinity of MLD as compared to regions deeper than MLD (Figure 5.1). Hence all the depths with χ^2 and m less than threshold limits are selected to determine the MLD. The depth of the iso-layer or MLD is the maximum depth among the selected depths. This method to determine MLD is outlined in the following section.

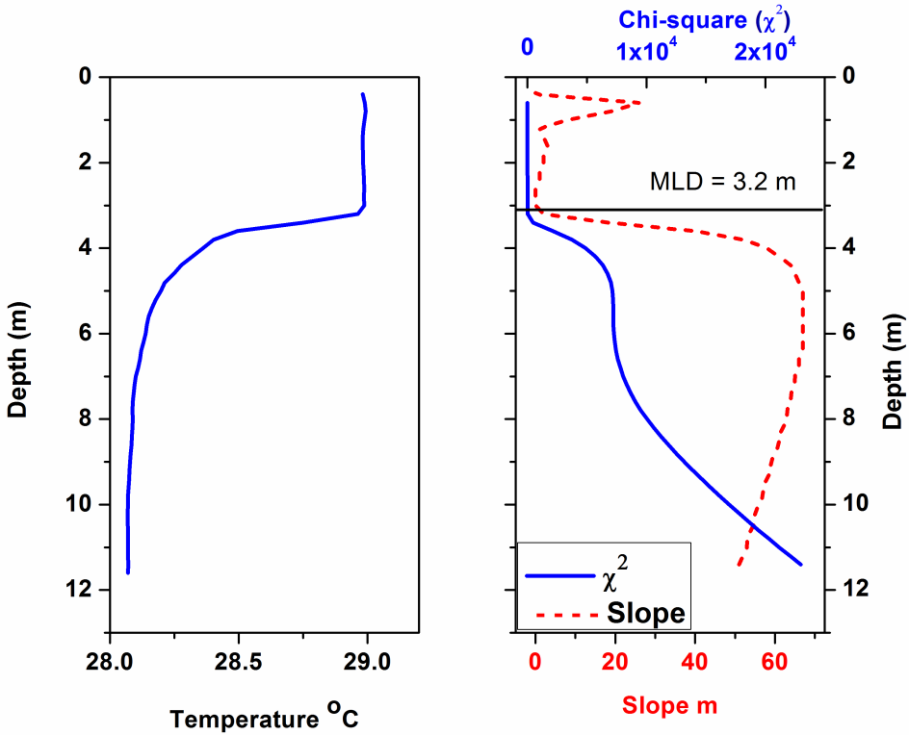

Figure 5.1 Depth profile of temperature at a coastal station off Goa (Left) and the variations of the slopes m and Chi-squares (χ^2) of the linear fits (Right)

The depth profile of parameter is given as [Z_i, P_i] with i = 0 to n-1, where Z is the depth and P are the parameters such as temperature, density with total depth profile data of n points. The Z_0 is depth at the surface or the minimum depth, Zn-1 is the maximum depth, and P0 and Pn-1 are the respective values of parameters at those depths respectively. The procedure is outlined below

Step 1: Smooth P using a boxcar averaging method with 5 data elements.

Step 2: Normalize the values of depth, Z, and parameters, P to a range of 0 to 100 (Normalized $P = 100\dfrac{[P - Min(P)]}{[Max(P) - Min(P)]}$).

Step 3: Find the linear fit of data pairs $[Z_i,P_i]$ with i = 0 to m-1 where m = (n-1) – k, and k is the iteration index (Linear fit, P = mZ +c, where m is the slope and c is the intercept).

Step 4: If the goodness of fit, chi-square, χ^2 and slope m are less than the threshold then accept the depth $Z = Z_m$. The threshold values used are 0.35 and 10.0 for the slope m and χ^2 respectively.

Step 5: Iterate through Step 3 and 4 for k =0 to n-4.

Step 6: Normalized iso depth or MLD = Maximum (Zm).

Step 7: Transform from normalized depth to original depth value to get MLD or iso depth.

The slope and the chi-square evaluated for the temperature profile data are given in Figure 5.1. It can be observed that the values of chi-square and slope tend to approach relatively very small values in the regions of iso-layer.

5.3 Results

5.3.1 MLD and ILD

MLD and ILD were derived with the above-described method for the coastal and estuarine waters. As usual, the chlorophyll maxima were observed below the MLD and ILD. The beam attenuation coefficient c(488) followed the chlorophyll in the coastal waters. In the coastal waters, the iso layers of c(488) and density were at similar depths, while in the estuarine waters the iso layer of c(488) was found to be deeper than isopycnal or MLD (Figure 5.2).

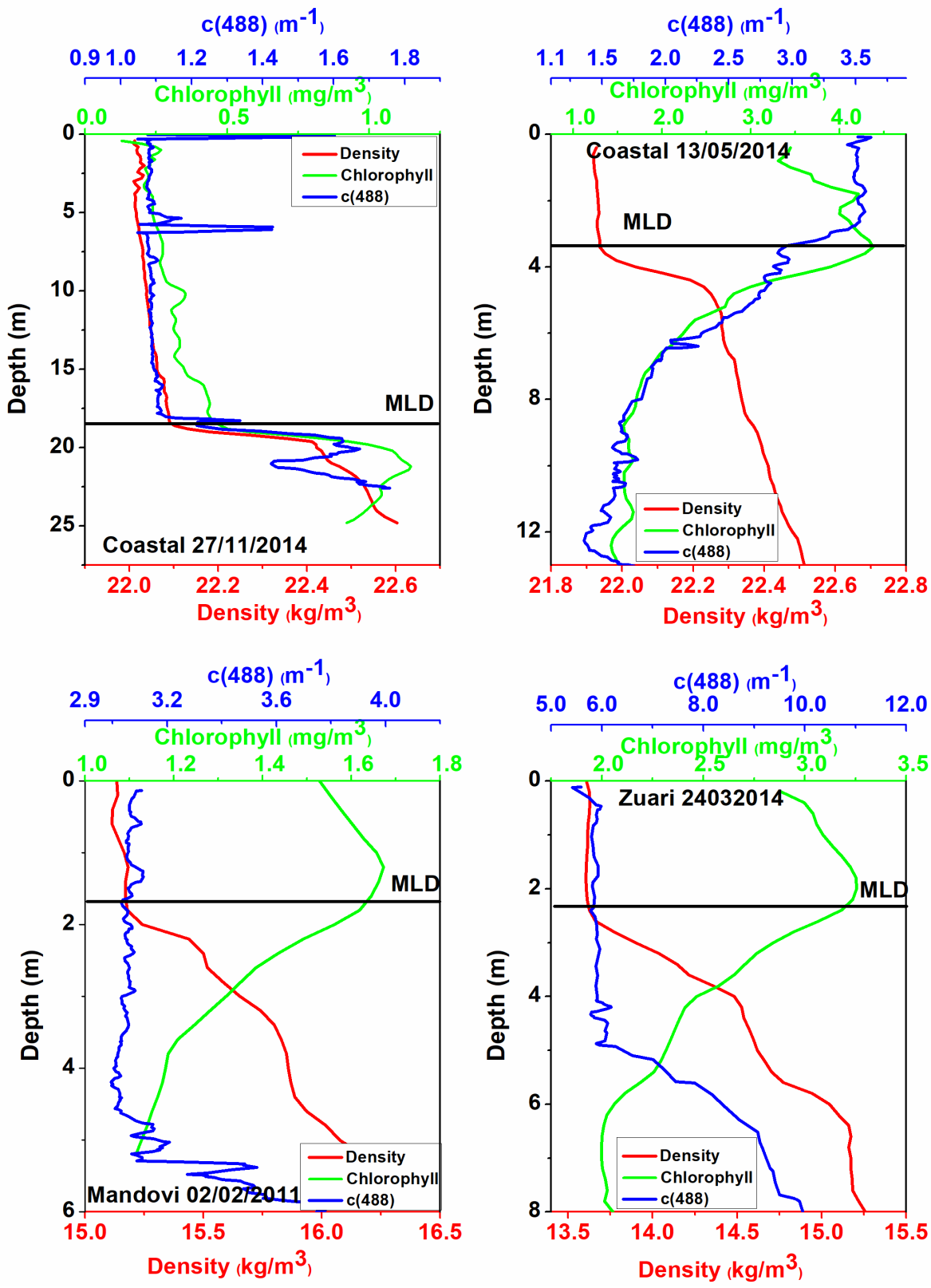

Figure 5.2 The MLD observed from the density profiles, chlorophyll and c(488) for the coastal water (top right and left), Mandovi (bottom left) and Zuari (bottom right).

5.3.2 Inversion

The temperature usually decreases with increase in depth and at times, temperature profiles depart from this and the subsurface water shows an increase in temperature and thereafter returns to the normal variations of decrease in temperature with depth. This is known as a temperature inversion. Temperature inversions are defined when the subsurface temperature increases by a threshold value from the surface temperature. Thus during a normal temperature inversion, a subsurface layer of higher temperature than the surface is observed. The temperature inversion in the Arabian Sea and Bay of Bengal have been reported and discussed of their frequency of occurrences and formations (Thadathil et al., 2016, Thadathil & Gosh, 1992). The earliest mention of thermal inversion in the estuaries of Goa was in 1973 (Singbal, 1973). During the present study, temperature inversions were observed in the temperature-depth profiles of coastal and estuarine waters of Goa. The subjective method to identify the temperature inversion in the ocean could not be adopted for the estuaries for two factors, threshold value and small range of variations in temperature. Since the temperature variation in the shallow water does not vary much, the method adopted for the open ocean cannot be used for these waters to define temperature inversion and threshold value cannot arrive for these waters as the range of temperature variations show temporal and seasonal changes. Here a simple method, not subjective but based on the changes in the slope was used to identify the inversion layers.

Observations from the temperature inversions analyses from the present study were as follows:

- The amplitudes of the temperatures inversions, ΔT was relatively small. The range of ΔT was 0.01 to 0.14 °C (Mean value of 0.035 °C) for the Mandovi and 0.01 to 0.16 °C (Mean value of 0.04 °C) for the Zuari.
- Most of the inversion occurred within 10 m of depth.
- Density inversions did not follow the temperature inversions.
- The inversions were found to occur during all seasons. During winter they were most often found in the waters near the mouth of the estuaries.
- In the estuaries, the occurrences were also site-specific. They were found to occur mostly near the mouth of the estuary, mouth of the tributaries such as in Mandovi at a distance of 8 Km from the mouth close to the tributary Mapusa River, the

entrance of the Cumburjua canals at either end of Mandovi and Zuari, upstream and the confluence of island such as St. Jacinto in Zuari.

- The depths where the temperature inversions occurred were related to the locations and seasons. The inversions were observed close to the surface during summer and winter and often upstream about 22 Km. During winter, it was observed near the bottom.

In case of thermal inversion, the barrier (BL) is formed when the layer which is uniform in temperature (ILD) is deeper than the layer which is homogenous in density (MLD) and is defined as the difference of isothermal layer depth (ILD) and mixed layer depth (MLD) and, BL = ILD -MLD (de Boyer Montégut et al., 2007). Unlike the ocean, the boundary layer BL did not vary by any large value and were limited to 0.8 m.

The temperature inversions and optical properties were observed to have some relations as given below :

- The c(488), K_d(490) and chlorophyll were found to mimic the temperature profile (Figure 5.3).
- Chlorophyll maximum was often observed just below the temperature inversion layer (Figure 5.3).
- CDOM fluorescence showed an increase whenever there was a sharp abrupt change in the temperature
- The backscattering coefficients, b_b was found to inversely follow the temperature during inversion. Wherever there is a temperature inversion, the b_b was found to dip at the corresponding depth. The density too followed the same pattern as b_b and correlated well with b_b (Figure 5.4 A and B). However, even when density was near zero as during the rains or freshwater flooding, the b_b continues to show similar behavior with temperature inversion (Figure 5.4 C and D).

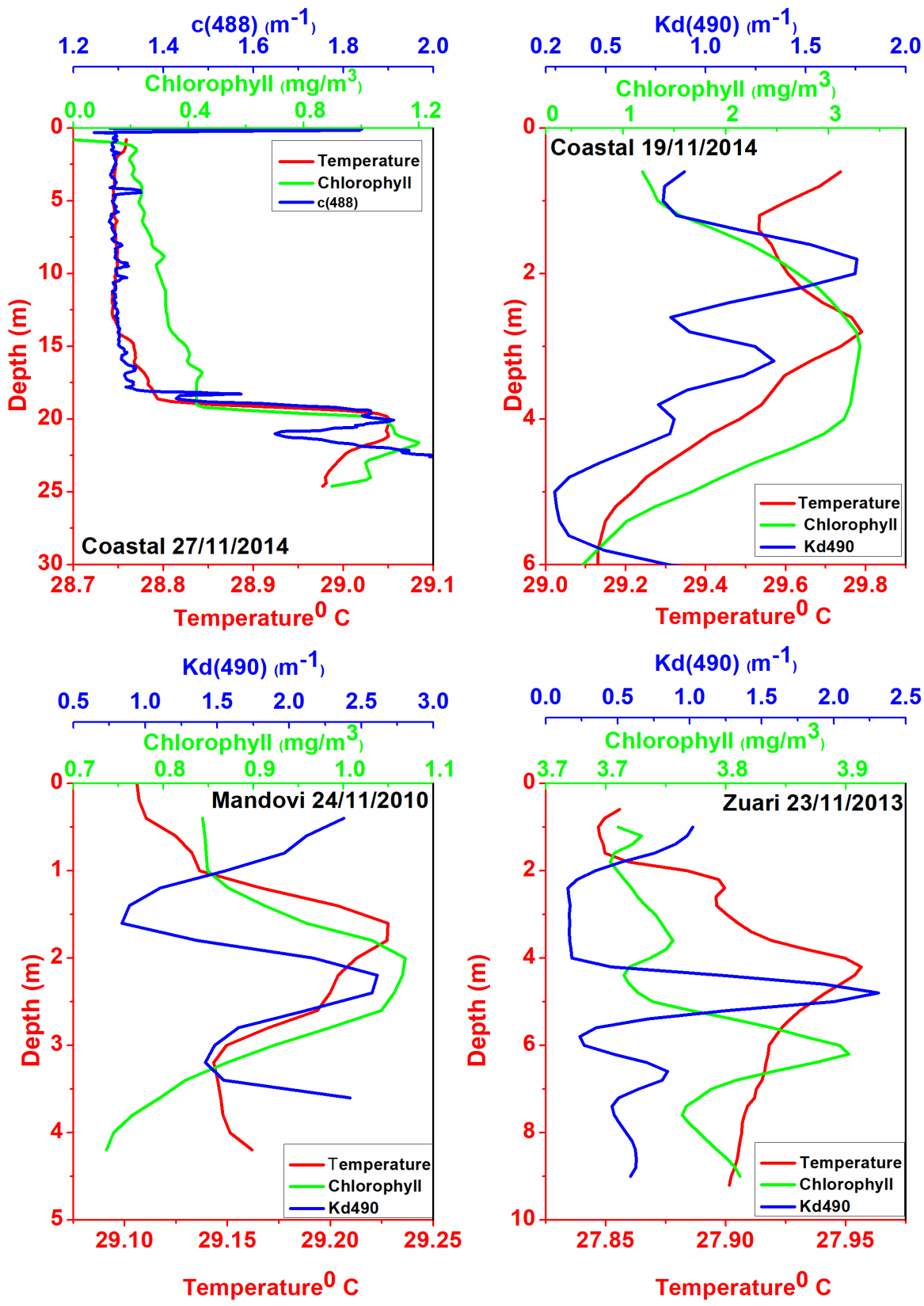

Figure 5.3 The thermal inversion observed from the temperature profiles, chlorophyll and c(488)(top right), K_d(490) (top left)for the coastal water, Mandovi (bottom left) and Zuari (bottom right).

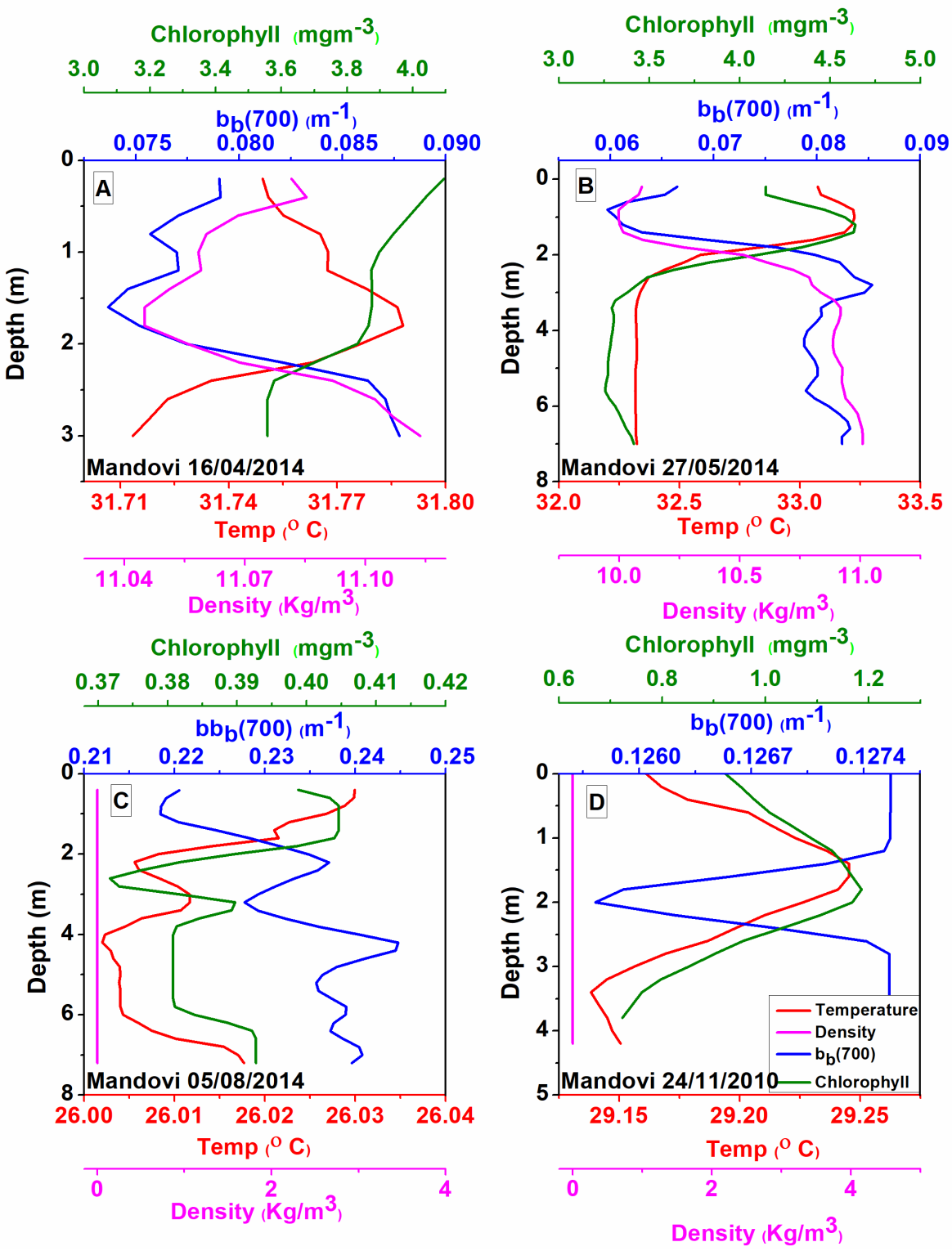

Figure 5.4 The thermal inversion observed from the temperature profiles (red), density (magenta), chlorophyll (green) and b_b (700) (blue) for the waters of Mandovi

5.3.3 Warm bottoms

A general trend of the depth variations of the temperatures is the gradual decrease of the temperature with depth. One of the features observed in these estuaries was the increase in the temperature with depth. This phenomenon has not been reported of these estuaries and probably went unnoticed. Such an increase in the temperature has been observed in these estuaries, though not discussed in detail or mentioned about it (Parab, Matondkar, Gomes, & Goes, 2013; Varma et al., 1975). This trend of the departure from the usual is observed usually in the waters close to the mouth and during winter (Figure 5.5).

Unlike the temperature inversion, where an increase in temperature at the subsurface was observed within a small depth interval, this phenomenon is a gradual increase in temperature from surface to the bottom and the density follows the temperature. The bottom temperature was always higher than the surface. Depending on the thermal stratifications at the surface layers, the chlorophyll maxima are located below it. Salinity follows typical variations increasing with depth. The backscattering coefficient follows density and increases with depth, indicating an abundance of particulate matter closer to bottom (Figure 5.5).

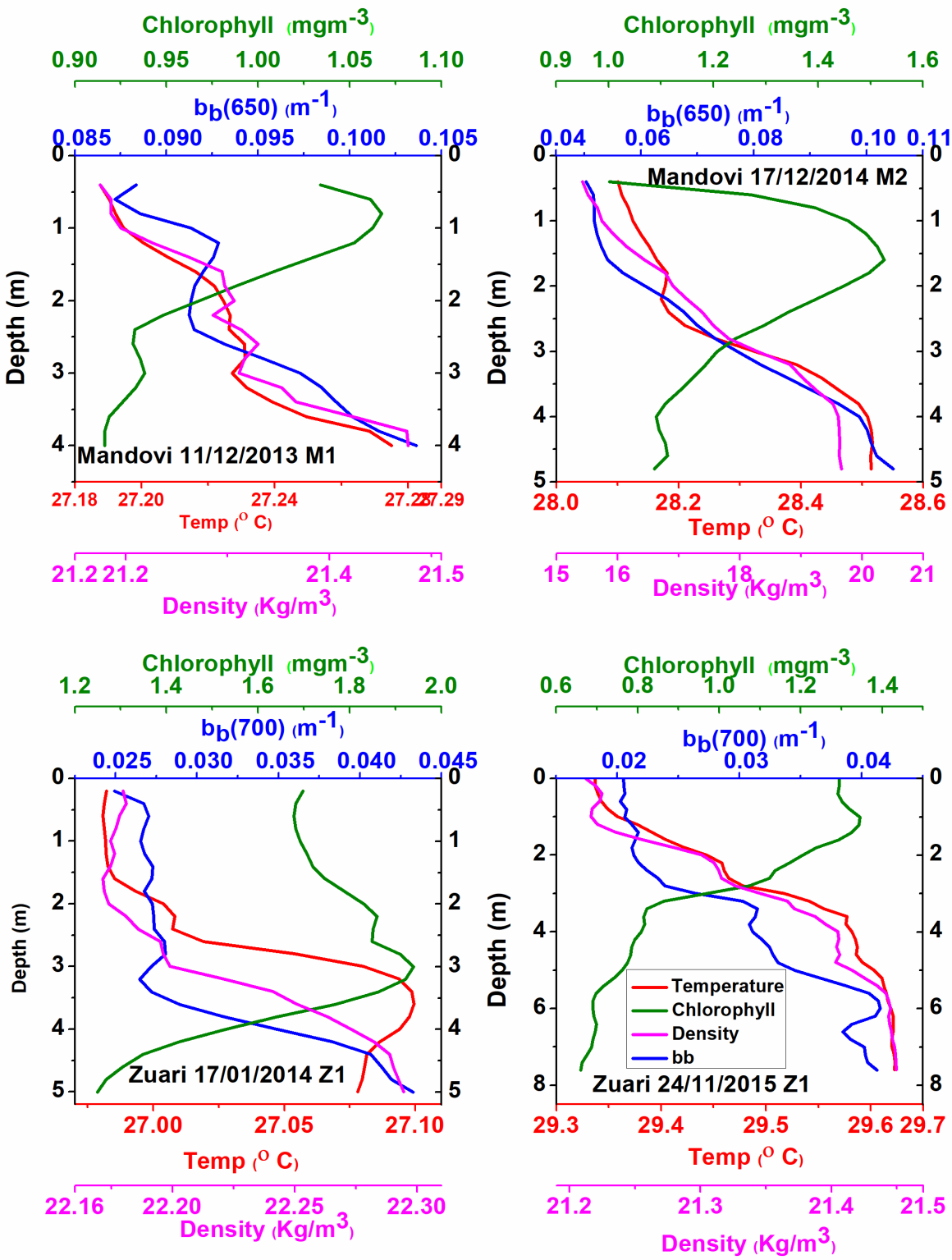

Figure 5.5 The bottom warming observed from the temperature profiles (red), density (magenta), chlorophyll(green) and b_b (700) (blue) for the waters of Mandovi (top) and Zuari (bottom).

5.3.4 Tidal variations

Tides in these estuaries play an important role in modulating the physical, biogeochemical and other water quality parameters during the non-monsoon periods. Due to the increase in the elevation factor upstream, the effect of the tide is felt till 50 Km from the mouth (Sundar & Shetye, 2005). The tides are semi-diurnal with variations in the high and low in the diurnal spring-neap cycle (Sundar et al., 2015). The average tidal ranges in the Mandovi and Zuari are similar, 2.3 m and 1.5m during Spring and Neap respectively (Vijith, 2014). During the non-monsoon period, the river-run off is very low and the freshwater availability is also low and the tidal circulation controls during this period in the estuaries. However, during the dry period there is discharge from the Selaulim dam in the Zuari. The water in the estuaries flows with denser saline water at the bottom upstream and freshwater near the surface flows out, creating a salt wedge. During the dry season, the estuary is flooded with saltwater compared to the monsoon season, when the saltwater is replaced with fresh water.

Time-series observations were carried out at two locations in the Mandovi River on 14 February 2019, near the first quarter of the lunar phase (13 February 2019). The two stations were located upstream in the Mandovi at 20 Km, station M6 off Divar (15.53093°N, 73.93166°E) and 26.8 Km, station M9 near the Amona bridge (15.5293°N, 73.96971°E). The measurements at M6 were carried out at 1000, 1400 and 1800 Hrs local time, while at M9 they were carried out at 1125 and 1600 Hrs. Three measurements were carried out. Since the tide stations of CSIR-NIO were not operational, the tidal variations for the day were obtained using software TASK2000 software developed by Proudman Oceanography Laboratory, Liverpool, UK. The tidal harmonics constituent's values used were derived from the data collected during the 1 month long tide observations carried out at a location in Mandovi (Latitude: 15 deg 31 min 53.7 sec, Long: 73 deg 55 min 50.5 sec) (Sundar et al., 2015).

IOPs from AC-9 were not considered as values that were found to be erroneous and rejected after a quality check.

Here were the observations of the parameters at station M6 (Figure 5.6).

- The transparency of the water changed with the tide and had a mean value of 1.55m. The lowest values were close to the ebb tide and increased with the tide. Z_{90} also showed a similar trend.
- Temperature, salinity, and densities of waters increased over the day.
- Water depth increased with an increase in the tide.
- Chlorophyll increased with tide height.
- The backscattering and diffuse attenuation were high during the ebb period.
- The slope of spectral variation of beam attenuation, γ was low during the ebb period.
- The bulk refractive index n_p also changed with the tide and was high during the ebb period.

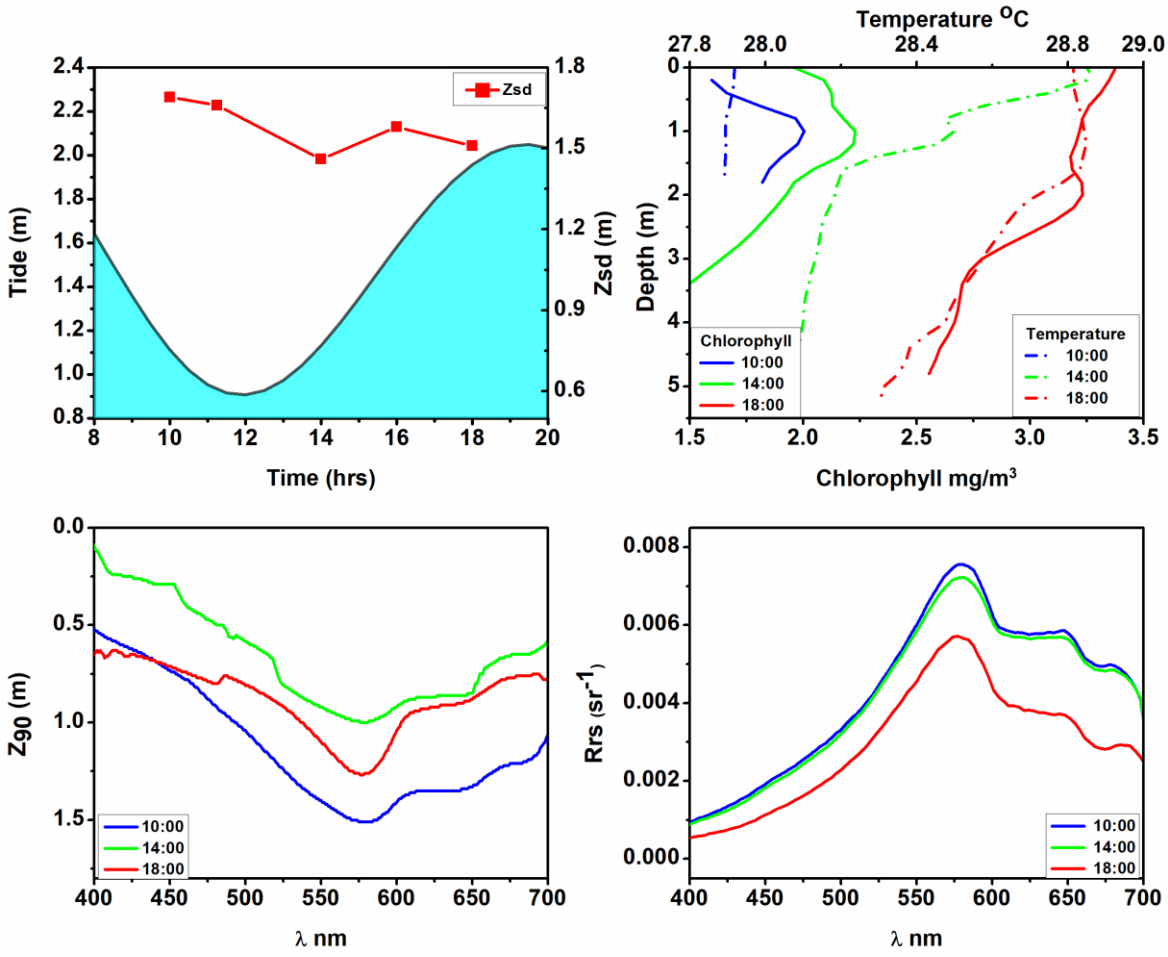

Figure 5.6 The tidal variations at station M6 in the Mandovi and the time-series observations of temperature, chlorophyll, $Z_{90}(\lambda)$ and Rrs(λ).

5.4 Discussions

5.4.1 MLD and ILD

It can be observed that in coastal waters particulate beam attenuation c(488) correlated well with chlorophyll while the same was not true for the estuaries. Particulate beam attenuation coefficients have been reported to hold a non-linear power relationship with the chlorophyll in the open ocean or Case-1 waters. However, such a relationship had a low correlation with noise and scatter, indicating that such a relationship may not hold good for all waters (Loisel & Morel, 1998; Voss,1992). The reasons for its failure to hold tight relationships for the estuarine waters could be because beam attenuation is the sum of absorption and scattering coefficients and a true relation with chlorophyll will hold if the absorptions due to CDOM and detritus and scattering covary with phytoplankton chlorophyll. Such a case may not hold in estuarine waters but could be valid in Case 1 waters where the sources are autochthonous.

In the estuaries, the backscattering coefficient was a better option to relate chlorophyll (Figure 5.4 C and D). Backscattering was found to hold a non-linear power relation with chlorophyll similar to beam attenuation (Huot et al., 2008).

It was also noticed that in the estuaries homogenous or iso-layer of beam attenuation extended beyond MLD, unlike in the coastal waters where this homogenous layer had a similar extent as the MLD. This implied that the mixing was sensitive to the optical parameters more than physical parameters.

The contributions by particulate matters were always higher near the bottom water, as the particulate matters transported by the rivers settle at the bottom and hydrodynamics impact and disturb them to be distributed in the water column. The vertical distributions and resident times of TSM in the water column will depend on settling velocities and flocculation of particulates.

Sediments are transported in the estuaries by currents which can be a function of the tide, density, wave or wind.

Here the subsurface chlorophyll maxima (SCM) were evident just below the mixed layer or the temperature inversion layer. This is a commonly observed feature. One of the

earliest reporting of the SCM in the Indian Ocean was by Dr. G.F. Humphrey at a Brunn Memorial lecture of IOC at UNESCO Paris, in 1972, wherein he mentioned about the observations of chlorophyll maximum during IIOE (Humphrey, 1972) and Dr. S.Z. Qasim mentioned about the SCM near thermocline and MLD (Qasim, Wafar, Royan, & Krishnakumari, 1978). Two limiting factors that are required for the growth, sustenance, and photosynthesis by phytoplankton are light and nutrients. Light is available at the surface and decrease with depth, while nutrients are usually available at depth and decreases moving towards the surface. Though mixing and turbulence factors are not limiting, they play an important role in determining the depth of SCM (Valenti et al., 2015). Since the density of the phytoplankton is greater than the medium, they will sink with gravity. Turbulence determines the size and types of phytoplankton that can sustain in the SCM. Under low turbulence small size phytoplankton can survive, while at intermediate turbulence large cells find it favorable. High turbulences are not favorable for phytoplankton growth. (Portalier et al., 2016). Turbulence caused due to stratification brings up the nutrients from the bottom. The subsistence of phytoplankton in the SCM will also depend on the grazing (Leach et al., 2018; Moeller, Laufkötter, Sweeney, & Johnson, 2019).

5.4.2 Thermal inversion

The reasons for the formations of temperature inversions could be due to cooling of the surface layer through heat loss, horizontal advection where low-temperature and low-salinity water is horizontally advected to superpose high-temperature and high-salinity water, cooling due to rain or warming of the subsurface layer through shortwave penetration below the mixed layer. The barrier layer (BL) has been observed to exhibit some association with the temperature inversion. Though during thick BL, strong thermal inversions were found to co-occur and were also found to correlate with inversion, all such thick BL may not result in thermal inversion (Girishkumar, Ravichandran, & Mcphaden, 2013).

The reasons for the chlorophyll maximum below the thermal inversion could be the same as discussed earlier for the MLD and ILD. Any large change in the physical parameters with a gradient above a threshold could create turbulence and allow for the pumping of nutrients into this layer from nutrient-rich waters below. If the light was not a limiting factor to this subsurface layer, the proliferation of phytoplankton could be expected, as will

be indicated by an increase in chlorophyll by a large factor compared to either below or above layer. The PSC (phytoplankton size classes) in this layer are reported to be maximum and which could depend on various factors such as depth of chlorophyll maximum, the strength of turbulence, sinking or buoyancy capabilities, growth, and mortality rate, grazing and other factors (Leach et al., 2018; Portalier et al., 2016).

5.4.3 Tidal variations

During this period of February, the runoff is relatively negligible in the Mandovi and the tide takes over circulation and mixing in these estuaries. There were variations observed in the physical, biological and optical properties of water with the changes in the tides. These estuaries are very narrow moving upstream and the tidal flows will have enhanced energy which will create turbulence and mixing, which will lead to resuspension of sediments (Kessarkar et al., 2013). Nutrients are distributed with little variations in the waters column, with bottom waters with relatively higher suspended sediment and nutrients (Fernandes, Purnachandra Rao et al., 2018; Kumari et al., 2002). This was the probable reason for the increase in chlorophyll with tide (Figure 5.6). In these estuaries, there is a spatial gradient of nutrients, with a low near the mouth and increase moving upstream towards the head (Pednekar et al., 2018; Subha Anand et al., 2014). With the availability of nutrients and light, the situations become conducive for the growth of phytoplankton, as indicated by the increase in the chlorophyll.

These estuaries have tidal asymmetries and thus favor vertical mixing during flood or spring tide and stratification during ebb (Vijith, 2014). During the ebb period, the flow velocities are low and there are stratifications, weak vertical mixing allow suspended sediment to settle down and all these favor trappings of particles, These particles are transported upstream by gravitational circulation and results in accumulation of suspended sediment upstream (Chant & Stoner, 2001). This is the plausible reason for the high attenuation of light than during the flood tide as seen from the high values of K_d. This resulted in low transparency and Z_{90}. Backscattering is also a proxy for the TSM and positively correlates with TSM, and backscattering $b_b(700)$ decreased with an increase in tides beginning from the ebb at noon.

These particulate loads will be of mineral types, as seen from the relatively higher values of bulk refractive index.

5.4.4 Bottom warming

This phenomenon has been overlooked and ignored though it was not inconspicuous. This occurs mostly during winter and at the mouth of the estuary. During winter the surface waters are relatively colder due to cold air temperature and transport of the low saline water and colder water from the Bay of Bengal through the WICC to these coastal waters (Thadathil & Gosh, 1992). Observations in this study also show that the surface waters are relatively colder than the bottom and less saline. Thus, low saline cold water is observed on top and subsurface warm and saline water which are moved into the estuary by the tidal circulation. The strength of this phenomenon may wane inside the estuary due to tidal effect and mixing. The particle load increases with depth as indicated by the backscattering coefficient, b_b. The chlorophyll also follows the typical trend, being controlled by the availability of limiting parameters of nutrients and light. Sub-surface chlorophyll maximum is also observed below the MLD and ILD. Since b_b was uniform in the mixed layer, probably this parameter could be used as a proxy to identify well-mixed waters.

5.5 Conclusions

The new method to determine the iso layers could identify the MLD and ILD of the estuaries and coastal waters.

The physical parameters of temperature and salinity of the coastal waters and estuaries exhibited their association and influence on the optical parameters.

The features of optical and biological variations often observed and reported with physical events and phenomena were similar, such as chlorophyll maxima.

Backscattering coefficient at 700 nm, $b_b(\lambda)$ was found to correlate with density and thus could be used as a proxy to determine MLD. There are algorithms to retrieve b_b from the ocean color satellite data (Lee, Carder, & Arnone, 2002; Sahay et al., 2011; Shanmugam, Ahn, Ryu, & Sundarabalan, 2010). Hence, either refining these algorithms or developing better algorithms for these waters of Goa, density maps can be generated of the estuaries and coastal waters using better resolution ocean color satellite data. Present high-resolution ocean color satellites like OCM-2 (360m), Sentinel-2(60m), Sentinel-3 (300m) can provide data close to the mouth of the estuaries and since the width of the channels is narrow

upstream these satellites may not be able to provide accurate estimations of products of these waters.

The time-series observations at a station though had limited data; it could show the variations of optical parameters with the tides.

The results of these studies attempted first times for these waters were encouraging and could be explored to carry-out further studies that would enable us to understand these waters better and would help in assessing the impacts on the climate changes and anthropogenic activities.

CHAPTER 6. CLASSIFICATION

6.1 Introduction

Considering the time-ordered methods used for the classification of water, it can be grouped into three categories, beginning with the earliest based on visual, then phytoplankton, and of recent the optical properties.

Human perception of clear or clean water and dirty and turbid water is often obtained from the visual observations of the waters. The ship logs of the ship voyages would classify the water according to the color, and one of the earliest records of Louis Ferdinand de Marsilli (1658–1730) described the water as misty, turbid or clear from the color of the water taken in a vase. The ship logs show that such a classification continued until the beginning of the nineteenth century when the waters were classified according to the transparency of water (Wernand, 2010).

With the advent of better instruments for measuring underwater light properties and understanding of the underwater light field, the qualitative, crude and vague methods of classifications of water paved the way for better methods of classifications of water based on the optical properties. It was then an accepted fact that optical parameters vary due to the constituents in water. During the earlier periods, most of the works related to optics and biology were carried-out in the open ocean, which was dominated by phytoplankton, and the classifications of water types were related to phytoplankton. One of the earliest methods of classification based by French scientists of repute Andre Morel and Louis Prieur who coined the words Case1 and Case 2 waters (Morel & Prieur, 1977). There were two water types, Case 1 waters which were dominated by phytoplankton and all other optical properties covaried with it, and Case 2 waters were those which were not Case 1 (Morel, 1980). This was further refined (Gordon & Morel, 1983; Morel, 1988). It was one of the earliest studies on the classifications of the reflectance spectra, $R(\lambda)$ and provide an explanation of the shapes of reflectance spectra based on the ratio of backscattering to absorption, $b_b(\lambda)/a(\lambda)$ and the spectral variations of the constituents in water. The reflectance model, $R(\lambda)$ model, was proportional to $b_b(\lambda)/a(\lambda)$ (Morel and Prieur, 1977). The shapes of reflectance $R(\lambda)$ and the $R_{rs}(\lambda)$ were similar, and these were functions of $b_b(\lambda)/a(\lambda)$. In Case 1 waters all other components in water such as NAP and CDOM

covaried with phytoplankton, while the same may not hold for the coastal and estuarine waters, as the sources of NAP and CDOM could be other than phytoplankton.

There were many shortcomings in restricting waters to just classes, Case 1 and Case 2. These water types did not give any proper definition for classifying Case 2 waters. These classifications were mostly restricted to deep waters and did not consider bottom reflectance and also CDOM and NAP, which may not always covary with phytoplankton. Hence, considering these ambiguities, it was suggested doing away with the Case 1 and Case2 mode of classification and use the constituents or the optical properties to classify waters which were debated to be better and meaningful (Mobley et al., 2004).

The classification of water, based on optical properties of water, can be attributed to Jerlov (1976), who formed classes based on depth, which was inversely proportional to diffuse attenuation coefficient, K_d. This classification also included coastal waters, and according to Jerlov, there were five typical oceanic spectra and nine coastal spectra. Open-ocean waters were identified as I, IA, IB, II, and III in the increasing order of the clarity of water with type I being the clearest and type III being the most turbid. There were 9 classes of coastal waters, identified as 1 through 9 in the increasing order of turbidity, with 1 being the clearest and 9 being the most turbid.

Apart from having two classes of water types and the fourteen water types suggested by Jerlov, the waters could also be categorized into various classes based on their spectral features of the optical properties. Some of the common optical properties which have been used for classifications have been $R_{rs}(\lambda)$ and $a(\lambda)$ (Lubac & Loisel, 2007; Mélin & Vantrepotte, 2015; Spyrakos et al., 2018; Vantrepotte, et.al., 2012). They have been used to classify water types in the ocean, sea, coastal waters, lakes, and reservoirs. These classifications have helped in the selective application of algorithms depending on the class to derive parameters such as chlorophyll with better accuracy (Moore et al., 2014; Jackson, Sathyendranath, & Mélin, 2017). It has also been observed from the results of studies undertaken here, how the judicious selection of algorithms depending on the class of $R_{rs}(\lambda)$ could improve the estimation of chlorophyll.

It has been observed that the optical and biological parameters of these waters of Goa show temporal and spatial variations, and some of the characteristic features could be used to identify and understand these waters (See Table 6.1 and 6.2). Very high values of

chlorophyll above 10 mg/m^3 could be due to blooms, and if they were from the coastal waters and if it was during the summer, it could be due to *Trichodesmium* or other algal blooms. These blooms affect spectral characteristics and shape of $R_{rs}(\lambda)$, $L_w(\lambda)$, $a_g(\lambda)$, and other optical parameters. The optical parameters were found to exhibit persistent patterns in their shapes, either spectral or depth profiles, which were consistent at some locations. Similarly, distinct shapes of depth profiles of parameters have been observed not only in optical parameters but also in physical and biological depth profiles.

There are classification methods based on clustering techniques, such as hierarchical clustering (Shi et al., 2014), *k*-means (Spyrakos et al., 2018; Vantrepotte et al., 2012), fuzzy *c*-mean (Moore et al., 2014), ISODATA (Iterative Self-Organizing Data Analysis Technique) (Mélin & Vantrepotte, 2015) and other statistical methods. For the classification studies of these waters of Goa, the k-means statistical method for clustering was adopted.

The studies carried out include cluster analysis of spectral $R_{rs}(\lambda)$ of coastal and estuarine waters and the depth profiles of optical parameters. Apart from studies to determine the classes, a closure of the $R_{rs}(\lambda)$ of each class for the estuaries and coastal waters were validated using the model and measured optical parameters of the class.

6.2 Methodology

Here there are two categories of cluster analysis based on the water types, estuaries which include both estuaries, Mandovi and Zuari, and the other of coastal waters, given here as Coastal. The decision to combine data from two estuaries and two transects in the coastal waters was taken only after having observed similarities in the variations of parameters between the two estuaries and along the transects of coastal waters.

The data were pre-processed, normalized, and k-means classification method was used to find classes or clusters. The spectra and depth profile data were smoothed to remove the noise, and some local variations and then it was normalized or standardized. These pre-processing the data allowed retaining the shape of the spectra or profile and removing the first order variability. The data were normalized by its integrated value within the region of interest (Lubac & Loisel, 2007; Vantrepotte et al., 2012; Mélin & Vantrepotte, 2015). Here $R_{rsN}(\lambda)$ was the normalized spectra (nm^{-1}), which was used for, k-means classification (Equation (1)). Since our interest was to classify based on the shape without considering

the amplitude of the data, normalized data were further normalized with the maximum value. A similar method was followed for the depth profile data. For the classifications of the profiles of data such as temperature, salinity, $K_d(490)$ from radiometer, spectral $a(\lambda)$ and $c(\lambda)$ from AC-9, the depth was also normalized with the maximum depth value. The spectral range for $R_{rs}(\lambda)$ was from 400 to 750 nm.

$$R_{rsN} = \frac{R_{rs}(\lambda)}{\int_{\lambda 1}^{\lambda 2} R_{rs}(\lambda)} \quad (1)$$

6.3 Results

6.3.1 $R_{rs}(\lambda)$ clusters of estuaries

There were 4 clusters for the normalized $R_{rs}(\lambda)$ with distinct shapes (Figure 6.1). These $R_{rs}(\lambda)$ were normalized spectra for the values from 400 to 750 nm. One of the clusters, Cluster 4 showed a maximum value of less than 1, as the highest values were in the spectral region above 700 nm. The variations of the measured parameters, Z_{90} and Z_{sd} (m), $a_{ph}(440)$, $a_g(440)$, $a_d(440)$ and $b_b(700)$ (m^{-1}), $a(440)$, $c(440)$, $K_d(490)$ (m^{-1}) and chlorophyll (mg/m^3) and TSM(g/m^3) corresponding to each cluster are given in Figure 6.1. The mean values of parameters for each cluster are summarized in Table 6.1. There were distinct variations of parameters for each cluster of $R_{rs}(\lambda)$. The clusters were distinctly separated spatially also, with Cluster 1 being close to the mouth while Cluster 4 was furthest upstream. A noteworthy observation was that none of the clusters had any affinity towards any season.

The $R_{rs}(\lambda)$ for all the clusters increased gradually from low at 400 nm till a peak around 570 nm and thereafter decreased to low values in the red region. The Z_{90} and Z_{sd} decreased with an increase in Cluster number. The optical properties, $a(\lambda)$, $c(\lambda)$, $K_d(\lambda)$, chlorophyll, and TSM, showed an inverse trend as compared to Z_{90}. Except for Cluster 1, the absorptions due to detritus $a_d(\lambda)$ were significantly higher than other components of absorption, CDOM, and phytoplankton for all other Clusters. Cluster 1 had the highest absorption due to CDOM.

The peaks of all $R_{rs}(\lambda)$ were at similar wavelengths about $\lambda \approx 575$ nm. Similar patterns were observed of the λ at maximum Z_{90}, λ of maximum underwater solar irradiance, $E_d(\lambda)$, λ of maximum $E_d(\lambda)$ at Secchi depth, Z_{sd}. All these wavelengths λ were close to 570 nm, except for Cluster 1, whose wavelength was lower in all cases (See Table 6.1). Among the components of absorption coefficients, contribution by detritus $a_d(\lambda)$ was found to be significant, and absorptions due to phytoplankton were relatively low. For Cluster 1, the contributions of CDOM were greater than the detritus.

Physical parameters such as temperature, salinity, the density of Cluster 1 differed from the other 3 clusters, and the physical parameters were similar for these 3 clusters, Cluster 2, 3, and 4.

Chlorophyll was the lowest for the first station and increased with cluster number.

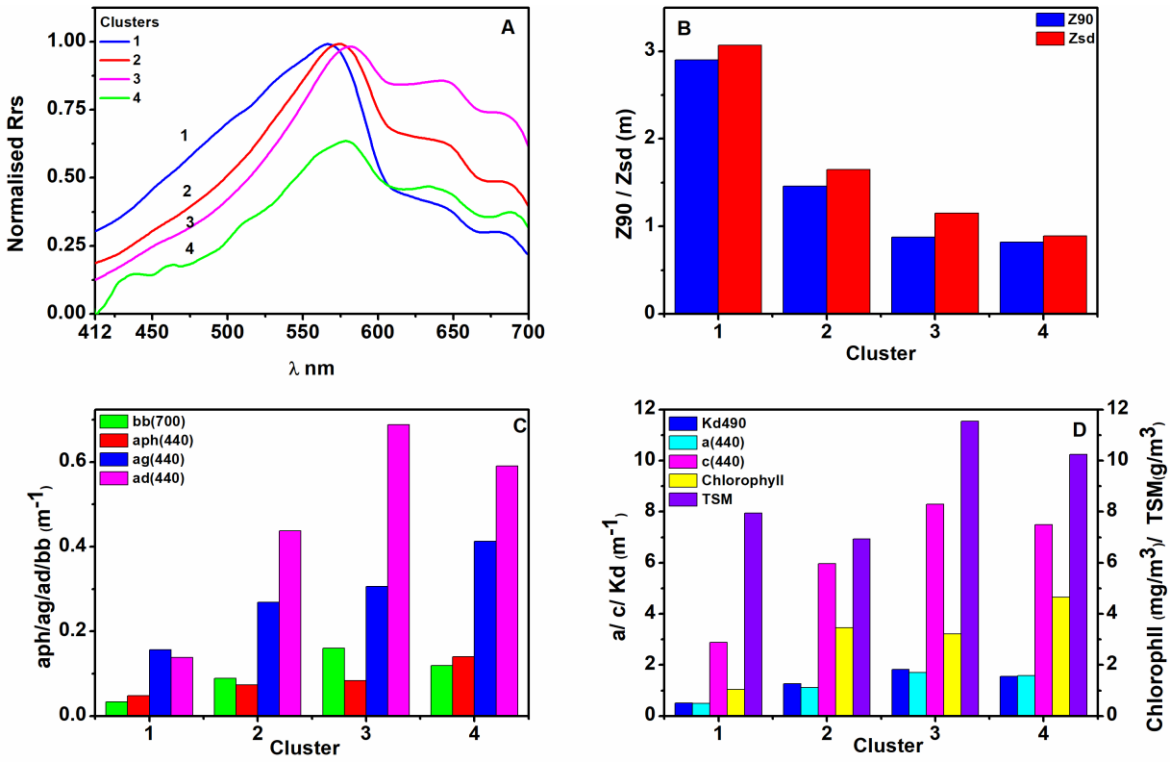

Figure 6.1 Clusters of normalized $R_{rs}(\lambda)$ and mean parameters of the corresponding clusters for the estuaries. A) Clusters of normalized $R_{rs}(\lambda)$ (top left) B) Z_{90} and Z_{sd} (m) (top right) C) $a_{ph}(440)$,$a_g(440)$,$a_d(440)$ and $b_b(700)$ (m^{-1})(bottom left) D) a(440), c(440),$K_d(490)$ (m^{-1}) and Chlorophyll (mg/m^3), TSM(g/m^3) (bottom right).

Table 6.1 Parameters of clusters

Parameter	Cluster 1	Cluster 2	Cluster 3	Cluster 4
Physical				
Distance (Km)	1.75	11.24	21.05	22.99
Temperature (°C)	28.44	29.38	29.76	29.52
Salinity	34.16	25.02	22.78	22.07
Density (Kg/m^3)	21.63	15.27	13.86	13.48
Light				
λ (of maximum Z_{90}) (nm)	562	571	575	577
Z_{90} (m)	2.9	1.46	0.88	0.82
Z_{Max} (m)	8.34	6.53	6.28	6.67
Z_{SD} (m)	3.07	1.65	1.15	0.89
Z_{eu} (m)	13.34	6.75	4.07	3.76
PAR (µmole/m^2)	278.4	338.42	226.78	192.38
%PAR at Z_{90}	22.26	24.54	25.79	21.37
PAR at Z_{SD}(µmole/cm^2)	209.82	236.44	155.81	90.99
%PAR at Z_{SD}	21.57	21.53	17.44	8.86
λ (of Maximum E_d) (nm)	554	576	580	578
E_d at Z_{90}(µW/cm^2)	40.18	50.2	44.51	42.37
E_d at Z_{SD}(µW/cm^2)	34.28	43.2	27.71	33.93
IOP				
$b_b(650)$ (m^{-1})	0.02502	0.07926	0.11395	0.09815

a(412) (m^{-1})	0.6678	1.473	2.2603	2.0519
a(440) (m^{-1})	0.4972	1.1078	1.7062	1.5775
a(488) (m^{-1})	0.3084	0.6382	1.0759	0.9107
a(490) (m^{-1})	0.3027	0.6246	1.0491	0.8936
a(510) (m^{-1})	0.247	0.4889	0.7946	0.6505
a(532) (m^{-1})	0.205	0.3685	0.6092	0.4971
a(555) (m^{-1})	0.1501	0.2537	0.4167	0.2932
a(650) (m^{-1})	0.0884	0.1007	0.1318	0.1366
a(676) (m^{-1})	0.1142	0.145	0.1526	0.1888
a(715) (m^{-1})	0	0	0	0
c(412) (m^{-1})	3.042	6.3361	8.7165	7.9471
c(440) (m^{-1})	2.8881	5.9606	8.301	7.4882
c(488) (m^{-1})	2.342	5.4257	7.8219	6.9047
c(490) (m^{-1})	2.3324	5.4059	7.7989	6.856
c(510) (m^{-1})	2.1678	5.2079	7.2942	6.3692
c(532) (m^{-1})	2.202	5.0854	7.6445	6.3991
c(555) (m^{-1})	2.096	4.8923	6.8544	6.6861
c(650) (m^{-1})	2.1297	4.1704	5.7626	5.2142
c(676) (m^{-1})	2.0673	4.0347	5.6341	4.8851
c(715) (m^{-1})	1.8172	3.8087	5.7036	4.6707
γ	1.07	1.05	1.21	0.91
ξ	4.01	4.02	4.2	3.8
n_p	1.0884	1.1088	1.0945	1.1029
AOP				
K_d(350) (m^{-1})	1.0937	2.3842	1.6078	0.4097
K_d(412) (m^{-1})	0.8309	2.0112	2.7945	0.8506
K_d(443) (m^{-1})	0.6803	1.665	2.4129	1.7688
K_d(490) (m^{-1})	0.5154	1.2676	1.829	1.5502
K_d(510) (m^{-1})	0.4779	1.1349	1.655	1.1706
K_d(532) (m^{-1})	0.4379	1.0086	1.5216	1.1688
K_d(555) (m^{-1})	0.4086	0.9014	1.3626	1.0631
K_d(566) (m^{-1})	0.4004	0.8553	1.3042	1.0095
K_d(620) (m^{-1})	0.5978	0.9873	1.3439	1.0146
K_d(650) (m^{-1})	0.644	1.0024	1.3105	0.9904
K_d(670) (m^{-1})	0.7462	1.1092	1.4018	1.1617
K_d(676) (m^{-1})	0.7572	1.1268	1.3696	1.1581
K_d(681) (m^{-1})	0.7623	1.1237	1.3724	1.176
K_d(700) (m^{-1})	0.8589	1.1925	1.4329	1.2181
R_{rs}(350) (sr^1)	0.00133	0.000665	0.00053	7E-006
R_{rs}(412) (sr^1)	0.002473	0.001435	0.001204	0.001163
R_{rs}(443) (sr^1)	0.003501	0.002219	0.002031	0.000789
R_{rs}(490) (sr^1)	0.005631	0.004344	0.003633	0.001186
R_{rs}(510) (sr^1)	0.006379	0.005547	0.004779	0.001819
R_{rs}(532) (sr^1)	0.007358	0.007374	0.006534	0.002333
R_{rs}(555) (sr^1)	0.008162	0.009127	0.008804	0.003361
R_{rs}(566) (sr^1)	0.008509	0.00994	0.009968	0.003786
R_{rs}(620) (sr^1)	0.003481	0.00659	0.008998	0.00319
R_{rs}(650) (sr^1)	0.003006	0.006147	0.009045	0.003211
R_{rs}(670) (sr^1)	0.002429	0.004754	0.00766	0.002706
R_{rs}(676) (sr^1)	0.002509	0.004737	0.007616	0.002757
R_{rs}(681) (sr^1)	0.002498	0.004791	0.007686	0.002848
R_{rs}(700) (sr^1)	0.001703	0.00367	0.006048	0.002652
Biology				

Chlorophyll (mg/m^3)	1.04	3.46	3.22	4.65
TSM (g/m^3)	7.94	6.94	11.55	10.24
pH	7.88	7.66	7.68	7.23
λ R_{rs} FLH nm	688	693	695	-99
FLH $R_{rs}(\lambda)$	0.00076	0.00139	0.00219	-99
λ FLH L_w nm	681	688	690	675
$L_w(\lambda)$ FLH	0.03431	0.03464	0.05191	0.15095
$a_{ph}(412)$ (m^{-1})	0.0488	0.0723	0.0943	0.1504
$a_{ph}(440)$ (m^{-1})	0.0479	0.0732	0.0834	0.1404
$a_{ph}(488)$ (m^{-1})	0.0433	0.0584	0.0728	0.1187
$a_{ph}(490)$ (m^{-1})	0.0325	0.0398	0.0554	0.083
$a_{ph}(510)$ (m^{-1})	0.0272	0.0311	0.0495	0.0627
$a_{ph}(532)$ (m^{-1})	0.0183	0.0238	0.0276	0.0184
$a_{ph}(555)$ (m^{-1})	0.0121	0.0139	0.0214	0.0234
$a_{ph}(650)$ (m^{-1})	0.0243	0.0386	0.0352	0.0421
$a_{ph}(676)$ (m^{-1})	0.0229	0.0368	0.0299	0.0419
$a_{ph}(715)$ (m^{-1})	0.0116	0.0172	0.0172	0.0185
$a_g(412)$ (m^{-1})	0.2442	0.3912	0.4446	0.6073
$a_g(440)$ (m^{-1})	0.1569	0.2683	0.3065	0.4126
$a_g(488)$ (m^{-1})	0.0888	0.14	0.1656	0.225
$a_g(490)$ (m^{-1})	0.0527	0.1012	0.1163	0.1583
$a_g(510)$ (m^{-1})	0.0482	0.0923	0.1043	0.1419
$a_g(532)$ (m^{-1})	0.0318	0.071	0.0774	0.0871
$a_g(555)$ (m^{-1})	0.0249	0.046	0.0518	0.0514
$a_g(650)$ (m^{-1})	0.0186	0.0211	0.025	0.0156
$a_g(676)$ (m^{-1})	0.0015	0.0008	0.0018	-99
$a_g(715)$ (m^{-1})	0.0009	0.0002	-99	-99
$a_d(412)$ (m^{-1})	0.1743	0.5273	0.8357	0.7001
$a_d(440)$ (m^{-1})	0.1387	0.4372	0.6881	0.5908
$a_d(488)$ (m^{-1})	0.0985	0.3314	0.5265	0.475
$a_d(490)$ (m^{-1})	0.0816	0.2801	0.4361	0.406
$a_d(510)$ (m^{-1})	0.0728	0.2535	0.3957	0.3694
$a_d(532)$ (m^{-1})	0.0606	0.2063	0.3254	0.3042
$a_d(555)$ (m^{-1})	0.0391	0.1388	0.2201	0.2024
$a_d(650)$ (m^{-1})	0.021	0.0778	0.118	0.1052
$a_d(676)$ (m^{-1})	0.0068	0.0253	0.0368	0.0292
$a_d(715)$ (m^{-1})	0.0026	0.0092	0.0136	0.0102

6.3.2 $R_{rs}(\lambda)$ clusters of coastal waters

There were 4 clusters here too in coastal waters of the normalized $R_{rs}(\lambda)$. Cluster 4 was close to the mouth while Cluster 1 furthest offshore. However, none of the clusters had any affinity towards any season. The peaks of all $R_{rs}(\lambda)$ increased with cluster identity or moving inshore, and similar patterns were observed of others, such as λ of maximum Z_{90}, λ of maximum underwater solar irradiance, $E_d(\lambda)$ and even the maximum $E_d(\lambda)$ at Secchi depth, Z_{sd} (See Table 6.2). Most of the optical parameters increased with an increase in cluster identity number or inshore. TSM and bulk refractive index were very high at

Cluster 1, though these waters were furthest from the coast and in the deepest waters of our studies.

Chlorophyll was the lowest for Cluster 1, which was furthest from the shore, and chlorophyll increased with cluster number or moving inshore.

The solar radiation also showed variations among the clusters, decreasing with an increase in cluster identity or distance from the shore.

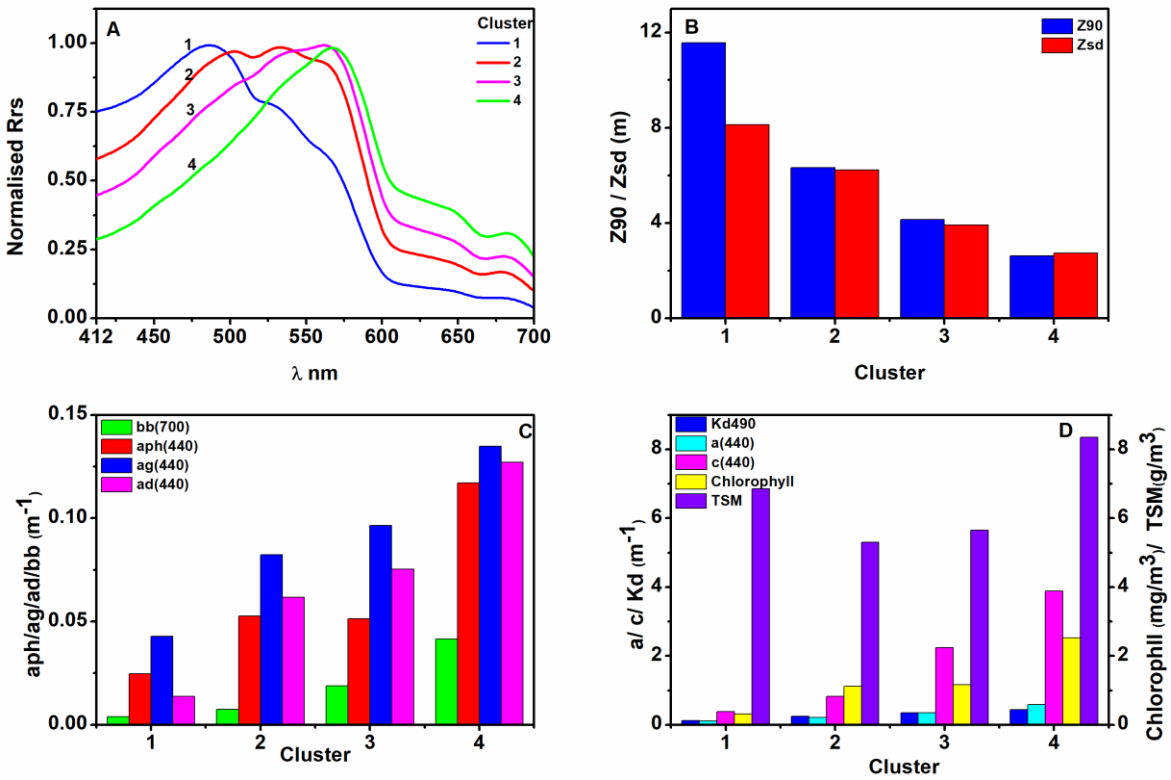

Figure 6.2 Clusters of normalized $R_{rs}(\lambda)$ and mean parameters of the corresponding clusters for the coastal waters. A) Clusters of normalized $R_{rs}(\lambda)$ (top left) B) Z_{90} and Z_{sd} (m) (top right) C) $a_{ph}(440)$,$a_g(440)$,$a_d(440)$ and $b_b(700)$ (m^{-1}) (bottom left) D) a(440), c(440), $K_d(490)$ (m^{-1}) and Chlorophyll (mg/m^3), TSM(g/m^3) (bottom right).

Table 6.2 Average values of various parameters corresponding to the clusters of coastal waters.

Parameter	Cluster 1	Cluster 2	Cluster 3	Cluster 4
Physical				
Distance	8.85	5.06	5.09	2.37
Temperature (°C)	29.86	29.56	28.64	28.97
Salinity	35.01	34.74	34.81	34.37
Density (Kg/m^3)	21.8	21.69	22.05	21.6
Solar				
$E_S(350)$ ($\mu W/cm^2$)	39.42	38.96	37.05	34.58
$E_S(490)$ ($\mu W/cm^2$)	124.04	120.41	115.73	111.8
PAR E_S ($\mu W/cm^2$)	34536.28	33535.6	32313.6	31196.02
Light				
PAR at Z_{90} ($\mu mole/m^2$)	278.37	317.15	324.32	321.84
%PAR at Z_{90}	17.62	20.61	21.87	22.61
PAR at Z_{SD} ($\mu mole/cm^2$)	436.33	340.45	372.95	344.66
%PAR at Z_{SD}	27.7	22.03	24.9	24.43
λ (at Maximum E_d) (nm)	492	533	554	565
E_d at Z_{90}($\mu W/cm^2$)	50.68	49.52	48.95	48.51
λ (at Maximum E_{SD}) (nm)	488	534	553	566
E_d at Z_{SD}($\mu W/cm^2$)	74.72	51.38	53.23	53.8
λ (of maximum Z_{90}) (nm)	491	533	556	559
Z_{90} (m)	11.57	6.32	4.15	2.62
Z_{Max} (m)	22.39	19.22	17.25	12.37
Z_{SD} (m)	8.12	6.23	3.91	2.74
Z_{eu} (m)	53.26	29.09	19.09	12.08
IOP				
$b_b(488)$ (m^{-1})	-99	0.01308	0.04842	0.0876
$b_b(532)$ (m^{-1})	-99	0.01933	0.0589	0.10213
$b_b(630)$ (m^{-1})	-99	0.01028	0.0395	0.07222
$b_b(650)$ (m^{-1})	0.00543	0.0099	0.01626	0.03491
$b_b(700)$ (m^{-1})	0.004	0.00746	0.0188	0.04158
a(412) (m^{-1})	0.135	0.271	0.4694	0.7547
a(440) (m^{-1})	0.1094	0.2096	0.3509	0.5843
a(488) (m^{-1})	0.0709	0.1455	0.2241	0.3617
a(490) (m^{-1})	0.0694	0.1431	0.2201	0.3547
a(510) (m^{-1})	0.0501	0.1197	0.1794	0.2877
a(532) (m^{-1})	0.0365	0.1145	0.1565	0.2203
a(555) (m^{-1})	0.0436	0.0884	0.1162	0.1635
a(650) (m^{-1})	0.0153	0.0563	0.0729	0.0926
a(676) (m^{-1})	0.03	0.067	0.0994	0.1487
a(715) (m^{-1})	0	0	0	0
c(412) (m^{-1})	0.387	0.9253	2.3115	4.0591
c(440) (m^{-1})	0.3803	0.8297	2.2421	3.8843
c(488) (m^{-1})	0.3103	0.7709	2.029	3.5577
c(490) (m^{-1})	0.3089	0.7674	2.0218	3.5425
c(510) (m^{-1})	0.2947	0.7187	1.9499	3.39
c(532) (m^{-1})	0.3025	0.7539	1.8858	3.2909
c(555) (m^{-1})	0.2781	0.727	1.8534	3.2402
c(650) (m^{-1})	0.2249	0.7149	1.5986	2.8295
c(676) (m^{-1})	0.2378	0.6852	1.5433	2.7533

c(715) (m^{-1})	0.1549	0.6037	1.4092	2.5942
γ3	-99	0.17	0.49	0.51
γ	0.59	0.95	1.03	1.14
ξ	3.31	3.79	4	4.1
n_p	1.1127	1.0826	1.0784	1.0709
AOP				
K_d(350) (m^{-1})	0.2732	0.5186	0.6285	0.7127
K_d(412) (m^{-1})	0.1757	0.3709	0.5176	0.6834
K_d(443) (m^{-1})	0.1485	0.3176	0.4538	0.5852
K_d(490) (m^{-1})	0.1212	0.2446	0.3465	0.4387
K_d(510) (m^{-1})	0.1258	0.237	0.3278	0.3924
K_d(532) (m^{-1})	0.131	0.227	0.307	0.3787
K_d(555) (m^{-1})	0.1398	0.2269	0.2944	0.3748
K_d(566) (m^{-1})	0.1439	0.2241	0.289	0.3671
K_d(620) (m^{-1})	0.3608	0.4561	0.4967	0.6293
K_d(650) (m^{-1})	0.4012	0.4956	0.5359	0.662
K_d(670) (m^{-1})	0.4368	0.5736	0.6194	0.7705
K_d(676) (m^{-1})	0.4757	0.5785	0.6157	0.7839
K_d(681) (m^{-1})	0.4715	0.5639	0.6129	0.7792
K_d(700) (m^{-1})	0.547	0.6952	0.6792	0.8501
R_{rs}(350) (sr^{-1})	0.003018	0.002098	0.002076	0.001533
R_{rs}(412) (sr^{-1})	0.003926	0.003244	0.003274	0.002425
R_{rs}(443) (sr^{-1})	0.004323	0.003888	0.003908	0.003198
R_{rs}(490) (sr^{-1})	0.005219	0.005599	0.005937	0.005351
R_{rs}(510) (sr^{-1})	0.004491	0.005578	0.006564	0.006304
R_{rs}(532) (sr^{-1})	0.004039	0.005763	0.00731	0.007524
R_{rs}(555) (sr^{-1})	0.003319	0.005377	0.007536	0.008417
R_{rs}(566) (sr^{-1})	0.003066	0.005286	0.007561	0.008854
R_{rs}(620) (sr^{-1})	0.000616	0.001195	0.001979	0.003356
R_{rs}(650) (sr^{-1})	0.000483	0.000979	0.001641	0.002938
R_{rs}(670) (sr^{-1})	0.000359	0.000829	0.001409	0.00249
R_{rs}(676) (sr^{-1})	0.000369	0.000866	0.001555	0.002529
R_{rs}(681) (sr^{-1})	0.000346	0.000885	0.001583	0.002567
R_{rs}(700) (sr^{-1})	0.000181	0.000511	0.001019	0.001739
Biology				
Chlorophyll (mg/m^3)	0.31	1.12	1.17	2.52
TSM (g/m^3)	6.85	5.3	5.65	8.35
pH	8.07	7.85	7.98	8.03
λ FLH R_{rs} nm	685	685	687	690
R_{rs}(λ) FLH	7E-005	0.00029	0.00052	0.00098
λ FLH L_w nm	682	682	682	686
L_w(λ) FLH	0.00836	0.02654	0.03718	0.03343
a_{ph}(412) (m^{-1})	0.0246	0.0534	0.0486	0.1204
a_{ph}(440) (m^{-1})	0.0247	0.0526	0.0514	0.117
a_{ph}(488) (m^{-1})	0.0228	0.0478	0.048	0.1135
a_{ph}(490) (m^{-1})	0.0165	0.0362	0.0365	0.0862
a_{ph}(510) (m^{-1})	0.0137	0.0283	0.0292	0.072
a_{ph}(532) (m^{-1})	0.0083	0.015	0.0185	0.0509
a_{ph}(555) (m^{-1})	0.0071	0.0083	0.0117	0.0319
a_{ph}(650) (m^{-1})	0.0085	0.0185	0.0203	0.0539
a_{ph}(676) (m^{-1})	0.0072	0.0172	0.0181	0.0523
a_{ph}(715) (m^{-1})	0.0033	0.0082	0.0076	0.0254

$a_g(412)$ (m^{-1})	0.0784	0.1227	0.1436	0.1982
$a_g(440)$ (m^{-1})	0.0428	0.0824	0.0964	0.1348
$a_g(488)$ (m^{-1})	0.0245	0.0371	0.0458	0.0498
$a_g(490)$ (m^{-1})	0.0156	0.0386	0.0268	0.034
$a_g(510)$ (m^{-1})	0.0134	0.0241	0.0223	0.0314
$a_g(532)$ (m^{-1})	0.0085	0.0387	0.016	0.0228
$a_g(555)$ (m^{-1})	0.0075	0.0187	0.0128	0.0164
$a_g(650)$ (m^{-1})	0.0083	0.0163	0.0088	0.0185
$a_g(676)$ (m^{-1})	0.0045	0.0033	0.0027	0.0014
$a_g(715)$ (m^{-1})	0	0	0.0003	0
$a_d(412)$ (m^{-1})	0.019	0.0772	0.0964	0.1583
$a_d(440)$ (m^{-1})	0.0137	0.0618	0.0754	0.1271
$a_d(488)$ (m^{-1})	0.0086	0.0477	0.0543	0.0952
$a_d(490)$ (m^{-1})	0.0066	0.0404	0.0499	0.0792
$a_d(510)$ (m^{-1})	0.006	0.0381	0.0526	0.0722
$a_d(532)$ (m^{-1})	0.0048	0.03	0.0444	0.0595
$a_d(555)$ (m^{-1})	0.0041	0.0208	0.0303	0.0414
$a_d(650)$ (m^{-1})	0.0029	0.0123	0.0163	0.0402
$a_d(676)$ (m^{-1})	0.0007	0.0041	0.0061	0.015
$a_d(715)$ (m^{-1})	0.0003	0.0015	0.0023	0.0055

6.3.3 Clusters of parameters with depth

Scanning through the depth profiles of optical parameters, similarities in the shape of depth profiles of optical parameters were noticed. The shape of the optical parameter with depth varied with locations. These depth variations mostly retained their shape regardless of the season. However, there were cases, mostly near the mouth, where there were typical shapes of depth profiles related to the season. Cluster analysis was carried-out of the depth profiles of optical parameters $K_d(490)$, $b_b(700)$, and spectral $a(\lambda)$ and $c(\lambda)$ at eight wavelengths of 412, 440, 488, 510, 532, 555, 650 and 676 nm. The method followed was similar to the spectral $R_{rs}(\lambda)$, with variations with wavelength being replaced by normalized depth. So here, both the variables were normalized, the values of the parameter and the depths. The variations of the clusters at the mouth, mid and upstream, exhibited distinct variations of all parameters with depth, and all of them had a similar pattern in depth variations at each section or location (Figure 6.3).

At the mouth, the optical parameters were low till mid-depth with very little variations and thereafter increased gradually with depth. At mid-reach, the values were low at the surface and increased linearly with depth. At the upstream, the values were high at the surface and then maintained till shallow depth with little variations and thereafter decreased gradually with depth.

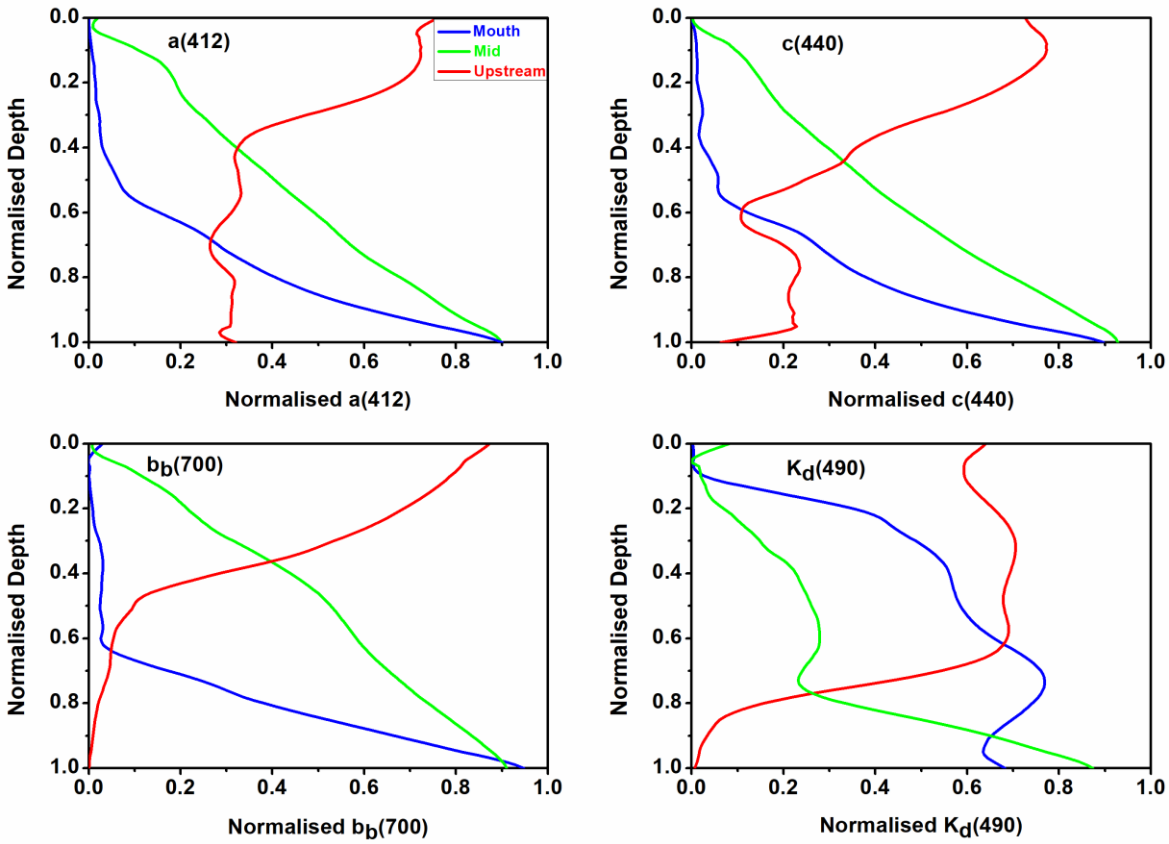

Figure 6.3 Clusters optical parameters with depth profiles

6.4 Discussions

6.4.1 $R_{rs}(\lambda)$ clusters of estuaries and coastal waters

The shape of reflectance R(λ) formed the basis of ocean color applications and various algorithms, and it has continued with $R_{rs}(\lambda)$ (Reilly et al., 1998; Huot et al., 2008; Szeto, Werdell, Moore, & Campbell, 2011). The shape and size of the $R_{rs}(\lambda)$ depend on the constituents in water (Prieur & Morel, 1971; Morel & Prieur, 1975). The optical and biological properties are observed to vary in these estuarine and coastal waters, and the same is translated to the shape and amplitude of $R_{rs}(\lambda)$.

The estuarine waters of Cluster 1 had the characteristics of being marine, with high salinity and density. These were relatively less productive, considering the low chlorophyll values. The rest of the clusters were from upstream waters, and the nutrients are reported to adequate to sustain higher levels of chlorophyll than the Cluster 1 which were close to the mouth with relatively fewer nutrients (Fernandes, Purnachandra Rao et al., 2018; Pednekar et al., 2018; Subha Anand et al., 2014). The optical properties which are proxies for the

phytoplankton abundance, the absorption from AC-9 at 676 nm, a(676), absorption due to phytoplankton at 440 and 650-676 nm, $a_{ph}(440)$, $a_{ph}(676)$, FLH and, n_p, had relatively low values compared to the values of other 3 clusters. The waters at Cluster 1 had relatively less particulate matter considering the low values of scattering ($c(\lambda) - a(\lambda)$) and backscattering at 650 and 700 nm. These particulate matters contained relatively less mineral or more algal particles, considering the lower value of the bulk refractive index, n_p(Twardowski et al., 2001).

It is observed that transparencies and light penetration depths of estuarine waters decrease in the order of increasing cluster numbers, which is consistent with the corresponding optical properties of waters, which indicate an increase in the attenuation of light. Transparency of water, indicated by Z_{sd} was inversely proportional to the total attenuation, $\alpha\ 1/(K_d + c)$ (Preisendorfer, 1986). One of the prime reasons for this reduction in the light penetration and transparencies are due to the abundance of particulate matter, which is indicated by the significant and sizeable contribution from scattering,($b(\lambda) = c(\lambda) - a(\lambda)$), backscattering, $b_b(650)$, absorption due to detritus, $a_d(\lambda)$. There were above two-fold increase of $K_d(\lambda)$, $a(\lambda)$, $b(\lambda)$ in the waters of Cluster 2, 3 and 4 as compared to Cluster 1.

The wavelength of maximum available light energy in water or the transparencies of water depends on the constituents of water and their spectral scattering absorption capabilities. Considering the spectral properties of the CDOM and detritus, most of the photons in the blue region will be absorbed, while the molecular absorptions of water itself increase in the longer wavelengths. $Kd(\lambda)$ is a function of absorption and scattering (Lee, Du, & Arnone, 2005; Satheyendranath and Plat 1988; Smith & Baker, 1981). These results of low attenuation of light in the green region, agree with spectra of diffuse attenuation coefficients, $K_d(\lambda)$ of clusters.

The coastal clusters were distinctly different from the clusters of estuaries. $R_{rs}(\lambda)$ from Cluster 1 was furthermost from the coast, and the $R_{rs}(\lambda)$ from other clusters moved closer to coast with increasing order of their identity numbers. Waters of Cluster 1 had the highest penetration of light, Z_{90}, and transparency of water, Z_{sd}. Corresponding to the high values of Z_{90} and Z_{sd}, the optical parameters also exhibited their characteristics being inversely proportional to transparency and penetration of light with lowest values of $c(\lambda)$, $K_d(\lambda)$, and b_b. One of the notable features of these waters was the lower values of CDOM $a_g(\lambda)$

compared to the detritus $a_d(\lambda)$. The TSM at Cluster 3 at a distance of about 5 Km from shore and an average depth of 17 m, had the highest particulate load, as indicated by TSM and abundance of mineral particles indicated by high values of bulk refractive index. Probably the nutrient levels increased moving closer to the shore, indicated by the increase in chlorophyll and the associated optical properties of $a_{ph}(\lambda)$. Productivity increase with a decrease in Cluster number or moving towards shallow water. The peak wavelength in the Cluster 1 in the lower wavelength, since there was less absorption in the blue due to relatively fewer contributions from CDOM, detritus, and chlorophyll, while their contributions increase as the Cluster numbers and move towards shallow waters towards shore and a corresponding increase in the wavelength of maximum penetration of light also increases.

6.4.2 Clusters of depth profiles

The distinct patterns observed depend solely on the physical characteristics of the estuaries. These estuaries are strongly convergent type, with a wide mouth and narrow moving upstream. Depths are also shallow at most places upstream. These are monsoon estuaries with large runoff during monsoon, transporting particulate matter in the channel. During non-monsoon tides control the flow (Shetye et al., 2007). At the upstream, the influence of the tides is low, but that of runoff is dominant. Circulations in the estuaries are controlled by tides and wind-driven currents during the non-monsoon period. The classic case will be that the particulate matter is transported by runoff from upstream and deposited at the bottom. So these materials which are resident at the bottom will be placed in the water column should any force disturb them, such as tidal current and turbulent mixing, and the concentrations will usually decrease from the bottom upwards or the suspended matter will increase will depth. Hence, the optical properties c, b_b, and Kd increased with depth till the upper region of estuaries. Absorptions were high due to the abundance of CDOM and detritus at the bottom compared to the surface. However, the upstream region of the study was an ore handling point, and numerous barges and canoes moved in these waters, with shallow depths and narrow width of the estuary. Due to these reasons, there were always high particulate matters in the surface waters, kept in suspension due to mechanically created turbulence aided by the tidal asymmetry of currents. Tidal straining due to tidal asymmetry also increases vertical mixing. The particulate matter is kept in the water column with low sinking velocity and convective

mixing and sediment pumping. During flood and vertical mixing, the flocs could break, resulting in smaller flocs having smaller settling velocity. Under these conditions, inverse variation patterns of density and suspended sediment were also observed upstream (Chant & Stoner, 2001; Geyer, Woodruff, & Traykovski, 2001; Scully & Friedrichs, 2007; Uncles, Stephens, & Law, 2006). This was the reason that the proxy for the turbidity and sediment, the optical parameters also exhibited high values of c, b_b, and K_d in the surface layers, which decreased with depth and thereafter maintained uniform values due to mixing. The inverse salinity variations in the estuaries with high values at the surface, which decrease with depth, have also been observed in other estuaries (Geyer et al., 2001; Uncles et al., 2006).

6.4.3 Validation of R_{rs} clusters

The classes of $R_{rs}(\lambda)$ were based on cluster analysis, and there were distinct characteristics of optical and biological parameters in these classes, which suggested these classes were true, unambiguous, and justifiable. These were put to test by the closure of $R_{rs}(\lambda)$ with the optical parameters in the model for $R_{rs}(\lambda)$.

From Equation (10) Chapter 2, it can be observed that in coastal and estuarine waters if the $a(\lambda) >> bb(\lambda)$, then $R_{rs}(\lambda) \alpha b_b(\lambda)/a(\lambda)$. Hence this ratio will determine the shape of $R_{rs}(\lambda)$. $R_{rs}(\lambda)$ at λ = 650 nm was validated using the model (See Equation 10, Chapter 2). The values of $f/Q(\lambda)$ at λ = 440,500,565,665 nm are 0.0936,0.0944,0.0929,0.0881 (Morel & Gentili, 1993). Interpolated value of f/Q at λ = 650 is 0.0888. Here the total absorption coefficient is given as $a_t(650) = a_w(650) + a(650)$, where a(650) is the measured absorption using AC-9 as given here in Table 6.1 and 6.2, and $a_w(650)$ is the absorption due to pure water, $a_w(650) = 0.34$(Pope & Fry, 1997).

$$R_{rs}(650) = 0.0479 \frac{b_b(650)}{a_t(650) + b_b(650)} \quad (2)$$

The model given in Equation (2) was validated using the measured values for each cluster given in Table 6.1 and 6.2 and their results are given in Figure 6.4. Though this simple model did not include contributions from bottom reflectance effects, the comparison of this validation exercise showed good agreement of the model with the measured $R_{rs}(650)$ ($R^2 >$ 0.97 discarding an outlier).

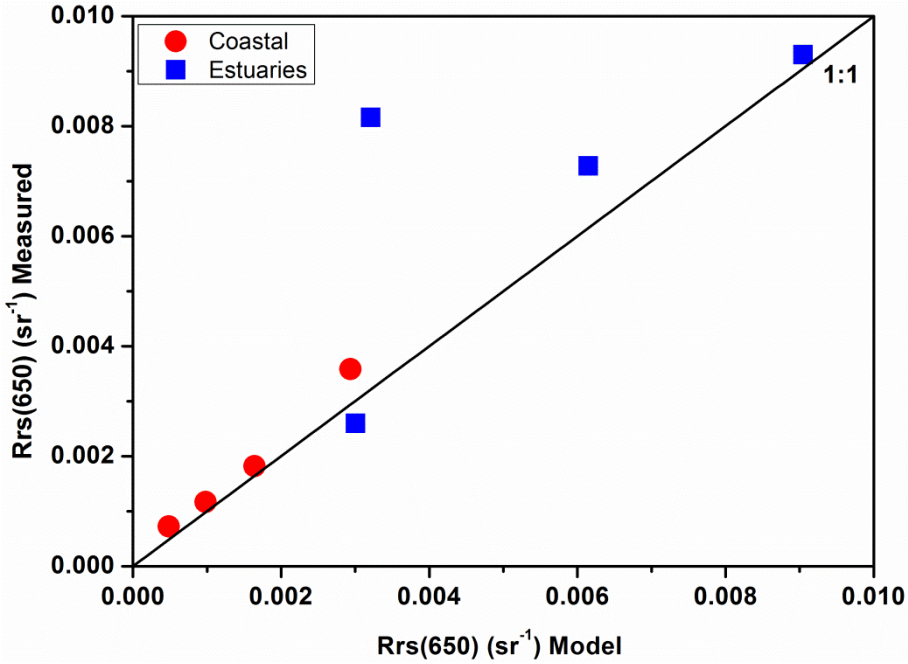

Figure 6.4 Comparisons of the measured and model of $R_{rs}(650)$ for 4 clusters of R_{rs}.

6.5 Conclusions

Cluster analysis has shown from the large data of optical properties from complex coastal and estuarine waters could be classified into distinct classes, and each class having similar optical, biological, and physical properties and the classes differed from each other in all these aspects. These classes were mostly season invariant but spatially apart. The validation and closure results of $R_{rs}(\lambda)$ from each class using a model with the associated optical data confirmed the validity of the classes.

Identifications of classes will allow understanding the reasons for spectral or depth variations and their associations with physical, biological, and chemical processes.

Since each class was identified with a unique shape of $R_{rs}(\lambda)$ and associated optical, biological, and physical properties, hence for any given $R_{rs}(\lambda)$, the range of the variations of optical properties could be surmised.

The classes of depth variations of optical properties attempted for the first time, showed clear, marked distinctions in the pattern of depth variations in each class, and they were

spatially separated. The definite and reproducible patterns of optical profile variations in each class are reasoned to be associated with physical processes.

The studies regarding clusters and algorithms to derive chlorophyll has also helped in selecting suitable algorithms to derive chlorophyll with better accuracy from satellite data (not included here).

The classes provide only a general framework to identify waters of similar properties, and the number of classes could be extended beyond four classes given here. These additional classes could provide classes on spatial and temporal basis rather than just spatial distributions as it was observed in the present analysis. The present analysis could be extended to include shape and magnitude, while the magnitude was ignored in our present studies.

CHAPTER 7. TRANSPARENCIES

7.1 Introduction

Turbidity and transparency are two terms often used to indicate the quality of water. It would be good to explain and clarify here the term 'turbidity' vis-à-vis with the transparency of water. Turbidity is an effect of the constituents in water that interacts with light and is not directly a measure of the constituents. Turbidity water is a physical appearance of water such as cloudy, murky or colored. Transparency and turbidity refer to water clarity and can be related to each other. Transparency of water relates to the depth of the penetration of sunlight in water.

In contrast to the turbidity and various issues related to its definition, methods, and instruments used to measure turbidity, the measurement, and definition of transparency of water have been rather simple with fewer ambiguities. There is no simpler instrument than the Secchi disk which has over the years been used by oceanographers and environmentalists to obtain first-hand information about the clarity or transparency of the water. The transparency has been measured using a flat disk of 20 to 30 cm diameter painted matt finish, either fully white or with four quadrants of alternately white and black color (Whipple's disk after George C. Whipple,1899), which is lowered in water till it disappears from the sight of the observer. This depth is known as Secchi depth and is indicated in meters. Deeper depths indicate water to be relatively more transparent or clear allows light to traverse deeper and smaller Secchi depth indicate turbid waters with higher attenuation with smaller penetration of light. Although the present term 'Secchi' has been attributed to an Italian astronomer, Father Pietro Angelo Secchi of 1865, the ship logs since 1658 have documentation of the measurements of the transparencies of water using various objects such as white towels, woodblocks, plates, tins, kitchen items, painted thermometers or copper balls which were lowered in water until they disappeared (Wernand, 2010). Since then the tradition of finding the transparency or clarity of water has continued and provided first-hand information on the water quality. Transparency of water is an important parameter about water quality, underwater visibility, and trophic state. Turbidity, transparency and Secchi depth are visual properties of water-based on light scattering and attenuation. Various empirical relations have been used with Secchi depth to understand the environmental parameters of water such as chlorophyll or productivity, suspended

matter, light penetration or availability and related studies. Long-term studies of Secchi depths have helped to monitor the health of the water bodies such as rivers, lakes, and sea(Capuzzo et al., 2015; Sandén & Håkansson, 1996). Secchi depth has been useful in understanding global trends in the phytoplankton concentrations for a period over a century (Boyce, Lewis, & Worm, 2010). Considering the importance of Secchi disk measurements, limnologists, and oceanographers have been advised to continue with the measurements of Secchi depth, even with the availability of sophisticated instruments for measuring optical parameters(Berman et al., 1985).

One of the earliest reporting of Secchi depths in the Zuari estuary, Goa was in 1970 (Dehadrai, 1970) and in the Mandovi and Kumbharjua canal of Goa was reported in 1976 (Bhattathiri et al., 1976). The light transmission studies were earlier carried-out in the coastal waters of Goa (Sathyendranath & Varadachari, 1982).

The objectives of the present studies have been to understand the optical properties that influence and control the transparencies of these waters and examine few factors such as bathymetry and monsoon that could affect the transparencies of these waters. The focus of the studies have been on a macro or gross level, rather than micro-level and hence the influence of tides or diurnal variations, factors such as natural or anthropogenic sources, environment, physical processes that affect the water quality of a small region and spatial variations at a fine scale, have not been included.

7.2 Methodology

The Secchi depths, Z_{sd}, and bio-optical parameters were measured at stations in the two estuaries, Mandovi and Zuari and the coastal waters. The Secchi disk used for the measurement was 30 cm matte painted white disk and the reflectivity of the disk was 0.89 which was obtained from the measurements using spectrometer and reflection probe (Ocean Optics Inc). There were 500 data of Secchi depths measured together with optical (apparent and inherent optical properties), biological and ancillary parameters from the coastal waters and two estuaries, Mandovi and Zuari from 2010 to 2018 (coastal waters - 183, Mandovi -187 and Zuari - 130). The data include only those where Secchi depth and other AOPS and IOPS were available and the parameter values used for this study were mean of the depth data within Z_{sd}. Data during algal blooms were not included since the optical and biological parameters varied by a large factor from the normal. Hence, there

will be small variations from the values of the gross and seasonal parameters listed in Chapter 4.

7.2.1 Theory of the transparency of waters

To understand the optical parameters of water that influence or control the transparency of water, it is essential to consider the theoretical formulation of Secchi depth, Z_{sd}. The Secchi depth has been theoretically derived using the radiative transfer model under the framework of the visual optics of natural waters or underwater visibility based on the contrast theory (Preisendorfer, 1986; Zaneveld & Pegau, 2003). The vertical visibility equation based on the Law of Contrast Reduction or photopic contrast reduction for a vertical path of sight in a homogeneous medium and deep water neglecting bottom reflectance is given as

$$Zsd = \frac{\Gamma}{c_v' + K_v'} \tag{1}$$

$$\Gamma = Ln\left[\frac{C_0}{C_{\min}}\right] \tag{2}$$

A new refined theory considers the angular resolution of a human eye, size of the target and viewing distance (Lee et al., 2015). In the above Equation (1) the $c_{v'}$ and $K_{v'}$ are the beam attenuation and diffuse attenuation coefficient in photopic units respectively. The spectral optical properties in photopic units were derived convolving with the spectral luminosity function of the eye (Mobley, 1994; Zaneveld & Pegau, 2003). For brevity at times, the spectral part is ignored for some optical parameters.

In Equation (2) the coupling constant Γ (dimensionless) is a function of apparent contrast, C_0 and threshold contrast C_{min}. The coupling constant Γ was found to vary within a small range with a mean value of 6.823 (σ = 0.7) for the waters of Goa and was modeled using underwater average cosine at 490 nm (Talaulikar, Thayapurath, Desa, et al., 2012; Thayapurath, Joshi et al., 2016).

Considering that the structure of formulation in photopic and radiometric remain the same as given in Equation (1), the optical parameters c_v and K_v in photopic units would be

analogous to c and K_d in radiometric units. The c_v and K_v in photopic units were also reported to hold a good relationship with the radiometric optical properties beam attenuation coefficient c, and, K_d (Doron, 2007, Thayapurath, Joshi et al., 2016). Hence, the transparency of water given by Z_{sd} becomes a function of the IOP, c and AOP, K_d. Thus, assuming Γ to be nearly a constant, the transparency or Secchi depth of water depends on just two optical parameters, c, and K_d and is inversely proportional to the sum of these attenuation coefficients (Tyler, 1968).

$$Zsd \propto \frac{1}{c_t + Kd} \tag{3}$$

The inherent optical properties are additive and thus $c_t = a_t + b_t$, where a is the absorption and b is the scattering coefficient. The model for K_d derived using the radiative transfer equations shows K_d as a function of absorption, a and backscattering coefficient, b_b (Gordon, 1989a,1989b; Morel, 1988; Stavn & Weidemann, 1989). In the simplest form, K_d is given as a sum of absorption and backscattering coefficient, $K_d \approx a_t + b_{bt}$ (Sathyendranath et al., 1989; Smith, and Baker 1981). The above model of Z_{sd} (Equation (3)) reduces to an approximate relation with c and K_d substituted with IOPs as given below

$$Zsd \propto \frac{1}{2a_t + b_t + b_{bt}} \tag{4}$$

Hence it can be observed that Z_{sd} is primarily controlled by total absorption a_t and scattering (total scattering b_t and backscattering b_{bt}). The contribution by backscattering is usually less significant compared to the total absorption and scattering. For the waters of Goa, the measured particulate backscattering $b_b(700)$ was found to be just about 2% of the total particulate scattering b(700). So the simple relation of the transparency could be approximated as

$$Zsd \propto \frac{1}{2a_t + b_t} \tag{5}$$

7.3 Results

The mean values of physical, optical and biological parameters along with the Z_{sd} for these waters are listed in Table 4.1 to 4.3 (Chapter 4) and the seasonal variations are shown in Table 4.4 to 4.6. The transparencies Z_{sd} were highest in the coastal waters and it was higher by nearly a factor of three compared to Mandovi and Zuari. Among the estuaries, Mandovi had better transparencies of water compared to Zuari. The variations in the transparencies of these waters were large, with values varying from 1.29 to 12 m in the coastal waters, 0.41 to 7m in the Mandovi and 0.42 to 4.65 m in the Zuari. The highest values of transparencies were observed in the coastal waters (12 m) and the lowest was in the estuaries (0.4 m).

7.3.1 Temporal variations of the transparencies

There were temporal and spatial variations observed in the transparencies of these waters. A general pattern of temporal variations on a monthly scale from January has the highest value and thereafter decreasing to minimum transparency during monsoon, and again increasing steadily from post-monsoon to December (Figure 7.1). Lowest transparencies were observed during monsoon (June to September) and highest during winter. In the coastal waters during non-monsoon periods, the high transparencies were observed during February, April and October and the lowest were during the winter period of January and December. In the Mandovi, it was the highest during February and lowest during August (0.4 m). In Zuari highest transparencies were observed during November (4.65 m) and January and lowest during the monsoon period of July (0.4 m). The patterns of monthly variations in the coastal waters and Zuari were nearly the same with high during April and October and then decrease after post-monsoon. There was a small deviation from the usual pattern in Zuari while moving from January to the monsoon, increasing from February to April and thereafter decreasing to the lowest values of transparencies during monsoon. However, since there was no data in the coastal waters during monsoon it can be assumed to follow a similar trend as in the estuaries with the lowest transparencies during monsoon.

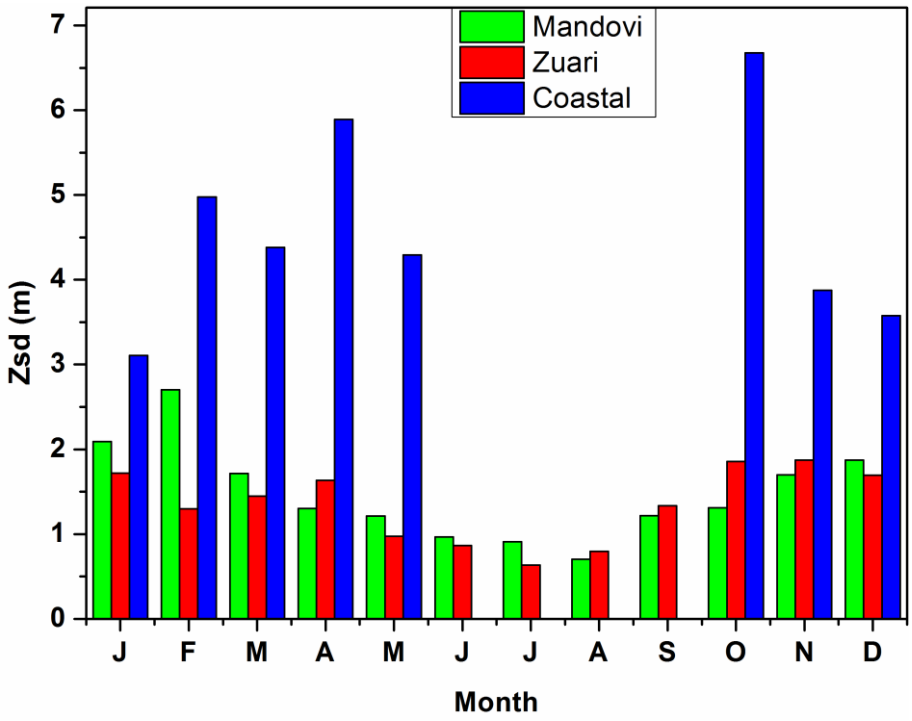

Figure 7.1 Average monthly variations of the Secchi depth, Z_{sd} (m) in the coastal waters and two estuaries, Mandovi and Zuari

7.3.2 Spatial variations of the transparencies

There were spatial variations of Z_{sd} observed in coastal and estuarine waters (Figure 7.2). In the coastal waters, Z_{sd} changed rapidly with a large positive gradient (~1.25 m/Km) till 4 Km away from the shore, then decreased gradually until 6 Km and thereafter remained nearly unchanged with a steady value. In the estuaries, the transparencies were high near the mouth and decreased moving upstream. There were regions with high-low pattern upstream, which varied with season. During non-monsoon seasons, the Z_{sd} was found to decrease moving upstream in the estuaries while during monsoon the pattern was reversed, with the lowest transparencies being observed near the mouth.

.

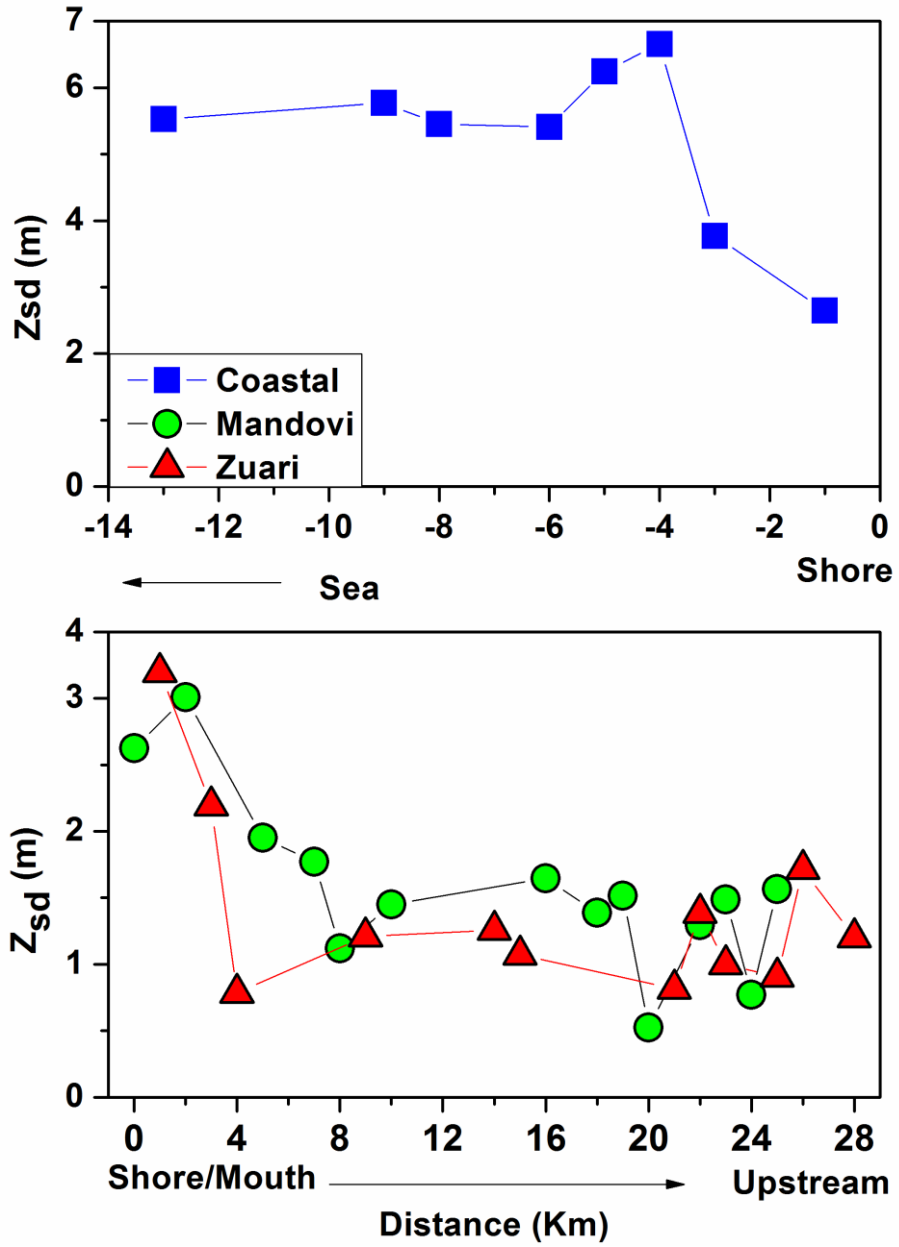

Figure 7.2 The average spatial variations of the Z_{sd} (m) in the coastal waters (top) showing the variations from the mouth towards offshore and in the estuaries moving from the mouth towards upstream (bottom).

Extremum of the transparencies was observed in both the estuaries and they varied with location and season. The distance is indicated from the shore or mouth, increasing moving upstream in the estuaries and offshore in the coastal waters. The Z_{sd} were without large variations in both the estuaries, with some very distinct low and high transparencies seen most of the time at some locations. Low transparencies were observed in the Zuari at locations 4, 9 15 and 28 Km and in the Mandovi low transparencies were observed at 8, 16-19 and 22-25 Km. Moving towards the mouths of both estuaries, the transparencies

increased rapidly and the same continued in the coastal waters. High transparencies in the Zuari were observed mostly 1 km away from the mouth and others were at 3, 15 and 22 Km.

7.3.3 Relationships of transparencies and optical properties

The transparency or Secchi depth is a function of the inherent and apparent optical properties (Equation 3 and 5). Hence, to understand the transparency or Secchi depth, Z_{sd} of the waters of Goa, it is essential to understand the variations of the optical properties that regulate the transparencies of these waters.

Since the Z_{sd} is inversely proportional to diffuse attenuation K_d, beam attenuation c_t, absorption a_t and scattering b_t, there have been many relations derived using such optical properties such as beam attenuation c_t (Holmes, 1970; Suresh Naik, Bandishte et al., 2006; Tyler, 1968) K_d or K_{PAR} (Holmes, 1970; Poole & Atkins, 1929; Suresh Naik, Bandishte et al., 2006), a ratio of remote sensing reflectance (Doron et al., 2011), and also other proxies such as chlorophyll (Boyce et al., 2010; Morel & Maritorena, 2001) and total suspended matter and turbidity (Davies-Colley et al., 2014) and other parameters (Lee et al., 2018). These relations to derive optical parameters using Z_{sd} usually hold good for the region of study and may not hold good for all water types and applying such relations using Z_{sd} to derive IOPs would only be a "foolish attempt"(Levin et al., 2000; Preisendorfer, 1986).

The inverse relation with Z_{sd} and optical properties as indicated by the relations given in Equations (3) and (5) were examined for the waters of Goa. Empirical relations with optical parameters were earlier developed for the Arabian Sea(Suresh et al., 2006). It can be observed that for the waters of Goa, the Z_{sd} was found to hold a good relations (R^2 > 0.8) with the inherent and apparent optical properties that control the Z_{sd} such as diffuse attenuation at 490, Kd490, beam attenuation at 412 nm, c412, particulate scattering (total scattering without the contribution of water) at 412, b412 and total absorption at 412 nm, a412 (without the contribution of water) (Figure 7.3 and Table 7.1).

Table 7.1 Empirical relations of log-log transformed optical parameters with Z_{sd} of the form y = mx +c (R^2 > 0.8)

Parameter	m	c
K_d(490)	-1.3197	0.709
a(412)	-1.137	0.86
b(412)	-1.293	2.589
c(412)	-1.3197	0.709

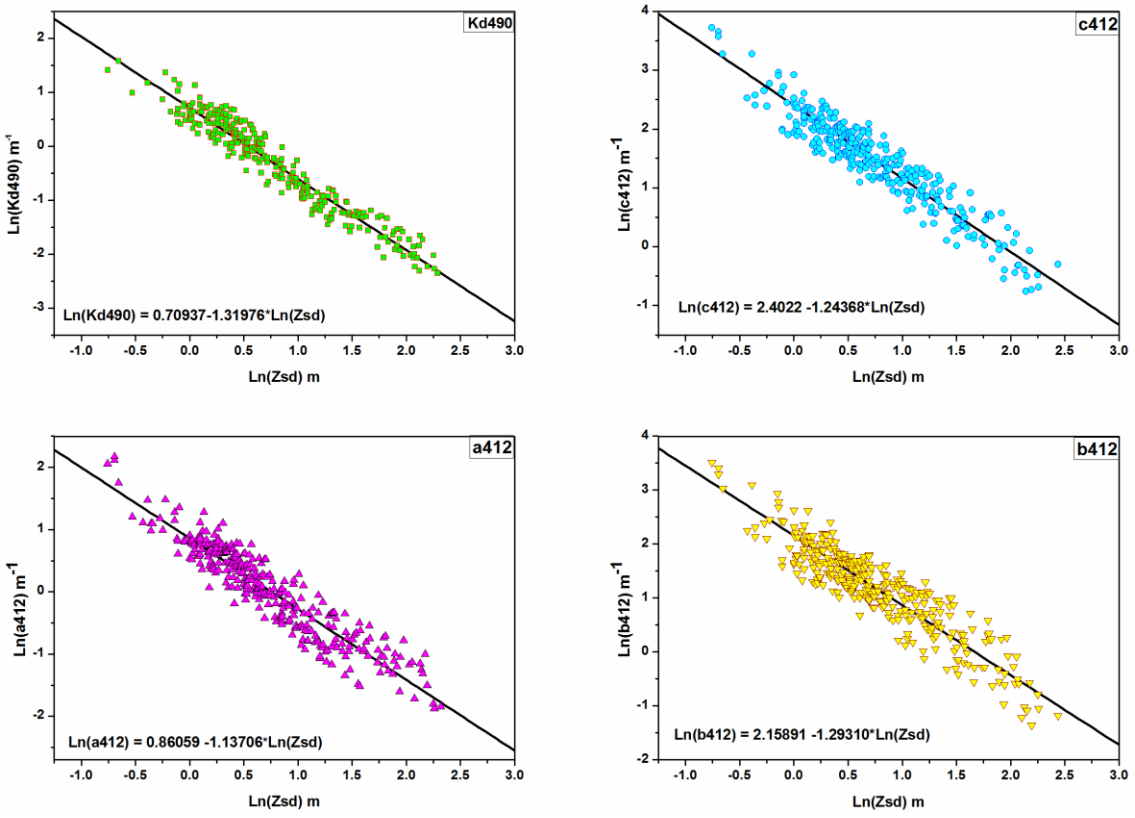

Figure 7.3 The log-log relationships of Z_{sd} with Kd490 (top left), c(412) (top right), a(412) (bottom left) and b(412) (bottom right).

The chlorophyll, which is an indicator of phytoplankton abundance and total suspended sediment (TSM) were inversely related indicating the degradation in the transparency with the increase of these constituents (Figure 7.4). Though the trends of the chlorophyll and TSM indicate a decrease in Z_{sd} with an increase of these constituents, the relationships were found to be weak. The correlation of Z_{sd} with the absorption due to combined CDOM and NAP, adg412 were better than absorption due to phytoplankton at 412 nm, aph412. (Lower Figure 7.4).

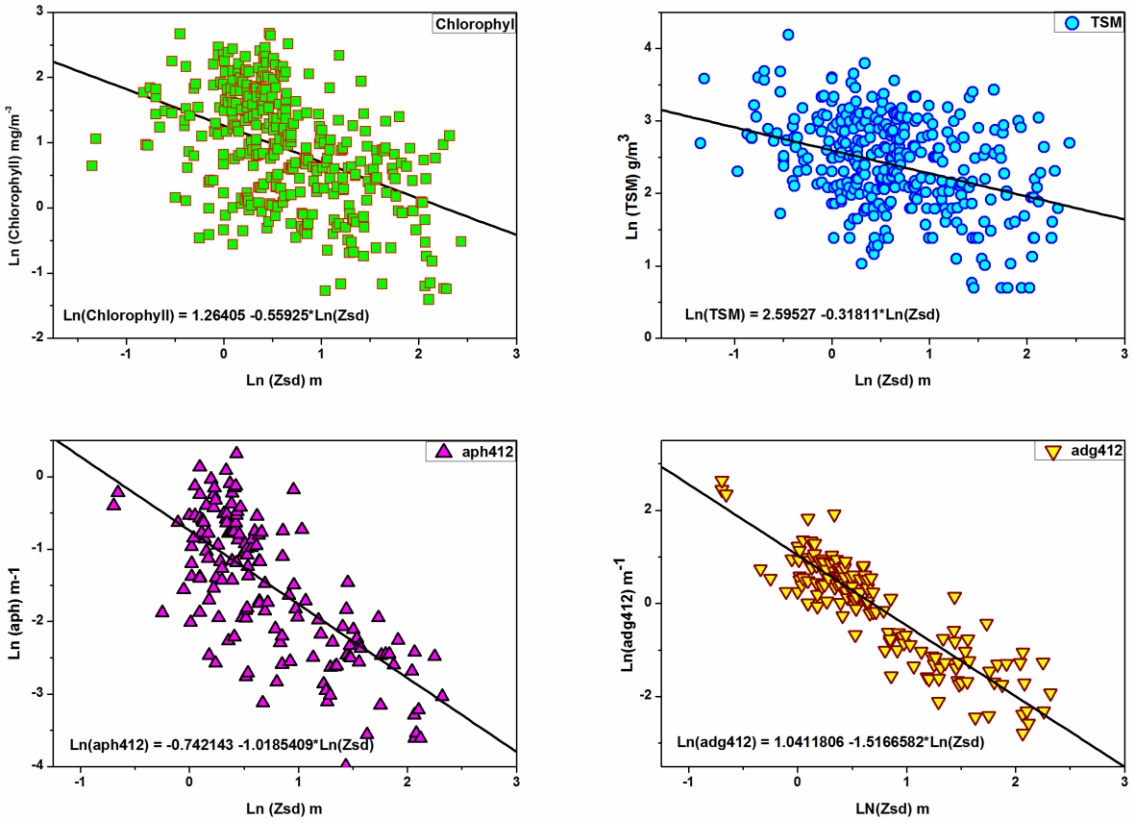

Figure 7.4 Variations of bio-optical parameters with Z_{sd} , Chlorophyll (top left), TSM(top right), $a_{ph}(412)$ (bottom left) and $a_{dg}(412)$ (bottom right).

7.3.4 Light levels at Z_{sd}

The average PAR light levels at Z_{sd} were about 22% and this was close to the light level at Z_{90}. Theoretically, the PAR light level of Z_{90} is about 37%. However, since the K_d values of these waters were high, the rate of change in light levels with depth would be rapid and hence the depth difference at 22% and 37% light levels would be relatively small. The linear relation between Z_{90} and Z_{sd} for these waters had a slope close to 1 (Figure 7.5 top left). For satellite validation the weighted average of the measured optical parameter within Z_{90} was used and hence using Z_{sd} an approximate value of Z90 and euphotic depth, Zeu could be determined (euphotic depth, Zeu ~ 4.6 times Z_{90}). The empirical relations which were used earlier was $Z_{eu} = \beta Z_{sd}$, where β varies between 1 to 10 and though the acceptable value was β = 2.4, the revised value determined from various water types was β = 3.5 (Lee et al., 2018). For the waters of Goa, it was higher, β = 4.439 (Figure 7.5 top right). A few places in the estuaries, plenty of light were available even at the bottom and the depth of the water column was shallower than Zeu. One of the notable results was the linear relation Z_{sd} had with the wavelength of maximum light penetration which would enable prediction

of approximate wavelength of light with maximum energy in the water at Z_{90} or Z_{sd} (Figure 7.5 bottom left). The inverse relation shows that if the transparency of water was high, the wavelength of light that penetrates water with maximum energy would be lower and vice versa. This simple relation could identify the optimum wavelength for underwater communication using light for any water types. Transparencies of water were better for deeper waters or higher bathymetry (Figure 7.5 bottom right).

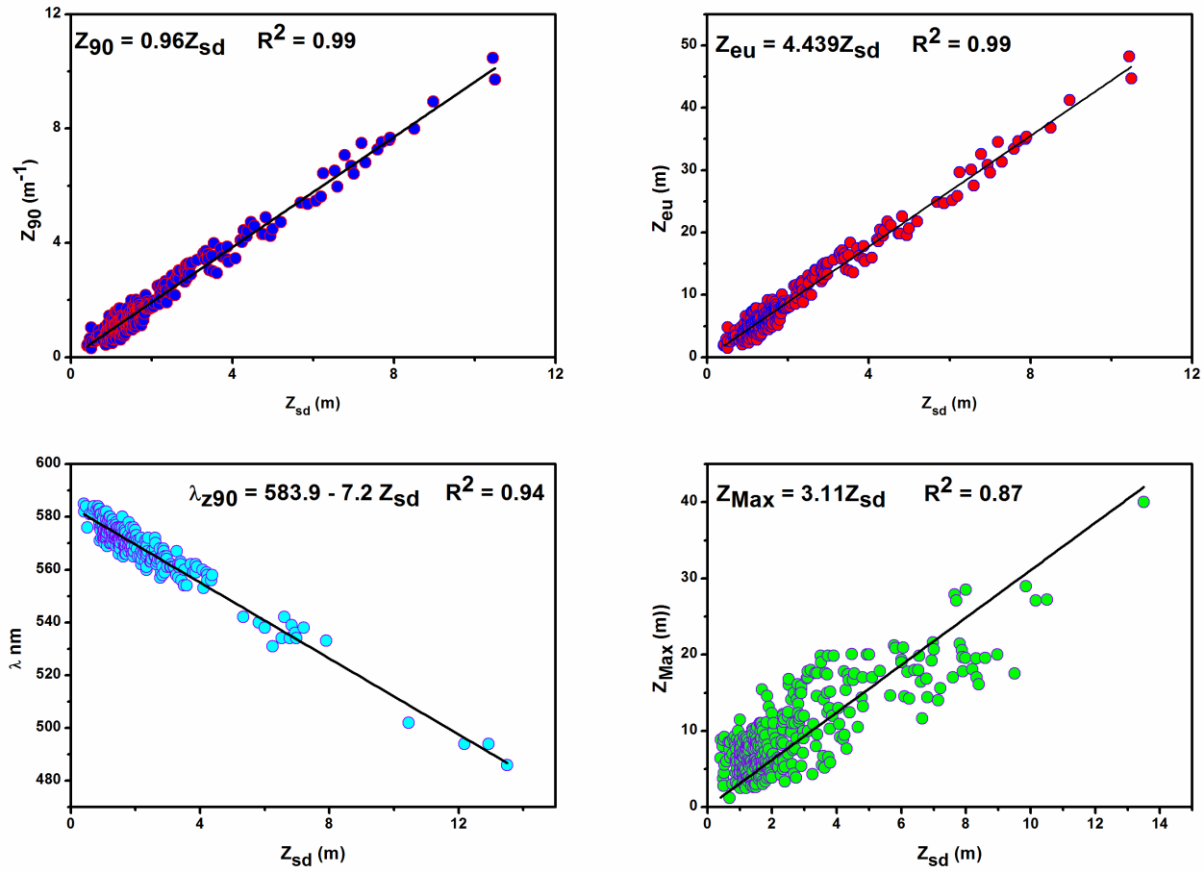

Figure 7.5 Empirical relations for Z_{90}, Z_{eu}, the wavelength of maximum light and Z_{max} with Z_{sd}.

7.3.5 Contributions of the measured optical properties

Zsd was found to be inversely proportional to c_t+K_d (see the relation given in Equation (3)) and also to $2a_t+b_t$ (as given by Equation (5)). The contributions of the optical parameters as given in the relations 3 and 5 were evaluated to examine the influence of these optical parameters. Here the fraction or the contributions to the total parameters are given as $f(c) = c_t/(c_t+K_d)$, $f(K_d) = K_d/(c_t+K_d)$, $f(2a) = 2*a_t/(2*a_t+b_t)$ and $f(b) = b_t/(2*a_t+b_t)$. Since the

contributions of spectral absorption and scattering were found to be relatively higher at lower wavelengths, the optical parameters for the studies here were considered at 412 nm.

The contribution of f(c) was found to be the highest, about 81% in the coastal waters and it was relatively lower in the estuaries to about, 75 to 78% (Table 7.2). Since c_t was the major contributor it was required to assess the contributions of the components of c_t ($c_t = a_t + b_t$). The contribution of scattering, b_t was found to be leading over all other optical properties of $a_t(412)$ and $K_d(412)$. The contribution of scattering was the highest in the coastal waters, about 63% and was also significant in the estuarine waters, 56 to 59%. Contributions of K_d were found to be the highest in the Mandovi (~ 25%). Scattering was higher in the Zuari compared to Mandovi which were also manifested by the contributions of TSM and chlorophyll which were higher in the Zuari. Earlier studies for the Arabian Sea have shown TSM and chlorophyll hold a positive correlation with the scattering coefficient (Suresh et al., 1998).

Table 7.2 Contributions of optical properties at 412 nm, in (c + Kd) and (b+2a)

Site	$c_t + K_d$				$b_t + 2a$		$a = a_{ph} + a_g + a_d$		
	f(a)	f(b)	f(c)	f(K_d)	f(b)	f(2a)	f(aph)	f(ag)	f(ad)
Coastal	0.18	0.63	0.81	0.19	0.63	0.37	0.25	0.34	0.41
Mandovi	0.19	0.56	0.75	0.25	0.60	0.40	0.17	0.20	0.63
Zuari	0.19	0.59	0.78	0.22	0.61	0.39	0.18	0.23	0.59

The contribution of various components of absorptions are given as f(ph) = a_{ph}/a_t, f(g) = a_g/a_t and f(d) = a_d/a_t. The contributions of absorptions due to phytoplankton in the coastal waters were observed to be relatively higher than in the estuaries (Figure 2.2, Chapter 2). Considering the contribution of each component to the total absorption (excluding due to water), it was observed that contribution due to NAP was the maximum. The contribution of NAP or detritus dominated in all waters and was about 60% in the estuaries and about 41% in the coastal waters. In the coastal waters, phytoplankton play an important role and the contribution f(ph) was about 25% and including the bloom data, it was about 68% (Figure 2.2, Chapter 2)

7.3.6 Optical parameters and temporal variations

Contributions of K_d in all waters were marginal compared to c_t. Contributions of K_d in the Mandovi were higher than Zuari and coastal waters. K_d values were lowest in the Zuari. The general pattern of variations of c_t+K_d in the estuaries was low during the non-monsoon

period and high during monsoon (Figure 7.6). During the monsoon period (July and August) in both the estuaries, the values of c were the highest. Since boat operations were barred by the local authorities due to bad weather conditions during the monsoon, there were no data available during the monsoon in the coastal waters, which probably would have followed a similar trend as in the estuaries. The attenuation values in the coastal waters were higher during winter (November, December, and January) and March.

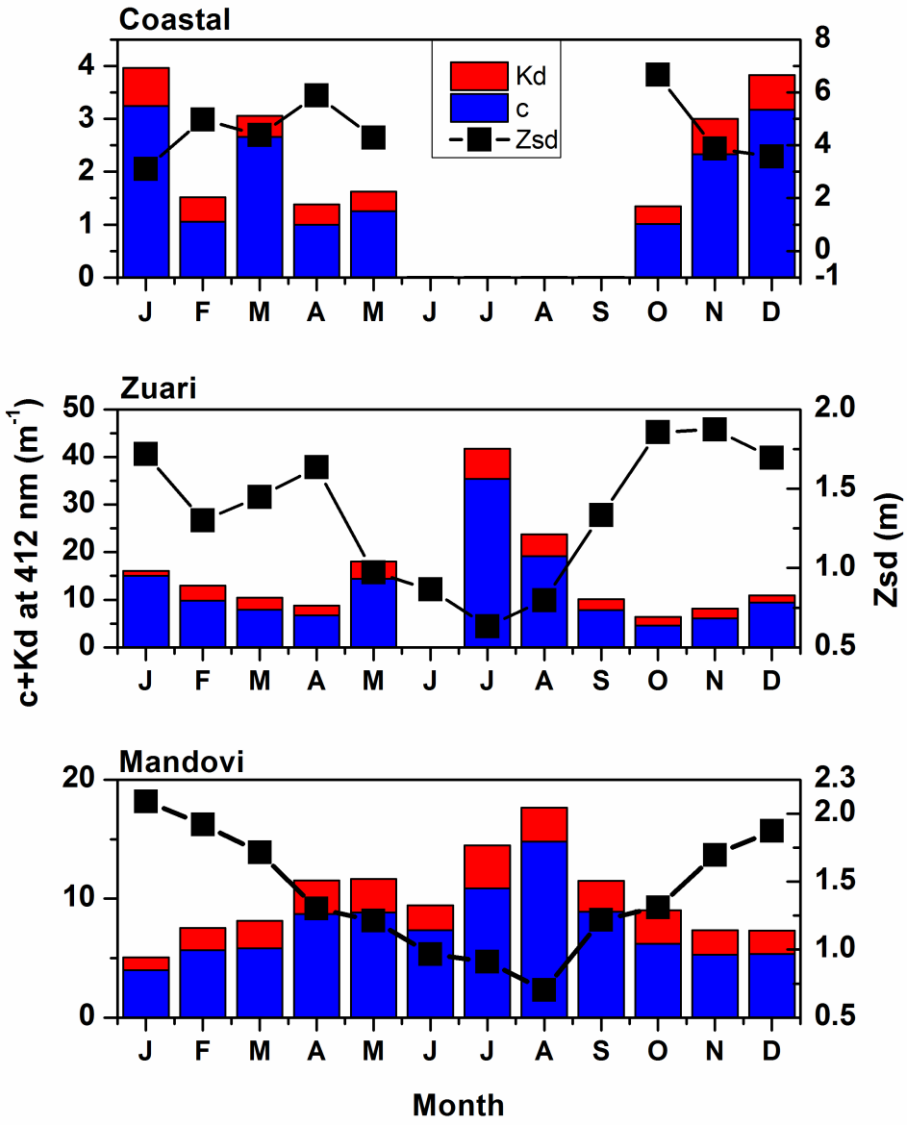

Figure 7.6 Monthly average variations of the Z_{sd} and the corresponding variations of c_t and K_d.

7.3.7 Contributions of absorption and scattering coefficient

The Z_{sd} was stated to be inversely proportioned to the $(2a_t+b_t)$ (Equation (5)) (here 2a refers to $2.0*a_t$) and the absorption a_t, and scattering b_t were found to be inversely related to Z_{sd} (Figure 7.3). The pattern of temporal variations was similar to c+ K_d, with the highest values of $2a +b_t$ observed during the monsoon period in the estuaries (Figure 7.7). The component 2a followed the trend of K_d and b had similar variations as c. In the estuaries, during the monsoon period of June-August, the contributions of 2*a(412) and scattering b(412) were higher and their combined effect was manifested in the lowest transparency of water observed. The contributions of absorptions in the Mandovi were relatively higher and the same was observed of K_d (Figure 7.6 and 7.7). K_d was modeled as a function of absorption and backscattering (Baker & Smith, 1980) and since backscattering coefficients were relatively insignificant compared to absorption, the variations of K_d and absorption were found to be similar (Figure 7.6 and Figure 7.7).

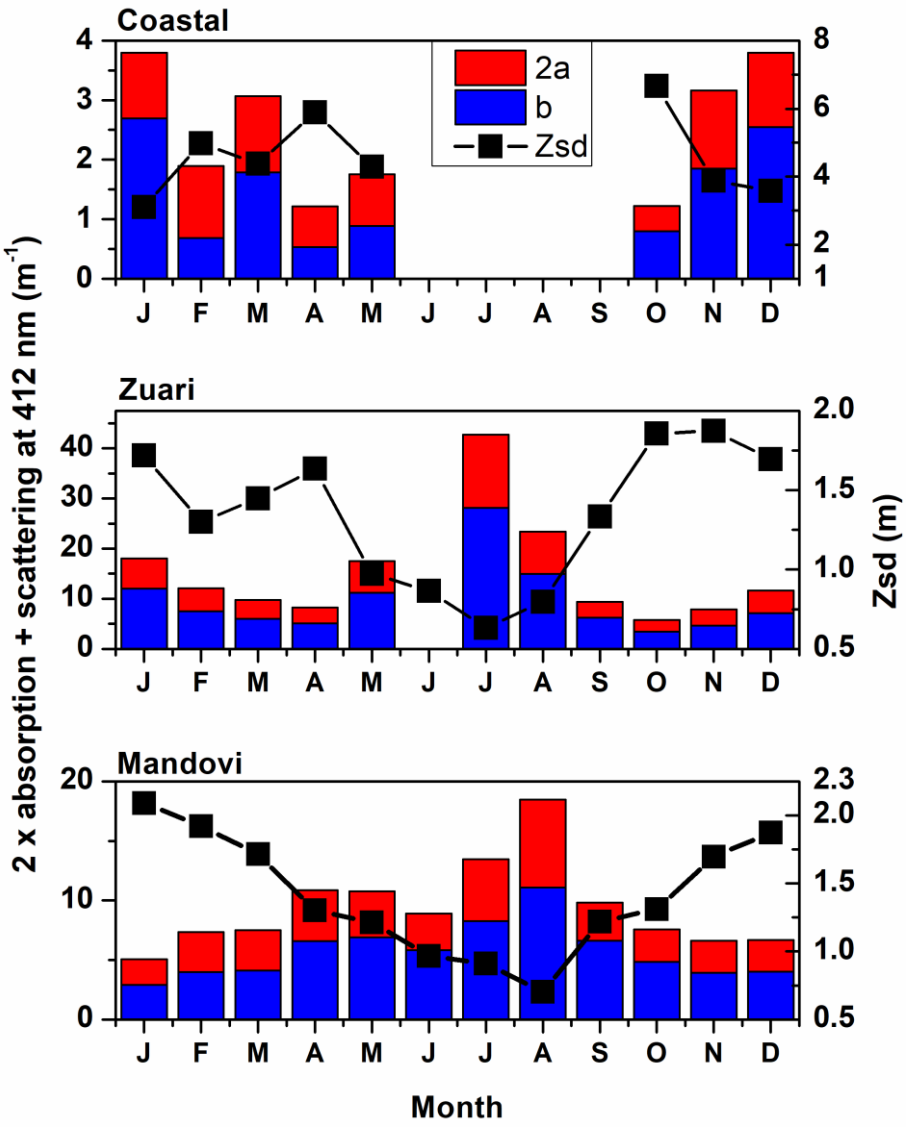

Figure 7.7 Monthly average variations of the Z_{sd} and the corresponding variations of 2*total absorption, 2*a, and scattering, b.

7.3.8 Contributions of various components of absorption coefficients

The temporal variations and contributions of the three components of absorption which are due to phytoplankton, NAP and CDOM were examined (Figure 7.8). In the coastal waters the contribution of phytoplankton, a_{ph} was highest during May and lowest during post-monsoon and March. The contributions of CDOM, f(g) were nearly the same for all the non-monsoon period. During the summer period of May, the contributions of absorptions in the coastal waters were the highest while the contribution of the NAP was the lowest, and the Z_{sd} was also lower compared to April. These results implied that the transparency of water in the coastal waters during May had the influence of phytoplankton and not NAP.

However, during January, transparencies were the lowest and the contributions of NAP were significant. During monsoon the absorption due to CDOM, a_g was high, a_d was the highest contributor and the transparencies of estuarine waters were the lowest. Contributions of NAP were significant and were found to modulate the transparencies of the estuaries.

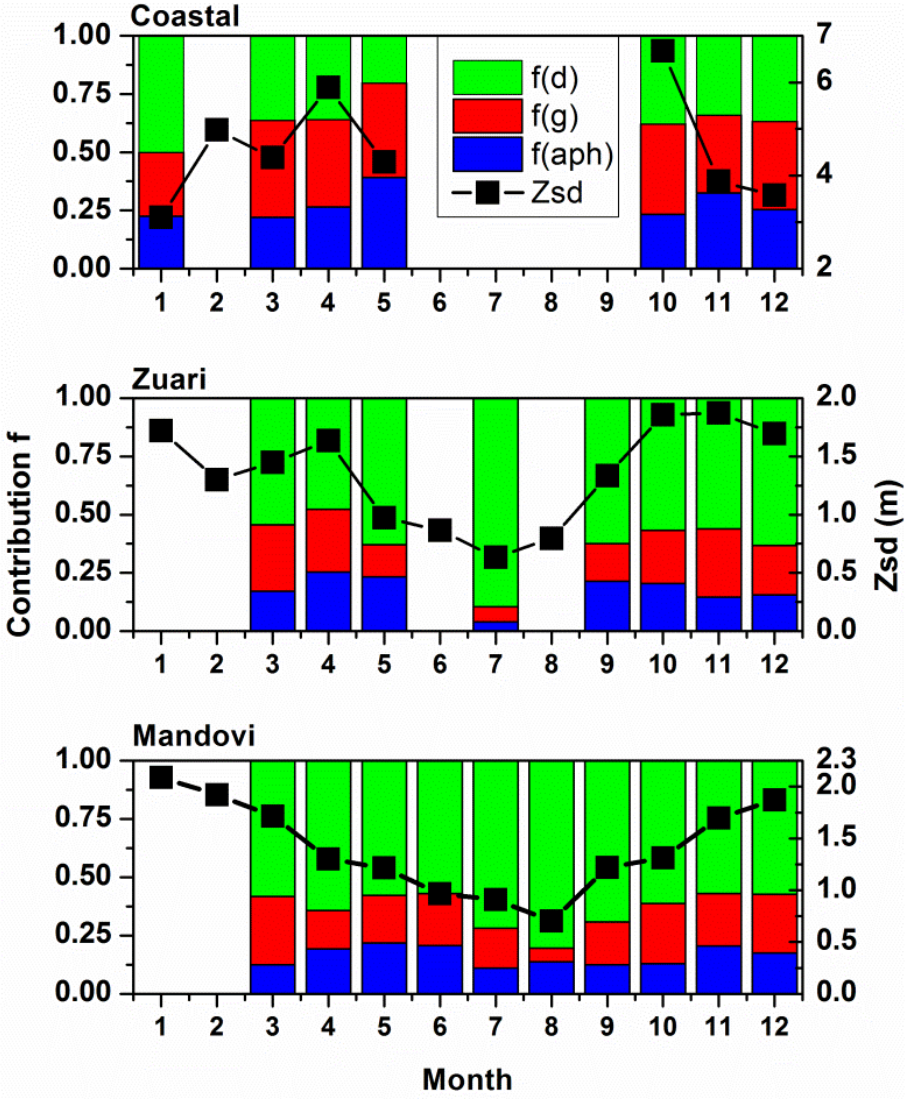

Figure 7.8 Monthly average variations of the Zsd and the corresponding variations of the contributions absorption due to phytoplankton, f(aph), CDOM, f(g) and detritus, f(d).

7.3.9 Particle size distribution (PSD)

It was observed that the transparencies of these waters of Goa were governed and controlled by the scattering of light and hence it was also required to examine the particle

size distribution (PSD) and bulk refractive index as they govern the scattering of light in water (Boss & Pegau, 2001; Buonassissi & Dierssen, 2010; Twardowski et al., 2001). PSD for the oceanic, estuarine and coastal waters was best described by a hyperbolic power-law function or "Junge type" with the power index or differential slope ξ and this slope ξ decreases with an increase in particle size. The slope ξ was usually in the range of around 2.5 to 5 and the measurements from various water types confirm it to lie between 2.7 to 4.7 (Buonassissi & Dierssen, 2010).

The slope ξ was derived from the spectral particle beam attenuation coefficient $c(\lambda)$ measured by AC-9 from the relations, $c \alpha \lambda^{-\gamma}$ and $\xi = \gamma + 3$. The average particle size measured was found to linearly relate to γ (Slade, 2015). The slope ξ deviates from the linear relation and the new relation derived was $\xi = \gamma + 3\text{-}0.5e^{-6\gamma}$ (Boss & Pegau, 2001). The bulk refractive index (relative to water) has been modeled as a function of particulate backscattering ratio $\tilde{b}_{bp}$ ($\tilde{b}_{bp}$ = (particulate backscattering,b_{bp})/(particulate scattering b_p) and ξ. Refractive index n_p can be used to identify and distinguish the particulate matter of organic or inorganic types. Refractive indexes of phytoplankton were lower and those of mineral particles were relatively higher (Twardowski et al., 2001).

Table 7.3 Mean values of PSD slope ξ, n_p, and ω_{0p}

Site	PSD slope ξ		np		ω_{0p}	
	Mean	σ	Mean	σ	Mean	σ
Coastal	4.083	0.34	1.06722	0.042	0.8368	0.14
Mandovi	4.257	0.53	1.09565	0.030	0.86799	0.02
Zuari	4.203	0.35	1.09305	0.038	0.88389	0.04

The particles in the estuaries were relatively finer (larger values of ξ) and mineral types ($n \approx 1.1$), while in the coastal waters they were more absorbing type, indicated by lower values of bulk refractive index and ω_{0p} (Table 7.3). The transparencies of these waters were inversely correlated with the PSD slope ξ and fraction of backscattering $\tilde{b}_{bp}$. However, there was no good correlation with the refractive index and transparency of water. The mean $\tilde{b}_{bp}$ values in the estuaries were 0.018 and this high value indicated an abundance of inorganic particles(Boss et al., 2001). The seasonal variations of n_p, ξ and Zsd were observed in these waters (Figure 7.9).

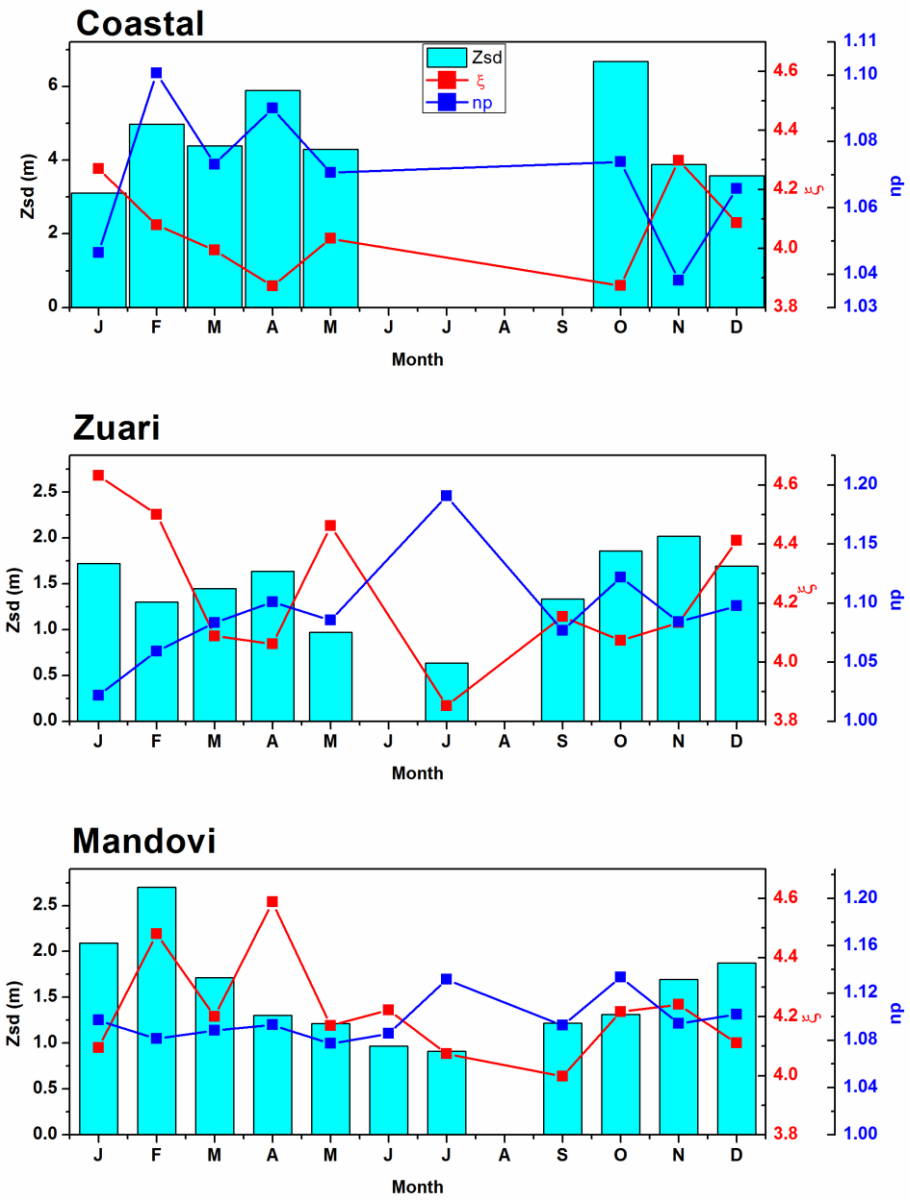

Figure 7.9 Monthly average variations of the Z_{sd} and the corresponding variations of the slope of the PSD,ξ and bulk refractive index, n_p.

7.3.10 Role of bathymetry

The bathymetry or the depth of the water column was found to influence the transparencies of coastal and estuarine waters. Transparencies of these waters correlated with maximum depths of water, Z_{max}. This linear relation was fairly good in the coastal waters, with a steady increase of the transparencies moving offshore (Figure 7.5). The constituents of water that control the optical properties such as the concentrations of particulate matter, CDOM and phytoplankton decreased moving offshore. In the estuaries too, bathymetries

were observed to affect the transparencies of water and this can be illustrated with a case in the Mandovi. In the Mandovi estuary at a region upstream there were three stations within close proximities of 2 Km between them and the maximum depths differed among them. The Z_{sd} values were 0.41, 1.05 and 1.39 m and the maximum depths at these stations were 6.4, 9.77 and 10.24 m respectively. Though these stations were in close proximity, within a distance of 2 Km from each other, the transparencies of waters differed and varied linearly with depth and c(412 also varied inversely with maximum depth (Figure 7.10). This illustrates the role of bathymetry in modulating the transparencies of water in the estuaries, with deeper depths having higher transparency than shallower waters (Figure 7.5).

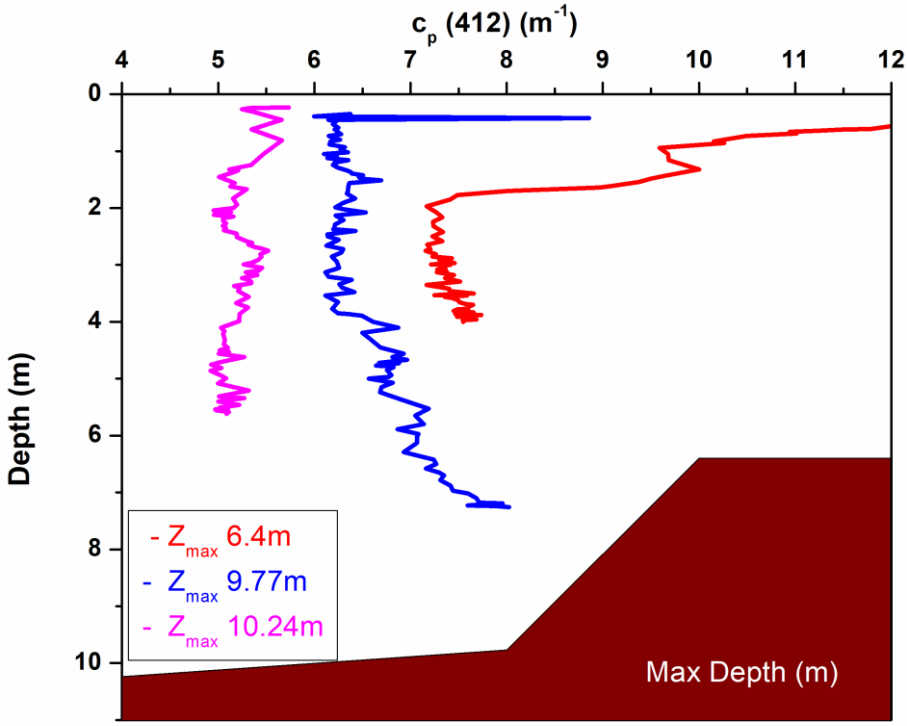

Figure 7.10 The Z_{sd} variations with bathymetry and the corresponding profiles of the total particulate beam attenuation, $c_p(412)$ (m^{-1}).

7.3.11 Role of monsoon

The monsoon plays an important role in the coastal and estuarine waters of Goa with large changes in the biogeochemical processes which, bring in profound changes in the environmental parameters. The transparencies of estuarine waters were the lowest during monsoon. The amount of rainfall in these regions also play an important role in modulating the magnitude of the transparencies of these waters and were found to proportionately decrease with an increase in the rainfall. The monthly average rainfall over Goa was found

to correlate well with the monthly average transparency of estuarine waters ($R^2 > 0.9$). The bias of 1.35 was closer to the average Z_{sd} of the estuaries. The TSM, Kd490, c412, and ad412 were found to positively correlate well with the rain ($R^2 > 0.9$) (Figure 7.11). During monsoon in the estuaries, the contribution of phytoplankton, CDOM, and NAP to the total were 13%,15%, and 72% respectively. During monsoon in the Zuari and Mandovi, transparencies increased moving upstream and the lowest was observed at the mouth. This is in agreement with the turbidity maximum observed at the mouth and the decrease in TSM moving upstream. (Fernandes, Purnachandra Rao et al., 2018; Purnachandra Rao et al., 2011).

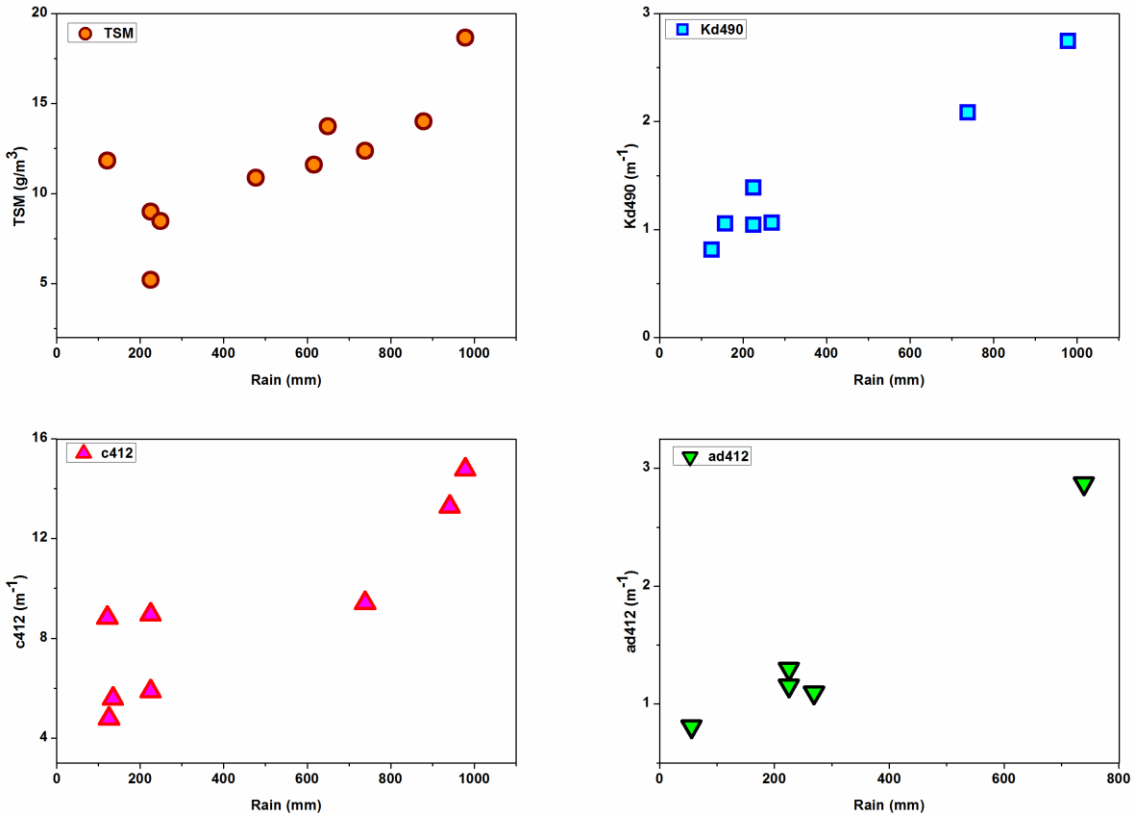

Figure 7.11 Variations of bio-optical parameters and the average monthly rainfall at Goa, TSM (top left), Kd490 (top right), c(412) (bottom left) and a_d(412) (bottom right).

7.4 Discussion

7.4.1 Optical components that influence the Z_{sd}

The theoretically derived relation shows the transparency of water to be inversely proportional to, $c_t + K_d$. The contributions of c_t in c_t+K_d have been observed to be the governing parameter in all waters, with above 75% contribution.

The scenario in the estuary was not as elementary as in the coastal and open ocean. The estuarine waters were more complex with significant contributions from more optical parameters and with relatively fewer correlations among these parameters. Scattering b, K_d, and absorption due to detritus, a_d had better correlations with Z_{sd} (higher R^2).

The contributions of K_d were relatively higher in coastal and Mandovi waters. K_d has been modeled as a function of absorption and backscattering and since absorption was relatively higher than backscattering, absorptions play a significant role in the K_d. In the coastal waters, the contributions of K_d were higher during the winter period, probably due to the contributions of phytoplankton abundance and algal blooms. The absorptions due to phytoplankton dominate in coastal waters and were the highest contributor compared to other waters. The higher contributions of K_d in the Mandovi were due to the absorptions of NAP, which were highest among these waters.

Considering individual components of the total attenuation c_t+K_d, scattering b_t is a principal contributor with about 60% of contributions in all waters. The value of scattering was the highest in the Zuari, also indicated by the suspended sediment abundance (Chapter 4) and reported by others. Scattering in the estuaries was the highest during the monsoon period as the estuaries had the large quantities of sediment and particulate matters from run-off (Shynu et al., 2015; Shynu et al., 2013).

The Z_{sd} was inversely proportional to $2a_t+b_t$ and the contribution of 2a was about 40% and this indicated that contributions of absorptions were relatively lower than scattering. Among the components of absorption, absorption due to detritus was significant and in the estuaries compared to other components it was about 60%, indicating the relevance of particulate matter in controlling the transparencies of these waters. The contribution of absorption due phytoplankton was about 25% and 18% in the coastal and estuarine waters respectively. The contribution of absorption due to phytoplankton in Zuari were also

higher than Mandovi and Zuari was more productive than Mandovi (Gauns et al., 2015; Qasim & Sen Gupta, 1981) (Chapter 4). The particulates in the coastal waters were usually more absorbing, except during February when values of n_p were relatively higher. During February, *Noctiluca* and other blooms have been reported in these coastal waters(D'Silva et al., 2012; Do Rosário Gomes et al., 2014). In the estuaries, there were more mineral particles which was manifested by larger values of n_p (> 1.1) and it was abundant during monsoon. The inverse correlation of the transparencies with the slope of PSD ξ and backscattering ratio $\tilde{b}_{bp}$ implied that transparencies reduce with smaller and mostly inorganic or mineral particles.

Since particulate matter control the transparencies of these estuaries, any contributions that will increase the particulate or total suspended matter (TSM) from natural contribution from river-runoff, mangroves, paddy fields, phytoplankton natural phenomenon or anthropogenic activities such as sand mining, iron ore spillage, ship repairs and building, dumping, will decrease the transparencies of these waters.

7.4.2 Spatial variations

There were spatial variations of Z_{sd} in both the waters which occur due to the variations in the optical properties beam attenuation coefficient, scattering coefficients, diffuse attenuation coefficients which control the Z_{sd} (Chapter 4). The coastal waters near the shore had low transparencies as the constituents in the waters were under the influence of external sources of the estuaries, coastal activities and the of this impact decreased and weakened moving away offshore, where it comes mostly under the autochthonous influence with relatively less particulate matter that increases the transparency.

Since scattering is the optical property that regulates the Z_{sd} in the estuaries, which implies that the Z_{sd} was chiefly controlled by the suspended particulate matter. The spatial variations would depend on the transport of the suspended matter in the estuaries and the availability of particulate matter from local sources. The sediment transport in the estuaries would be influenced largely by suspended sediment mode than bedload. The transport and trapping of sediments in the estuary would depend on the river discharge, gravitational circulation, tidal elevation, and tidal velocity asymmetries, mixing, wind, bathymetry, mud pools, and flocculation. (Burchard, Schuttelaars, & Ralston, 2018; McNally, Mehta, &

McNally, 2004). Various factors associated with suspended sediment and ETM of these two estuaries have been studied which include wind (Fernandes, Purnachandra Rao et al., 2018; Kessarkar et al.,2009), tidal asymmetries(Manoj, Unnikrishnan, & Sundar, 2009), salinities (Purnachandra Rao et al., 2011; Shynu et al., 2015), flocculation (Kessarkar et al., 2009), river runoff and discharges (Fernandes, Purnachandra Rao et al., 2018; Fernandes, Kessarkar et al., 2018; Purnachandra Rao et al., 2011), shape of the bay (Shynu et al., 2015) and the indisputable factor of monsoon rains (Shynu et al., 2015, 2013). The turbulence created by salinity gradients was reported to create ETMS in these estuaries and they were observed at the mouth during the wet season and upstream during the dry season (Fernandes, Purnachandra Rao et al., 2018; Fernandes, Kessarkar et al., 2018; Purnachandra Rao et al., 2011). The other factors could be natural such as tributaries, rivulets (only for Mandovi), dams, barrages, khazans, and anthropogenic activities.

Low transparencies were observed in the Mandovi estuaries at 4, 15 and 21 Km and in the Zuari at 8, 16 to 19, 22 to 25 Km. In Zuari at 4 Km, near the mouth where highest TSM were observed and the reasons attributed were due to turbulence as it was the juncture of fresh and saline water mixing and helped in the formation of ETM (Shynu et al., 2015, 2013), at 15 Km was the region of Kumbharjua canal, which interconnects Mandovi and Zuari. This region has busy traffic from fishing trawlers as there is a jetty close by at Cortalim, barges carrying ores and ferryboat which operate all through the day. CDOM was also reported to be higher here than in neighboring regions (Dias et al., 2017). The movements of barges, ferryboats and fishing boats create turbulence and resuspension of sediments (Schoellhamer, 1996). At 21 Km in Zuari, there is a ship repair yard with frequent transport of vessels and activities related to boat and ship repairs. Further ahead are regions with shallow water depths with khazan, mangrove on the banks and these shallow waters have sediment deposits at the bottom (Shynu et al., 2015, 2013).

In the Mandovi at 8 Km was the hub of activities with Panjim the capital city of Goa, a major fishing jetty at Britona, tourist boats for pleasure cruises, floating casinos, barges carrying ores and these waters are also affected by the waste discharges and outcomes of anthropogenic activities. There is also a small river, Mapusa which is a tributary of Mandovi and drains close to this site. River Mapusa is heavily polluted due to untreated waste discharges, industrial wastes, and anthropogenic activities on its banks (Pradhan, 2016). Another site of low transparency was observed at 15 Km upstream, close to the

Cumbarjua canal which has been exploited by sand miners and was a regular route of barges carrying ores. Due to these activities and being relatively shallow in-depth, there would be resuspension of material. During the field measurements, these water columns were often found to be turbid. The regions in the upstream beyond 20 Km in both the estuaries the transparencies were low as these were shallow sediment-laden water (Shynu et al., 2015, 2013).

Resuspension of particulate matters in the water plays an important role in the transparency of water. Tidal resuspension has been reported as a prime factor in maintaining high suspended particulate matter concentration in the estuaries(Allen et al., 1980; Brenon & Le Hir, 1999; Vinh, Ouillon, & Van Uu, 2018). Bathymetry in the estuaries plays an important role in the tidal current and sediment trapping (Ralston, Geyer, & Warner, 2012). Considering the general pattern of spatial variations of Z_{sd} for both estuarine and coastal waters, a linear positive relation of Z_{sd} with the depth of the water column was observed. The decrease in the transparencies of water with a decrease in the depth of water column within a short distance was observed in these estuaries and such a gradient in bathymetry help in modulating the currents and trapping of particulate matters (Ralston et al., 2012). This was probably one of the prime reasons for the changes in the transparencies of water within a small distance in the estuaries. These estuaries of Goa were the routes for the transport of ores by barges to the Marmugao port, there was fishing, and pleasure boat jetties which also operate many boats and trawlers during non-monsoon seasons. The long waves and water velocities generated by the transport of vessels like barges could resuspend the sediments in the estuaries and whose effects could be more than those induced by wind (Schoellhamer, 1996). Sand mining in these estuaries also help in resuspension of sediments.

7.4.3 Temporal variations of Coastal waters

The sediment dynamics in these estuaries were mainly controlled by two natural processes which were the river runoff during the monsoon period and tidal currents during non-monsoon periods (Shynu et al., 2015, 2013).

In the coastal waters, highest transparencies were observed during October with lowest attenuation $c+K_d$, lowest contribution of c of all season, relatively higher contribution of scattering b compared at absorption, and lowest values of PSD slope, ξ. These waters have

low oxygen during post-monsoon (Naqvi et al., 2009). High transparencies were also observed in coastal waters during the pre-monsoon or inter-monsoon period of February and April and during these periods chlorophyll was also reported to be low (Madhupratap et al., 2001). During April the *Trichodesmium* blooms are observed in these coastal waters (Desa et al., 2005a; Devassy & Goes, 1989). One of the notable features during these bloom period was the relatively higher transparencies observed for the same locations as compared during a non-bloom period. One of probable mechanism that creates low transparencies during bloom would be that the algal blooms tend to sink or settle down in the water column during some phase of the bloom and carry with it the particulate matters suspended in water and these tend to clean the water and raise the transparency of water. High attenuations during winter (November, December, and January) in the coastal water were probably attributed to high phytoplankton abundance due to the winter cooling process (Madhupratap et al., 1996).

The TSM values were found to be the highest at the mouth of the estuaries during monsoon (Shynu et al., 2015, 2013). Hence, in the coastal waters lowest transparencies should be observed probably in the monsoon season, which however could not be validated due to the lack of data. The lowest transparencies during the non-monsoon period were observed in the winter season of January, with the highest c, high scattering, b, highest a_d, very low np, and very high PSD slope, which could be due to the abundant phytoplankton and blooms. Thus, in the coastal waters, the transparencies were controlled by the optical parameters that were related to autochthonous sources during the non-monsoon period and during the monsoon period, it will have the influence of particulate matters from the estuaries. Since the f(ph) was significant in the coastal waters, phytoplankton concentrations play an important role in altering the optical properties of these waters and hence seasonally occurring blooms of *Noctiluca* during February and *Trichodesmium* during March And April and other episodic blooms will affect the transparencies of these waters (D'Silva et al., 2012).

7.4.4 Temporal variations of Estuaries

The monthly variations in the estuaries show two distinct variations with respect to monsoon. The optical parameters show very contrasting values during monsoon and non-monsoon seasons in these estuaries, which could be attributed to biological and particulate suspended matter that contribute to the absorption and scattering of light. The lowest values of Z_{sd} were observed during the peak monsoon period of June to August and the highest during the non-monsoon period of winter. The particulate load in the estuaries increase by a large factor during monsoon as compared to dry on non-monsoon periods and the highest total suspended sediment was observed in Zuari during monsoon (Fernandes et al., 2017). The Zuari River is dammed upstream and without any the tributaries, while Mandovi has few tributaries. In the Mandovi, the lowest values of Z_{sd} were observed during July-August, with the highest values of attenuation, scattering, contributions of detritus and relatively large particle sizes in water (low PSD slope ξ) and with a probable abundance of mineral particles (high refractive index). One of the major contributors of suspended sediments to the Mandovi and Zuari comes from the mining rejects along with slime, materials dumped close to the riverbanks from anthropogenic activities(Pradhan, 2016). A similar situation was observed in the Zuari.

7.4.5 Rain

These estuaries are known as monsoon estuaries as monsoon plays a vital role in the biogeochemistry and physical characteristics of these estuaries (Vijit, 2014). Suspended matter in the water column holds a linear positive relation with river discharge (Sarma et al., 2014; Suja et al., 2016). The rain was found to have a large influence on the transparencies of these waters, with transparencies being reduced drastically during monsoon. The transparency was found to negatively correlate with rain and transparencies of water in the estuaries decrease with an increase in rainfall. This was obvious as the rain was responsible for the sediment and particulate matter load in the estuaries and the peaks in suspended matter often coincided with the peak rainfall. (Purnachandra Rao et al., 2011). During the monsoon period, the total suspended matters in these estuaries were twice that during a non-monsoon period (Fernandes, Kessarkar et al., 2018).

The rainwater affects the constituents of water and hence the optical parameters such as K_d, c, particulate scattering, absorption due to detritus and the TSM were found to be

correlated positively with rain. The particulate matters could have an abundance of the organic matter indicated by the higher absorption due to NAP or detritus, a_d. There were many opencast mines in the regions around the upstream of both these estuaries, and the abundance of inorganic matter or mineral particles in waters were indicated by the higher refractive index of particles. The transparencies of the estuaries were found to decrease moving from upstream towards the mouth, with the lowest being observed at the mouth and this pattern was due to the transport of TSM.

7.4.6 Inter-annual variation and future trends

The annual variations in both the estuaries followed similar trends, indicating that the factors that influence to bring changes in the optical properties of waters were similar in both the estuaries. The inter-annual variations of transparencies of waters in the estuaries showed that transparencies of water decreased steadily from 2011 to 2015 and thereafter it increased at a steady pace. The iron exports were high from 2010 to 2011 and the impact of the same could have affected the transparency, as it was the lowest noted in both the estuaries. There was an order to ban mining in Goa from September 2012 and the following year 2013 showed an improvement in the transparency of waters of these estuaries. Another reason could be the influence of the monsoon, which is also found to be negatively correlated with the transparencies.

7.5 Conclusions

There were spatial and temporal variations of Secchi depths or transparencies of water of the estuaries and coastal waters of Goa, with Z_{sd} values were higher in the coastal waters.
The spatial variations of the Z_{sd} in the coastal waters showed a gradual increase in moving offshore from the near mouth. The waters near the mouth were under the influence of the estuaries as compared to the offshore waters, which were indicated by the optical properties of scattering. During non-monsoon seasons the transparencies of these waters were controlled by the optical properties such as scattering, absorption due to NAP, CDOM and phytoplankton which come mostly from autochthonous sources of phytoplankton. There is a large impact due to regular blooms of *Noctiluca* and *Trichodesmium* and other episodic algal blooms on the transparencies of these waters, with increasing the transparencies at times and cleansing the water column. The monsoon

seasons should have very low transparencies due to large river-runoff increasing the optical properties of attenuation, scattering, and absorption due to NAP and CDOM.

The spatial variations were also observed in the estuaries, which probably were affected during the natural processes of particulate matter transportations, local sources from tributaries and considerably as consequences of anthropogenic activities. The variations in the bathymetry affect the circulations and trappings of sediments. The optical properties that control the transparencies of water such as beam attenuation, scattering, and diffuse attenuation increased by a large factor during the monsoon season which reduced the transparencies of water. The estuarine waters were abundant with fine mineral particles.

The temporal variations in the transparencies in the costal and estuaries generally had two categories of monsoon and non-monsoon periods, with the highest values of optical parameters that control the transparencies during monsoon and relatively lower values during non-monsoon. In the coastal waters, the transparencies during the non-monsoon periods were largely influenced by the phytoplankton abundance and autochthonous sources. There were definite patterns of seasonality in the transparencies which coincided with the occurrences of seasonal blooms of *Noctiluca* and *Trichodesmium*, an abundance of phytoplankton due to winter cooling and oligotrophic and anoxic conditions during post monsoon. The temporal transparencies variations of Zuari mimicked the coastal variations.

Monsoon plays a vital role in regulating the transparencies of these waters and the amount of rainfall is inversely proportional to the transparencies.

Values of Z_{sd} and Z_{90} were nearly similar, and since they correlated well, Z_{sd} could be used to determine a rough estimate of Z_{90}.

The wavelength of maximum downwelling irradiance available at Zsd varied inversely varied with Zsd and this wavelength was low in the coastal waters (~483 nm) and high in the estuaries (~583 nm).

The transparencies of the estuarine waters have improved since 2015 which probably could be attributed to the ban in the mining. Since particulate matter governs and controls the transparencies of these estuaries, any contribution that will increase the particulate or total suspended matter (TSM) will lower the transparency of water and reduce the light availability in the water column. Controlling and curtailing contributions of particulate matter primarily from anthropogenic activities such as sand mining, waters transports such as boats, barges, pleasure cruises, iron ore spillage, industrial discharges and dumping, settlements close to the banks, ship repair activities and other similar activities will help in improving the transparencies of these waters.

CHAPTER 8. ALGORITHMS

8.1 An algorithm to determine the slope of the spectral absorption of colored dissolved organic matter (CDOM) and detritus

8.1.1 Introduction

The inherent optical property of absorption is additive, and the total absorption coefficient of water is given as the sum total of the absorption coefficients of the partitioned components, as given in Equation (1) (Mobley 1994).

$$a(\lambda) = a_w(\lambda) + a_{ph}(\lambda) + a_g(\lambda) + a_d(\lambda) \quad (1)$$

CDOM exhibits a simple pattern of spectral variation, exponentially decaying with increasing wavelength (Jerlov, 1976). It has been observed that the absorption of non-algal particles (NAP) or detritus, too, shows a similar pattern of spectral variations (Bricaud, Morel, & Prieur, 1981; Roesler, Perry, & Carder, 1989). Hence the spectral variations of the CDOM, detritus, and the combined CDOM + detritus follow the pattern of the exponential decay with an increase in wavelength and are generally given by Equation (2). Here x = g for CDOM and x = d for detritus and x = dg for CDOM + detritus.

$$a_x(\lambda) = a_x(\lambda_o)e^{-S_x(\lambda-\lambda_o)} \quad (2)$$

Where $a_x(\lambda)$ is the spectral absorption coefficient (m^{-1}), $a_x(\lambda_o)$ is the absorption coefficient (m^{-1}) at a reference wavelength, λ_o(nm), and S_x is the slope (nm^{-1}). (Hereafter units for slope S_x and a_x were avoided for clarity and brevity). The slope is found by a linear fit of the log-transformed $a_x(\lambda)$ over a spectral range. The $a_x(\lambda_o)$ is usually considered as a representative of the concentration, and the slope of CDOM provides information about its source. This slope also varies with the spectral range (Twardowski, Boss, Sullivan, & Donaghay, 2004). The reference wavelength λ_o is usually selected from the lower wavelength of UV or blue region and for remote sensing applications; it is usually 412 or 443 nm. Thus, the two variables that define the spectral absorptions of CDOM, detritus, or CDOM + detritus are their absorption at λ_o and slope S_x.

The four components model given in Equation (1) is reduced to three components with combination of $a_g(\lambda) + a_d(\lambda) = a_{dg}(\lambda)$.This alliance has been for convenience, and it helped in the developments of optical inversion algorithms with fewer parameters to derive and reduce the errors. The light properties of both CDOM and NAP differ, as NAP can scatter light while CDOM only absorbs and does not scatter. The merger of CDOM and NAP is also known as colored detrital material, CDM = CDOM + NAP (Siegel, 2002). For the open ocean and case 1 water, CDOM and NAP were reported to covary well with phytoplankton (Morel & Prieur, 1977). In the open ocean, the contribution of CDOM and detritus could be negligible, which, however, may not be the scenario in coastal and estuarine waters.

The slope of CDM, S_{dg}, was often taken as constant in most models with low values of S_{dg} for open ocean or case 1 waters and relatively higher values for other waters. The typical values of S_{dg} which were representative of the water or generic and considered for the algorithm were 0.0206 for GSM model (Garver & Siegel, 1997; Maritorena, Siegel, & Peterson, 2002), 0.015 for QAA(Lee et al., 2002), 0.0225 for MODIS semi-analytical algorithm (Carder et al., 2004), 0.014 for the semi-analytical model by Sathyendranath (Sathyendranath et al., 2001; Sathyendranath & Platt, 1998) and 0.018 for the constrained linear matrix inversion method (Hoge & Lyon, 1996). However, some models derived S_{dg} using empirical relations within the defined boundaries such as the updated QAA version 5 and 6 (http://ioccg.org/resources/software/).

It was observed that the spectral shape of the $a_{dg}(\lambda)$ and $a_t(\lambda)$, where $a_t(\lambda) = a(\lambda) - a_w(\lambda)$, had similar spectral variations for the measured data of Goa and this information of similarity in shape of spectral variations of $a_t(\lambda)$ and $a_{dg}(\lambda)$ formed the basis for the development of a simple algorithm to determine S_{dg}. The objective of this study was to derive S_{dg} exploiting a simple similarity in shape property of $a(\lambda) - a_w(\lambda)$ and $a_{dg}(\lambda)$, show its application, validate and evaluate its performance by applying this method in an available semi-analytical model and also compare with the $a_{dg}(\lambda)$ derived from the ocean color satellite data.

In the next section, the rationale and the condition for the applicability of this simple method to derive S_{dg} are established. Thereafter S_{dg} obtained with this method was compared with S_{dg} derived from a semi-analytical model, and the suitability of this new

method for remote sensing application was demonstrated, validating measured $a_{dg}(\lambda)$ with those derived from the satellite data.

8.1.2 Method

The data used were the optical data measured in the coastal and estuarine waters of Goa, India, a region on the west coast of India, the NOMAD data (Werdell & Bailey, 2005), and the satellite derived data from SeaBASS (Bailey & Werdell, 2006). The measurements were carried out in the coastal waters and both Mandovi and Zuari estuaries from March 2014 – May 2016. The total CDOM data records used were 364. The measured data for the Goa was the absorption due to CDOM, detritus, and phytoplankton measured from the water samples collected at discrete depths from various stations of the coastal waters and two estuaries, Mandovi and Zuari of Goa. These measurements were carried out with a double-beam spectrophotometer (Shimadzu, UV2600), following the standard protocol (Kahru, Diego, & Stramska, 2002; Mitchell et al., 2000, 2003). NOMAD: the NASA bio-Optical Marine Algorithm Data set Version 2.0 ALPHA, created on 18 July 2008, was the publicly available high quality in-situ bio-optical data measured from various waters over the globe and have been used often for the ocean color algorithm developments and also satellite data product validations. (http://seabass.gsfc.nasa.gov/wiki_files/NOMAD/files/nomad_seabass_v2.a_2008200.txt). All the NOMAD data were used for this study. The satellite validation data included the in-situ measured data measured from various global waters, and the satellite derived optical parameters using various algorithms from the co-located locations. The SeaBASS data available was last updated on 2016-10-05, and the data for SeaWiFS, MODIS Aqua and Terra were downloaded for this study on 31 October 2016 from http://seabass.gsfc.nasa.gov/search.

The slope was determined by the log-transformed spectral absorption in the spectral range of 400-650 nm with the linear least-square fitting model. The slopes of CDOM + detritus, S_{dg} and the slopes of the spectral $a_t(\lambda)$, S_{at} was compared for the waters of Goa and NOMAD data, and they showed close match for both the data (Figure 8.1) with R^2, slope, and intercept of the fit of 0.73, 0.82, 0.003 respectively for NOMAD data and 0.84, 0.7 and 0.004 respectively for the waters of Goa. The close match of S_{dg} with S_{at} affirmed the reasons to accept S_{at} in lieu of S_{dg}. Next, the conditions for its validity were examined.

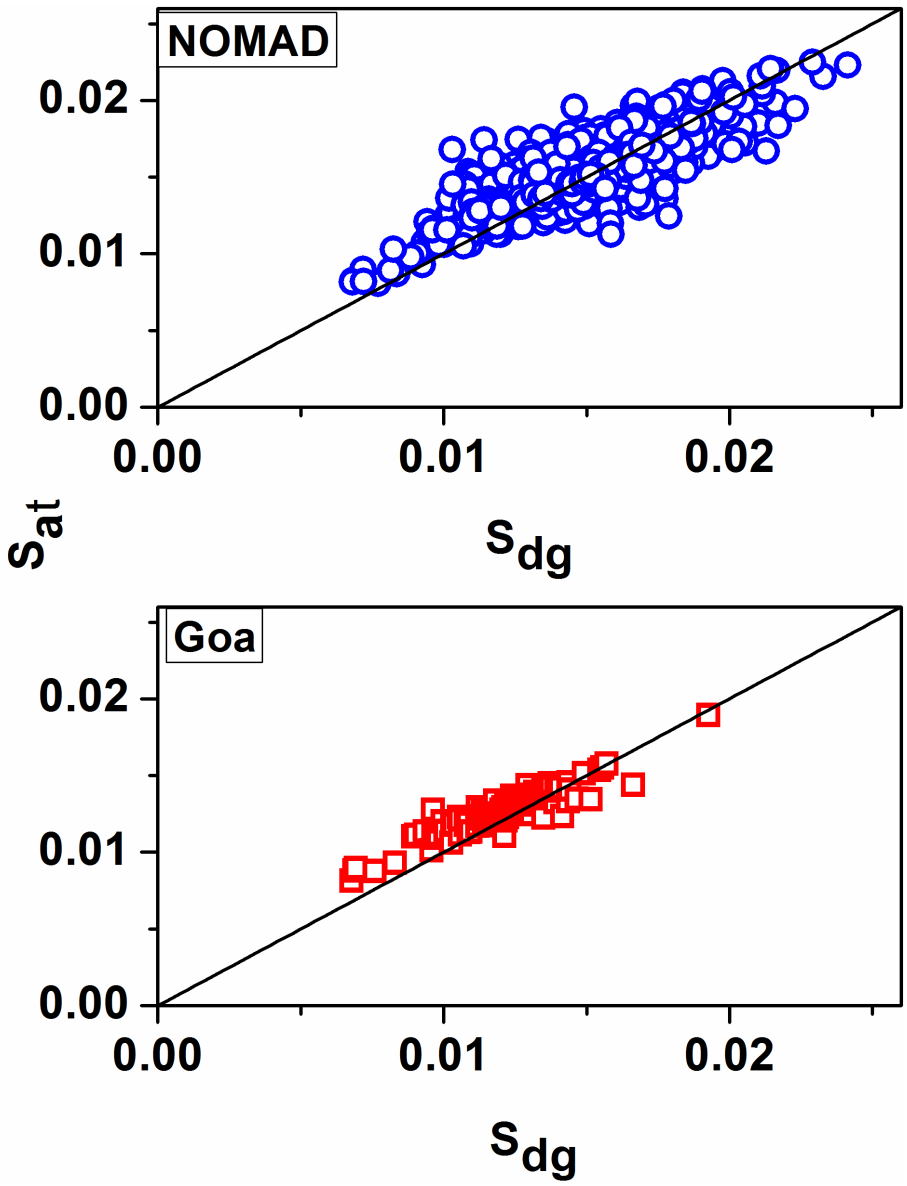

Figure 8.1 Variations of S_{at} and S_{dg} showing high correlation between them indicated by 1:1 line. The data used were from NOMAD (top) and the waters of Goa (bottom)

Since total absorption is the sum total of the absorption of each component (see Equation (1)), the $a_t(\lambda)$ will be closer to $a_{dg}(\lambda)$ if $a_{ph}(\lambda)$ was relatively low. Hence the spectral shape of $a_t(\lambda)$ will mimic $a_{dg}(\lambda)$ under situations when the absorption of CDM is relatively higher than the absorption due to phytoplankton. The errors in S_{dg} by equating S_{at} to S_{dg} will depend on how close the $a_t(\lambda)$ is to $a_{dg}(\lambda)$. Three data sets, from the coastal and estuarine waters of Goa, NOMAD, and the synthesized optical data of IOCCG (http://ioccg.org/resources/data/) were used to study these errors. In all the three data sets, the errors decreased as $a_{dg}(\lambda)/a_t(\lambda)$ ratio increased, and the errors were minimum when $a_{dg}(\lambda)/a_t(\lambda)$ approached closer to unity (Figure 8.2). Since the coastal and estuarine waters

of Goa were rich in CDM and $a_{dg}(\lambda)/a_t(\lambda)$ values were close to 1, the S_{at} compared well with the S_{dg}. NOMAD data were from various water types, and the ratio $a_{dg}(\lambda)/a_t(\lambda)$ varied from 0.1 to 0.93, and for the synthesized data of IOCCG, the ratio varied from 0.26 to 0.85. In all cases, the relative percentage errors in S_{at} the with respect to S_{dg} were mostly limited to a maximum of 40%. The relative percent error is given in Equation (6). For absorption ratio $a_{dg}(\lambda)/a_t(\lambda) > 0.6$, the errors were less than 10%, and hence the new method to use S_{at} in lieu of S_{dg} was self-evident for such data types available from the coastal and estuarine waters.

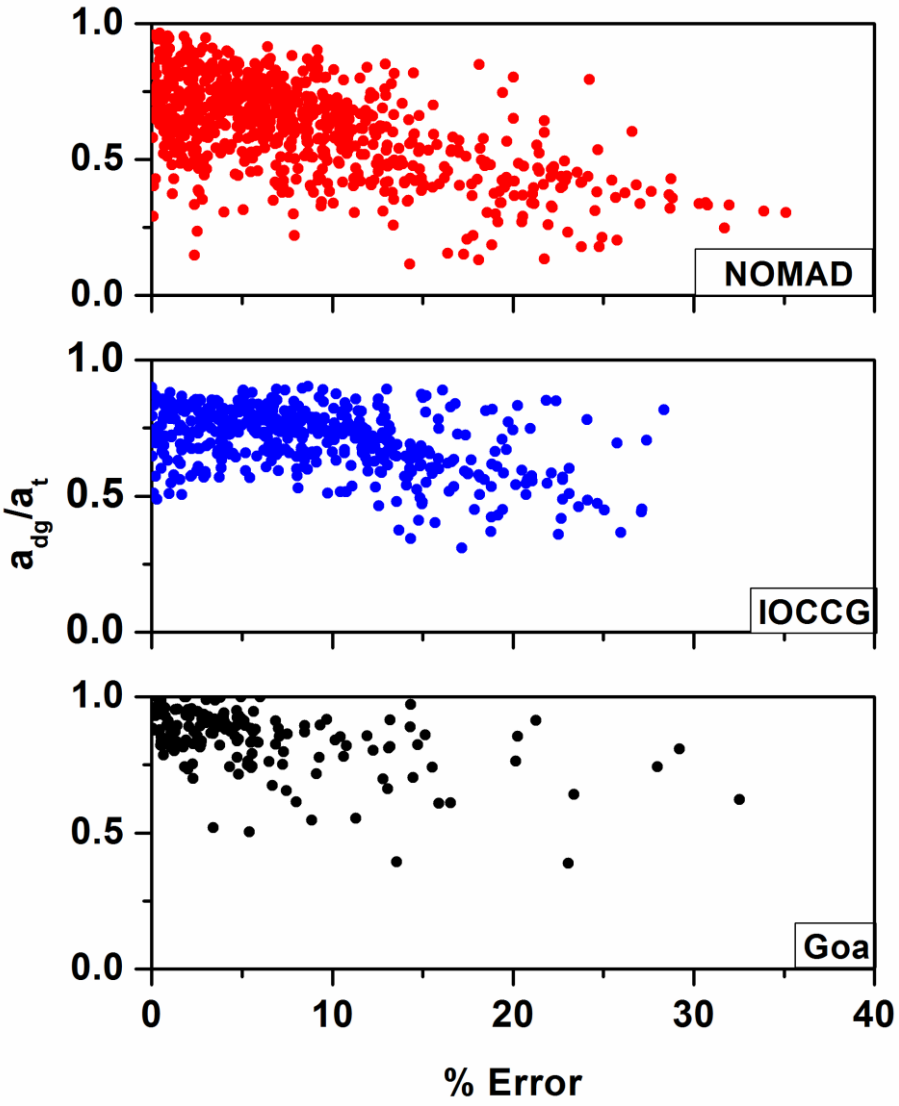

Figure 8.2 Variations of the contributions of CDM to the total absorption of water, a_{dg}/a_t at 532 nm and the % error in the slope S_{at} compared to S_{dg}

Having confirmed and verified the assumption of S_{at} and S_{dg} being comparable for most water types within an upper limit of 40% error, the S_{at} was applied in lieu of S_{dg} in a semi-

analytical algorithm to derive IOPs. The latest available version of QAA V6 updated in 2015was used to test the new method (http://www.ioccg.org/groups/Software_OCA/QAA_v6_2014209.pdf). The QAAV6 was tweaked, and the new method was used to determine S_{dg}. NOMAD data was used for testing the new method in QAAV6 and the original QAAV6. The modified flow of the QAAV6 algorithm that used this similarity property of S_{at} is given in Figure 8.3. The quasi semi-analytical algorithm QAAV6 used remote sensing reflectance $R_{rs}(\lambda)$ from NOMAD data and derived the $a_t(\lambda)$ (Step 6) as in Figure 8.3. The slope S_{at} was derived using $a_t(\lambda)$. This S_{at} was used in lieu of S_{dg} to derive $a_{dg}(\lambda)$. All other parameters and the semi-analytical and empirical methods used in QAAV6 remained the same without any change. The S_{dg} in the earlier version of QAA used a constant value of 0.015, while in later versions, S_{dg} was derived using an empirical relation based on the ratio of remote sensing reflectance at 443 and 555 nm. The $a_{dg}(\lambda)$ was derived using QAAV6 and compared with the modified method using S_{at}.

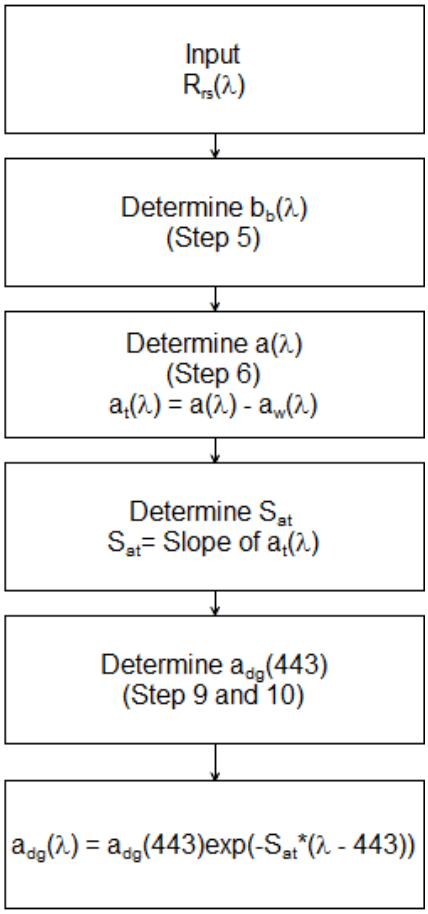

Figure 8.3 Determining the spectral $a_{dg}(\lambda)$ as in QAAV6, using the slope S_{at} inlieu of S_{dg}

This method was also applied to the satellite data. The SeaBASS data used for the validations of satellites were used for this study. The in-situ measured data and co-located satellite derived products a-giop and adg-giop derived using an inversion model were downloaded for the satellites, SeaWiFS, MODIS Terra and MODIS Aqua from the SeaBASS site. The method, as given in Figure 8.3, was adopted, with $a_t(\lambda)$ obtained from a-giop(λ) of each satellite data, and then the slope S_{at} of $a_t(\lambda)$ was determined. The $a_{dg}(\lambda o)$ was the $a_{dg}(\lambda)$ at the lowest band of the adg-giop(λ), which was 412 nm. The in-situ measured $a_{dg}(\lambda)$ of the respective satellite data were then compared with the satellite derived adg-giop(λ).

8.1.3 Results

The error analyses were carried out with statistical parameters such as bias, RMSE (root mean square error), the coefficient of determination R^2, the regression between the model

and the measured. a_{dg_Model} refers to $a_{dg}(\lambda)$ derived using the model, and $a_{dg\_Measured}$ refers to $a_{dg}(\lambda)$ measured from the waters samples.

$$Bias = \frac{1}{n}\sum_{1}^{n}(a_{dg\_Model} - a_{dg\_Measured}) \quad (3)$$

$$RMSE = \sqrt{\frac{1}{n-2}\sum_{1}^{n}(a_{dg\_Model} - a_{dg\_Measured})^2} \quad (4)$$

$$a_{dg\_Measured} = m(a_{dg\_Model}) + c \quad (5)$$

$$Error = 100\frac{S_{at} - S_{dg}}{S_{dg}} \quad (6)$$

8.1.3.1 NOMAD data

The S_{dg} derived using the NOMAD data varied from 0.0023 to 0.024. The S_{at} using $a_t(\lambda)$ derived from QAAV6 compared well than S_{dg} obtained from the empirical relation in QAA V6 (Figure 8.4). The S_{dg} derived using empirical method varied within a narrow range 0.01 to 0.017, maintaining almost a constant value over a wide range of S_{dg} from NOMAD data, while S_{at} maintained a wider variability of 0.0014 to 0.03 and correlated better with S_{dg} calculated with NOMAD $a_{dg}(\lambda)$. For S_{dg} values less than zero obtained using QAAV6, the lower limit was set to 0.01.

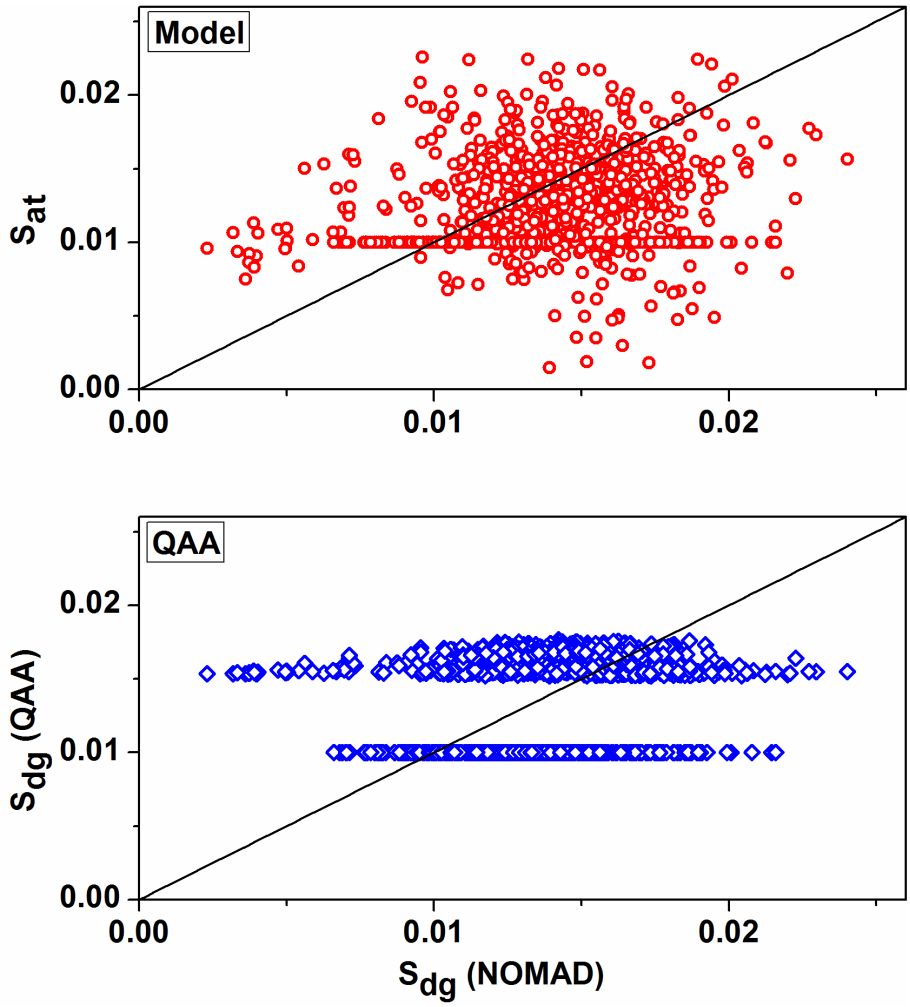

Figure 8.4 Comparisons of S_{at} using $a_t(\lambda)$ and S_{dg} derived using empirical relations in QAAV6 with S_{dg} of the measured NOMAD data

The tweaked QAAV6 with the new method performed relatively better with higher R^2 (> 0.95) at all wavelengths, lower RMSE, and regression slope close to 1 and very low intercept as compared to QAAV6 (Figure 8.5).

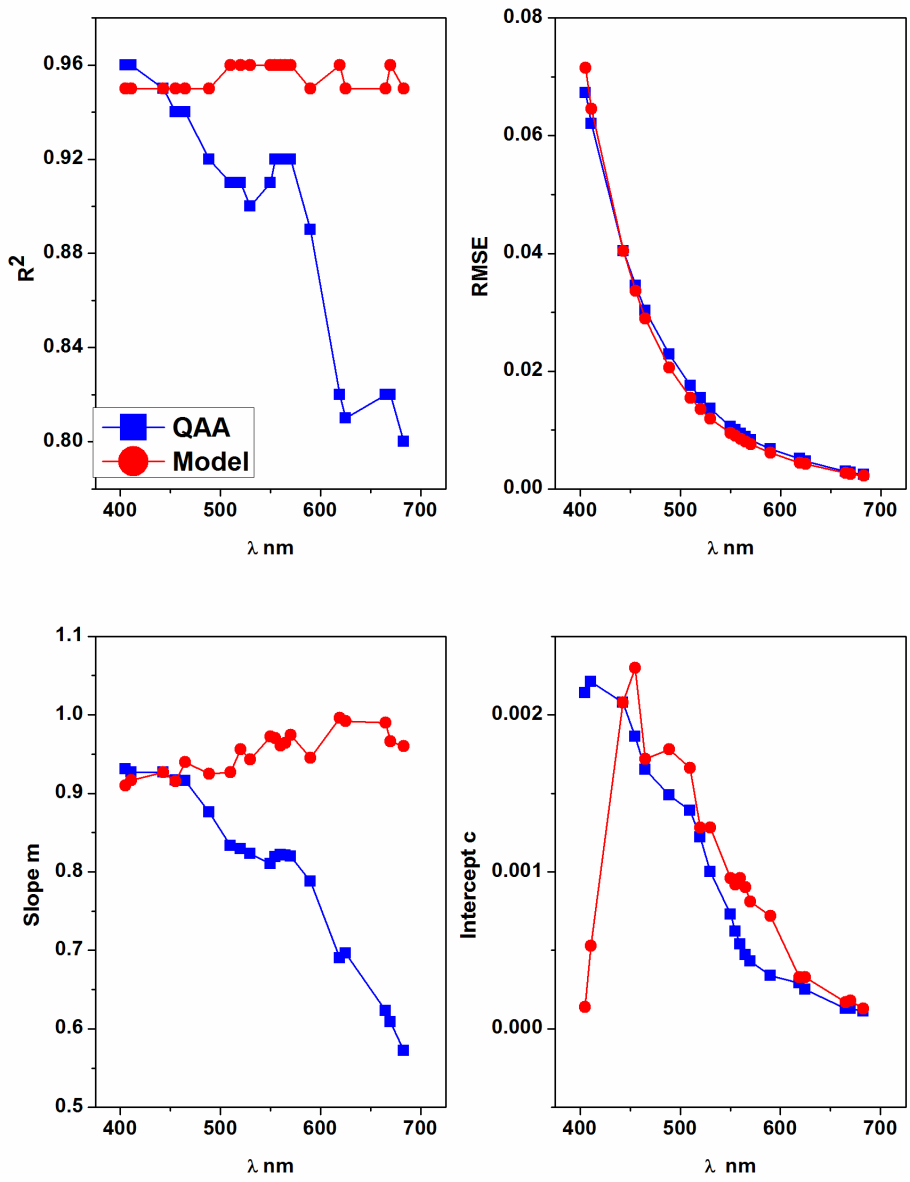

Figure 8.5 Error statistics to indicate the performance of the QAAV6 with S_{at} (Model) and the original QAAV6 (QAA) indicated by the R^2 (top left), RMSE (top right), slope m (bottom left) and the intercept c (bottom right).

8.1.3.2 Satellite data

The satellite validation data from the SeaBASS site had the measured data and the satellite-derived products of the co-located locations. The satellite products of absorptions of waters with its components, which included total, CDM, and phytoplankton absorptions, were derived using the GIOP algorithm. The $a_{dg}(\lambda)$ derived using the method described here compared better than those derived using the inversion model from the satellite data of SeaWiFS, MODIS Terra and MODIS Aqua with better scores of error statistics for all bands, such as higher R^2, lower RMSE (Figure 8.6). Here all the data were used for

comparisons without discarding any outliers. There were enhanced improvements observed using the new method by discarding few outliers, as compared to the same satellite derived $a_{dg}(\lambda)$. The RMSE at 443 was 0.163, 0.119, 0.16 for SeaWiFS, MODIS Terra, and MODIS Aqua, respectively.

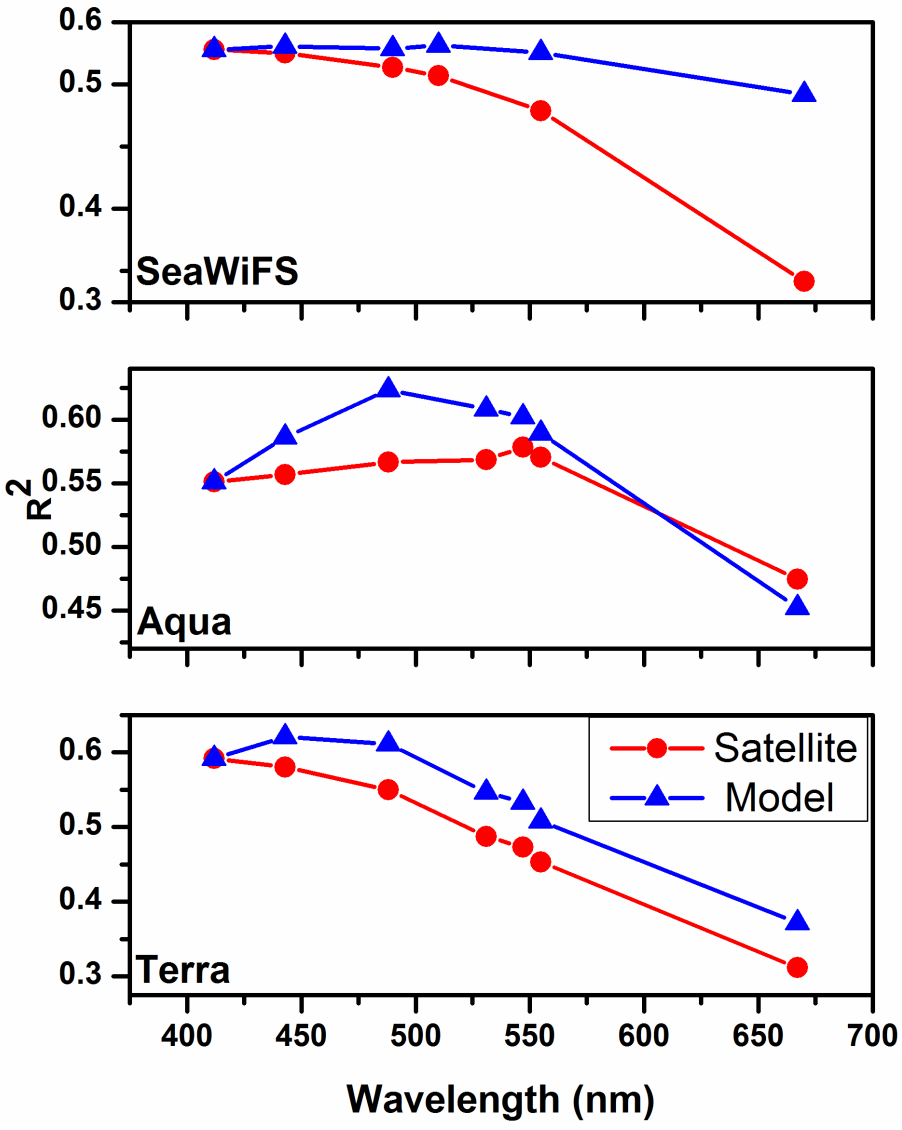

Figure 8.6 The coefficient of determination R^2 for the comparison of the $a_{dg}(\lambda)$ with the measured, new method (indicated as Model) and those derived from using the original inversion method in satellite data processing (Satellite)

8.1.4 Discussion

The new method to use S_{at} in lieu of S_{dg} was found as a good option for waters with high CDOM and detritus. When the contributions of CDM to the total absorption (excluding absorption by water) were above 60%, the errors were limited only to 10%. These errors

too decreased as the contribution of both CDOM and detritus increased (Figure 8.2). Though this method was better suited for waters rich in CDOM and detritus as compared to phytoplankton, considering CDOM from various water types and with the contributions of CDM varying from a lower limit of 25%, the maximum errors observed between S_{at} and S_{dg} were less than 40%.

The $a_{dg}(\lambda)$ derived showed better performance after implementing the new method in the semi-analytical model, QAAV6, than deriving $a_{dg}(\lambda)$ from the original QAAV6 method. The new method, when applied to the IOPs from the satellite data of Terra, Aqua, and SeaWiFS, could derive spectral $a_{dg}(\lambda)$ with better accuracy. The performance of the same IOP inversion algorithms to derive $a_{dg}(\lambda)$ from satellite data has been observed to vary with satellite sensors (Naik, D'Sa, Goés, & Gomes, 2009) and similarly here too the performance of MODIS was better than that of SeaWiFS.

This method to determine the slope, S_{dg} could be easily implemented in any model, as it was very generic, simple, did not involve any mathematical model, and avoid empirical methods. Since the method is also independent of any specific bands, it can be used for most ocean color satellite data.

Since the spectral model given by Equation (2) requires only two parameters, the slope S_{dg} and $a_{dg}(\lambda_o)$, the model accuracy to derive $a_{dg}(\lambda_o)$ will depend on two parameters, $a_t(\lambda)$ the total spectral absorption and the $a_{dg}(\lambda_o)$, the CDM at a reference wavelength. The accuracy of $a_t(\lambda)$ is not important; rather, its spectral variation does matter, as the slope must match the slope of the spectral variations of $a_{dg}(\lambda)$. There should be sufficient values of $a_t(\lambda)$ at wavelengths spaced apart from blue towards red, which will allow modeling the $a_t(\lambda)$ with better accuracy as given in Equation (2). However, apart from the slope of $a_t(\lambda)$, the $a_{dg}(\lambda)$ can only be determined with better accuracy if $a_{dg}(\lambda_o)$ is available with minimum error.

Though the $a_{dg}(\lambda)$ can be determined with, better accuracy, there is no assurance of having any improvements in the accuracy of the $a_{ph}(\lambda)$. This will solely depend on the method used to derive $a_{ph}(\lambda)$. If it is obtained as a remnant of the $a_{dg}(\lambda)$ from $a_t(\lambda)$ i.e. $a_{ph}(\lambda) = a_t(\lambda) - a_{dg}(\lambda)$, the accuracy of $a_{ph}(\lambda)$ will depend on both, $a_t(\lambda)$ and $a_{dg}(\lambda)$. Hence with a method to derive $a_t(\lambda)$ with better accuracy over the spectral range from blue to red such (Thayapurath, Talaulikar, Desa, & Lotlikar, 2016) or others and a good empirical

algorithm to derive CDM at a reference $a_{dg}(\lambda_o)$, $a_{ph}(\lambda)$ could be obtained with much improved accuracy by applying this method.

8.1.5 Conclusions

The new method to use S_{at} in lieu of S_{dg} was found as a good option for waters with high CDOM and detritus absorption compared to phytoplankton. The relative errors in S_{at} compared with S_{dg} decreased as the contribution of both CDOM and detritus increased. When the contributions of CDM to the total absorption (excluding absorption by water) were above 60%, the errors between S_{at} and S_{dg} were limited only to 10 %. Though this method was suited for waters rich in CDOM and detritus as compared to phytoplankton, even with the contributions of CDM varying from a lower limit of 25%, the maximum errors observed between S_{at} and S_{dg} were less than 40%. The simple method to derive the slope of $a_{dg}(\lambda)$, using the similarity in the shapes of spectral variations of $a_t(\lambda)$ and $a_{dg}(\lambda)$ was found to be a better option than assuming a constant value of S_{dg}, or using empirical relation to derive S_{dg}. S_{dg} cannot be taken as a constant as it varies with water types and the sources of CDOM.

This was a simple method to derive S_{dg} that could be used with most available IOP models as it is generic in nature, independent of the bands, does not use any mathematical model or empirical relations. The $a_{dg}(\lambda)$ derived using this new method performed better when compared to the empirical relation used in the semi-analytical algorithm. The accuracy of the $a_{dg}(\lambda)$ derived from the satellite data of SeaWiFS, MODIS Aqua, and Terra improved when this method was applied to the IOPs derived from the satellite data.

8.2 A Simple Algorithm To Determine Absorption of Colored Dissolved Organic Matter And Detritus

8.2.1 Introduction

The inherent optical property of absorption is additive, and the total absorption coefficient of water is given as the sum total of the absorption coefficients of the partitioned components, as given in (7) (Mobley, 1994). Here $a_t(\lambda) = a(\lambda) - a_w(\lambda)$.

$$a_t(\lambda) = a_w(\lambda) + a_{ph}(\lambda) + a_d(\lambda) + a_g(\lambda) \quad (7)$$

Where, the subscripts w, ph, d, and g represent pure water, phytoplankton, non-algal particles (NAP), and colored dissolved organic matter (CDOM), respectively. The spectral absorption due to CDOM and NAP, have similar absorption spectra and the combined absorption due to CDOM and NAP are often called as colored detrital matter (CDM = CDOM + NAP). Thus the four component model given in (Equation (7)) is reduced to three with combination of $a_g(\lambda) + a_d(\lambda) = a_{dg}(\lambda)$. This alliance has been for convenience, and it helped in the development of optical inversion algorithms with fewer parameters to derive, and reduce errors.

Generally, it has been observed that the absorption of non-algal particles (NAP) or detritus show a similar pattern of spectral variations of the exponential decay with an increase in wavelength given by (Equation (8)) (Roesler et al., 1989). Here x=g for CDOM and x=d for detritus and x= dg for CDOM + detritus.

$$a_x(\lambda) = a_x(\lambda_0)\exp[-S_x(\lambda - \lambda_0)] \quad (8)$$

To describe spectral $a_{dg}(\lambda)$, two parameters are required;$a_{dg}(\lambda_0)$ and the slope S_{dg}. A simple algorithm to derive S_{dg} for such waters has been developed, which is a better solution than opting for a constant value or obtaining S_{dg} using empirical methods (Thayapurath Suresh, Dias, Desa, & Sahay, 2018).

Although the contribution of CDOM to the CDM at 440 nm was reported to be about 82% (Siegel, 2002), it may vary by a large factor for open ocean, coastal and estuarine waters. For the waters of Goa, the contribution of CDOM to CDM, a_g/a_{dg} for the coastal waters was 46% while it was about 19% for the Mandovi estuary and 26% for the Zuari estuary. Though the contribution of detritus or NAP was marginally higher for coastal waters, it was significantly higher for the estuaries - typically 75% making them the dominant contributors in such waters. The fractions of CDOM to CDM vary spectrally and will be relatively lower at 440 nm than at 412 nm. In the estuaries, the contribution of the absorption at 412 nm due to detritus (a_d) to the total absorption (without water) (a_t) i.e.a_d/a_t was about 60% and about 20% for the CDOM. Since there are large influences of the estuaries that drain into the coastal waters, as is the case of the waters of Goa, these estuarine and coastal waters cannot be identified and handled in isolation while developing algorithms to derive optical parameters. Hence an algorithm that caters to both these waters to derive $a_{dg}(\lambda_0)$ has been developed, which can also be used to derive this parameter from ocean color satellite data. Having determined $a_{dg}(\lambda_0)$, and S_{dg} using empirical methods (Thayapurath Suresh, Dias, Desa, & Sahay, 2018), $a_{dg}(\lambda)$ can be determined and with $a_t(\lambda)$ (Thayapurath, Talaulikar, Desa, & Lotliker, 2016), it would help to determine absorption due to phytoplankton $a_{ph}(\lambda)$.

CDM has a definite role in the ocean-climate studies with regards to photochemistry, photobiology, and productivity (Nelson & Siegel, 2013). CDOM mixing is usually of non-conservative type for these waters, and monsoon plays an important role (Dias et al., 2017). All studies related to CDOM in estuaries and coastal waters and their importance will also apply to CDM such as dissolved organic carbon (DOC) (Mannino, Russ, & Hooker, 2008) and assessing terrestrial carbon transportation to coastal water (Nelson, Siegel, Carlson, & Swan, 2010). The accuracy of satellite derived chlorophyll decreases with an increase in CDM as the assumption that chlorophyll covaries with detritus may not hold for the coastal and estuarine waters (Qin et al., 2007; Siegel, 2005)**.**

There were two types of algorithms developed earlier based on the ease of obtaining $a_{dg}(\lambda_0)$ from simple empirical using the band ratio of Rrs (Carder et al., 1999; IOCCG, 2006) and inversion optical semi-analytical model such as QAA (Lee et al., 2002) such as and rigorous mathematical models (Hoge & Lyon, 1996; IOCCG, 2006). The simple empirical method gave just $a_{dg}(\lambda_0)$ directly (Carder et al., 1999), while others provided it as

a byproduct of other optical parameters. For most algorithms, λ_0 was chosen at 440 or 443 nm. QAA was chosen for comparison with the new algorithms discussed here, as it was found to be better in comparison to most algorithms for high CDOM waters (Mannino et al., 2014). The empirical algorithm by Carder (Carder et al., 1999) was better suited to open ocean with low values of optical parameters (Qin et al., 2007).

Empirical algorithms were found to be better than semi-analytical algorithms for retrieving parameters from the satellite data (Mannino et al., 2014). The empirical methods used here use diffuse attenuation at 490 nm, $K_d(490)$ as input as it was found to be the right choice. K_d in the lower wavelengths has been found to hold good relations with CDOM (Mannino et al., 2014) and has been used to model CDM (Siegel, 2005). This quasi-absorption AOP $K_d(490)$ can be derived from satellite data with good accuracy (Thayapurath & Talaulikar, 2011)**.**

8.2.2 Methodology

8.2.2.1 Data

The data included the measured optical data from the coastal and estuarine waters of Goa, India, a region on the west coast of India; the NOMAD data; and the satellite data for the waters of Goa. The optical properties were measured from the coastal waters and the two estuaries of Goa, namely Mandovi and Zuari, during the period 2014-2016 with a total of 140 samples.

The data set used was NOMAD (NASA bio-Optical Marine Algorithm Data set Version 2.0 ALPHA), which was created on 18 July 2008. It is a publicly available high quality in-situ bio-optical dataset measured from various waters over the globe and has been used often for the ocean color algorithm developments as well as satellite data product validations
http://seabass.gsfc.nasa.gov/wiki_files/NOMAD/files/nomad_seabass_v2.a_2008200.tx.
The satellite Level-1b, LAC data of the satellite sensors OCM-2 and MODIS Aqua over the waters of Goa were processed using the free software available from NASA for processing ocean color satellite data, SeaDAS version 7.4 with all default values, atmospheric corrections, and algorithms available in the package (http:\\seadas.gsfc.nasa.gov).

The satellite derived parameter $K_d(490)$ and $a_{dg}(\lambda)$ were the averages of these parameters derived from the satellite Level-2 data from a window of 3x3 pixel matrix around the location of the field measurement station. $K_d(490)$ was the standard product available from OCM-2 and MODIS Level-2 data. The a_{dg} for OCM-2 was at 415 nm band, and for MODIS, it was at 412 nm band. The $a_{dg}(\lambda)$ from OCM-2 and MODIS data were derived using the default version of the QAA algorithm available with SeaDAS.

The diffuse attenuation $K_d(490)$ and $K_d(405)$ are referred here as Kd490 and Kd405, respectively. The absorption due to CDM a_{dg} at 412 nm and 415 nm are designated as adg412 and adg415, respectively. The CDOM, CDM, and a_{dg} mentioned here are synonymous with the spectral absorptions of these components. The measured a_{dg} and Kd490 data used for the satellite validation for the waters of Goa were the weighted depth averaged values within the first optical depth, Z_{90}.

8.2.2.2 Development of the algorithm

The algorithms were developed to derive $a_{dg}(\lambda_0)$ at two reference wavelengths: 412 and 415 nm. Two forms of algorithms were developed, which were designated as Algλ_0_1 and Algλ_0_2, where λ_0 values were 412 and 415 nm. Algorithms were based on just the single optical parameter, Kd490. Both algorithms Algλ_0_1 and Algλ_0_2 were developed using NOMAD data. The parameters used for the developments of algorithms, a_{dg}, and K_d, covered a wide range of values, ensuring the applicability of these empirical relations to various water types. The reasons for developing algorithms at the two wavelengths 412 nm and 415 nm were to cater to the satellite data from two sensors MODIS and OCM-2, which had bands at 412 and 415 nm, respectively. Apart from these, it was thought prudent to avoid deriving a_{dg} at 440 nm, as this was a region of peak absorption due to phytoplankton. Additionally, the empirical relations to derive a_{dg} were observed to have better performance at lower wavelengths.

The empirical relationships were simple linear regression types of the natural logarithm of transformed data (Equation (9)). The coefficients for the empirical relations are given in Table 8.1.

$$Ln(Y) = P_0 + P_1 Ln(X) \tag{9}$$

The algorithm Algλ_0_1is implemented in two steps :

1. Determine Kd405 using Kd490
2. Determine adg(λ_0) using the relation with Kd405.

The diffuse attenuation at 405 nm, Kd405 was found to hold a better relationship with $a_{dg}(\lambda_0)$ where λ_0 is 412 or 415 nm. K_d at any wavelength can be determined with a simple linear model using Kd490(Austin & Petzold, 1981). Here Kd405 is determined using Kd490 (Figure 8.7).

Table 8.1 Coefficients of the algorithms

Parameter	**Alg412_1**	**Alg412_1**	**Alg412_2**	**Alg415_1**	**Alg415_2**
X(m^{-1})	Kd490	Kd405	Kd490	Kd405	Kd490
Y($m^{-}1$)	Kd405	adg412	adg412	adg415	adg415
P_0	0.651776	-0.60760	0.048257	-0.64242	0.015586
P_1	1.10497	0.971351	1.07575	0.971160	1.07975
n	513	420	452	422	451
R^2	0.99	0.98	0.95	0.97	0.95
Minimm X (m^{-1})	0.0087	0.00589	0.017	0.00589	0.01697
Maximm X (m^{-1})	2.6592	5.23611	2.6592	5.23611	2.6592
Minimm Y(m^{-1})	0.0113	0.00243	0.0093	0.00235	0.0089
Maximm Y(m^{-1})	5.2361	2.7517	2.7517	2.6528	2.6528

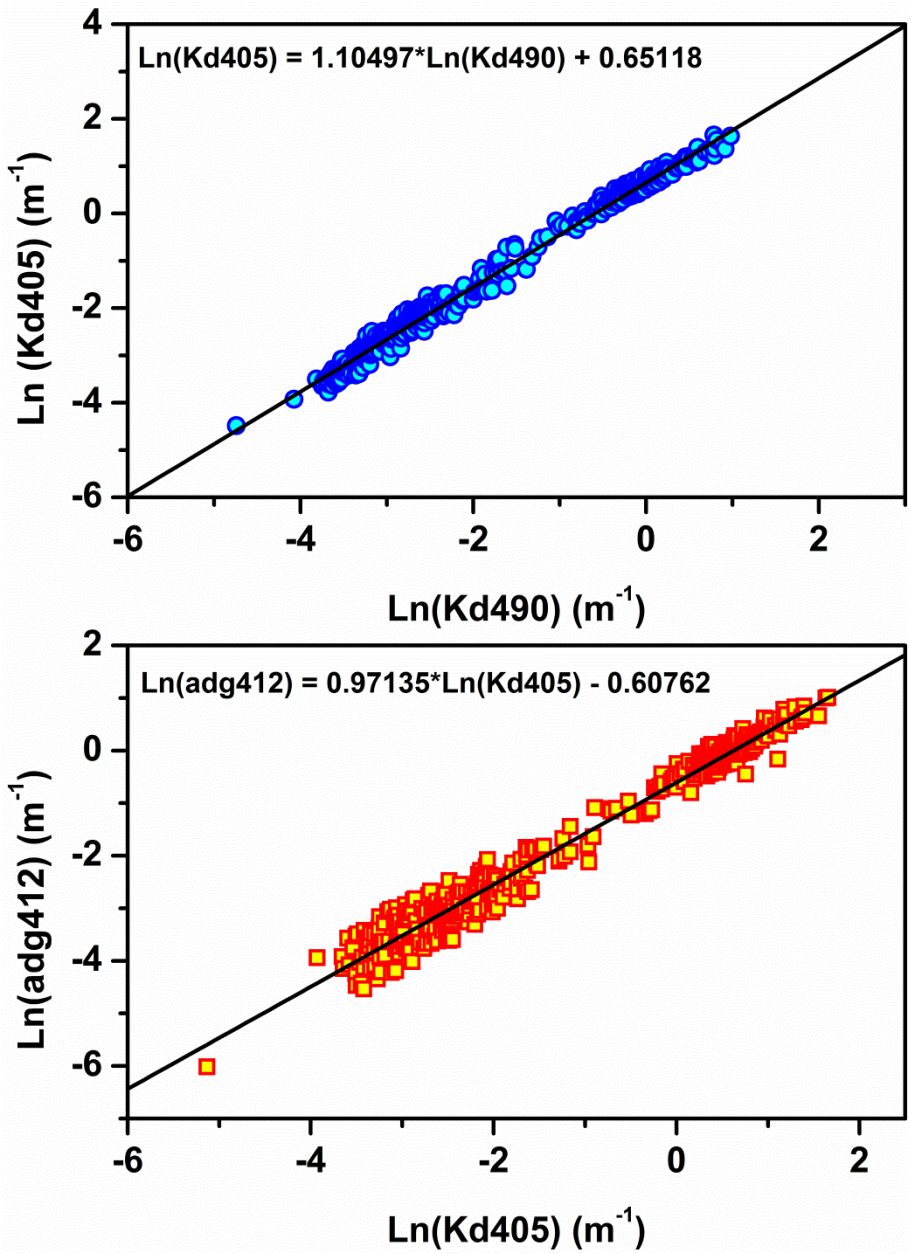

Figure 8.7 Empirical relations of Alg412_1 to derive Kd405 using Kd490 (top) and adg412 using Kd405 (bottom) with the NOMAD data

Algorithm Algλ_0_2 is a simple empirical relation to derive adg at 412 and 415 nm using Kd490 as given by (9) (Figure 8.8). The coefficients for the two algorithms and other statistics are given in Table 8.1.

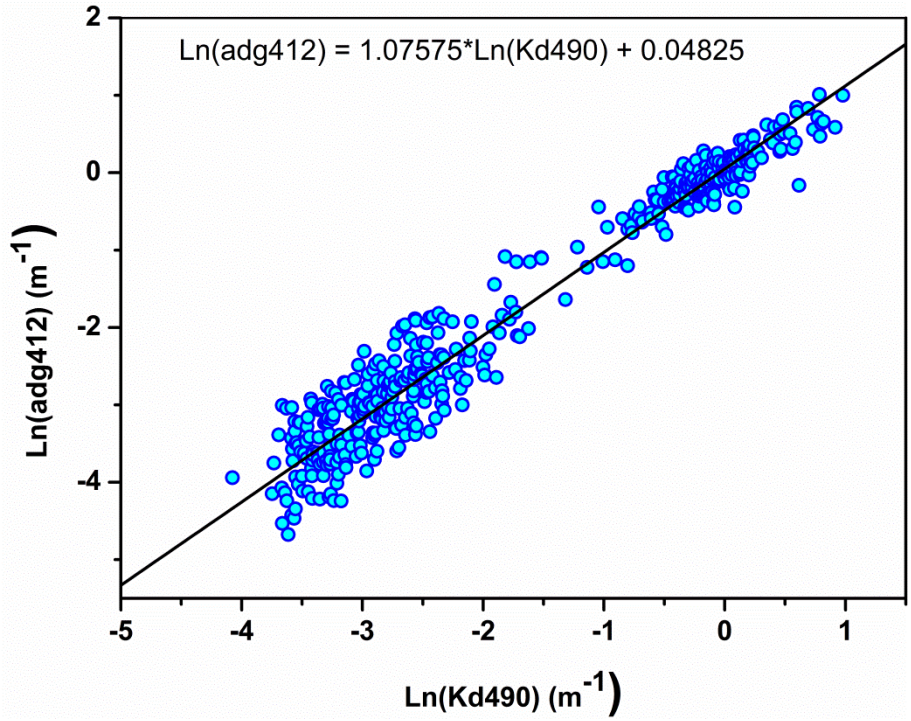

Figure 8.8 Empirical relation of Alg412_2 to derive adg412 with Kd490 using NOMAD data

8.2.3 Validation of the algorithms

Data included nonzero values of optical parameters and K490 values greater than $K_w(490)$, the pure water component of K_d, where $K_w(490) = 0.0166$. Algorithms that did not provide either adg412 or adg415, such as Carder et al. (Carder et al., 1999), IOCCG (IOCCG, 2006) were not considered for validation and comparisons with the present new algorithms using the measured optical data from Goa. The QAA algorithm available with the satellite-processing package was used to derive adg415 from the satellite data, while the updated QAA version 6 was used to derive adg412 using the measured data of Goa (Lee, 2014).

The algorithms Alg412_1, Alg412_2, Alg415_1, and Alg415_2 were validated with measured optical data of the coastal and estuarine waters of Goa (given here as GOA) satellite data from MODIS and OCM-2 and the measured optical data of Goa. The performances of the new algorithms were also compared with QAA QAAV6 using measured optical data of Goa and a_{dg} derived from satellite OCM-2 using the QAA algorithm available with SeaDAS for the waters of Goa.

8.2.4 Results

The error analysis was carried out with statistical parameters such as RMSE (root mean square error), the coefficient of determination R^2, and regression between the total absorption-derived from the model and the measured data. The regression between measured and model provides a slope, m, and intercept, c (Thayapurath et al., 2018).

8.2.4.1 Alg1_λ_0 and Alg2_λ_0 with Goa data

The validation of the algorithms Alg1_λ_0 and Alg2_λ_0 provided a close match with the measured a_{dg} (Figure 8.9). Among all the validation exercises, the results of these provided the highest R^2, lowest RMSE, and regression slope close to 1(Table 8.2). Though the algorithms were developed with a_{dg} limited to an upper limit of 2.76 m^{-1}, the relation was found to hold good for measured a_{dg} beyond this maximum value. The algorithm results did not show any bias over the complete range of values, as indicated by the value of regression slope close to 1 and very low intercept (Figure 8.9 and Table 8.2). The two-step algorithm Alg1_λ_0 was found to be relatively better than the simple Alg2_λ_0, and hence Alg1_λ_0 was chosen for all other validations and used for the inter-comparisons of algorithms.

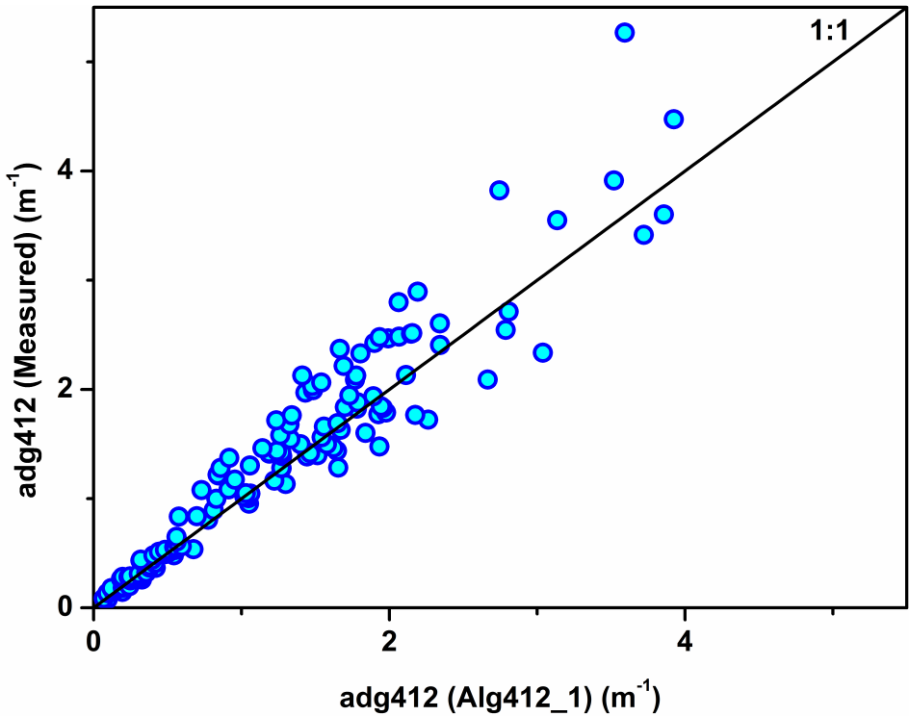

Figure 8.9 Validation of the algorithm Alg412_1 with the optical data measured from the waters of Goa.

Table 8.2 Error statistics of the validations of the algorithms using the measured data of Goa.

Id	Alg412_1	Alg412_2	Alg415_1	Alg415_2	QAAV6 (adg412)
n	133	135	135	135	137
R^2	0.91	0.91	0.91	0.91	0.85
RMSE	0.086	0.086	0.089	0.086	0.175
c	-6E-005	-0.00438	0.00145	-0.00248	0.18755
m	1.07508	1.08504	1.07656	1.07929	0.65674
Minimum adg (m^{-1})	0.07806	0.07806	0.07239	0.07239	0.07806
Maximum adg(m^{-1})	5.26837	5.26837	5.09868	5.09868	5.26837

8.2.4.2 QAA V6 with Goa data

The latest available and improved QAA algorithm, QAA version 6, was used for the validation of adg412 with the measured optical parameters for the waters of Goa. adg412 derived from QAAV6 was found to match well below 2 m^{-1}, and it showed an overestimation of adg412 for values above 2 m^{-1} (Figure 8.10). The overestimation could also be inferred from the low value of the slope, 0.66.

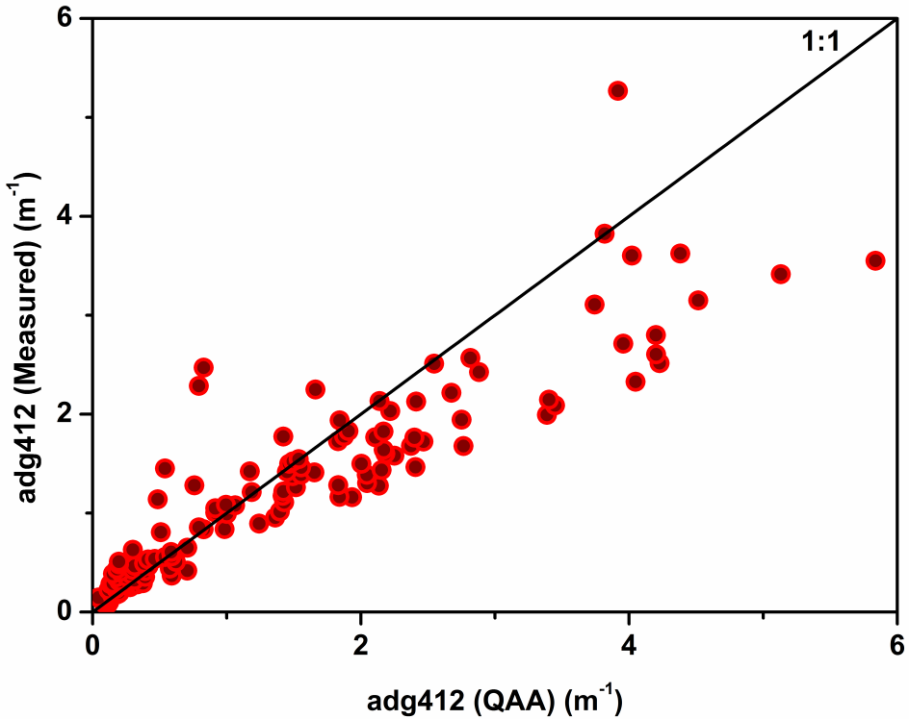

Figure 8.10 $a_{dg}412$ derived with the algorithm QAA V6 with the measured optical data of Goa

8.2.4.3 Satellite data OCM-2 at 415 nm

The performance of Alg415_1 was again found to be consistent with high R^2 (Table 8.3). Earlier studies also concluded that the QAA based algorithm did not perform as well for the parameters retrieved from satellite data (Mannino et al., 2014). As observed with the validation using measured data, QAA grossly underestimated the values of a_{dg}. The performance of Alg415_1 was relatively better than QAA. The performance of QAA to derive CDM was reported to be better for measured data than from satellite data, as is the case observed here too (Mannino et al., 2014).

Table 8.3 Error statistics of the validations of the algorithms using the measured data of the waters of Goa and the OCM-2 satellite data.

Id	Alg415_1	Alg415_2	QAA (adg415)
n	20	20	17
R^2	0.84	0.84	0.36
RMSE	0.410	0.410	0.667
c	0.08569	0.08708	-0.006
m	0.95162	0.92212	5.3
Minimum adg (m^{-1})	0.0864	0.0864	0.0864
Maximum adg(m^{-1})	2.51154	2.51154	2.51154

8.2.4.4 Satellite data MODIS at 412nm

Data available for the validation of adg412 with MODIS Aqua and measured data were limited due to the availability of matchup satellite data values (total 4 values). Most of the measured values were masked as bad values by the SeaDAS software and the reasons attributed were due to the coastal and estuarine waters being close to the land, improper atmospheric corrections, and negative values of the adg412 derived from the algorithms implemented in the SeaDAS. Another valid reason for MODIS to have fewer matchup points as compared to OCM-2 was the better spatial resolution of 360 meters for OCM-2 as compared to 1.1 Km for MODIS. The adg412 retrieved from MODIS data using Alg412_1 and QAA algorithms were underestimated. Alg412_1 was better (R^2=0.94 and RMSE = 0.224) than QAA (R^2=0.83 and RMSE = 0.81). However, the data was sparse and the range of adg412 being limited to low values, these results may not provide conclusive evidence for the accuracy of CDM or the performance of the algorithms using MODIS data.

8.2.5 Conclusion

New empirical methods using the vertical attenuation coefficient of the downwelling irradiance, Kd490 nm have been developed to assess the colored dissolved organic matter and detritus for coastal and estuarine waters. The algorithms which derive the absorption of CDM at two wavelengths viz. 412 and 415 nm would also help to derive CDM from satellite data of MODIS and OCM-2.

The algorithms have been developed with a large data set, and a wide range of optical parameters with the absorption of CDM and diffuse attenuation at 490 nm will cater to most water types.

The performances of the new algorithms have been confirmed to be better than others by applying them to coastal and estuarine waters and validation with the ocean color satellite data from MODIS and OCM-2.

8.3 An algorithm to determine the spectral total absorption coefficient of coastal waters

8.3.1 Introduction

Inherent optical properties (IOPs) form the basis of the radiative transfer equation and helps in understanding the underwater light field. A review of inverse algorithms to derive IOPs from AOPs suggests that providing solutions to derive total absorption with minimal errors is a challenging task (Gordon, 2002). Deriving IOPs with better accuracy from satellite data could greatly help in various studies related to marine optics, climate change, and biogeochemical processes (Brewin et al., 2015; IOCCG, 2006).

There are two types of algorithms to determine the total absorption of water, one that totals up the contributions from various components and the other that determines the total absorption directly, without partitioning the contributions of the components in water. Most of the available semi-analytical and empirical algorithms derive the absorption by summing these partitioned constituents. There are various algorithms available that use both the approaches (Brewin et al., 2015; IOCCG, 2006). Most of such algorithms lose on performance due to their weakness in parameterizing the partitioned components.

This algorithm is based on an explicit method that relates the IOP, total absorption to AOPs, and was derived rigorously from the radiative transfer model, often designated as Gershun's equation (Gershun, 1939). This is an updated and refined method to the earlier reported algorithm (Suresh et al., 2016). The present algorithm described here SAGE490 (Spectral Absorption using Gershun's Equation) determines the spectral total absorption of water using the AOPs, remote sensing reflectance and diffuse attenuation at 490 and thus can be derived from the ocean color satellite data and data from in-situ measurements using a radiometer.

8.3.2 Methodology

8.3.2.1 Data

The optical measurements for IOP and AOPs were carried out in the coastal waters and in both Mandovi and Zuari estuaries. NOMAD data was only used for the validation of the algorithm.

Radiative transfer model Hydrolight version 5.1 was used to derive those optical parameters which were required for the development of the algorithms, and that could not be measured. The variations of optical parameters derived from Hydrolight, which were used for the developments of the algorithms, $K_E(z, \lambda)$ and $\mu(\lambda)$ are given in Figure 8.11.

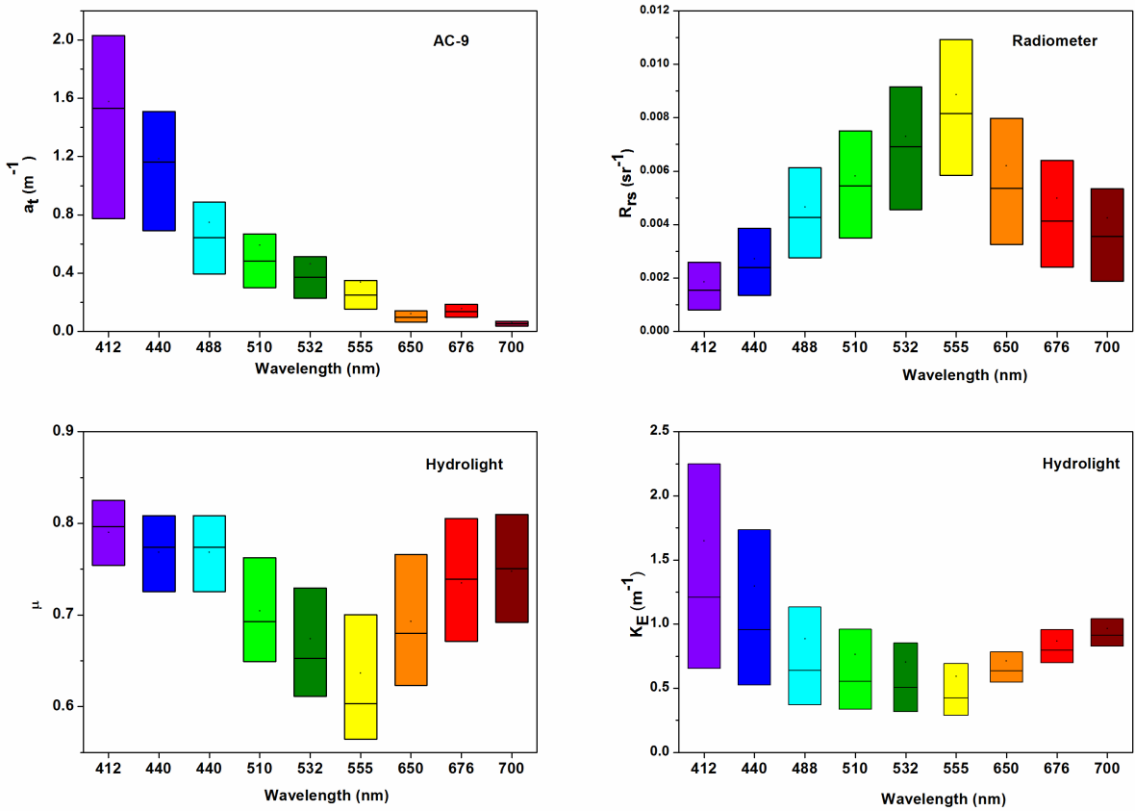

Figure 8.11 Variations of the measured optical parameters, $a_t(\lambda)$ using AC-9 (top left) and $R_{rs}(\lambda)$ using profiling radiometer (top right). The data derived from the Hydrolight simulations were $\mu(\lambda)$ (bottom left) and $K_E(\lambda)$ (bottom right).

There were two types of satellite data, one that was available from the archive of SeaBASS (https://seabass.gsfc.nasa.gov/), which contained measured bio-optical parameters and the satellite-derived products from the co-located measured sites. The SeaBASS data were exclusively available for the validation of satellite-derived products from the site (Bailey &

Werdell, 2006). The SeaBASS data at the site was last updated on 24-02-2017, and the data for MODIS Terra were downloaded for this study on 7 April 2017 from the SeaBASS site. The second satellite data were those which were processed to derive parameters to compare with the measured optical data for the waters of Goa. The Level-1 data of Indian ocean color satellite OCM-2 were processed using SeaDAS 7.4 (https://seadas.gsfc.nasa.gov) to derive a(λ) with algorithm GSM available in SeaDAS. The Level-1 data were processed to Level-2 using the default parameters and the atmospheric correction method in SeaDAS. The climatological data of meteorological parameters were used for processing satellite data in SeaDAS. The $a_t(\lambda)$ from SAGE490 used R_{rs}, Kd490, and solar zenith angle from the Level-2 OCM-2 satellite data. Unlike MODIS, which has a resolution of 1 Km, OCM-2 was better suited for coastal waters with a higher resolution of 0.3 Km.

Since the objective was to develop an algorithm to derive the optical parameters from the ocean color satellite data, the weighted averages of parameters were derived using the two methods (Gordon & Clark, 1980; Sokoletsky & Yacobi, 2011) and both the depth averaged optical parameters matched closely. Since the NOMAD data used for validation were the weighted average data obtained using the method of Gordon and Clarke(1980), the same method was adopted to calculate the weighted average for the profile data.

8.3.3 Development of the algorithms

To derive the total spectral absorption a(λ), Gershun's equation was opted (Gershun,1939), also known as divergence law for irradiance. This explicit relationship derived rigorously from radiative transfer equations ignoring the inelastic contributions, was cited as the honest relation, and the oldest available relation to derive inherent optical property of absorption coefficient from the apparent optical properties (Gordon, 2002). (See Equation (10)).

$$a(\lambda) = \mu(\lambda) K_E(\lambda) \tag{10}$$

Here μ(λ) is the spectral underwater average cosine, and $K_E(\lambda)$ is the spectral diffuse attenuation of the net irradiance.

Though the relation of Gershun has been used earlier to estimate the absorption coefficient (Pegau, Zaneveld, & Voss, 1995) this algorithm reported here is one of the few attempts to derive spectral absorption from ocean color satellite data applying this simple relation (Thayapurath, Talaulikar, Desa, & Lotlikar, 2016). Though the relationship seems simple and available since long, the constraints in using this relationship to derive spectral absorption coefficients were due to the unavailability of any instruments to measure the optical parameter to derive $\mu(\lambda)$ (Gordon, 2002). The radiometer available did not have the sensor to measure $E_u(\lambda)$ hence $K_E(\lambda)$ could not be determined. Hence, both these optical parameters $\mu(\lambda)$ and $K_E(\lambda)$ were first derived using empirical algorithms and then used in the Gershun's equation.

The $a(\lambda)$ derived using the Gershun's equation is corrected using in-situ measured $a(\lambda)$ (Thayapurath, Talaulikar, Desa, & Lotlikar, 2016). Here $\Delta(\lambda)$ is the residual spectral factor that is used to correct the total absorption derived here using Gerhun's equation.

$$a_t(\lambda) = a(\lambda) - a_w(\lambda) + \Delta(\lambda) \tag{11}$$

The algorithm was also modified to suit the ocean color satellite application, and hence the total absorption was developed using parameters that are commonly derived from the ocean color satellite such as $R_{rs}(\lambda)$ and $K_d(490)$. In the present algorithm SAGE490, $K_E(\lambda)$ is modeled as a function of $K_d(490)$. Algorithms to determine $K_d(490)$ were more robust as compared to $K_d(\lambda)$ (Thayapurath et al., 2011). The algorithm SAGE490 to derive $a_t(\lambda)$ is given in Figure 8.12. First, determine $\mu(\lambda)$ and $K_E(\lambda)$, then use Gershun's equation to calculate $a_t'(\lambda) = a(\lambda) - a_w(\lambda)$ and in the last step apply corrections to $a_t'(\lambda)$ to get $a_t(\lambda)$. All the parameters that were used to determine $\mu(\lambda)$ and $K_E(\lambda)$ could be derived from the ocean color data, either from measurements using radiometer or satellite data. All the spectral coefficients used in the empirical relations to derive $\mu(\lambda)$, $K_E(\lambda)$ and the corrected $a_t(\lambda)$ are given in Table 8.5 for every 1 nm interval from 400 to 700 nm. (Note: The Log here refers to natural log, Log_e) .

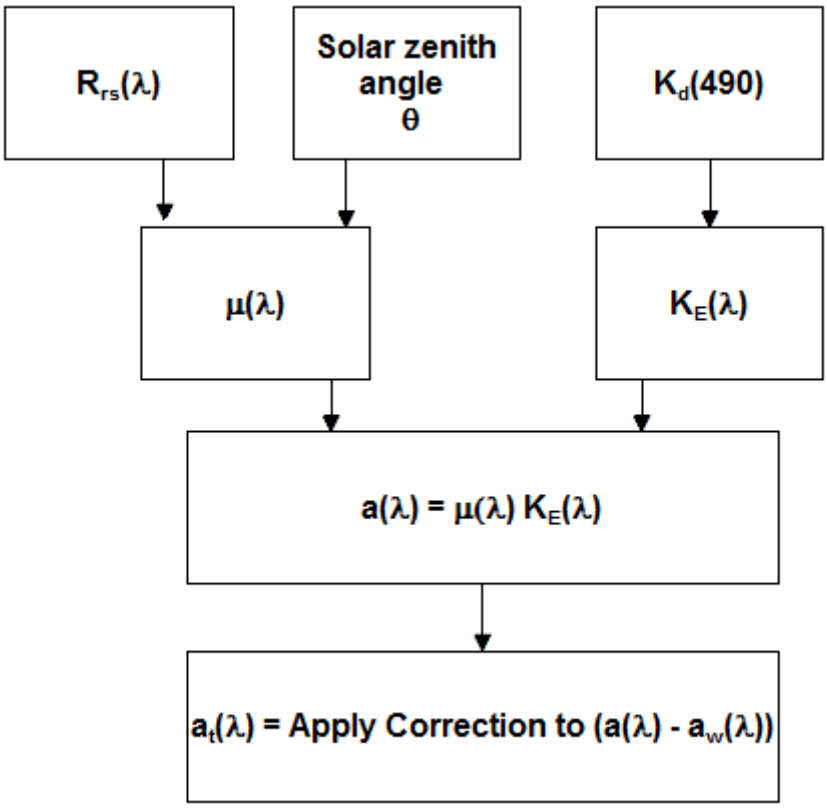

Figure 8.12 SAGE490 algorithm

8.3.3.1 Algorithm to derive spectral underwater average cosine, μ(λ)

Underwater average cosine is defined as follows

$$\mu(z,\lambda) = \frac{E_d(z,\lambda) - E_u(z,\lambda)}{E_o(z,\lambda)} \tag{12}$$

Where $E_d(z, \lambda)$, $E_u(z, \lambda)$, $E_d(z, \lambda)$ - $E_u(z, \lambda)$ and $E_o(z, \lambda)$ are the spectral downwelling irradiance, upwelling irradiance, net irradiance and scalar spectral irradiance at depth z and wavelength λ. μ(λ) can only be evaluated using the above parameters obtained from Hydrolight simulations. Hence, μ(λ) was obtained using a refined empirical algorithm with the larger data set and followed the same methodology (Talaulikar et al., 2014a). The new coefficients M_0, M_1, and M_2, are given in Table 8.5. The model to derive μ(λ) is a function of spectral remote sensing reflectance, $R_{rs}(\lambda)$, $R_{rs}(\lambda_0)$ and solar zenith angle, θ, where λ_0 = 620 nm.

$$\mu(\lambda) = M_0(\lambda) + M_1(\lambda)X(\lambda) + M_2(\lambda)X(\lambda)^2 \quad (13)$$

$$X(\lambda) = \frac{R_{rs}(\lambda)}{Log[R_{rs}(\lambda_o) + R_{rs}(\lambda)]} \frac{1}{\cos(\theta)} \quad (14)$$

8.3.3.2 Algorithm to derive vertical attenuation for net irradiance $K_E(\lambda)$

The vertical attenuation for net irradiance $K_E(\lambda)$ is given as

$$K_E(\lambda) = -\frac{d(Log[E_d(\lambda) - E_u(\lambda)])}{dz} \quad (15)$$

Considering $E_u(\lambda)$ to be relatively negligible as compared to $E_d(\lambda)$, $K_d(\lambda)$ was often found to be a good match for $K_E(\lambda)$ (Albert et al., 2002; Rehm, Mccormick, & Mobley, 2013; Zaneveld et al., 2005). $K_E(\lambda)$ has been modeled as a function of absorption, scattering coefficient, and the asymmetry factor of the scattering phase function (Kirk 2003). Here $K_E(\lambda)$ and $K_d(\lambda)$ were derived from the Hydrolight simulations. The log-transformed variables $K_E(\lambda)$ and $K_d(\lambda)$ were found to hold a good linear relation for the entire spectral range. The spectral $K_d(\lambda)$ can be modeled as a function of $K_d(\lambda_0)$ at a reference wavelength λ_0 (Austin & Petzold, 1981, 1984, 1990). Following a similar approach here in the empirical method to derive $K_E(\lambda)$, $K_E(\lambda)$ is modeled using $K_d(490)$ with a polynomial fit (Equation (16)). The polynomial model was found to be a better solution than a linear model (Figure 8.13). $K_d(490)$ was reported to be derived with better accuracy from ocean color satellite data than spectral $K_d(\lambda)$ (Thayapurath & Talaulikar, 2011). Hereafter the $K_d(490)$ is referred to as Kd490 for brevity. The spectral coefficients K_0, K_1, and K_2, are given in Table 8.5.

$$Log[K_E(\lambda)] = K_0(\lambda) + K_1(\lambda)Log[Kd490] + K_2(\lambda)(Log[Kd490])^2 + K_3(\lambda)(Log[Kd490])^3 \quad (16)$$

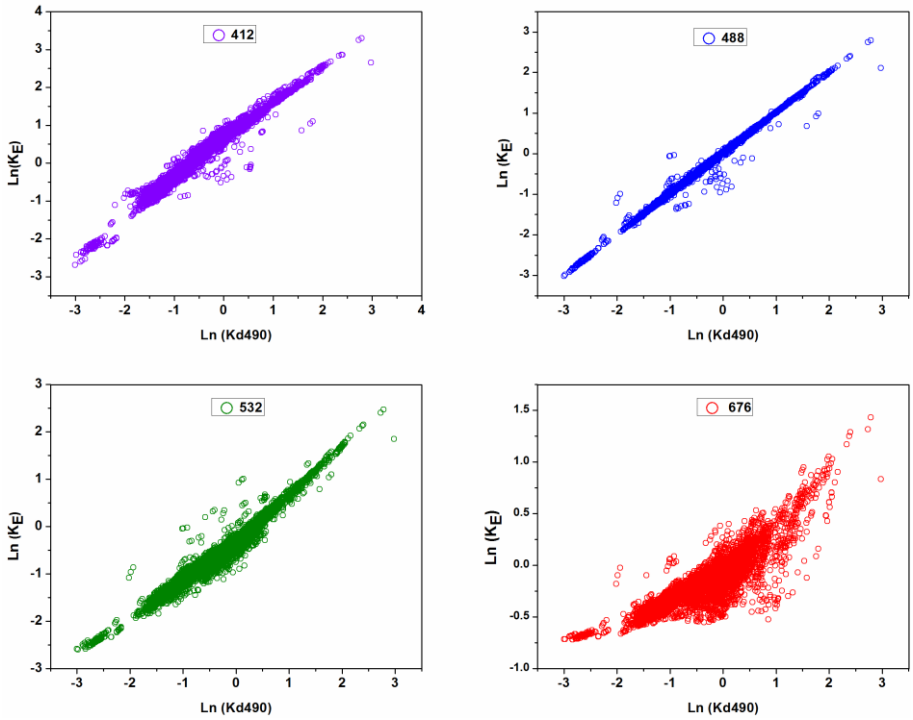

Figure 8.13 Log-log variations of $K_d(490)$ and $K_E(\lambda)$ for 412, 488, 532 and 676 nm.

8.3.3.3 Corrections to the $a_t(\lambda)$

The spectral total absorption derived using the Gershun's equation with the parameters $\mu(\lambda)$ and $K_E(\lambda)$ obtained from the empirical relations were corrected using the measured absorption data. This correction was required to take care of the errors in AC-9, AOP measurements, and empirical relations. The data measured till 2015 were used for the calibration of the total absorption, $a_t'(\lambda) = a(\lambda) - a_w(\lambda)$ to find the corrected spectral absorption, $a_t(\lambda)$ using the following linear model with the log transformed $a_t'(\lambda)$ (Equation (17)). The spectral coefficients A_0 and A_1 are given in Table 8.5.

$$Log[a_t(\lambda)] = A_0(\lambda) + A_1(\lambda) Log[a_t'(\lambda)] \qquad (17)$$

8.3.4 Results

8.3.4.1 Error descriptions and performance indicators

The error analysis was carried out with statistical parameters such as bias, RMSE (root mean square error), the coefficient of determination R^2, mean relative error (MRE), and regression between the total absorption derived using the model and the measured data. Since the optical properties were considered to be log-normal distributions (Campbell,

1995), the error estimators RMSE and MRE were calculated using log-transformed variables (Brewin et al., 2015; Shanmugam, 2011). The regression provides a slope, m, and intercept c. MRE is given in percent.

8.3.4.2 Closure of optical properties

The results of the simulations using Hydrolight provided optical parameters that closely matched the measured data. The spectral $Z_{90}(\lambda)$ and Rrs(λ) compared well with the measured for most of the stations (Thayapurath, Talaulikar, Desa, & Lotlikar, 2016). This closure assured that the optical parameters derived from the Hydrolight and those that were not measured such as underwater average cosine $\mu(\lambda)$ scalar irradiance, $E_0(\lambda)$, the attenuation coefficient of net irradiance, $K_E(\lambda)$ would match and agree closely with the optical properties of the same environment.

8.3.4.3 Validation of the SAGE490 algorithm

The SAGE490 algorithm was validated with the in-situ measured and satellite data. In both these cases of validation, the $a_t(\lambda)$ were derived with SAGE490 algorithm using two optical parameters, $R_{rs}(\lambda)$, Kd490, and solar zenith angle, and they were compared with the measured $a_t(\lambda)$. The in-situ measured data included measured data of Goa after 2015 (i.e. excluding data used for the calibration of $a_t(\lambda)$) and the NOMAD data. The satellite data from SeaBASS and OCM-2 were also validated. SAGE490 algorithm was also compared with another algorithm, QAA (Lee et al., 2002), using the measured optical data of Goa.

8.3.4.4 Measured data of Goa

The SAGE490 was validated from 400 to 700 nm using the optical data measured in the coastal and estuarine waters of Goa. The comparisons of the measured at 412, 490, 555, and 600 nm and those derived using SAGE490 are given in Figure 8.14. The error statistics indicate that the SAGE490 performed better over the spectral range of 400 to 700 nm (Figure 8.15). The linear regression model between the measured and model indicated a good match of the measured and the model over the complete spectrum 400 to 700 nm. Above 650 nm, there was a slight underestimation of the SAGE490 values, and close to 700 nm, there was an overestimation.

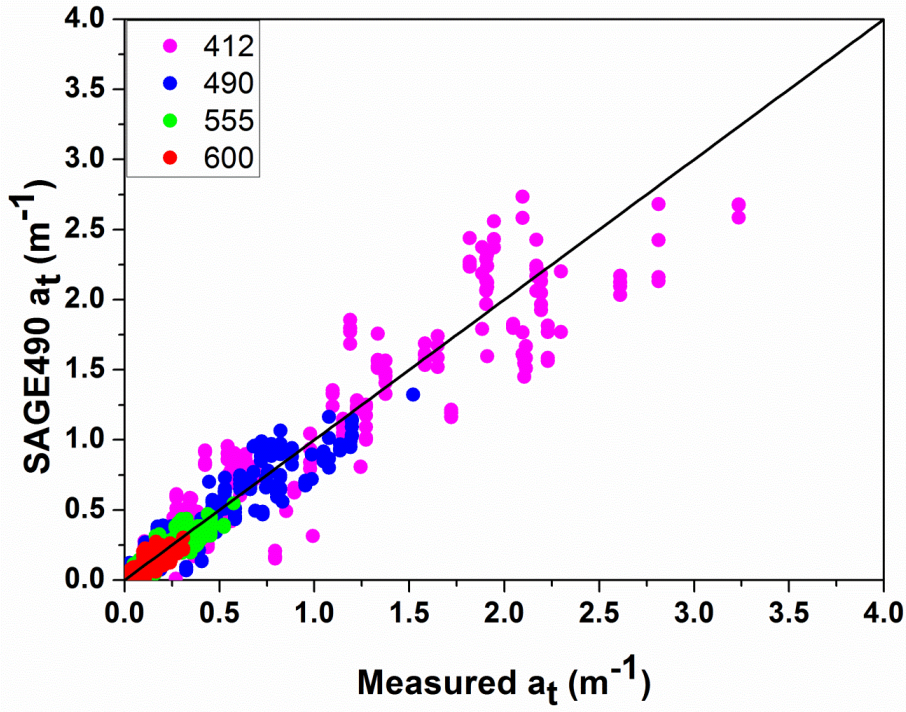

Figure 8.14 The comparison s of $a_t(\lambda)$ at 412, 490, 555 and 600 nm with the measured $a_t(\lambda)$ in the waters of Goa and those derived using SAGE490

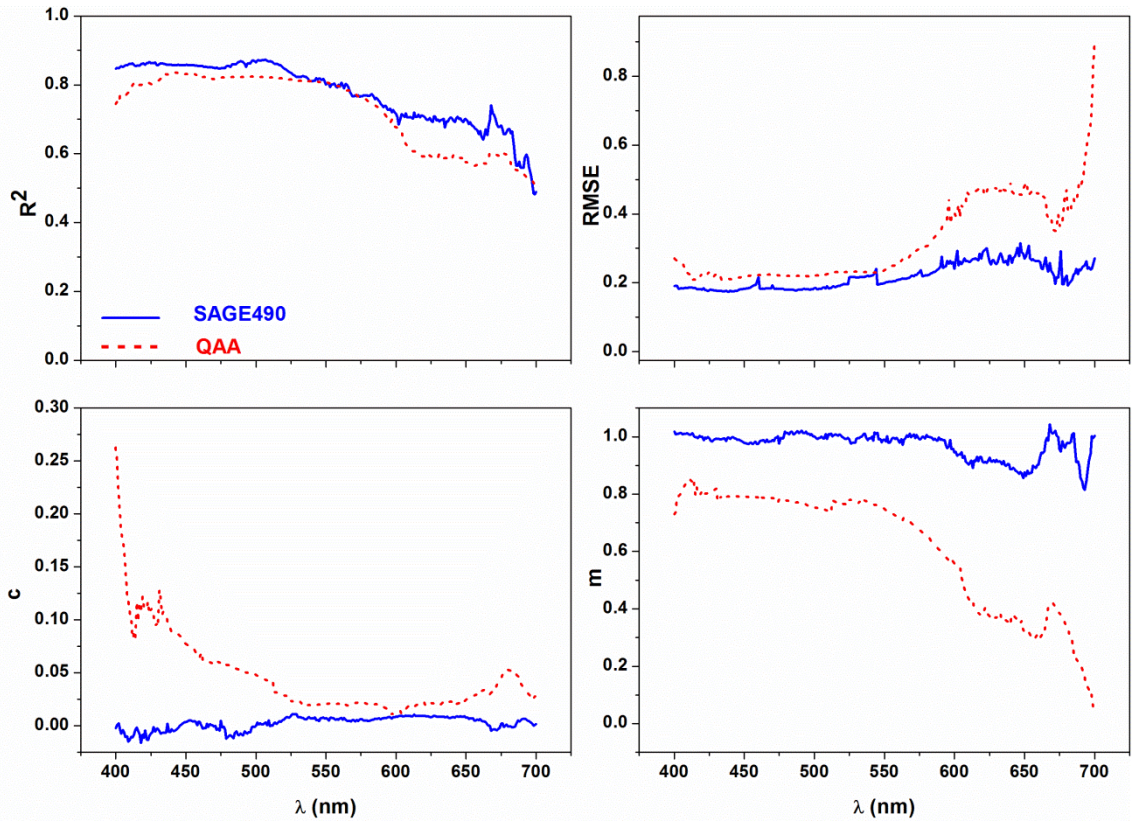

Figure 8.15 Error statistics of the comparisons of the $a_t(\lambda)$ derived using SAGE490 and QAA and measured $a_t(\lambda)$ for the waters of Goa.

8.3.4.5 Comparison with QAA

QAA has been rated to be a robust and proven algorithm for deriving $a_t(\lambda)$ from oceanic, as well as some coastal waters. Here the updated QAA version 6 was used (http://www.ioccg.org/groups/Software_OCA/QAA_v6_2014209.pdf). There were semi-analytical and empirical algorithms available that can determine $a_t(\lambda)$ and among these, QAA was found to score over others (Lee and Carder 2004, IOCCG 2006, Zhu et al. 2011). The $a_t(\lambda)$ using the QAA algorithm with the measured optical data of Goa, $R_{rs}(\lambda)$ were compared with the measured $a_t(\lambda)$. The performance indicators of QAA were compared with SAGE490 (Figure 8.15). The SAGE490 was found to perform better over the full spectral range of 400 to 700 nm, with comparatively higher R^2, lower RMSE, c values close to zero, and values of m close to 1.0. QAA model though it was well correlated with the measured $a_t(\lambda)$, was overestimated beyond 600 nm. In both models, R^2 decreased beyond 600 nm. The performance of QAA degraded beyond the 550 nm, while it was relatively better for SAGE490.

8.3.4.6 NOMAD data

SAGE490 was also validated using the NOMAD data. Though there were 4459 data records available, only that met the requirements were used. The data records that included all the optical parameters $R_{rs}(\lambda)$, Kd490, and $a_t(\lambda)$. The comparisons of the $a_t(\lambda)$ derived with NOMAD data for the wavelengths, 405, 489, 555, and 625 nm using SAGE490 were found to compare well with the measured $a_t(\lambda)$ (Figure 8.16).

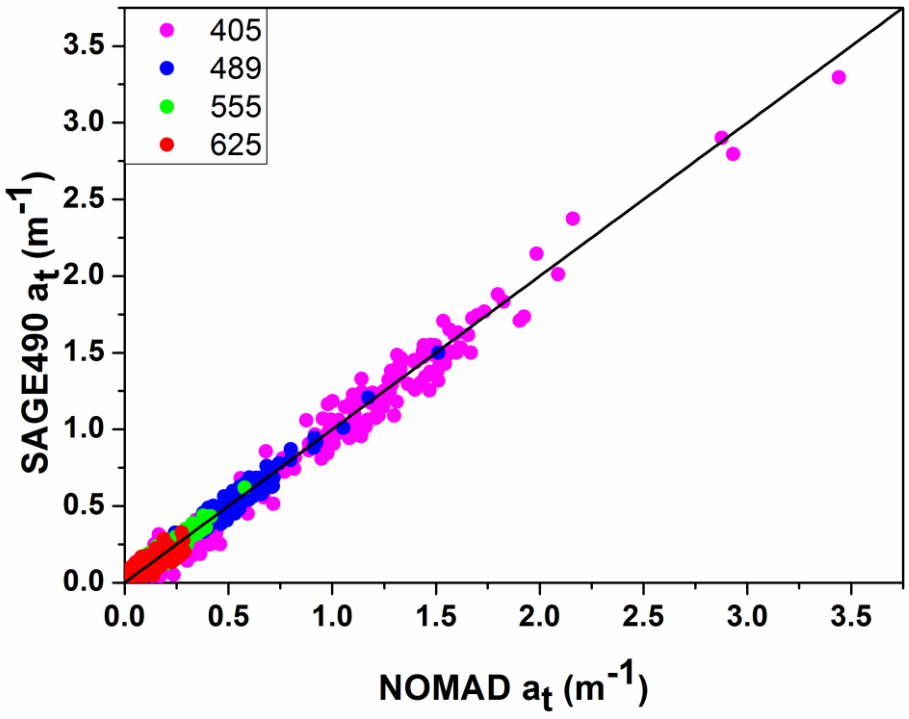

Figure 8.16 The comparisons of $a_t(\lambda)$ at 405,489,555 and 625nm with the measured $a_t(\lambda)$ in the NOMAD data with those derived using SAGE490

8.3.4.7 SeaBASS satellite data

The SAGE490 algorithm was applied to the satellite data of MODIS Terra and compared with the measured data available with SeaBASS. The SAGE490 algorithm used the satellite derived $R_{rs}(\lambda)$, Kd490, and solar zenith angle to derive $a_t(\lambda)$, and these were compared with the measured and the satellite derived $a_t(\lambda)$ available from the SeaBASS data. The $a_t(\lambda)$ were derived with SAGE490 at eight wavelengths 412, 443, 488, 531, 547, 555, and 667 nm of MODIS Terra data and the $a_t(\lambda)$ derived from the MODIS Terra data available in SeaBASS were derived using the model, GIOP. The performance of the SAGE490 algorithm was found to be better than the GIOP model, with comparatively better R^2 and lower RMSE (Figure 8.17). The linear regression model between the measured and those derived from the algorithms showed SAGE490 to underestimate (higher values of m), while the $a_t(\lambda)$ derived from the GIOP model were overestimated (lower values of m).

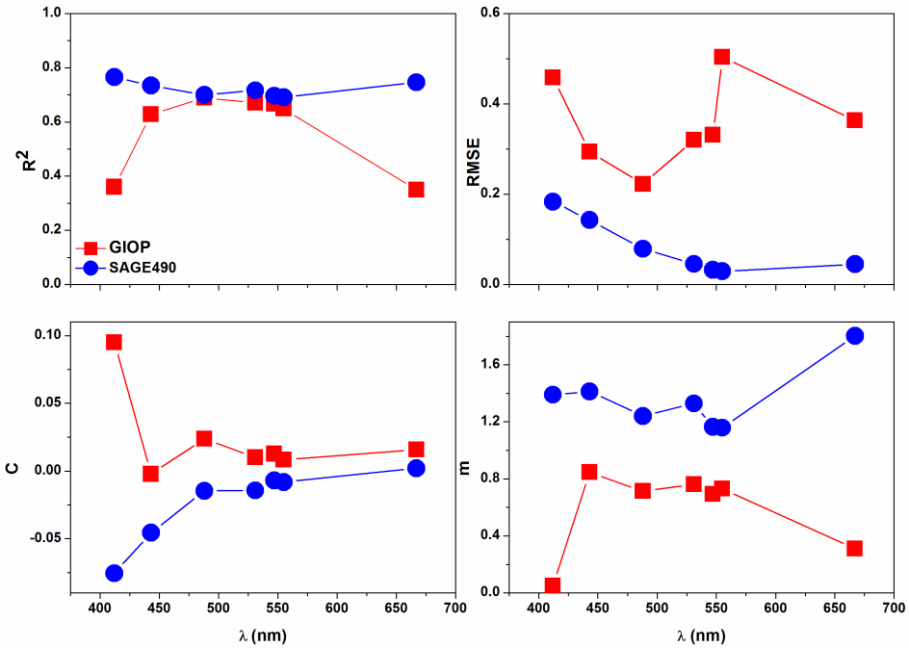

Figure 8.17 Comparisons of $a_t(\lambda)$ derived using the MODIS Terra data with SAGE490 and GIOP algorithms

8.3.4.8 OCM-2 satellite data for the waters of Goa

The $a_t(\lambda)$ were derived from OCM-2, and the error statistics indicating the performance of the algorithms are given in Table 8.4. The performance of SAGE490 was found to be comparatively better than GSM, except at 415 nm. At 415, the satellite derived $a_t(\lambda)$ with SAGE490 was relatively poor with the total number of data that qualified were much less (indicated by n in Table 8.4), larger RMSE and mean relative error and also the values were underestimated as indicated by the higher value of m. For GSM $a_t(\lambda)$ were overestimated.

Table 8.4 Error statistics of $a_t(\lambda)$ from OCM-2

λ nm	Algorithm	n	R^2	RMSE	MRE	c	m	Min at(λ)	Max at(λ)
415	GSM	99	0.47	0.914	256.70	0.324	0.071	0.1007	2.7284
	SAGE490	**26**	**0.94**	**1.316**	**123.46**	**0.131**	**2.4297**	**0.1007**	**2.7284**
442	GSM	99	0.59	0.654	56.60	0.2141	0.0435	0.0549	1.9124
	SAGE490	**99**	**0.79**	**0.421**	**59.7**	**0.1263**	**0.7773**	**0.0549**	**1.9124**
491	GSM	99	0.57	0.636	61.72	0.1142	0.0764	0.0262	1.0639
	SAGE490	**99**	**0.78**	**0.413**	**42.61**	**0.0734**	**0.7712**	**0.0262**	**1.0639**
512	GSM	99	0.57	0.659	18.96	0.0816	0.0771	0.0166	0.8026
	SAGE490	**99**	**0.78**	**0.476**	**21.48**	**0.0614**	**0.7109**	**0.0166**	**0.8026**
557	GSM	99	0.54	0.761	26.87	0.0461	0.2138	0.0104	0.4246
	SAGE490	**99**	**0.73**	**0.439**	**13.89**	**0.0261**	**0.7604**	**0.0104**	**0.4246**
620	GSM	99	0.47	0.686	-7.69	0.0254	0.1961	0.006	0.2022
	SAGE490	**97**	**0.63**	**0.697**	**23.74**	**0.0251**	**0.5706**	**0.006**	**0.2022**

8.3.5 Discussions

The performance of the SAGE490 algorithm was found to be robust and could derive spectral $a_t(\lambda)$ with good accuracy over the spectral range of 400-700 nm. This simple algorithm to derive spectral total absorption performed well even at the longer wavelengths, unlike many other algorithms that have reported its validity and performance only till the green region of spectra (Loisel & Stramski, 2000; Smyth et al., 2006). SAGE490 algorithm had the edge over various other algorithms whose regions of operations were limited in the blue and green region of spectra, while SAGE490 was observed to perform even in the red region of spectra. This algorithm was validated with measured values, and the $a_t(\lambda)$ derived from the algorithm compared well over the complete visible range from 400 to 700 nm with high R^2, low bias, RMSE, and MRE and slope close to 1.

Apart from $a(\lambda)$, algorithms have also been developed for other optical parameters, the underwater average cosine, $\mu(\lambda)$, and the diffuse attenuation coefficient of net solar irradiance, $K_E(\lambda)$, to derive them from the measured AOP or the ocean color satellite data. The underwater average cosine $\mu(\lambda)$ is a parameter that cannot be measured.

Though the algorithm has been developed using the optical data for the coastal and estuarine waters, the algorithm performed well for the NOMAD data, which was a collection of optical data from various water types over the globe, with larger variations in optical properties.

Though QAA has been developed for oceanic and coastal waters, the algorithm was found inaccurate and unfit for the turbid waters (Darecki & Stramski, 2004). SAGE490 algorithm was suited for waters with high absorption as the errors in the derived absorption were found to decrease with an increase in the absorption coefficients (not shown here).

The errors in the optical data used here could originate from the measurements and Hydrolight simulations. There were only four optical parameters used in the developments of the SAGE490 algorithm, namely, Rrs, K_d, K_E, and μ. The $R_{rs}(\lambda)$ was obtained from the radiometer data and Hydrolight, while the others were derived from the Hydrolight simulations. The radiometer sensors were calibrated periodically at the factory. The data from the radiometer were often missed from the layer close to the surface due to an

inherent problem observed in the free-falling radiometer of the Satlantic (Suresh et al., 2012). The outputs from Hydrolight simulations depend on the measured data, and the inputs are primarily the inherent optical properties from AC-9 and the solar irradiance measured by the radiometer sensor above the surface of the water. The Hydrolight simulations did not include the effects of inelastic scattering. The natural fluorescence in the red region due to pigments from phytoplankton could also add to the radiance in the water. Since these waters of Goa have high absorption coefficients, the contribution from Raman scattering could be minimal, as the Raman scattering effects are significant in clear, low productive, open ocean waters at a longer wavelength (Westberry, Boss, & Lee, 2013). The other source of errors would be from the empirical algorithms to derive $K_d(490)$, $K_E(\lambda)$ and $\mu(\lambda)$ and the corrections applied to the $at(\lambda)$ derived from Gershun's equation.

8.3.6 Conclusion

The algorithms SAGE490 to derive the spectral total absorption coefficient were proved to perform well over the spectral range from 400 to 700 nm. The special advantages of this method include : (a) Its derivation from a radiative transfer model; (b) spectral total absorption coefficient derived from the ocean color satellite data; (c) superior performance of this method in the red region of the spectrum as compared to other methods; (d) validation for all water types over a wide range of the total absorption coefficient and its suitability for coastal waters in particular; (e) total absorption coefficient was calculated and thus obviated the need to consider the absorptions due to individual components; (f) the parameters in the algorithm were relatively fewer with only two empirical relations, making the implementation simpler and reducing the errors in the calculations.

The algorithm had the advantage of its applications with special regards to derive spectral total absorption coefficients from ocean color satellite data. The results of the validations with GSM and GIOP algorithms using from the satellite also proved the superiority of the SAGE490 algorithms.

Most algorithms partition the total absorption and find the total absorption coefficients of all contributors to arrive at $a_t(\lambda)$ (Brewin et al., 2015). In contrast to such algorithms, the approach adopted here was from the radiative transfer model to derive directly $a(\lambda)$. Since it does not have to handle multiple parameters and empirical relationships, the cumulative error was reduced. This algorithm was straightforward, relatively simpler and there were

only two empirical relationships used to derive a(λ) namely μ(λ) and $K_E(\lambda)$ and hence the errors in deriving a(λ) were just limited to these empirical relations. There could be two sources of errors - the algorithms and the data used for the development.

Though the algorithm was found to be valid over a wide range of values of absorption, it was found to be better estimable with certainty at higher values of $a_t(\lambda)$, indicating its suitability for coastal waters and waters with large contributions from CDOM and detritus, eutrophic and algal blooms.

Table 8.5 Coefficients of empirical relations

λ nm	M0	M1	M2	K0	K1	K2	K3	A0	A1
400	0.85911	-26.01489	-45464.72656	0.66229	1.01297	-0.05092	-0.00963	-0.08173	0.86589
401	0.85810	-28.69556	-46863.52344	0.66210	1.01312	-0.05111	-0.00956	-0.08730	0.86825
402	0.85919	-25.08920	-44844.30078	0.66190	1.01326	-0.05126	-0.00948	-0.10483	0.86306
403	0.86754	5.07961	-30530.45117	0.66170	1.01335	-0.05134	-0.00936	-0.10919	0.86153
404	0.86000	-24.06705	-48356.55078	0.66149	1.01351	-0.05150	-0.00927	-0.11591	0.86180
405	0.86001	-23.99755	-48954.52734	0.66133	1.01370	-0.05174	-0.00921	-0.12564	0.85948
406	0.87928	55.57254	-3011.37988	0.66122	1.01377	-0.05183	-0.00916	-0.12199	0.86114
407	0.86047	-23.40635	-48377.77734	0.66113	1.01384	-0.05190	-0.00911	-0.13607	0.86084
408	0.86159	-20.88678	-47596.31641	0.66099	1.01376	-0.05193	-0.00904	-0.14297	0.86030
409	0.85928	-27.89808	-50134.84766	0.66090	1.01394	-0.05206	-0.00902	-0.15214	0.86230
410	0.86253	-17.76741	-46042.42188	0.66081	1.01409	-0.05213	-0.00896	-0.15506	0.86557
411	0.85953	-28.43331	-49509.19141	0.66075	1.01409	-0.05225	-0.00895	-0.16658	0.86539
412	0.86709	-5.01797	-38775.60547	0.66065	1.01415	-0.05221	-0.00888	-0.17685	0.86856
413	0.86084	-23.77074	-51401.69531	0.65294	1.01425	-0.05202	-0.00889	-0.17766	0.85914
414	0.86106	-22.19170	-52175.21094	0.64518	1.01434	-0.05191	-0.00894	-0.17937	0.85679
415	0.86082	-21.91529	-51145.86719	0.63732	1.01443	-0.05168	-0.00894	-0.17962	0.85822
416	0.86151	-19.34816	-47629.46875	0.62945	1.01450	-0.05144	-0.00898	-0.18149	0.85979
417	0.87616	67.09229	1775.88403	0.62150	1.01455	-0.05121	-0.00901	-0.16107	0.85901
418	0.87693	46.87479	-3426.57007	0.61347	1.01463	-0.05088	-0.00903	-0.17394	0.86400
419	0.86260	-14.85669	-36078.89453	0.60540	1.01467	-0.05072	-0.00909	-0.18735	0.86740
420	0.86769	-0.03263	-29925.17188	0.59725	1.01478	-0.05044	-0.00912	-0.18704	0.86623
421	0.87952	42.74865	1423.96289	0.58897	1.01476	-0.05011	-0.00913	-0.18816	0.86866
422	0.86303	-12.55521	-33693.33203	0.58066	1.01483	-0.04980	-0.00918	-0.19033	0.87168
423	0.87221	25.87661	-10991.39844	0.57227	1.01492	-0.04947	-0.00922	-0.18728	0.87100
424	0.86279	-10.98355	-34195.11328	0.56381	1.01490	-0.04929	-0.00930	-0.19842	0.87911
425	0.86283	-10.87118	-33419.44531	0.55523	1.01496	-0.04892	-0.00932	-0.19649	0.87089
426	0.87539	38.98145	-161.33012	0.54657	1.01503	-0.04858	-0.00936	-0.19107	0.87449
427	0.86401	-6.22569	-32206.57031	0.53786	1.01505	-0.04837	-0.00943	-0.19999	0.86869

428	0.86412	-5.42965	-28084.11914	0.52901	1.01509	-0.04800	-0.00945	-0.20357	0.86988
429	0.86669	3.64611	-29350.17188	0.52006	1.01510	-0.04767	-0.00949	-0.20980	0.85782
430	0.86618	3.05238	-29168.35742	0.51108	1.01517	-0.04736	-0.00953	-0.21429	0.85667
431	0.86649	1.66472	-24663.21680	0.50199	1.01517	-0.04701	-0.00958	-0.21705	0.86037
432	0.86733	3.51643	-24027.07422	0.49280	1.01521	-0.04664	-0.00964	-0.21763	0.86035
433	0.86716	3.81644	-24129.78711	0.48351	1.01518	-0.04627	-0.00967	-0.21909	0.85976
434	0.86975	14.22503	-18793.22461	0.47412	1.01522	-0.04585	-0.00971	-0.22193	0.85858
435	0.87077	15.03579	-17530.97070	0.46462	1.01523	-0.04546	-0.00976	-0.22812	0.85778
436	0.86833	8.63809	-20430.18164	0.45514	1.01512	-0.04506	-0.00986	-0.23326	0.85714
437	0.86841	9.44878	-19955.50586	0.44556	1.01506	-0.04457	-0.00996	-0.23815	0.85630
438	0.86876	10.20747	-18864.13477	0.43583	1.01499	-0.04404	-0.01004	-0.24395	0.85611
439	0.87082	15.14117	-16890.97070	0.42603	1.01487	-0.04362	-0.01015	-0.24916	0.85538
440	0.86956	15.68596	-17611.10742	0.41607	1.01476	-0.04313	-0.01025	-0.24459	0.85731
441	0.87148	19.25261	-15246.57617	0.40935	1.01449	-0.04247	-0.01013	-0.26135	0.85412
442	0.87129	18.16950	-15340.36035	0.40255	1.01416	-0.04183	-0.01000	-0.27026	0.85370
443	0.87032	15.51200	-14521.85254	0.39572	1.01385	-0.04120	-0.00990	-0.28047	0.85483
444	0.87050	16.04301	-14994.23438	0.38883	1.01353	-0.04052	-0.00976	-0.28664	0.85496
445	0.87152	19.14020	-14239.66211	0.38187	1.01318	-0.03987	-0.00965	-0.29252	0.85527
446	0.86975	14.75270	-14480.26660	0.37498	1.01274	-0.03918	-0.00956	-0.30259	0.85693
447	0.86971	15.77681	-14856.62012	0.36799	1.01231	-0.03841	-0.00945	-0.30780	0.85712
448	0.86996	17.46977	-14493.70020	0.36096	1.01185	-0.03766	-0.00935	-0.31312	0.85736
449	0.87156	22.12651	-13390.28809	0.35390	1.01143	-0.03688	-0.00925	-0.31693	0.85738
450	0.87038	17.76999	-13176.94336	0.34679	1.01098	-0.03614	-0.00916	-0.32719	0.85904
451	0.87220	22.58804	-12136.81250	0.33936	1.01069	-0.03549	-0.00897	-0.33102	0.85795
452	0.87269	24.56047	-11758.35742	0.33191	1.01045	-0.03484	-0.00880	-0.33569	0.85753
453	0.87267	25.76844	-11205.04199	0.32439	1.01014	-0.03423	-0.00863	-0.34121	0.85731
454	0.87155	24.16982	-11303.83789	0.31681	1.00987	-0.03352	-0.00842	-0.34649	0.85793
455	0.87194	24.54078	-11182.09570	0.30913	1.00953	-0.03286	-0.00823	-0.35019	0.85590
456	0.87128	21.71771	-10586.63379	0.30139	1.00927	-0.03223	-0.00804	-0.35607	0.85705
457	0.87137	23.17943	-10661.23145	0.29357	1.00897	-0.03160	-0.00783	-0.36057	0.85441

458	0.87146	29.56942	-10384.29102	0.28568	1.00871	-0.03092	-0.00762	-0.35971	0.85393
459	0.87175	24.93599	-9749.77344	0.27771	1.00841	-0.03025	-0.00741	-0.36924	0.85126
460	0.87203	26.07144	-9213.30664	0.26965	1.00813	-0.02952	-0.00719	-0.37305	0.84974
461	0.87186	26.01228	-9065.97266	0.26157	1.00779	-0.02880	-0.00696	-0.37469	0.85013
462	0.87197	27.10534	-8786.57617	0.25342	1.00744	-0.02810	-0.00676	-0.37805	0.84864
463	0.87203	27.83421	-8476.04883	0.24518	1.00710	-0.02734	-0.00654	-0.37869	0.84793
464	0.87416	32.12476	-7291.18994	0.23686	1.00676	-0.02656	-0.00630	-0.38347	0.84701
465	0.87358	31.90378	-7186.63379	0.22846	1.00639	-0.02579	-0.00608	-0.38694	0.84645
466	0.87146	28.78885	-7722.80273	0.22001	1.00598	-0.02496	-0.00584	-0.39034	0.84716
467	0.87161	30.28627	-7276.38818	0.21151	1.00564	-0.02411	-0.00561	-0.39340	0.84477
468	0.87138	30.31181	-7350.89844	0.20289	1.00516	-0.02333	-0.00539	-0.39609	0.84283
469	0.87234	30.06836	-6515.93457	0.19421	1.00477	-0.02242	-0.00514	-0.40151	0.84230
470	0.87160	28.61911	-6301.76416	0.18543	1.00433	-0.02160	-0.00492	-0.39930	0.84522
471	0.87283	33.33134	-5714.19727	0.17664	1.00386	-0.02065	-0.00468	-0.40490	0.84492
472	0.87235	31.70442	-5717.83594	0.16774	1.00337	-0.01969	-0.00445	-0.40433	0.84847
473	0.86875	19.78532	-9435.93750	0.15875	1.00282	-0.01874	-0.00422	-0.41654	0.84612
474	0.87303	36.26608	-4901.59277	0.14967	1.00231	-0.01772	-0.00397	-0.41242	0.84172
475	0.87197	34.50211	-5982.42529	0.14050	1.00179	-0.01673	-0.00373	-0.42092	0.83987
476	0.87246	40.33028	-4155.35645	0.13135	1.00112	-0.01569	-0.00353	-0.41669	0.84302
477	0.87263	38.32899	-4068.16138	0.12206	1.00048	-0.01454	-0.00329	-0.42059	0.84491
478	0.87287	38.78648	-3869.28223	0.11270	0.99976	-0.01346	-0.00308	-0.41940	0.83881
479	0.87319	37.56368	-3556.39453	0.10324	0.99909	-0.01229	-0.00283	-0.42034	0.83960
480	0.87261	35.44714	-3568.39136	0.09366	0.99839	-0.01110	-0.00258	-0.42130	0.84312
481	0.87354	39.31206	-2960.16113	0.08390	0.99774	-0.00999	-0.00232	-0.42245	0.84514
482	0.87376	41.87321	-2535.76416	0.07403	0.99710	-0.00881	-0.00206	-0.42275	0.84396
483	0.87354	37.61394	-2571.13428	0.06404	0.99647	-0.00757	-0.00176	-0.42701	0.85079
484	0.87370	44.30605	-1904.91223	0.05392	0.99574	-0.00643	-0.00149	-0.42009	0.84308
485	0.87296	38.51472	-2188.67651	0.04370	0.99504	-0.00517	-0.00117	-0.43101	0.85532
486	0.87324	40.84883	-1897.97815	0.03347	0.99425	-0.00383	-0.00090	-0.42848	0.86032
487	0.86918	31.88644	-4946.93115	0.02309	0.99333	-0.00246	-0.00060	-0.42774	0.86366

488	0.87258	38.48660	-1758.92163	0.01261	0.99248	-0.00108	-0.00032	-0.42282	0.86464
489	0.87223	39.04894	-2710.55640	0.00504	0.99125	-0.00022	0.00019	-0.40816	0.86986
490	0.87250	42.60221	-1297.81226	-0.00264	0.98999	0.00064	0.00068	-0.41038	0.86864
491	0.87228	41.66334	-1235.69104	-0.01014	0.98855	0.00158	0.00110	-0.41449	0.86803
492	0.87158	42.37423	-1118.67004	-0.01772	0.98705	0.00257	0.00156	-0.41692	0.86688
493	0.87242	42.63294	-943.14716	-0.02541	0.98556	0.00359	0.00199	-0.42608	0.85645
494	0.87122	41.70971	-1154.71875	-0.03316	0.98413	0.00470	0.00245	-0.43104	0.86457
495	0.87151	42.32922	-967.16974	-0.04102	0.98261	0.00577	0.00293	-0.44926	0.85934
496	0.87103	45.42563	-500.83774	-0.04873	0.98088	0.00697	0.00334	-0.44405	0.86094
497	0.87132	42.30559	-601.61078	-0.05651	0.97918	0.00819	0.00375	-0.44826	0.88702
498	0.87075	47.07048	-164.78821	-0.06439	0.97743	0.00943	0.00418	-0.43935	0.88914
499	0.86888	47.78579	-175.02925	-0.07235	0.97563	0.01068	0.00462	-0.44821	0.88925
500	0.86982	46.86457	-117.90327	-0.08039	0.97388	0.01198	0.00506	-0.44553	0.89449
501	0.87019	46.49990	-63.02501	-0.08796	0.97158	0.01356	0.00536	-0.44659	0.91068
502	0.86974	47.21724	28.31457	-0.09562	0.96921	0.01521	0.00569	-0.47291	0.90401
503	0.86806	48.31430	37.55120	-0.10335	0.96682	0.01682	0.00600	-0.47950	0.90296
504	0.86904	47.35466	166.08969	-0.11115	0.96442	0.01855	0.00637	-0.48951	0.90612
505	0.86874	47.24849	197.80754	-0.11906	0.96194	0.02025	0.00672	-0.49735	0.90575
506	0.86890	44.55290	20.28333	-0.12652	0.95909	0.02219	0.00697	-0.49325	0.91468
507	0.86888	44.67941	74.68388	-0.13413	0.95608	0.02416	0.00725	-0.49921	0.91832
508	0.86872	45.89270	323.27209	-0.14177	0.95308	0.02612	0.00753	-0.52473	0.90644
509	0.86725	50.12606	765.74738	-0.14952	0.95000	0.02818	0.00785	-0.50281	0.91435
510	0.86809	45.42268	342.57275	-0.15735	0.94688	0.03023	0.00818	-0.54213	0.90125
511	0.86781	47.71468	587.00165	-0.16286	0.94308	0.03223	0.00799	-0.54922	0.89715
512	0.86718	46.47158	502.05792	-0.16841	0.93915	0.03421	0.00783	-0.55997	0.89723
513	0.86634	44.79525	347.00555	-0.17401	0.93523	0.03628	0.00774	-0.57197	0.89474
514	0.86640	45.65842	493.20477	-0.17968	0.93116	0.03827	0.00763	-0.57843	0.89704
515	0.86607	41.41204	189.81099	-0.18537	0.92703	0.04019	0.00755	-0.59086	0.90559
516	0.86585	43.06808	358.70413	-0.19290	0.92448	0.04155	0.00775	-0.59807	0.90487
517	0.86577	44.37400	578.67029	-0.20055	0.92175	0.04287	0.00796	-0.59897	0.90787

518	0.86593	41.82982	373.03522	-0.20822	0.91900	0.04411	0.00815	-0.61220	0.90861
519	0.86454	45.08942	633.29828	-0.21602	0.91620	0.04542	0.00836	-0.60696	0.90891
520	0.86548	39.64995	331.23633	-0.22390	0.91341	0.04679	0.00859	-0.62047	0.91351
521	0.86528	39.86208	391.77289	-0.23202	0.91065	0.04809	0.00885	-0.62456	0.91368
522	0.86512	42.74063	614.11304	-0.24019	0.90787	0.04937	0.00909	-0.62530	0.91183
523	0.86274	50.52964	1354.18066	-0.24851	0.90498	0.05069	0.00937	-0.61487	0.90569
524	0.86421	48.89006	1229.06140	-0.25688	0.90210	0.05207	0.00966	-0.62414	0.90886
525	0.86339	49.05869	1291.38977	-0.26539	0.89909	0.05334	0.00992	-0.62240	0.91112
526	0.86451	49.93624	1443.08118	-0.27367	0.89587	0.05486	0.01020	-0.61469	0.91423
527	0.86345	48.98919	1367.04321	-0.28204	0.89260	0.05636	0.01047	-0.61815	0.91395
528	0.86314	49.75417	1470.54028	-0.29052	0.88923	0.05788	0.01076	-0.61771	0.91400
529	0.86193	49.42395	1448.49744	-0.29905	0.88581	0.05939	0.01105	-0.61854	0.91520
530	0.86194	49.89960	1529.85632	-0.30775	0.88229	0.06097	0.01137	-0.63538	0.91057
531	0.86177	48.62074	1426.61963	-0.31644	0.87868	0.06247	0.01167	-0.64113	0.90995
532	0.86145	49.94421	1530.73022	-0.32531	0.87511	0.06414	0.01201	-0.63969	0.91086
533	0.86146	50.43531	1649.51453	-0.33362	0.87285	0.06550	0.01236	-0.65245	0.90807
534	0.86166	49.26554	1542.05151	-0.34205	0.87048	0.06684	0.01270	-0.65855	0.90779
535	0.86141	51.20655	1788.80591	-0.35050	0.86813	0.06816	0.01305	-0.65911	0.90571
536	0.86182	50.05593	1669.51379	-0.35896	0.86567	0.06970	0.01342	-0.66539	0.90462
537	0.86195	50.83871	1767.91272	-0.36743	0.86310	0.07107	0.01376	-0.66307	0.90465
538	0.86054	50.75745	1774.39905	-0.37613	0.86045	0.07259	0.01415	-0.65684	0.90335
539	0.86150	49.50272	1674.39319	-0.38478	0.85783	0.07409	0.01453	-0.67679	0.89607
540	0.86176	48.68652	1613.24500	-0.39356	0.85506	0.07549	0.01490	-0.68023	0.89799
541	0.86058	49.93408	1722.45227	-0.40189	0.85182	0.07717	0.01528	-0.67005	0.90349
542	0.86070	47.89636	1539.74524	-0.41038	0.84845	0.07895	0.01570	-0.68425	0.90149
543	0.86027	49.03930	1650.11816	-0.41885	0.84510	0.08067	0.01610	-0.69222	0.89875
544	0.85917	49.92886	1753.14832	-0.42749	0.84166	0.08244	0.01652	-0.69009	0.89971
545	0.85853	51.12722	1855.20032	-0.43621	0.83812	0.08421	0.01697	-0.68891	0.89933
546	0.85619	52.87447	2033.88135	-0.44433	0.83396	0.08614	0.01738	-0.66230	0.91286
547	0.85754	51.27406	1878.19861	-0.45249	0.82978	0.08810	0.01781	-0.64894	0.92439

548	0.85750	51.35908	1884.18323	-0.46078	0.82551	0.09012	0.01827	-0.63767	0.93257
549	0.85690	50.51394	1805.88818	-0.46921	0.82111	0.09214	0.01875	-0.64013	0.92632
550	0.85766	47.63359	1570.99353	-0.47777	0.81659	0.09421	0.01927	-0.65787	0.92205
551	0.85457	52.79963	2013.92468	-0.48736	0.81279	0.09603	0.01981	-0.63506	0.92090
552	0.85410	52.79966	2021.16870	-0.49714	0.80885	0.09796	0.02041	-0.67053	0.90371
553	0.85792	46.74088	1508.94263	-0.50701	0.80490	0.09989	0.02100	-0.65792	0.91797
554	0.85903	45.05161	1388.38440	-0.51711	0.80075	0.10191	0.02166	-0.66595	0.93072
555	0.85792	45.96440	1446.93616	-0.52734	0.79649	0.10394	0.02233	-0.66216	0.93940
556	0.85680	47.93232	1598.68274	-0.53015	0.79437	0.10413	0.02238	-0.67840	0.93647
557	0.85726	46.45673	1481.21838	-0.53299	0.79227	0.10439	0.02245	-0.69866	0.92808
558	0.85701	46.30042	1464.29700	-0.53585	0.79004	0.10449	0.02249	-0.70264	0.93036
559	0.85431	50.18810	1779.47449	-0.53873	0.78798	0.10480	0.02258	-0.69363	0.93249
560	0.85557	49.04580	1680.91553	-0.54162	0.78577	0.10498	0.02264	-0.69977	0.93442
561	0.85653	52.80919	2228.05249	-0.54452	0.78356	0.10521	0.02273	-0.76300	0.91143
562	0.85188	52.03001	1921.27344	-0.54745	0.78135	0.10543	0.02281	-0.76055	0.90673
563	0.85581	49.04044	1671.80627	-0.55043	0.77916	0.10567	0.02287	-0.72646	0.92977
564	0.85330	50.44700	1791.42468	-0.55329	0.77690	0.10587	0.02297	-0.77957	0.91456
565	0.85341	50.33897	1769.69727	-0.55621	0.77468	0.10606	0.02303	-0.78777	0.91582
566	0.85276	50.17047	1748.85974	-0.55776	0.77140	0.10645	0.02305	-0.79640	0.91147
567	0.85254	50.61311	1785.73840	-0.55929	0.76818	0.10687	0.02309	-0.80979	0.89917
568	0.85240	50.53478	1781.78223	-0.56082	0.76495	0.10720	0.02310	-0.82060	0.89305
569	0.85080	51.34963	1855.67383	-0.56241	0.76166	0.10761	0.02318	-0.81066	0.89660
570	0.85042	51.22331	1850.72852	-0.56387	0.75837	0.10798	0.02322	-0.81671	0.89852
571	0.85060	51.17406	1835.70984	-0.56432	0.75435	0.10847	0.02322	-0.82263	0.90130
572	0.85151	49.99468	1705.98169	-0.56472	0.75032	0.10895	0.02324	-0.82228	0.90734
573	0.85134	50.13159	1730.09521	-0.56515	0.74630	0.10945	0.02326	-0.83710	0.90612
574	0.85000	50.48466	1748.52197	-0.56555	0.74221	0.10984	0.02327	-0.83487	0.91121
575	0.85141	49.61494	1674.71191	-0.56597	0.73820	0.11032	0.02329	-0.83855	0.91606
576	0.85134	49.43075	1660.31506	-0.56410	0.73274	0.11095	0.02327	-0.84025	0.91897
577	0.85111	49.35937	1652.89868	-0.56223	0.72731	0.11155	0.02326	-0.83526	0.92768

578	0.85132	49.03601	1623.71387	-0.56042	0.72185	0.11212	0.02324	-0.83491	0.93369
579	0.85139	48.98322	1604.50159	-0.55864	0.71646	0.11271	0.02325	-0.83415	0.93939
580	0.85037	49.48083	1642.53638	-0.55680	0.71111	0.11316	0.02322	-0.85326	0.93266
581	0.85111	49.03899	1601.75024	-0.55127	0.70349	0.11404	0.02319	-0.84565	0.94373
582	0.85208	48.23372	1524.02673	-0.54577	0.69594	0.11480	0.02317	-0.84549	0.95701
583	0.85142	48.72643	1569.79065	-0.54034	0.68851	0.11542	0.02311	-0.84799	0.95942
584	0.85346	47.16222	1428.58789	-0.53496	0.68122	0.11612	0.02312	-0.86146	0.95997
585	0.85471	45.15892	1269.76721	-0.52958	0.67397	0.11666	0.02310	-0.87683	0.95831
586	0.85675	46.81453	1491.49951	-0.52211	0.66555	0.11720	0.02305	-0.88031	0.96291
587	0.85529	45.13884	1233.32837	-0.51479	0.65736	0.11782	0.02306	-0.88801	0.96360
588	0.85559	44.94470	1213.07886	-0.50745	0.64934	0.11832	0.02306	-0.89405	0.96600
589	0.85596	44.83242	1204.20959	-0.50025	0.64135	0.11868	0.02304	-0.91743	0.95418
590	0.85676	44.44781	1175.06458	-0.49307	0.63358	0.11908	0.02307	-0.93055	0.94998
591	0.85639	45.73298	1246.88513	-0.48306	0.62425	0.11943	0.02303	-0.93831	0.94566
592	0.85744	45.02642	1188.29138	-0.47314	0.61514	0.11972	0.02303	-0.93912	0.95589
593	0.85806	44.15354	1103.53992	-0.46334	0.60625	0.11998	0.02305	-0.94952	0.95692
594	0.85851	43.89487	1055.20325	-0.45363	0.59763	0.12015	0.02305	-0.96014	0.95056
595	0.85851	45.16748	1165.11023	-0.44405	0.58916	0.12024	0.02305	-0.96329	0.95057
596	0.85913	44.62545	1072.18604	-0.42532	0.57639	0.12041	0.02303	-0.96746	0.96325
597	0.86074	44.90204	1111.93054	-0.40708	0.56414	0.12047	0.02301	-0.99968	0.95754
598	0.86114	44.12675	1003.82153	-0.38925	0.55239	0.12039	0.02298	-0.98635	0.96636
599	0.86188	44.47577	1027.93372	-0.37179	0.54101	0.12016	0.02296	-1.00199	0.95580
600	0.86313	43.33877	931.99768	-0.35466	0.53012	0.11984	0.02291	-1.00724	0.95551
601	0.86298	44.13558	973.71008	-0.34506	0.52259	0.11948	0.02291	-1.02844	0.92964
602	0.86377	44.22095	1004.67297	-0.33557	0.51522	0.11905	0.02288	-1.07514	0.89117
603	0.86428	43.97975	972.79956	-0.32628	0.50795	0.11868	0.02290	-1.03793	0.92485
604	0.86525	43.31255	914.06042	-0.31702	0.50087	0.11820	0.02288	-1.01887	0.95736
605	0.86521	43.27644	893.52222	-0.30788	0.49391	0.11764	0.02284	-1.02773	0.96421
606	0.86546	43.00335	881.47937	-0.30865	0.49091	0.11724	0.02287	-1.03231	0.95086
607	0.86550	43.04312	888.58551	-0.30951	0.48793	0.11688	0.02289	-1.01469	0.97316

608	0.86613	42.29847	860.33801	-0.31033	0.48492	0.11649	0.02292	-1.03325	0.94695
609	0.86558	43.45865	931.14325	-0.31114	0.48191	0.11605	0.02293	-1.02098	0.95366
610	0.86546	43.51744	892.39703	-0.31195	0.47887	0.11560	0.02295	-1.00851	0.96212
611	0.86591	43.03103	908.81476	-0.31396	0.47617	0.11503	0.02292	-1.01889	0.95784
612	0.86547	43.38245	919.69733	-0.31593	0.47366	0.11469	0.02296	-1.02372	0.95972
613	0.86304	45.19179	1056.07581	-0.31792	0.47100	0.11424	0.02297	-0.95076	0.99332
614	0.86567	43.57919	952.01428	-0.31996	0.46828	0.11368	0.02296	-1.00529	0.97180
615	0.86533	43.87401	956.13855	-0.32197	0.46563	0.11322	0.02296	-0.99699	0.97304
616	0.86578	43.59538	933.98816	-0.32248	0.46244	0.11275	0.02297	-0.98711	0.99632
617	0.86583	43.54618	925.04321	-0.32299	0.45922	0.11221	0.02296	-0.99248	0.98346
618	0.86457	44.76747	960.59015	-0.32348	0.45598	0.11160	0.02292	-0.97460	0.99670
619	0.86461	45.42151	1106.63684	-0.32403	0.45275	0.11111	0.02293	-0.97024	0.99791
620	0.86433	45.46606	1046.49341	-0.32452	0.44950	0.11045	0.02287	-0.96294	0.98829
621	0.86584	44.11101	978.67810	-0.32502	0.44621	0.10989	0.02286	-0.98174	0.97759
622	0.86584	44.12332	1020.86646	-0.32547	0.44294	0.10931	0.02284	-0.98356	0.97598
623	0.86580	44.00342	992.21442	-0.32596	0.43965	0.10873	0.02282	-0.97610	0.97955
624	0.86588	43.96462	980.75262	-0.32640	0.43635	0.10804	0.02276	-0.97114	0.98759
625	0.86559	44.83465	1047.96399	-0.32686	0.43308	0.10744	0.02273	-0.97851	0.98515
626	0.86514	45.28716	1103.45923	-0.32721	0.42965	0.10665	0.02265	-0.97424	0.97927
627	0.86554	45.44236	1151.17371	-0.32757	0.42639	0.10609	0.02264	-0.94618	1.00263
628	0.86548	45.04530	1082.65942	-0.32797	0.42296	0.10532	0.02257	-0.93756	1.00763
629	0.86573	44.87750	1039.48230	-0.32832	0.41965	0.10465	0.02251	-0.95381	0.99405
630	0.86547	45.21185	1101.95728	-0.32872	0.41619	0.10385	0.02244	-0.94791	1.00047
631	0.86558	44.80410	1045.75696	-0.32861	0.41264	0.10307	0.02236	-0.95528	0.99055
632	0.86618	44.42522	1001.80792	-0.32851	0.40908	0.10228	0.02228	-0.94889	0.99022
633	0.86633	44.09923	983.66003	-0.32841	0.40550	0.10146	0.02220	-0.94829	0.99112
634	0.86475	45.83094	1083.26733	-0.32830	0.40200	0.10069	0.02212	-0.92586	1.00394
635	0.86627	44.43636	957.09656	-0.32822	0.39835	0.09980	0.02203	-0.99055	0.97208
636	0.86606	44.81584	974.29358	-0.32558	0.39411	0.09890	0.02190	-0.93693	1.00282
637	0.86493	45.44376	1021.03882	-0.32302	0.38975	0.09790	0.02176	-0.92985	1.00295

638	0.86779	42.78780	862.08374	-0.32043	0.38542	0.09687	0.02161	-0.92535	1.01534
639	0.86831	42.51132	849.18781	-0.31785	0.38121	0.09590	0.02147	-0.91878	1.03386
640	0.86738	44.15730	914.67108	-0.31532	0.37686	0.09481	0.02131	-0.91806	1.03326
641	0.86619	44.91347	974.15228	-0.31609	0.37361	0.09391	0.02119	-0.91280	1.02706
642	0.86848	42.39760	814.21484	-0.31688	0.37034	0.09298	0.02107	-0.94583	0.99825
643	0.86910	42.71016	863.06293	-0.31771	0.36693	0.09192	0.02091	-0.91891	1.02242
644	0.86756	43.79478	847.64032	-0.31852	0.36358	0.09091	0.02078	-0.88931	1.03426
645	0.86731	44.71370	963.84308	-0.31935	0.36012	0.08980	0.02061	-0.89987	1.02070
646	0.86747	44.44011	912.60266	-0.31738	0.35603	0.08859	0.02039	-0.89886	1.02497
647	0.86792	44.40523	936.94989	-0.31546	0.35189	0.08739	0.02020	-0.90965	1.01133
648	0.86775	44.78576	957.89069	-0.31347	0.34788	0.08619	0.01998	-0.90330	1.01075
649	0.86775	44.66922	918.53693	-0.31151	0.34373	0.08484	0.01973	-0.90194	1.01937
650	0.86965	41.49770	686.08575	-0.30965	0.33955	0.08353	0.01950	-0.92457	1.01479
651	0.86969	42.87096	785.89813	-0.29695	0.33664	0.08206	0.01908	-0.93116	1.00801
652	0.87029	41.33533	645.88647	-0.28450	0.33379	0.08068	0.01870	-0.98392	0.97228
653	0.87104	41.87189	652.55402	-0.27225	0.33092	0.07928	0.01832	-0.98689	0.97235
654	0.87156	41.74850	637.93451	-0.26019	0.32810	0.07790	0.01793	-1.01677	0.96630
655	0.87188	41.34526	622.83521	-0.24833	0.32524	0.07649	0.01756	-1.02617	0.96954
656	0.86561	29.85906	-1807.29407	-0.23408	0.32209	0.07513	0.01715	-1.08800	0.92543
657	0.86612	28.83191	-2034.86511	-0.22011	0.31871	0.07368	0.01677	-1.09276	0.91756
658	0.86915	33.30390	-797.71704	-0.20627	0.31577	0.07244	0.01641	-1.09812	0.91412
659	0.86885	31.79985	-1078.38342	-0.19280	0.31250	0.07102	0.01604	-1.13452	0.88544
660	0.88254	40.06494	107.75638	-0.17946	0.30956	0.06980	0.01571	-1.08545	0.93874
661	0.86820	28.54618	-1903.53284	-0.17222	0.30783	0.06868	0.01542	-1.12811	0.88314
662	0.86880	33.84985	-1135.82837	-0.16500	0.30604	0.06743	0.01511	-1.11913	0.86481
663	0.86961	33.42649	-1195.09363	-0.15788	0.30424	0.06624	0.01481	-1.11379	0.86713
664	0.87068	31.03532	-1278.89221	-0.15078	0.30264	0.06517	0.01452	-1.12383	0.86770
665	0.86999	26.69008	-2146.53809	-0.14373	0.30099	0.06402	0.01422	-1.18638	0.82742
666	0.87110	30.40958	-1411.50269	-0.13939	0.29967	0.06292	0.01397	-1.14310	0.84217
667	0.87129	30.72431	-1344.28186	-0.13496	0.29857	0.06189	0.01372	-1.12075	0.84629

668	0.87148	29.80021	-1363.96460	-0.13054	0.29752	0.06090	0.01347	-1.13439	0.83490
669	0.87155	28.74454	-1456.49976	-0.12629	0.29616	0.05972	0.01319	-1.16440	0.81357
670	0.87176	31.29255	-1268.15967	-0.12192	0.29518	0.05885	0.01298	-1.14505	0.82127
671	0.87081	26.99378	-2154.00708	-0.11791	0.29408	0.05777	0.01272	-1.16483	0.80780
672	0.86880	28.31562	-2470.26294	-0.11403	0.29273	0.05654	0.01243	-1.15681	0.79604
673	0.87067	26.35830	-2312.62671	-0.11004	0.29176	0.05557	0.01219	-1.18081	0.79057
674	0.87008	30.97227	-1652.79883	-0.10609	0.29075	0.05464	0.01196	-1.17213	0.79781
675	0.87120	23.26550	-2286.18750	-0.10214	0.28974	0.05361	0.01170	-1.22163	0.78920
676	0.87188	21.36513	-2063.00635	-0.09613	0.28818	0.05252	0.01143	-1.30691	0.74449
677	0.87107	31.75695	-1141.17615	-0.09652	0.28602	0.05231	0.01131	-1.22311	0.77045
678	0.87230	24.68333	-1769.68359	-0.09667	0.28433	0.05218	0.01116	-1.26791	0.75759
679	0.87255	23.63054	-1676.82239	-0.09693	0.28236	0.05197	0.01102	-1.27838	0.76742
680	0.87250	21.43834	-1529.08459	-0.09716	0.28042	0.05171	0.01086	-1.31071	0.75885
681	0.87240	22.98478	-1596.62012	-0.09641	0.27830	0.05160	0.01075	-1.28515	0.78605
682	0.87253	22.94524	-1452.43250	-0.09554	0.27621	0.05131	0.01057	-1.34610	0.74625
683	0.87248	23.96902	-1399.22888	-0.09476	0.27412	0.05117	0.01044	-1.36604	0.74590
684	0.87261	23.99507	-1377.02454	-0.09395	0.27202	0.05095	0.01029	-1.39233	0.74484
685	0.87274	24.34376	-1343.62036	-0.09317	0.26978	0.05065	0.01014	-1.42862	0.73369
686	0.87185	22.49439	-1598.22046	-0.08997	0.26724	0.05039	0.00999	-1.47769	0.72559
687	0.87158	24.51249	-1706.65442	-0.08685	0.26462	0.05010	0.00984	-1.49407	0.72827
688	0.87196	26.40957	-1352.96667	-0.08369	0.26205	0.04981	0.00969	-1.49787	0.75034
689	0.87058	29.87500	-1139.48438	-0.08056	0.25951	0.04952	0.00954	-1.52497	0.74250
690	0.87251	25.32455	-1471.87061	-0.07743	0.25695	0.04916	0.00937	-1.58223	0.73969
691	0.87222	25.22092	-1481.47644	-0.07090	0.25398	0.04886	0.00921	-1.63593	0.72590
692	0.87297	27.06992	-1117.03796	-0.06443	0.25106	0.04851	0.00902	-1.61031	0.77123
693	0.87406	26.83406	-867.87769	-0.05808	0.24798	0.04818	0.00889	-1.64851	0.77275
694	0.87369	26.92621	-914.45593	-0.05170	0.24506	0.04776	0.00870	-1.70203	0.77420
695	0.87298	24.26978	-1105.99792	-0.04543	0.24214	0.04740	0.00854	-1.82022	0.74875
696	0.87383	25.46304	-1040.26282	-0.03363	0.23849	0.04701	0.00838	-1.90868	0.72962
697	0.87369	26.05263	-1018.39624	-0.02201	0.23477	0.04643	0.00817	-1.99123	0.70418

698	0.87358	25.18481	-1134.43713	-0.01059	0.23112	0.04590	0.00798	-2.11162	0.64733
699	0.87177	27.93423	-1115.14587	0.00071	0.22768	0.04553	0.00785	-2.15380	0.64904
700	0.87429	24.98221	-1056.67944	0.01191	0.22437	0.04509	0.00767	-2.22542	0.65385

8.4 Algorithms to Derive Phase Function and Volume Scattering Function

8.4.1 Introduction

Since absorption and scattering are the processes, a photon undergoes when entering the water, and hence two IOPs, a(λ) and b(λ), are very important parameters that define the underwater light completely. All other AOPs can be derived from the knowledge of these IOPs (Mobley, 2013). The important parameters for ocean color remote sensing, the radiance that exits the surface of water $L_w(\lambda)$, and $R_{rs}(\lambda)$ are functions of scattering in water. One of the most important parameters of these is the inherent optical property of scattering coefficient, b(λ), and to understand the scattering, knowledge of the angular intensities of scattering is essential, which is defined by the phase function or volume scattering function of the water. The volume scattering function (VSF), β(ψ,λ) is the scattered intensity (I_s) per unit incident irradiance (E_i) per unit volume of water (ΔV) (unit is m^{-1} sr^{-1}).

$$\beta(\psi,\lambda) = \lim_{\Delta V \to 0} \frac{I_s(\psi,\lambda)}{E_i(\lambda)\Delta V} \tag{18}$$

It is the fraction of incident power scattered at an angle ψ forming a solid angle ΔΩ (Mobley, 1994). Integrating β(ψ,λ) over the complete solid angle, gives the much required scattering coefficient b(λ),

$$b(\lambda) = \int_{4\pi} \beta(\psi,\lambda) d\Omega = 2\pi \int_0^{\pi} \beta(\psi,\lambda) \sin\psi d\psi \tag{19}$$

Integrating over scattering angles ψ from 0 to π/2 will provide forwarding scattering coefficients, while backscattering is from π/2 to π. The backscattering coefficient is an essential parameter that determines the water leaving radiance and remote sensing reflectance. VSF can be used to determine the properties of particles in water, such as their refractive index and size distribution. VSF and absorption coefficients completely determine the inherent optical properties of the water (Mobley, Sundman, & Boss, 2002). The VSF is the total of the contributions from three components, pure water, particulates,

and from the turbulence of water (Mobley, 1994). Phase function, $\tilde{\beta}(\psi,\lambda)$ (hereafter referred to as FF) is defined as (unit is sr^{-1})

$$\tilde{\beta}(\psi,\lambda) = \frac{\beta(\psi,\lambda)}{b(\lambda)} \tag{20}$$

The FF provides information on the angular variations of the scattering. Despite the importance of VSF in understanding the underwater light field and deriving other optical parameters, there is very little information available on the VSF of waters of the world and no information of any waters around India. An instrument developed by the Marine Hydrophysical Institute (Ukraine) in cooperation with Satlantic Inc. (Canada) could measure VSF between 0.68° to 177.38° (Lee & Lewis, 2003). One of the earliest measurements carried-out of VSF was by Petzold (Petzold, 1972), and the same values are being used as the default for many applications and models. Hydrolight simulations have shown large errors in assuming VSF of Petzold for the waters of Goa (Talaulikar et al., 2014a; Thayapurath, Talaulikar, Desa, & Lotlikar, 2016). For most of the water types, the shape of VSF is similar and is asymmetrical. Looking at the five decade old measured FF of Petzold, it can be observed that above 50% of light is scattered into angles smaller than 5°, and above 96% of light is scattered into the forward hemisphere (scattering angle ψ from 0 to $\pi/2$).

8.4.2 Methodology

FF can be obtained by three approaches – by using earlier measured FF values such as Petzold for similar waters, actual measurement, and empirical or semi-analytical mathematical models. Using a standard FF such as Petzold could lead to erroneous results without considering the actual contributions and properties from various water constituents such as particles, phytoplankton, and even bubbles. Actual measurements are very difficult due to the non-availability of commercially proven instruments at all angles and the cost. Hence, empirical formulations were widely accepted due to their simplicity, and there are some accepted models (Freda & Piskozub, 2007, 2012; Gordon, 1989b; Haltrin, 1998,1999b; Sokoletsky, Kokhanovsky, & Shen, 2013).

Here the FF of Fournier-Forand (Fournier & Forand, 1994;Freda & Piskozub, 2007; Fournier, 2007) was used. This FF is modeled based on Mie theory, assuming Junge type

particle size distribution with properties of particles, namely refractive index and slope of the Junge particle size distribution. All the parameters were modeled using only the fraction of particle backscattering $B_p = b_{bp}/b_{p,}$ where b_{bp} is the particle backscattering coefficient i.e. excluding the contribution of water from total backscattering coefficient and similarly for scattering coefficient b_p (Mobley, Sundman, & Boss, 2002). The parameter b_p is the particle scattering coefficient that includes forward and backscattering. According to the quasi-single-scattering approximation, the remote-sensing reflectance depends only on the backscatter fraction, which represents the probability that a photon will be scattered through an angle $\psi > \pi/2$ (Gordon et al., 1988; Gordon, 1989b, 2019). Hence, algorithms to derive scattering coefficient or particulate scattering b_p were seldom used or available to derive the same from satellite data. Here however, an algorithm was developed to derive $b_p(650)$ using $b_{bp}(650)$, as they were found to covary with the measured values of the waters off Goa. The scattering coefficient b(650) was measured using the instrument AC-9 (WetLabs). AC-9 measures the spectral absorption and beam attenuation at nine wavelengths. The data on the backscattering coefficient $b_b(650)$ were obtained using the ECO-bb (WetLabs) backscattering sensor at 650nm available with the hyperspectral radiometer, Hyper-OCR (Satlantic). The relationship between scattering b(650) and backscattering coefficient $b_b(650)$ is given as

$$b(650) = m + nb_b(650)\ln[b_b(650)] \tag{21}$$

where m = -0.05678 and n= -14.379

The procedure to derive the FF is given in Figure 8.18. The Level-1B satellite data of OCM-2 were processed using the software SeaDAS (hhtp://seadas.gsfc.nasa.gov) to derive Level-2 products of spectral b_b. The spectral b_b at wavelengths of bands were obtained using the QAA algorithm (Lee et al., 2002) in the SeaDAS. Values of $b_{bp}(650)$ were derived from the spectral b_b using the power law relations of b_{bp} and λ. b(650) was derived using the empirical relationship given by Equation (21). The phase function was calculated using the fraction of scattering $B= B_p = b_{bp}(650)/b_p(650)$ as given by (Mobley et al., 2002).

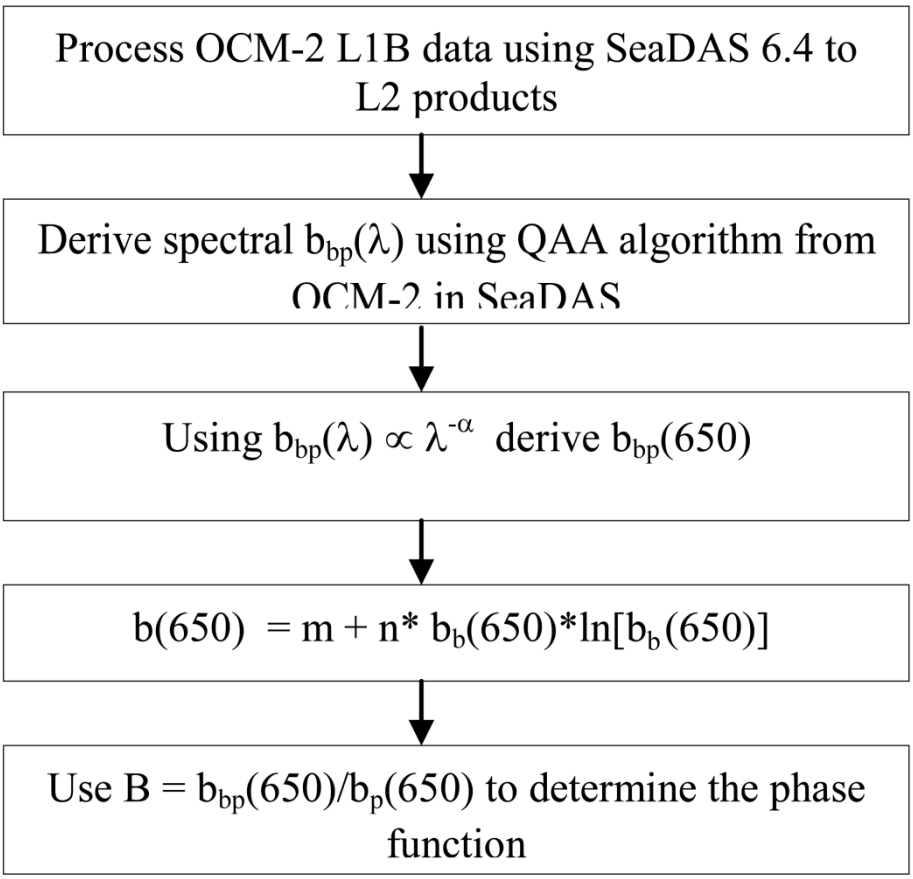

Figure 8.18 Procedure to derive phase function from OCM-2 satellite data.

8.4.3 Results

The PF at 117° (650 nm) derived using the measured and model data are given in Figure 8.19. The measured values compared well with the model (coefficient of determination R^2 = 0.99) and with slight underestimation (mean percentage deviation, MPD = -5.7 %). The $b_b(650)$ derived from OCM-2 data and those measured during the satellite pass correlated well with the coefficient of determination, R^2 = 0.82, however, with those derived from the satellite being underestimated (Figure 8.20).

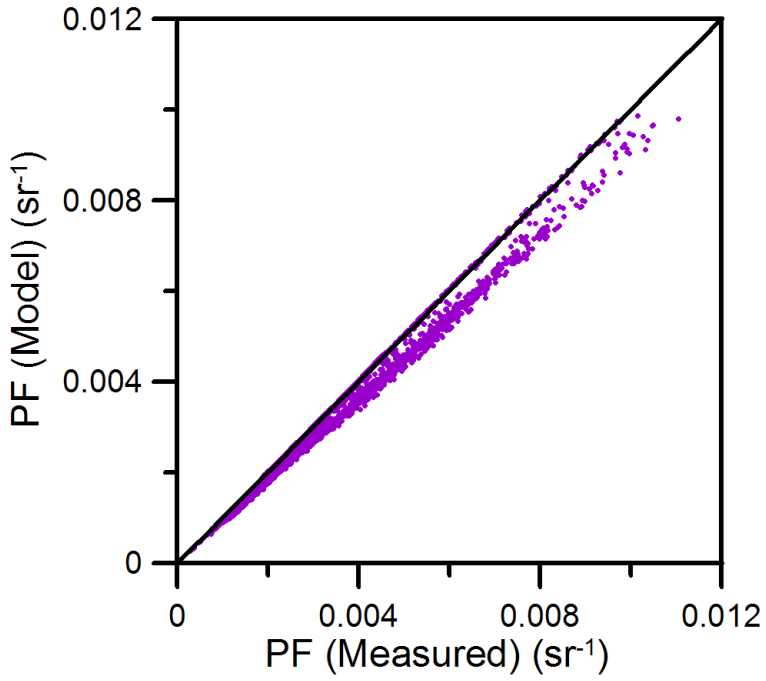

Figure 8.19 Comparison of PF at 117° with the measured and those derived using the model

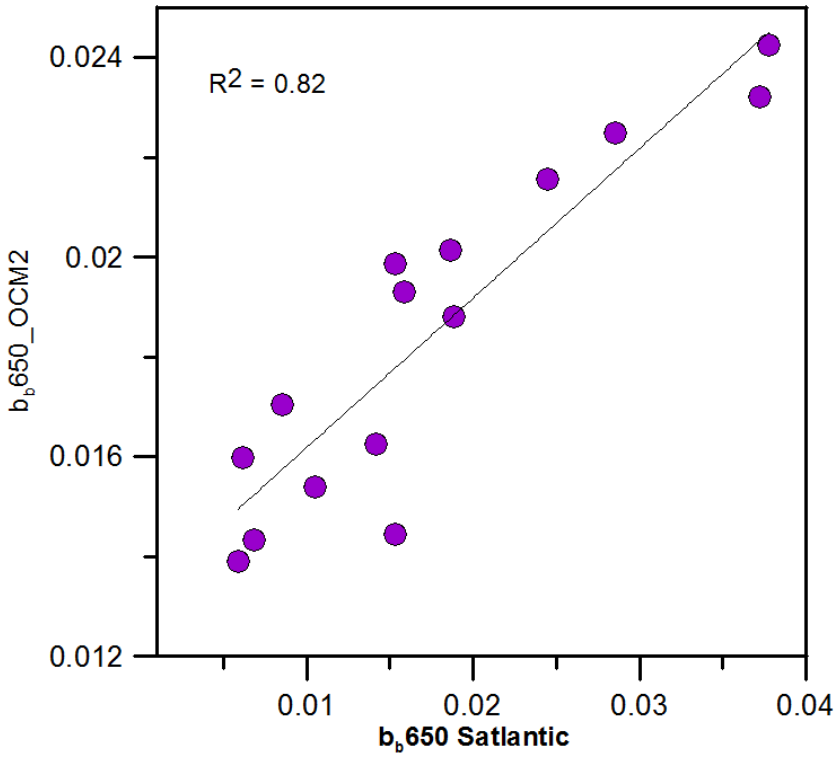

Figure 8.20 Comparison of backscattering coefficient derived from the satellite OCM-2 and the in-situ measured.

The phase function derived from the OCM-2 satellite data compared well and closely matched with the phase function of Petzold (See Figure 8.21).

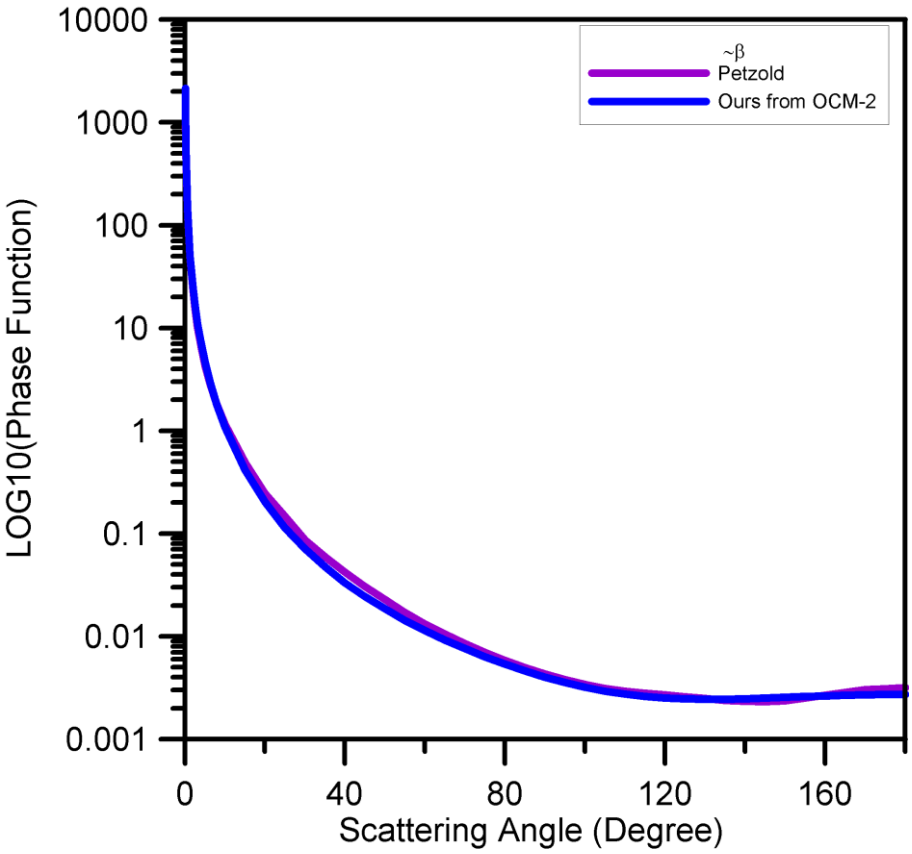

Figure 8.21 Comparison of FF derived from the satellite OCM-2 and the Petzold.

8.4.4 Conclusion

An algorithm was developed to determine the phase function and volume scattering function of water from the ocean color satellite data. The phase function (FF) is an important marine optical parameter required to understand the underwater light field. It is associated with scattering of light in water and provides information on the angular distribution of intensity or strength of scattering at any wavelength. The phase function measured at 117° compared well with the model. The empirical algorithm to derive the scattering coefficient developed using the backscattering coefficient at 650 nm could be used to derive the scattering coefficient at 650 nm.

The simple method to determine the VSF and FF to determine from satellite data will provide information on the water types, particulate matter, and parameters such as water leaving radiance and remote sensing reflectance. This method developed was relatively simpler compared to other methods reported to derive VSF from ocean color satellite (Desa, Desa, & Suresh, 2005b). It can also be considered as a probability density function

of the scattering in any direction. The parameter b_b can be determined with better accuracy from satellite data, and there are no proven algorithms to determine b from satellite data. The b_b determined from the OCM-2 satellite data at the wavelengths of the satellite bands and interpolated at 650nm correlated well with the in-situ measured $b_b(650)$. (R^2 =0.82), though it was overestimated. The root-mean-squared percentage difference between the two phase functions of Petzold and those derived from OCM-2 for all stations were and water types were less than 10%.

8.5 Algorithms to determine horizontal and vertical underwater visibilities

8.5.1 Introduction

Underwater visibility is the ability of a human to detect objects in the water, and it is measured as the distance that an object can be identified from the observer. It has importance and relevance to the Navy, marine archaeology, salvage operations, maintenance of ships, inspections of underwater structures, studies of marine flora and fauna and leisure sports, and other related applications. Underwater visibility is a function of three factors – an underwater environment, the object to be recognized or identified, and the diver or observer**.**

The vertical visibility is observed looking at an angle of 0 degrees or in the nadir direction normal to the surface of the water, and the horizontal visibility is the visibility inside the water looking at the target at 90 degrees with respect to the nadir. These visibilities are functions of the optical properties of water. The simple measurement of the vertical visibility suggested by Fr. Pietro Angelo Secchi, an Italian astrophysicist in April 1865 using a disk lowered in the water, is presently known as Secchi depth and has been used since long by the oceanographers. There have been many empirical relationships between vertical visibility and bio-optical parameters (Boyce, Lewis, & Worm, 2010; Holmes, 1970; Tyler, 1968). Though there are methods used to determine the vertical visibility or Secchi depth from the satellite data, there are few methods available to determine horizontal visibility from the satellite data (Doron et al.,2007; Haltrin, 1999a).

Here algorithms are described to determine both vertical and horizontal visibilities from the satellite data and their validations for the waters off Goa.

8.5.2 Methodology

The underwater visibility depends on four parameters - a radiation source (sunlight), a medium that the radiation travels through (water), an object or target, and a sensor (human eye). Here the luminous flux or the brightness of light as observed by the human eye is determined, which is given in lumens per cross-sectional area per solid angle centered in the direction of viewing. (Lumens/m^2/sr). A fundamental law of visibility as derived by

Duntley, 1960, Jerlov N.G., (1976) and Preisendorfer R. W.,(1976) is based on the contrast of the object with reference to the background. The derivation of this law follows directly from the equation of radiative transfer (Zaneveld & Pegau, 2003). The theory is based on determining the brightness contrast of the target in water with respect to the background. The contrast *C* (also known as Weber contrast) is defined as the normalized luminance or brightness with respect to the background.

$$C = \frac{I_T - I_B}{I_B} \tag{22}$$

where I_B is the luminance of the background, and I_T is the luminance of the target. Luminance is analogous to brightness and is the photometric equivalent of radiance. The contrast theory of visibility has been developed using the radiative transfer and the visibility model based on the contrast of the target and the background, with some valid assumptions and empirical approximations. The contrast theory derived fundamental contrast model is given below (Duntley, 1960; Preisendorfer, 1986; Zaneveld & Pegau, 2003). The range of visibility Z in meters is given as

$$Z = \frac{\Gamma}{c + K_d \cos(\theta)} \tag{23}$$

where c is the beam attenuation coefficient (an inherent optical property of water), K_d is the diffuse attenuation coefficient (an apparent optical property of water) and $\Gamma = -\ln(C_t)$ is the coupling parameter that is a function of limiting contrast of the eye and θ is the viewing angle with respect to the nadir. For vertical viewing and finding vertical visibility $\theta = 0°$ and for horizontal visibility $\theta = 90°$. The target is assumed to be darker than the background; hence, the limiting contrast is a negative value. Contrast that leads to a 50% probability of detection is called the threshold contrast and is identified as C_t and this depends on the lighting of the background and the angular size of the target. There is a limiting contrast for humans, which is assumed to be reasonably constant. Though the low value of $C_t = 0.003$ is reported to be acceptable (Gordon & Wouters, 1978; Preisendorfer, 1986), it is argued that the smallest value of $C_t = 0.01$. The reported values of Γ were close to 9 (Tyler, 1968).

Equation (24) is applicable to monochromatic light. The diver or the observer views the target with the eye. The eye views spectral light with a weighting function is known as the luminosity function of the eye, and the maximum region known as the photopic region of the eye is around 555 nm under adequate lighting conditions. Hence, for a human viewer, the underwater vertical visibility (Equation (24)) and horizontal visibility (Equation (25)) were derived using the photopic optical properties as given here

$$Vertical\,Visibility = \frac{\Gamma}{c(v) + K_d(v)} \tag{24}$$

$$Horizontal\,Visibility = \frac{\Gamma}{c(v)} \tag{25}$$

These models are applicable for the photopic equivalent of the radiometric optical properties, and c(v) and K_d(v) are the photopic beam attenuation and diffuse attenuation coefficient, respectively. Though the models use the photopic optical properties, most algorithms just use the radiometric optical properties of water. The algorithms described here finds the relationships between the photopic and radiometric optical properties to have some precise meaning to the underwater visibilities models based on contrast theory. The approach towards the formulations of the algorithms for the vertical and horizontal visibilities is given in Figure 8.22.

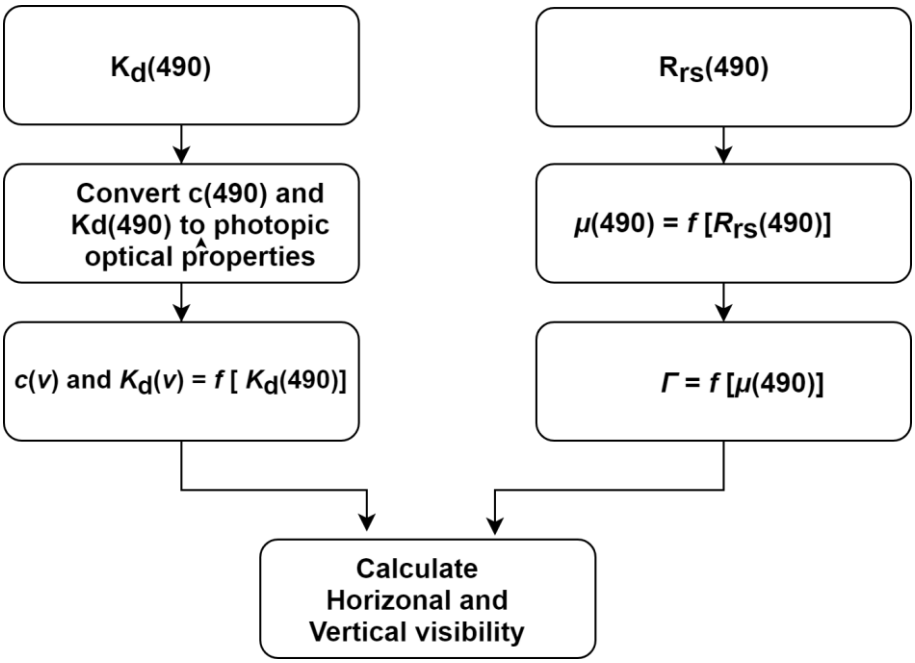

Figure 8.22 Approach towards the development of the visibilities algorithm

The algorithms require only two optical parameters, $K_d(490)$ and $R_{rs}(490)$, both of which can be derived from the ocean colour satellite data. The $R_{rs}(490)$ is available directly from the satellite data after atmospheric correction, while there are robust algorithms that can determine $K_d(490)$ from the satellite data (Thayapurath & Talaulikar, 2011). The algorithms have been developed using the apparent optical properties $K_d(490)$ and $R_{rs}(490)$ measured by a hyper-spectral radiometer of Satlantic make, and the beam attenuation at 490 nm was obtained from the in-situ measurements using AC-9 instrument of WetLabs make. The measurements were carried out in the coastal waters off Goa.

The photopic values of beam attenuation, $c(v)$ and diffuse attenuation coefficient, $K_d(v)$ were derived from the radiometric value of K_d at 490 nm using Equation (26) and Equation (27) respectively.

$$c(v) = 4.16566 K_d(490) \tag{26}$$

$$K_d(v) = 0.1128 + (0.726650\, K_d 490) - (0.0197436 * (K_d 490^2)) \tag{27}$$

The underwater average cosine at 490 nm was calculated using the value of R_{rs} at 490 nm (Talaulikar, Thayapurath, & Desa, 2012).

$$\mu(490)=0.2035\left(Rrs(490)^{-0.223}\right) \quad (28)$$

The coupling parameter Γ was found to be in the range of 4.8 to 6.8 (Figure 8.23). Unlike most others who have assumed a constant value of Γ, considering the variations of this coupling parameter Γ it was modeled as a function of underwater average cosine at 490 nm (Equation (29)).

$$\Gamma=10.17530\,\mu(490) \quad (29)$$

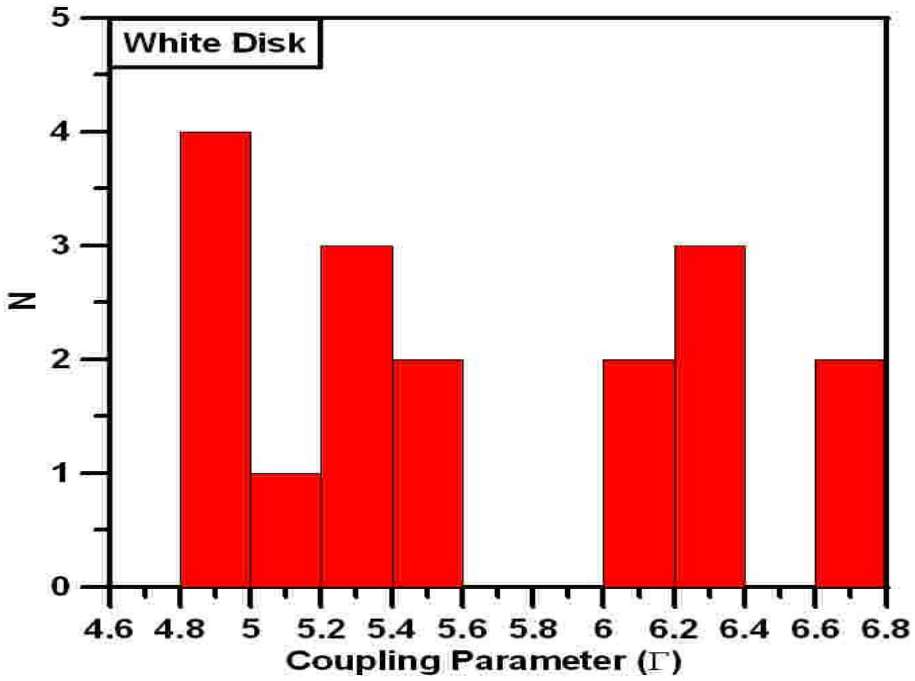

Figure 8.23 Histogram of Γ

8.5.3 Results and discussion

8.5.3.1 Validation using measured data

The measurements were carried out in the coastal waters off Goa. The target was a white disk of 30 cm diameter with a Lambertian type surface. To measure vertical visibility, the disk was mounted on a line and lowered slowly down in the water till it disappeared. It was then slowly raised till it appeared again. The depth of the water where the disk vanished and reappeared was measured as the vertical visibility depth (m). To measure horizontal visibility, the target disk was mounted at the center of a large black square metal plate to avoid any reflection from the boat. The target mounted on the dark plate was placed at a

depth of 2 m from the water surface. To determine the horizontal visibility, one end of a measuring tape was tied to the center of the target while the other end was held by the diver who moved horizontally away from the target till it disappeared. Optical properties were measured of the same waters using profiling optical instruments. The optical parameters were averaged within the depth of vertical visibility, and it was observed that there were no large variations in the water column of the optical properties. Hence, the average was assumed to be close to the average within the satellite penetration depth of first optical depth, Z_{90}.

The measured vertical and horizontal visibilities compared well with the model (Figure 8.24).

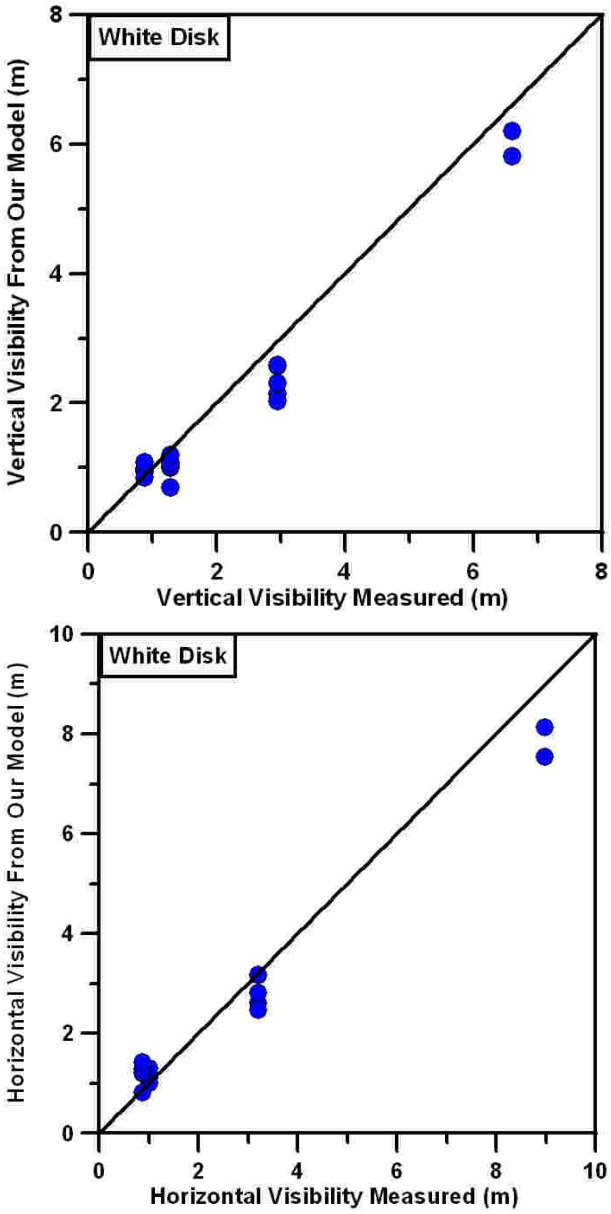

Figure 8.24 Comparisons of vertical (Left) and horizontal visibilities (Right) measured during validation as compared to those derived using the models.

The visibilities models were also validated with Z_{sd} measured in the coastal and estuaries. Here Z_{sd} was considered equivalent to measured vertical visibility (VV). The derived vertical visibility (VV) using the model compared well with the measured values, Measured Zsd = 1.0097*VV + 0.0029 (R2 = 0.98 and RMSE =0.01(Figure 8.25).

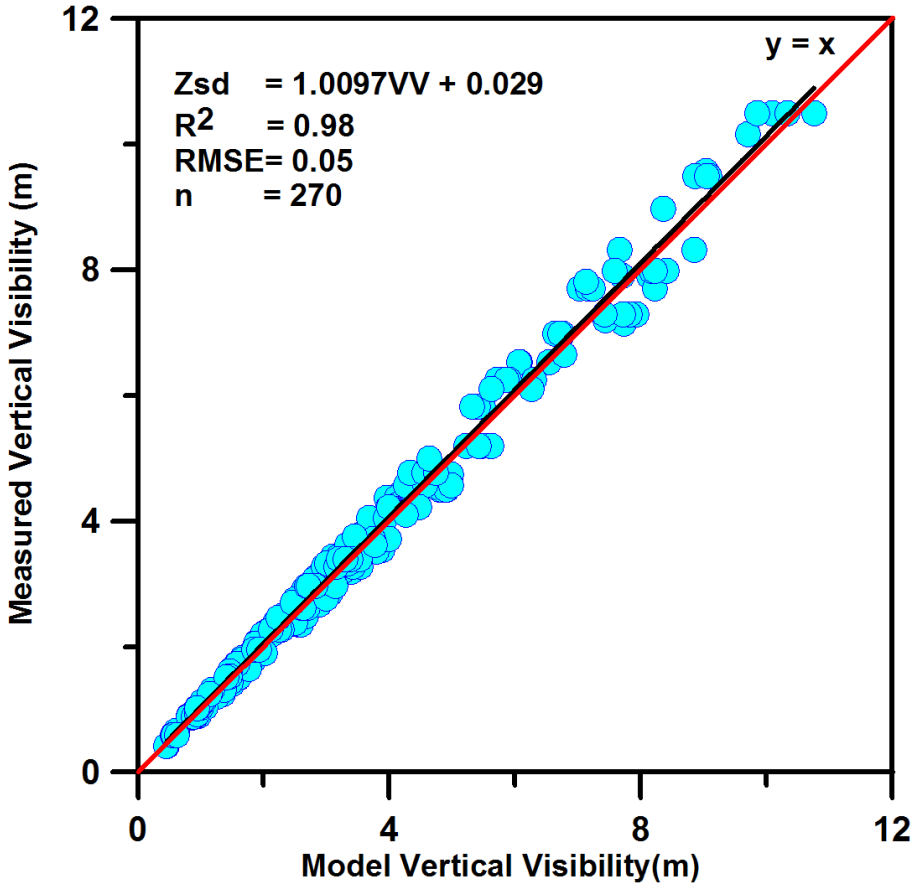

Figure 8.25 Validation of the model with measured values of the coastal and estuaries of Goa

The relationship between vertical visibility and horizontal visibility was found to be linear. The horizontal visibility was about 1.3 times the vertical visibility, HV ≈ 1.3 VV (Figure 8.26). For a limiting case with the pure water values in Equations (24) and (25), the approximate value of this factor would be about 2.0.

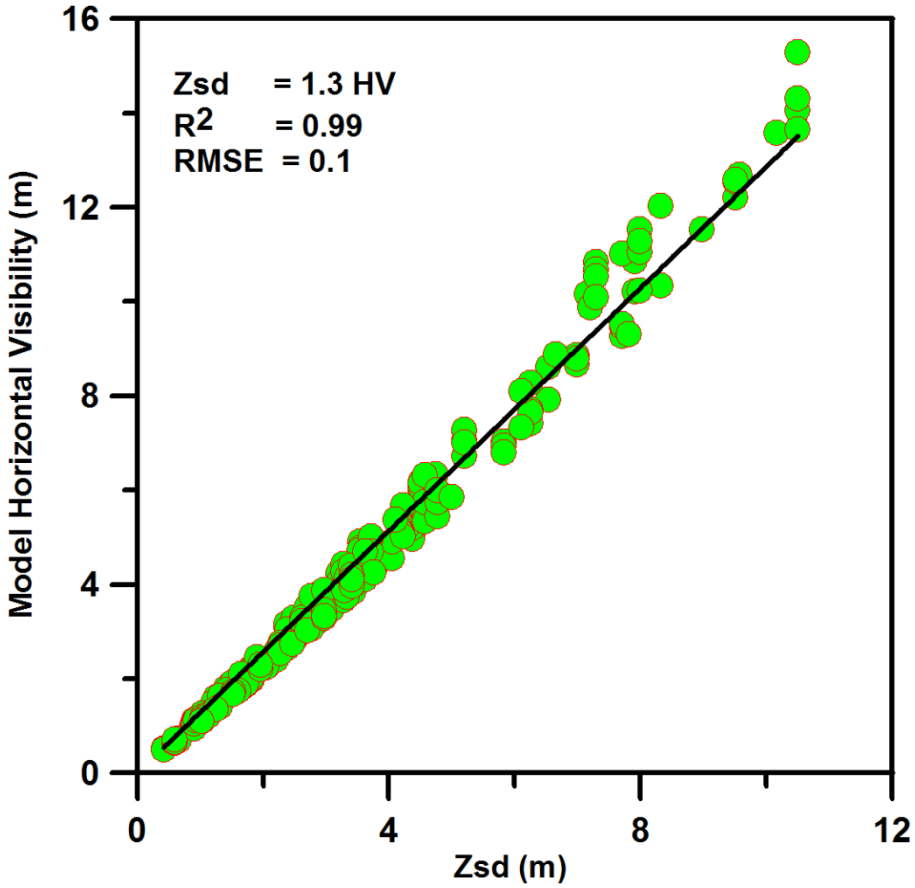

Figure 8.26 Relationship of vertical (Z_{sd}) and horizontal visibility

8.5.3.2 Validation using the satellite data

The model was validated deriving the horizontal and vertical visibilities from the ocean color satellite data of OCM-2 (Figure 8.27 and 8.29) and MODIS (Figure 8.28) for the day of the validation experiment of 20 February 2015. The satellite data were processed using the software SeaDAS 7.2

Table 8.6 Vertical and horizontal visibilities measured and derived from OCM-2 in the coastal waters off Goa

Vertical Visibility Measured (m)	Vertical Visibility from OCM-2 (m)	Horizontal Visibility Measured (m)	Horizontal Visibility from OCM-2 (m)
2.95	4.06	3.19	5.19
6.6	6.02	8.98	8.06

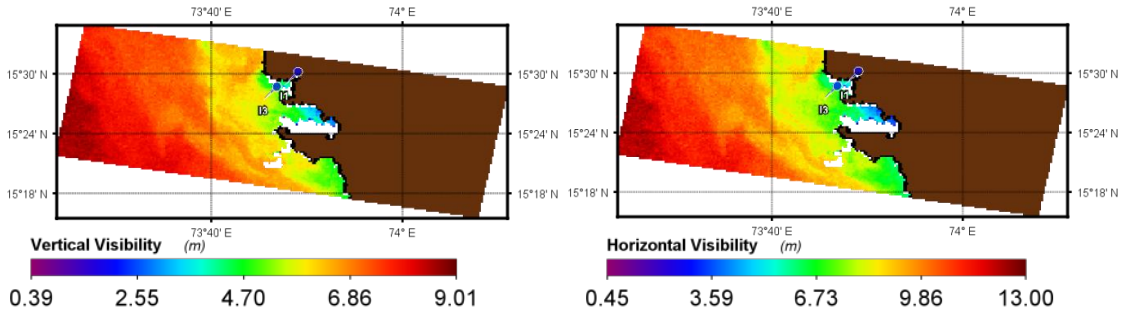

Figure 8.27 Vertical(left) and horizontal (right) visibilities derived from satellite data, OCM for 20 February, 2015

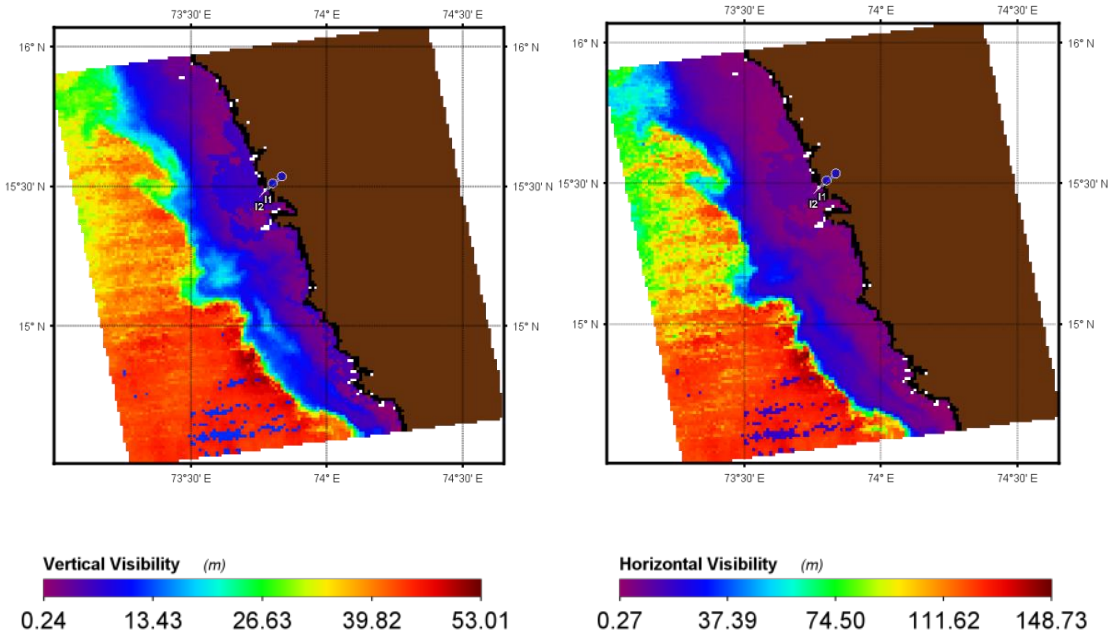

Figure 8.28 Vertical(left) and horizontal (right) visibilities derived from satellite data, MODIS for 20 February, 2015

Table 8.7 Vertical and horizontal visibilities measured and derived from MODIS in the coastal waters off Goa

Vertical Visibility Measured (m)	Vertical Visibility from MODIS (m)	Horizontal Visibility Measured (m)	Horizontal Visibility from MODIS (m)
2.95	3.83	3.19	4.82
6.6	5.76	8.98	7.56

The vertical visibilities derived in the low visibility coastal waters from the satellite data were over-estimated (37.6% from OCM-2 and 29.8% from the MODIS), while it was marginally underestimated in the high visibility coastal waters. (-8,8% for OCM-2 and -

12.7% for the MODIS). Similar trends were also observed for the horizontal visibilities derived from the satellite, with overestimation of above 50% for the low visibility coastal waters and underestimated by -10.24% for OCM-2 and -15.8% for MODIS in the high visibility coastal waters.

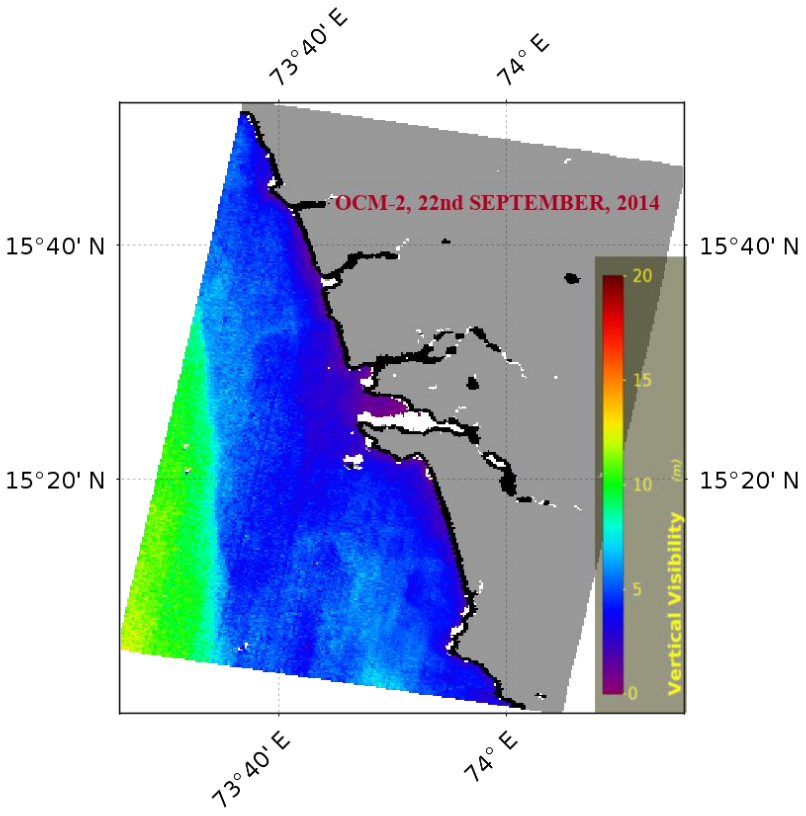

Figure 8.29 Vertical visibility or Zsd using the algorithm for the waters off Goa from OCM-2

8.5.3.3 Conclusion

The models to determine vertical and horizontal visibilities of coastal waters performed well for a wide range of visibilities in the coastal and estuarine waters. The model uses the photopic values rather than radiometric values for the optical parameters in the model.

The horizontal and vertical visibilities derived from the MODIS and OCM-2 satellite data provided very promising results. The errors were larger for lower visibility ranges as compared to the higher visibilities of coastal waters. This probably could be due to the errors in the optical parameters derived from the satellite.

The model required only two apparent optical parameters at 490 nm, K_d and R_{rs} and was easy to implement.

It uses the contrast model and does not relate the visibilities with any other parameters directly to provide any empirical relations. It is a function of optical properties alone. do not use any other parameters such as turbidity or chlorophyll

Limiting contrast or coupling factor, Γ is derived using a model and is not considered as constant.

The model for vertical visibility compared well with the measured values.

Horizontal visibility ≈ 1.3x Vertical visibility

CHAPTER 9. CONCLUSIONS

The objectives were to study the optically complex waters which had large variations of various parameters, features, and factors that controlled the optical properties and develop algorithms to derive optical parameters for ocean color applications from such waters. Hence, the chosen coastal and monsoonal estuaries Mandovi, and Zuari provided the opportunities to carry-out studies not done earlier using large data of IOPS, AOPs, the biological, physical, and ancillary parameters measured in these waters spanning from coastal waters to upstream of the estuaries all through the year. The optical and other parameters of *Trichodesmium* spp. described will be useful for various studies. The novel method could determine the distinct peaks in $R_{rs}(\lambda)$ measured during *Trichodesmium* spp. and the troughs in $R_{rs}(\lambda)$ could be used to find the spectral absorption peaks of pigments. This method could be used to identify blooms. The studies were carried-out with RTE simulations, measured, and satellite data. The results showed the spatial and temporal variations of optical properties during monsoon and dry seasons of the estuaries, and dry seasons of the coastal waters. Most studies earlier had emphasized salinity as the driving parameter in these estuaries; while the studies undertaken here have shown that, the temperature also plays an important role in modifying and regulating the optical and biological parameters. The study revealed the behavior of optical parameters and physical features like MLD, ILD, thermal inversion, and bottom warming observed in these waters which were never reported earlier. These were distinct classes of waters identified. In the estuaries, particulate matter controlled the underwater light penetration, clarity, and transparencies. The cluster analysis showed waters with distinct optical, biological, and physical properties, which were spatially separated and season invariant. The results could help in applying switching algorithms to derive parameters such as chlorophyll and other applications. The objectives of deriving optical parameters from ocean color satellites with new and novel approaches from these optically complex waters yielded favorable and encouraging results.

There were studies undertaken that could not be completed due to lack of time such as radiant heating rates and errors in the estimation of chlorophyll due to the contributions of picoplankton (Suresh, Ramakrishnan et al., 2019). The results of the study on the radiant heat of these waters show that the temperature rise could be influenced by fine particles, CDOM, and detritus. The present method of using the GF/F filter for the chlorophyll

analysis could miss out on the contributions from picoplankton, and these contributions in the estuaries are found to be significant. Hence, the studies suggest using a smaller pre size of 0.2-micron filters to minimize errors in estimating chlorophyll from these waters.

A spinoff of and outcome of the present studies was the recommendation to the Indian Space Research Organisation (ISRO) for the bands to detect *Trichodesmium* blooms from the forthcoming next of the series of Oceansat, OCM-3 satellite sensor, which has been considered. As recommended, OCM-3 will have bands close to 566 nm.

The coastal and estuaries are important and using satellite remote sensing could help in various studies of these waters. Ocean color satellites provide products that would help in water quality assessments and the productivity of these waters. The new algorithms have been developed for these waters which differ from open ocean Case-1 waters and such algorithms are the focus of the present studies undertaken by ocean color community world over, thus would find applications in ocean color remote sensing and models. Since no other studies have been carried-out of these waters using large data of various parameters, the data and the findings become important for the long-term assessments of the health of these waters and future studies.

Though few studies undertaken here have not been attempted earlier, these studies have lots of scope for further investigations and research in similar and other unexplored ocean color related topics.

An estuary is derived from the Latin word *aestuarium and aestus* associated with tides. Most studies in the estuaries have focused on the tides to understand the variations of parameters of these estuaries and considering the relevance of the tides a time-series study was undertaken. Since the prime objectives were to understand the optical parameters and develop algorithms, it was thought prudent to measure and acquire large data of these waters with wide variations. Hence, because of time and some logistic constraints studies related to the tides were not undertaken. However, time-series studies together with chemical, biological and physical parameters should be undertaken, which will provide results to understand the interactions and processes of these estuaries with tides. There is a need to understand the Phytoplankton Functional Types (PFT) and phytoplankton size Classes (PSC) of these estuaries and develop suitable algorithms for their assessment.

Ocean color has been considered important to understand climate change. Apart from chlorophyll, there are other ocean color essential climate variables (ECV) which include AOPs and IOPS that need to be measured accurately. There are many parameters to be derived with better accuracy in these waters, such as the much sought after chlorophyll, absorption due to phytoplankton, CDOM, detritus, VSF, bottom reflectance, particles size distribution parameters, refractive index, various attenuations coefficients, scalar irradiance, average cosine, and others. Methods to derive these parameters with accuracy from such optically complex waters are challenging. There is also a need to develop sensors and instruments to measure some of the optical parameters.

The studies undertaken should be continued which will help in understanding these waters around us better and also help in ocean color applications with the continued support from ISRO in launching state of the art sensors in the future.

APPENDIX A

Publications

1. **Thayapurath, Suresh**, Albertina Balbina Dias, Erwin J.A. Desa, and Arvind Sahay. 2018. "An Algorithm to Determine the Slope of the Spectral Absorption of Colored Dissolved Organic Matter (CDOM) and Detritus." Journal of the Indian Society of Remote Sensing 46 (4). Springer India: 625–31. doi:10.1007/s12524-017-0722-6.
2. **Thayapurath, Suresh**, Shreya Joshi, Madhubala Talaulikar, and Erwin J. A. Desa. 2016. "Preliminary Results of Algorithms to Determine Horizontal and Vertical Underwater Visibilities of Coastal Waters." SPIE 9878: 98781I. doi:10.1117/12.2238595.
3. **Thayapurath Suresh**, Madhubala Talaulikar, Erwin J. A. Desa, and Aneesh Lotlikar. 2016. "Preliminary Results of an Algorithm to Determine the Total Absorption Coefficient of Water" 9878: 98780E. doi:10.1117/12.2235777.
4. **Suresh T**, Talaulikar M, Desa Erwin, 2013. Preliminary results of algorithms to derive phase function and volume scattering function from OCM-2. Proceedings of OSICON 2013, 298-300

Papers presented at conferences

1. **Suresh T**., Reshmitha Ramakrishnan, Albertina Dias, Choudhury S.B. Underestimation of chlorophyll in the estuarine waters of Goa. WOSC, Vishakhapatnam, 25-27 February, 2019.
2. **Suresh T**., Albertina Dias, Erwin J.A. Desa, Some insight into the transparencies of the coastal and estuarine waters of Goa, ICESAL-2018, Mysore, 2-3 July, 2018.
3. **Suresh T**., Albertina Dias, Erwin J.A. Desa , Some factors that control the transparencies of coastal and estuarine waters of Goa, WOSC-2019, Vishakpatnam, 25-27 February, 2019.
4. **Suresh T**., S. Joshi, M.Talaulikar, and Erwin J. A. Desa. 2016. Preliminary results of algorithms to determine horizontal and vertical underwater visibilities of coastal waters, SPIE Asia-Pacific Remote Sensing, New Delhi, 4-7 April, 2016
5. **Suresh T**., Madhubala Talaulikar, Erwin J. A. Desa, and Aneesh Lotlikar. 2016. Preliminary results of an algorithm to determine the total absorption coefficient of water, SPIE Asia-Pacific Remote Sensing, New Delhi 4-7 April, 2016.
6. **Suresh T**., Albertina Dias, Madhubala Talaulikar, Erwin J. A. Desa, and Aneesh Lotlikar, Preliminary results of an algorithm to determine absorption coefficient due to the phytoplankton - an effective tool to identify phytoplankton types, SPIE Asia-Pacific Remote Sensing, New Delhi 4-7 April, 2016.

Under review/to be submitted after revision/

1. **Thayapurath Suresh**, Albertina Dias, Erwin J.A. Desa, Examining optical properties and the transparencies of coastal and estuarine waters of Goa
2. **Thayapurath Suresh**, Madhubala Talaulikar, Albertina Dias, Erwin J.A. Desa**,** An algorithm to determine the spectral total absorption coefficient of water
3. **Thayapurath Suresh**, Albertina Balbina Dias, Erwin Joseph Alfred Desa, Arvind Sahay, A Simple Algorithm To Determine Absorption of Colored Dissolved Organic Matter And Detritus
4. **Thayapurath Suresh**, Albertina Balbina Dias, Erwin Joseph Alfred Desa, Radiant heating rates of estuaries and coastal waters of Goa
5. **Thayapurath Suresh**., Mithilesh Mane, Erwin J.A. Desa, A simple method to determine the upper surface iso-layer of coastal and estuarine waters

Other publications in bio-optics/ ocean color (2014-2019)

1. Ramakrishnan, R., **Thayapurath, Suresh**, Manguesh, U.G. and Dias, A.B., 2018. "Low light phytoplankton genera observed in the coastal and estuarine waters of Goa, India". *Applied Ecology And Environmental Research*, *16*(2), pp.1783-1796
2. Talaulikar, M., **Suresh, T**., Desa, E., &Inamdar, A. (2015). "Optical closure of apparent optical properties in coastal waters off Goa". *Journal of the Indian Society of Remote Sensing*, 43(1), 163-171002E. IF: 0.68
3. Nagamani, P.V., Latha, T.P., Rao, K.H., **Suresh, T**., Choudhury, S.B., Dutt, C.B.S. and Dadhwal, V.K., (2015). "Setting of cloud albedo in the atmospheric correction procedure to generate the ocean colour data products from OCM-2". *Journal of the Indian Society of Remote Sensing*, *43*(2), pp.439-444.
4. Talaulikar, M., **Suresh, T**., Desa, E., & Inamdar, A. (2015). Optical closure of apparent optical properties in coastal waters off Goa. *Journal of the Indian Society of Remote Sensing*, *43*(1), 163-171.
5. Silveira, N., **Suresh, T**., Talaulikar, M., Desa, E., PrabhuMatondkar, S. G., &Lotlikar, A. (2014). "Sources of errors in the measurements of underwater profiling radiometer". *Indian Journal of Marine Sciences*, 43(1), 88-95.
6. Tholkapiyan, Muniyandi, Palanisamy Shanmugam, and **Suresh T**.. (2014) "Monitoring of ocean surface algal blooms in coastal and oceanic waters around India." *Environmental monitoring and assessment* 186.7 4129-4137
7. Talaulikar, M., **Suresh T**., Elgar Desa, Arun Inamdar. 2014. "An empirical algorithm to estimate spectral average cosine of underwater light field from remote sensing data in coastal oceanic waters". *Limnology and Oceanography: Methods*, 12, 74-85
8. Albertina Balbina Dias, **Suresh Thayapurath**, Aravind Sahay, Prakash Chauhan. (2017). "Contrasting Characteristics Of Colored Dissolved Organic Matter Of The Coastal And Estuarine Waters Of Goa During Summer". *Indian Journal Of Geo-Marine Science*. 46(05): 860-870.

REFERENCES

1. Aguirre-Gómez, R., Weeks, A. R., & Boxall, S. R. (2001). The identification of phytoplankton pigments from absorption spectra. *International Journal of Remote Sensing*, *22*, 315–338.
2. Albert, A., & Mobley, C. (2003). An analytical model for subsurface irradiance and remote sensing reflectance in deep and shallow case-2 waters. *Optics Express*, *11*, 2873–2890.
3. Albert, A., Gordon, H., Loisel, H., Stramski, D., Mitchell, B. G., Fell, F., … Aiken, J. (2002). Inverse methods in hydrologic optics. *Applied Optics*, *40*, 9–58.
4. Allen, G. P., Salomon, J. C., Bassoullet, P., Du Penhoat, Y., & De Grandpre, C. (1980). Effects of tides on mixing and suspended sediment transport in macrotidal estuaries. *Sedimentary Geology*, *26*(1-3), 69-90. https://doi.org/10.1016/0037-0738(80)90006-8
5. Alvain, S., Moulin, C., Dandonneau, Y., & Bréon, F. M. (2005). Remote sensing of phytoplankton groups in case 1 waters from global SeaWiFS imagery. *Deep-Sea Research Part I: Oceanographic Research Papers*, *52*, 1989–2004.
6. Austin, R. W. (1974). The remote sensing of spectral radiance from below the ocean surface. *Optical aspects of oceanography*, 317-344.
7. Austin, R. W., & Petzold, T. J. (1981). The Determination of the Diffuse Attenuation Coefficient of Sea Water Using the Coastal Zone Color Scanner. In *Oceanography from Space*. https://doi.org/10.1007/978-1-4613-3315-9_29
8. Austin, R. W., & Petzold, T. J. (1984, September). Spectral dependence of the diffuse attenuation coefficient of light in ocean waters. In *Ocean Optics VII* (Vol. 489, pp. 168-178). International Society for Optics and Photonics. https://doi.org/10.1117/12.943302
9. Austin, R. W., & Petzold, T. J. (1990, September). Spectral dependence of the diffuse attenuation coefficient of light in ocean waters: a reexamination using new data. In *Ocean Optics X* (Vol. 1302, pp. 79-93). International Society for Optics and Photonics. https://doi.org/10.1117/12.21436
10. Bailey, S. W., & Werdell, P. J. (2006). A multi-sensor approach for the on-orbit validation of ocean color satellite data products. *Remote Sensing of Environment*, *102*(1-2), 12-23. https://doi.org/10.1016/j.rse.2006.01.015
11. Baker, K. S., & Smith, R. C. (1980). Quasi-inherent characteristics of the diffuse attenuation coefficient for irradiance. *Ocean Optics VI*, 60–63.
12. Banse, K. (2004). Should we continue to use the 1% light depth convention for estimating the compensation depth of phytoplankton for another 70 years? *Limnology and Oceanography Bulletin*, *13*, 49–72.
13. Berman, T., Walline, P. D., Schneller, A., Rothenberg, J., & Townsend, D. W. (1985). Secchi disk depth record: A claim for the eastern Mediterranean 1. *Limnology and oceanography*, *30*(2), 447-448. https://doi.org/10.4319/lo.1985.30.2.0447
14. Bhargava, R. M. S., & Dwivedi, S. N. (1976). *Seasonal Distribution of Phytoplankton Pigments in the Estuarine System of Goa*. *5*, 87–90.
15. Bhatnagar, G., & Purushothaman, A. (1974). Light Penetration in Vellar Estuary. *Indian Journal of Geo-Marine Sciences (IJMS)*, *178*.
16. Bhattathiri, P., Devassy, V., & Bhargava, R. (1976). Production at different trophic levels in the estuarine system of Goa. *Indian Journal of Geo-Marine Sciences (IJMS)*, *05*, 83–86.
17. Bidigare, R. R., Ondrusek, M. E., Morrow, J. H., & Kiefer, D. A. (1990). In-vivo absorption properties of algal pigments. *Ocean Optics X*,f *1302*, 290.

18. Boss, B. Y. E., & Amski, Dariusz S T R, Trisha Bergman, W.Scott Pegau, M. L. (2004). Why should we measure optical backscattering ? *Oceanography*, *17*, 45–49.
19. Boss, E, & Pegau, W. S. (2001). Relationship of light scattering at an angle in the backward direction to the backscattering coefficient. *Applied Optics*, *40*, 5503–5507.
20. Boss, Emmanuel, D'Sa, E. J., Freeman, S., Fry, E., Mueller, J. L., Pegau, S., … Zaneveld, J. R. V. (2018). *Ocean Optics & Biogeochemistry Protocols for Volume 1: Inherent Optical Property Measurements and Protocols: Absorption Coefficient (v1.0)*. *1*, 83.
21. Boss, Emmanuel, Twardowski, M., & Herring, S. (2001). Shape of the particulate beam attenuation spectrum and its inversion to obtain the shape of the particulate size distribution. *Applied Optics*, *40*, 4885–4893.
22. Boyce, D. G., Lewis, M. R., & Worm, B. (2010). Global phytoplankton decline over the past century. *Nature*, *466*, 591–596.
23. Brenon, I., & Le Hir, P. (1999). Modelling the turbidity maximum in the Seine estuary (France): identification of formation processes. *Estuarine, coastal and shelf science*, *49*(4), 525-544. https://doi.org/10.1006/ecss.1999.0514
24. Brewin, R. J. W., Sathyendranath, S., Müller, D., Brockmann, C., Deschamps, P. Y., Devred, E., … White, G. N. (2015). The Ocean Colour Climate Change Initiative: III. A round-robin comparison on in-water bio-optical algorithms. *Remote Sensing of Environment*, *162*, 271–294.
25. Bricaud, A., & Morel, A. (1986). Light attenuation and scattering by phytoplanktonic cells: a theoretical modeling. *Applied Optics*, *25*, 571–580.
26. Bricaud, A., Morel, A., & Prieur, L. (1981). Absorption by dissolved organic matter of the sea (yellow substance) in the UV and visible domains. *Limnol. Oceanogr*, *26*, 43–53.
27. Buonassissi, C. J., & Dierssen, H. M. (2010). A regional comparison of particle size distributions and the power law approximation in oceanic and estuarine surface waters. *Journal of Geophysical Research: Oceans*, *115*(C10). https://doi.org/10.1029/2010JC006256
28. Burchard, H., Schuttelaars, H. M., & Ralston, D. K. (2018). Sediment trapping in estuaries. *Annual review of marine science*, *10*, 371-395. https://doi.org/10.1146/annurev-marine-010816-060535
29. Campbell, J. W. (1995). The lognormal distribution as a model for bio-optical variability in the sea. *Journal of Geophysical Research: Oceans*, *100*(C7), 13237-13254. https://doi.org/10.1029/95jc00458
30. Capuzzo, E., Stephens, D., Silva, T., Barry, J., & Forster, R. M. (2015). Decrease in water clarity of the southern and central North Sea during the 20th century. *Global change biology*, *21*(6), 2206-2214. https://doi.org/10.1111/gcb.12854
31. Carder, K. L., Chen, F. R., Cannizzaro, J. P., Campbell, J. W., & Mitchell, B. G. (2004). Performance of the MODIS semi-analytical ocean color algorithm for chlorophyll-a. *Advances in Space Research*, *33*(7), 1152-1159. https://doi.org/10.1016/S0273-1177(03)00365-X
32. Carder, K L, Chen, F. R., Lee, Z. P., Hawes, S. K., & Kamykowski, D. (1999). Semianalytic Moderate-Resolution Imaging Spectrometer algorithms for chlorophyll a and absorption with bio-optical domains based on nitrate-depletion temperatures. *Journal of Geophysical Research*, *104*, 5403.
33. Carder, K. L., Tomlinson, R. D., & Beardsley Jr, G. F. (1972). A technique for the estimation of indices of refraction of marine phytoplankters 1. *Limnology and Oceanography*, *17*(6), 833-839. https://doi.org/10.4319/lo.1972.17.6.0833

34. Chang, G. C., & Dickey, T. D. (1999). Partitioning in situ total spectral absorption by use of moored spectral absorption-attenuation meters. *Applied Optics*, *38*, 3876–3887.
35. Chant, R. J., & Stoner, A. W. (2001). Particle trapping in a stratified flood-dominated estuary. *Journal of Marine Research*, *59*, 29–51.
36. Chen,G., F. Y. (2015). An objective algorithmfor estimating maximum oceanic mixed layer depth using seasonality indices derived fromArgo temperature/salinity profiles. *Journal of Geophysical Research: Oceans*, *120*, 582–595.
37. Chu, P. C., & Fan, C. (2011). Maximum angle method for determining mixed layer depth from seaglider data. *Journal of Oceanography*, *67*, 219–230.
38. Clarke, G. L., Ewing, G. C., & Lorenzen, C. J. (1970). Spectra of backscattered light from the sea obtained from aircraft as a measure of chlorophyll concentration. *Science*, *167*(3921), 1119-1121.
39. D'Silva, M. S., Anil, A. C., Naik, R. K., & D'Costa, P. M. (2012). Algal blooms: A perspective from the coasts of India. *Natural Hazards*, *63*, 1225–1253.
40. Darecki, M., & Stramski, D. (2004). An evaluation of MODIS and SeaWiFS bio-optical algorithms in the Baltic Sea. *Remote sensing of Environment*, *89*(3), 326-350. https://doi.org/10.1016/j.rse.2003.10.012
41. Das, P., Murty, C., & Varadachari, V. (1972). Flow characteristics of Combarjua canal connecting Mandovi and Zuari estuaries. *Indian Journal of Geo-Marine Sciences (IJMS)*, *01*, 95–102.
42. Davies-Colley, R. J., Ballantine, D. J., Elliott, S. H., Swales, A., Hughes, A. O., & Gall, M. P. (2014). Light attenuation–a more effective basis for the management of fine suspended sediment than mass concentration?. *Water Science and Technology*, *69*(9), 1867-1874. https://doi.org/10.2166/wst.2014.096
43. de Boyer Montégut, C., Madec, G., Fischer, A. S., Lazar, A., & Iudicone, D. (2004). Mixed layer depth over the global ocean: An examination of profile data and a profile-based climatology. *Journal of Geophysical Research C: Oceans*, *109*, 1–20.
44. de Boyer Montégut, C., Mignot, J., Lazar, A., & Cravatte, S. (2007). Control of salinity on the mixed layer depth in the world ocean: 1. General description. *Journal of Geophysical Research*, *112*, C06011.
45. Dehadrai, P., & Bhargava, R. (1972). Seasonal organic production in relation to environmental features in Mandovi & Zuari estuaries, Goa. *Indian Journal of Geo-Marine Sciences (IJMS)*, *01*, 52–56.
46. Dehadrai, B. Y. P. V. (1970). Changes in the environmental features of the Zuari and Mandovi estuaries in relation to tides. *Proceedings of the Indian Academy of Sciences-Section B*, *72*, 68–69.
47. Desa, E., Suresh, T., Matondkar, S. G. P., Desa, E., Goes, J., Mascarenhas, A., … Fernandes, C. E. G. (2005a). Detection of Trichodesmium bloom patches along the eastern Arabian Sea by IRS-P4/OCM ocean color sensor and by in-situ measurements. *Indian Journal of Marine Sciences*, *34(4)*, 374-386.
48. Desa, Elgar, Desa, E., & Suresh, T. (2005b). *Method of determining the volume scattering function of ocean waters in the backward direction using a satellite ocean color sensor*. (Patent no 6,868,361).
49. DeSousa, S., & SenGupta, R. (1986). Variations of dissolved oxygen in Mandovi and Zuari estuaries. *Indian Journal of Geo-Marine Sciences (IJMS)*, *15*, 67–71.
50. Devassy, V., Bhattathiri, P., & Qasim, S. (1979). Succession of organisms following Trichodesmium phenomenon. *Indian Journal of Geo-Marine Sciences (IJMS)*, *08*, 89–93.
51. Devassy, V., & Nair, S. (1987). Discolouration of water and its effect on fisheries along the Goa Coast. *Mahasagar*, *20*, 121–128.

52. Devassy, V. P., & Goes, J. I. (1989). Seasonal patterns of phytoplankton biomass and productivity in a tropical estuarine complex (west coast of India). *Proceedings: Plant Sciences*, *99*, 485–501.
53. Dhargalkar, V. K., D'Souza, R., Kavlekar, D. P., & Untawale, A. G. (2014). *Mangroves of Goa*. Goa: Government of Goa Forest Department.
54. Dias, Albertina Balbina, Thayapurath, S., Sahay, A., & Chauhan, P. (2017). Contrasting characteristics of colored dissolved organic matter of the coastal and estuarine waters of goa during summer. *Indian Journal of Geo-Marine Sciences, 46(05),* 860-870.
55. Dias, A., Suresh, T., Gauns, M., Sahay, A., Chauhan, P. (2015, March). *Spatial and temporal variations of colored dissolved organic matter in the estuarine and coastal waters of Goa*. Presented at OSICON, Goa.
56. Dias, A.**,** Suresh, T., Talaulikar, M., Lotlikar, A. (2013, November). Influence of Subsurface Chlorophyll Maxima on the Chlorophyll Derived from the Satellite Data, *conference proceedings, OSICON*, 333-336.
57. Dias, A., Kurian, S., Suresh, T. (2019, February). *Some observations on colored dissolved organic matter during blooms in the coastal waters off Goa*. Presented at WOSC, Vishakhapatnam.
58. Do Rosário Gomes, H., Goes, J. I., Matondkar, S. G. P., Buskey, E. J., Basu, S., Parab, S., & Thoppil, P. (2014). Massive outbreaks of Noctiluca scintillans blooms in the Arabian Sea due to spread of hypoxia. *Nature Communications*, *5*, 4862. https://doi.org/10.1038/ncomms5862
59. Dong, S., Sprintall, J., Gille, S. T., & Talley, L. (2008). Southern ocean mixed-layer depth from Argo float profiles. *Journal of Geophysical Research: Oceans*, *113*, 1–12.
60. Doron, Maéva,Babin, M., Mangin, A., Hembise, O., Doron, M., & Babin, M. (2007). Estimation of light penetration, and horizontal and vertical visibility in oceanic and coastal waters from surface reflectance. *Journal of Geophysical Research*, *112*, C06003.
61. Doron, M., Babin, M., Hembise, O., Mangin, A., & Garnesson, P. (2011). Ocean transparency from space: Validation of algorithms estimating Secchi depth using MERIS, MODIS and SeaWiFS data. *Remote Sensing of Environment*, *115*, 2986–3001.
62. Duntley, S Q. (1960). The Visibility of Submerged Objects. *Scripps Institution of Oceanography*.
63. Eppley, R. W. (1972). Temperature and phytoplankton growth in the sea. *Fishery Bulletin*, Vol. 70, pp. 1063–1085.
64. Fernandes, L. L., Kessarkar, P. M., Suja, S., Ray, D., & Bhat, M. (2018). Seasonal variations in the water quality of six tropical micro- and mesotidal estuaries along the central west coast of India. *Marine and Freshwater Research*, *69*, 1418–1431.
65. Fernandes, L. L., Purnachandra Rao, V., Kessarkar, P. M., & Suresh, S. (2018). Estuarine turbidity maximum in six tropical minor rivers, central west coast of India. *Hydrology Research*, *49*(4), 1234-1254.
66. Fournier, G. R., & Forand, J. L. (1994). Analytic phase function for ocean water. In J.S. & J. (ed.) (Eds.), *Ocean Optics XII* (pp. 194–201). SPIE.
67. Fournier, G. R. (2007). Backscatter corrected Fournier-Forand phase function for remote sensing and underwater imaging performance evaluation. In I. M. Levin, G. D. Gilbert, V. I. Haltrin, C. C. Trees (Eds.), *Current Research on Remote Sensing, Laser Probing, and Imagery in Natural Waters* (pp. 66150N), Proc SPIE: International Society for Optics and Photonics. Vol. 6615.
68. Freda, Wlodzimierz, & Piskozub, J. (2007). Improved method of Fournier-Forand marine phase function parameterization. *Optics Express*, *15*, 12763–12768.

69. Freda, Włodzimierz, & Piskozub, J. (2012). Revisiting the role of oceanic phase function in remote sensing reflectance. *Oceanologia*, *54*, 29–38.
70. Garver, S., & Siegel, D. (1997). Inherent optical property inversion of ocean color spectra and its biogeochemical interpretation: 1. Time series from the Sargasso Sea. *Journal of Geophysical Research: Oceans*, *102*, 18607–18625.
71. Gauns, M., Mochemadkar, S., Patil, S., Pratihary, A., Naqvi, S. W. A., & Madhupratap, M. (2015). Seasonal variations in abundance, biomass and grazing rates of microzooplankton in a tropical monsoonal estuary. *Journal of Oceanography*, *71*, 345–359.
72. Gershun, A. (1939). The Light Field. *Journal of Mathematics and Physics*, *18*(1-4), 51-151. https://doi.org/10.1002/sapm193918151
73. Geyer, W. R., Woodruff, J. D., & Traykovski, P. (2001). Sediment transport and trapping in the Hudson River estuary. *Estuaries*, *24*, 670–679.
74. Girishkumar, M. S., Ravichandran, M., & Mcphaden, M. J. (2013). Temperature inversions and their influence on the mixed layer heat budget during the winters of 2006 – 2007 and 2007 – 2008 in the Bay of Bengal. *Journal Of Geophysical Research: Oceans*, *118*, 2426–2437.
75. Glamore, W. C., Rayner, D. S., & Rahman, P. F. (2016). Estuaries and climate change. Technical Monograph prepared for the National Climate Change Adaptation Research Facility.Water Research Laboratory of the School of Civil and Environmental Engineering, UNSW.
76. Gonsalves, M. J., Nair, S., Loka Bharathi, P. a., & Chandramohan, D. (2009). Abundance and production of particle-associated bacteria and their role in a mangrove-dominated estuary. *Aquatic Microbial Ecology*, *57*, 151–159.
77. Gordon, H. R., Brown, O. B., Evans, R. H., Brown, J. W., Smith, R. C., Baker, K. S., & Clark, D. K. (1988). A semianalytic radiance model of ocean color. *Journal of Geophysical Research*, *93*, 10909–10924.
78. Gordon, H. R. (1989a). Can the Lambert-Beer law be applied to the diffuse attenuation coefficient of ocean water?. *Limnology and Oceanography*, *34*(8), 1389-1409. https://doi.org/10.4319/lo.1989.34.8.1389
79. Gordon, Howard R. (2002). Inverse methods in hydrologic optics. *Oceanologia*, *44*, 9–58.
80. Gordon, H. R., & Clark, D. K. (1980). Remote sensing optical properties of a stratified ocean: an improved interpretation. *Applied Optics*, *19*(20), 3428-3430. https://doi.org/10.1364/ao.19.003428
81. Gordon, Howard R., & McCluney, W. R. (1975). Estimation of the Depth of Sunlight Penetration in the Sea for Remote Sensing. *Applied Optics*, *14*, 413.
82. Gordon, H. R., & Wouters, A. W. (1978). Some relationships between Secchi depth and inherent optical properties of natural waters. *Applied Optics*, *17*(21), 3341-3343. https://doi.org/10.1364/ao.17.003341
83. Gordon, Howard R. (1989b). Theoretical aspects of hydrologic optics. *Limonology And Oceanography*, *34*, 1389–1409.
84. Gordon, Howard R. (2019). *Principles of Ocean Color Remote Sensing*. 1–9.
85. Gordon, H. R., & Morel, A. Y. (1983). Lecture notes on coastal and estuarine studies. In *Remote assessment of ocean color for interpretation of satellite visible imagery. A review* (p. 114). Springer-Verlag
86. Grimaud, G. M., Le Guennec, V., Ayata, S. D., Mairet, F., Sciandra, A., & Bernard, O. (2015). Modelling the effect of temperature on phytoplankton growth across the global ocean. *IFAC-PapersOnLine*, *28*, 228–233.

87. Haltrin, V. I. (1998, July). An analytic Fournier-Forand scattering phase function as an alternative to the Henyey-Greenstein phase function in hydrologic optics. In *IGARSS'98. Sensing and Managing the Environment. 1998 IEEE International Geoscience and Remote Sensing. Symposium Proceedings.(Cat. No. 98CH36174)* (Vol. 2, pp. 910-912). IEEE.
88. Haltrin, V. I. (1999a). Horizontal visibility of Lambertian object submerged in seawater. *IEEE 1999 International Geoscience and Remote Sensing Symposium. IGARSS'99 (Cat. No.99CH36293)* (vol.*2*, pp.1417–1419). IEEE.
89. Haltrin, V. I. (1999b, June). Two-term Henyey-Greenstein light scattering phase function for seawater. In *IEEE 1999 International Geoscience and Remote Sensing Symposium. IGARSS'99 (Cat. No. 99CH36293)* (Vol. 2, pp. 1423-1425). IEEE.
90. Hoepffner, N., & Sathyendranath, S. (1991). Effect of pigment composition on absorption properties of phytoplankton. *Marine Ecology Progress Series*, *73*, 11–23.
91. Hoge, F. E., & Lyon, P. E. (1996). Satellite retrieval of inherent optical properties by linear matrix inversion of oceanic radiance models: An analysis of model and radiance measurement errors. *Journal of Geophysical Research C: Oceans*, *101*(C7), 16631-16648. https://doi.org/10.1029/96JC01414
92. Holmes, R. W. (1970). The Secchi disk in turbid coastal waters. *Limnology and Oceanography*, *15*(5), 688-694. https://doi.org/10.4319/lo.1970.15.5.0688
93. Holte, J., & Talley, L. (2009). A New Algorithm for Finding Mixed Layer Depths with Applications to Argo Data and Subantarctic Mode Water Formation*. *Journal of Atmospheric and Oceanic Technology*, *26*, 1920–1939.
94. Humphrey, G. F. (1972). The Biology of the Indian Ocean. *Brunn Memorial Lectures, IOC, UNESCO, 1971*, 7–22.
95. Huot, Y., Morel, A., Twardowski, M. S., Stramski, D., & Reynolds, R. A. (2008). Particle optical backscattering along a chlorophyll gradient in the upper layer of the eastern South Pacific Ocean. *Biogeosciences*, *5*, 495–507.
96. IOCCG. (2000). *Remote Sensing of Ocean Colour in Coastal, and Other Optically-Complex, Waters* (S Sathyendranath, Ed.). Dartmouth, Canada: IOCCG.
97. IOCCG. (2006). Remote Sensing of Inherent Optical Properties: Fundamentals, Tests of Algorithms, and Applications. In Z.-P. Lee (Ed.), *Reports of the International Ocean Colour Coordinating Group*. Dartmouth, Canada: IOCCG.
98. IOCCG. (2010). *Atmospheric Correction for Remotely-Sensed Ocean-Colour Products* (M. Wang, Ed.). Dartmouth, Canada: IOCCG.
99. IOCCG. (2014). *Phytoplankton Functional Types from Space* (S Sathyendranath, Ed.). Dartmouth, Canada: IOCCG.
100. IPCC, (2018). *IPCC report Global Warming of 1.5 C: Summary for Policymakers*.
101. Iqbal, M. (1983). An Introduction to Solar Radiation. In *An Introduction to Solar Radiation*. https://doi.org/10.1016/b978-0-12-373750-2.x5001-0
102. Jackson, T., Sathyendranath, S., & Mélin, F. (2017). An improved optical classification scheme for the Ocean Colour Essential Climate Variable and its applications. *Remote Sensing of Environment*, *203*, 152–161.
103. Jagtap, T. (1987). Seasonal distribution of organic matter in mangrove environment of Goa. *Indian Journal of Geo-Marine Sciences (IJMS)*, *16*, 103–106.
104. Jerlov, N. G. (1976). *Marine optics* (pp. 231). Amsterdam, Netherlands: Elsevier Scientific.
105. Johnson, A. N. (2015). *Effects of Salinity and Temperature on Phytoplankton Community of San Francisco Estuary*. PhD thesis, San Francisco State University.
106. Kahru, M., Diego, S., & Stramska, M. (2002). *Determination of spectral absorption coefficients of particles , dissolved material and phytoplankton for discrete water*

samples Ocean Optics Protocols Revision 3 , Volume 2 for Satellite Ocean Color Sensor Validation.

107. Kara, A. B., Rochford, P. A., & Hurlburt, H. E. (2000). An optimal definition for ocean mixed layer depth. *Journal of Geophysical Research*, *105(C7)*. 16803–16821.
108. Kessarkar, Pratima M., Purnachandra Rao, V., Shynu, R., Ahmad, I. M., Mehra, P., Michael, G. S., & Sundar, D. (2009). Wind-driven estuarine turbidity maxima in Mandovi Estuary, central west coast of India. *Journal of Earth System Science*, *118*, 369–377.
109. Kessarkar, Pratima M., Shynu, R., Rao, V. P., Chong, F., Narvekar, T., & Zhang, J. (2013). Geochemistry of the suspended sediment in the estuaries of the Mandovi and Zuari rivers, central west coast of India. *Environmental Monitoring and Assessment*, *185*, 4461–4480.
110. Kessarkar, Pratima Mohan, Rao, V. P., Shynu, R., Mehra, P., & Viegas, B. E. (2010). The nature and distribution of particulate matter in the Mandovi estuary, central west coast of India. *Estuaries and Coasts*, *33*, 30–44.
111. Kirk, J. T. O. (2010). Light and photosynthesis in aquatic ecosystems, third edition. In *Light and Photosynthesis in Aquatic Ecosystems, third edition*. https://doi.org/10.1017/CBO9781139168212
112. Kirk, J. T. (2003). The vertical attenuation of irradiance as a function of the optical properties of the water. *Limnology and Oceanography*, *48*(1), 9-17.
113. Kothawale, D. R., & Rajeevan, M. (2017). Monthly , Seasonal and Annual Rainfall Time Series for All-India , Homogeneous Regions and Meteorological Subdivisions : 1871-2016. In *ESSO/IITM/STCVP/SR/02(2017)/189, Indian Institute of Tropical Meteorology (IITM) , Pune*.
114. Kumari, L. K., Bhattathiri, P. M. A., & John, J. (2002). Primary productivity in Mandovi -Zuari estuaries in G o a. *J. Mar. Biol. Ass. India*, *44*, 1–13.
115. LaFond, E. C., & Sastry, J. S. (1957). Turbidity of waters off the east coast of India. *Indian J. Met. & Geophy*, *8*, 183-192.
116. Lavender, K. L., Davis, R. E., & Owens, W. B. (2002). Observations of open-ocean deep convection in the Labrador Sea from subsurface floats. *Journal of Physical Oceanography*, *32*, 511–526.
117. Leach, T. H., Beisner, B. E., Carey, C. C., Pernica, P., Rose, K. C., Huot, Y., … Verburg, P. (2018). Patterns and drivers of deep chlorophyll maxima structure in 100 lakes: The relative importance of light and thermal stratification. *Limnology and Oceanography*, *63*, 628–646.
118. Lee, Z. P., Lubac, B., & Werdell, J. (2014). Update of the Quasi-Analytical Algorithm (QAA_v6)[R/OL]. *Interna-tional Ocean Color Group Software Report [2013-04-03]. http://www. ioccg, org/groups/Software-OCA/OAA _*, *5*.
119. Lee, M., & Lewis, M. (2003). A new method for the measurement of the optical volume scattering function in the upper ocean. *Journal of Atmospheric and Oceanic Technology*, *20*, 563–571.
120. Lee, Z. P., Du, K. P., & Arnone, R. (2005). A model for the diffuse attenuation coefficient of downwelling irradiance. *Journal of Geophysical Research C: Oceans*, *110*, 1–10.
121. Lee, Z. P., Shang, S., Hu, C., Du, K., Weidemann, A., Hou, W., … Lin, G. (2015). Secchi disk depth: A new theory and mechanistic model for underwater visibility. *Remote Sensing of Environment*, *169*, 139-149. https://doi.org/10.1016/j.rse.2015.08.002

122. Lee, Z, Carder, K. L., Mobley, C. D., Steward, R. G., & Patch, J. S. (1999). Hyperspectral remote sensing for shallow waters. 2. Deriving bottom depths and water properties by optimization. *Applied Optics*, *38*, 3831–3843.
123. Lee, ZhongPing, Carder, K. L., & Arnone, R. A. (2002). Deriving inherent optical properties from water color: a multiband quasi-analytical algorithm for optically deep waters. *Applied Optics*, *41*, 5755–5772.
124. Lee, Zhongping, Carder, K. L., Hawes, S. K., Steward, R. G., Peacock, T. G., & Davis, C. O. (1994). Model for the interpretation of hyperspectral remote-sensing reflectance. *Applied Optics*, *33*, 5721.
125. Lee, Zhongping, Marra, J., Perry, M. J., & Kahru, M. (2015). Estimating oceanic primary productivity from ocean color remote sensing: A strategic assessment. *Journal of Marine Systems*, *149*, 50–59.
126. Lee, Zhongping, Shang, S., Du, K., & Wei, J. (2018). Resolving the long-standing puzzles about the observed Secchi depth relationships. *Limnology and Oceanography*, *63*, 2321–2336.
127. Lee, ZhongPing, Weidemann, A., Kindle, J., Arnone, R., Carder, K. L., & Davis, C. (2007). Euphotic zone depth: Its derivation and implication to ocean-color remote sensing. *Journal of Geophysical Research*, *112*, C03009.
128. Lee, Z., & Carder, K. L. (2004). Absorption spectrum of phytoplankton pigments derived from hyperspectral remote-sensing reflectance. *Remote sensing of environment*, *89*(3), 361-368.
129. Levin, I. M., Desa, E. E., Desa, E. E., Suresh, T., Radomyslskaia, T., & Radomyslskaya, T. (2000). Can the Secchi depth measurements be used for determination of water inherent optical properties. *Ocean Optics, St. Petersberg*, 63–73.
130. Loisel, H, & Stramski, D. (2000). Estimation of the inherent optical properties of natural waters from the irradiance attenuation coefficient and reflectance in the presence of Raman scattering. *Applied Optics*, *39*, 3001–3011.
131. Loisel, Hubert, & Morel, A. (1998). Light scattering and chlorophyll concentration in case 1 waters: A reexamination. *Limnology and Oceanography*, *43*, 847–858.
132. Lorbacher, K., Dommenget, D., Niiler, P. P., & Köhl, a. (2006). Ocean mixed layer depth: A subsurface proxy of ocean-atmosphere variability. *Journal of Geophysical Research: Oceans*, *111*, 1–22.
133. Lubac, B., & Loisel, H. (2007). Variability and classification of remote sensing reflectance spectra in the eastern English Channel and southern North Sea. *Remote Sensing of Environment*, *110*, 45–58.
134. Lukas, R., & Lindstrom, E. (1991). The mixed layer of the western equatorial Pacific Ocean. *Journal of Geophysical Research*, *96*, 3343–3357.
135. Madhupratap, M., Nair, K. N. V, Gopalakrishnan, T. C., Haridas, P., Nair, K. K. C., Venugopal, P., & Gauns, M. (2001). Arabian Sea oceanography and fisheries of the west coast of India. *Current Science*, *81*, 355–361.
136. Madhupratap, M., Prasanna Kumar, S., Bhattathiri, P. M. A., Dileep Kumar, M., Raghukumar, S., Nair, K. K. C., & Ramaiah, N. (1996). Mechanism of the biological response to winter cooling in the northeastern Arabian Sea. *Nature, 384*(6609), 549. https://doi.org/10.1038/384549a0
137. Mannino, A., Novak, M. G., Hooker, S. B., Hyde, K., & Aurin, D. (2014). Algorithm development and validation of CDOM properties for estuarine and continental shelf waters along the northeastern U.S. coast. *Remote Sensing of Environment*, *152*, 576–602.

138. Mannino, A., Russ, M., & Hooker, S. (2008). Algorithm development and validation for satellite-derived distributions of DOC and CDOM in the US Middle Atlantic Bight. *Journal of Geophysical Research: Oceans*, *113(C7)*, C07051.
139. Manoj, N. T. (2008). *Numerical modelling of tidal circulation and studies on salinity distribution in Mandovi and Zuari estuaries*. Goa University.
140. Manoj, N. T., Unnikrishnan, A. S., & Sundar, D. (2009). Tidal Asymmetry in the Mandovi and Zuari Estuaries, the West Coast of India. *Journal of Coastal Research*,1187-1197. https://doi.org/10.2112/08-1056.1
141. Maritorena, S., Siegel, D. a, & Peterson, A. R. (2002). Optimization of a semianalytical ocean color model for global-scale applications. *Applied Optics*, *41*, 2705–2714.
142. McKinna, L., Furnas, M., & Ridd, P. (2011). A simple, binary classification algorithm for the detection of Trichodesmium spp. within the Great Barrier Reef using MODIS imagery. *Limnology and Oceanography: Methods*, *9*, 50–66.
143. McKinna, L. I. W. (2015). Three decades of ocean-color remote-sensing Trichodesmium spp. in the World's oceans: A review. *Progress in Oceanography*, *131*, 177–199.
144. McNally, H., Mehta, A. J., & McNally, W. H. (2004). Sediment Transport in Estuaries. *Encyclopedia of Life Support Systesm (EOLSS)*, 31.
145. Mélin, F., & Vantrepotte, V. (2015). How optically diverse is the coastal ocean? *Remote Sensing of Environment*, *160*, 235–251.
146. Menon, H. B., Lotliker, a., & Nayak, S. R. (2005). Pre-monsoon bio-optical properties in estuarine, coastal and Lakshadweep waters. *Estuarine, Coastal and Shelf Science*, *63*, 211–223.
147. Mishra, D. R., & Gould, R. W. (2016). Preface: Remote sensing in coastal environments. *Remote Sensing*, *8*, 1–6.
148. Mitchell, B. G., Bricaud, A., Carder, K., Cleveland, J., Ferrari, G., Gould, R., … Vodacek, A. (2000). Determination of spectral absorption coefficients of particles, dissolved material and phytoplankton for discrete water samples. *NASA Technical Memorandum*.
149. Mitchell, B.G., M. Kahru, J. Wieland, and M. Stramska, 2003: Determination of spectral absorption coefficients of particles, dissolved material and phytoplankton for discrete water samples, in Ocean Optics Protocols for Satellite Ocean Color Sensor Validation, Revision 4, Volume IV: Inherent Optical Properties: Instruments, Characterizations, Field Measurements and Data Analysis Protocols, NASA/TM-2003-211621/Rev4-Vol. IV, edited by J.L. Mueller, G.S. Fargion, and C.R. McClain, pp. 39-64, NASA Goddard Space Flight Center, Greenbelt, Maryland
150. Mitrovic, S. M., Lorrainehardwick, & Forughdorani. (2011). Use of flow management to mitigate cyanobacterial blooms in the Lower Darling River, Australia. *Journal of Plankton Research*, *33*, 229–241.
151. Mitrovic, S. M., Oliver, R. L., Rees, C., Bowling, L. C., & Buckney, R. T. (2003). Critical flow velocities for the growth and dominance of Anabaena circinalis in some turbid freshwater rivers. *Freshwater Biology*, *48*, 164–174.
152. Mobley, C. D., Stramski, D., Bisset, W. P., & Boss, E. (2004). Optical Modeling of Ocean Water Is the Case 1 - Case 2 Classifi cation Still Useful? *Oceanography*, *17*, 61–67.
153. Mobley, C. D. (1994). Light and water: radiative transfer in natural waters. In *Light and water: radiative transfer in natural waters*. https://doi.org/10.4304/jsw.9.4.847-858

154. Mobley, C. D., Sundman, L. K., & Boss, E. (2002). Phase function effects on oceanic light fields. *Applied Optics*, *41*, 1035–1050.
155. Mobley, CD, Gentili, B., & Gordon, H. (1993). Comparison of numerical models for computing underwater light fields. *Applied Optics*, *32*, 7484–7504.
156. Mobley, Curtis. (2013). *The Volume Scattering Function and Models for Scattering Why is Scattering Important ?*
157. Moeller, H. V., Laufkötter, C., Sweeney, E. M., & Johnson, M. D. (2019). Light-dependent grazing can drive formation and deepening of deep chlorophyll maxima. *Nature Communications*, *10*, 1978. https://doi.org/10.1038/s41467-019-09591-2
158. Moore, T. S., Dowell, M. D., Bradt, S., & Ruiz Verdu, A. (2014). An optical water type framework for selecting and blending retrievals from bio-optical algorithms in lakes and coastal waters. *Remote Sensing of Environment*, *143*, 97–111.
159. Morel, A, & Gentili, B. (1993). Diffuse reflectance of oceanic waters. II Bidirectional aspects. *Applied Optics*, *32*, 6864–6879.
160. Morel, A, & Maritorena, S. (2001). Bio-optical properties of oceanic waters: A reappraisal. *Journal of Geophysical Research: Oceans*, *106*, 7163–7180.
161. Morel, Anclré, & Prieur, L. (1977). Analysis of variations in ocean color. *Limnology and Oceanography*, *22*, 709–722.
162. Morel, Andre. (1980). In-water and remote measurement of ocean color. *Boundary Layer Meteorology*, *18*, 177–201.
163. Morel, André. (1988). Optical modeling of the upper ocean in relation to its biogenous matter content (case I waters). *Journal of Geophysical Research*, *93*, 10749.
164. Morel, A., & Prieur, L. (1975). Analyse spectrale des coefficients d'atténuation diffuse, de réflexion diffuse, d'absorption et de retrodiffusion pour diverses régions marines. *Cent. Rech. Oceanogr. Villefranche sur Mer*, *17*, 1-157.
165. Morrow, J. H., Booth, C. R., Lind, R. N., & Hooker, S. B. (2010). Advances in Measuring the Apparent Optical Properties (AOPs) of Optically Complex Waters: The Compact-Optical Profiling System (C-OPS). *NASA, Goddard Space Flight Center, Greenbelt, MD*, 42–50.
166. Mueller, J. L. (1973). *The influence of phytoplankton on ocean color spectra* (Oregon State University). Oregon State University.
167. Mueller, J. L., Morel, A., Frouin, R., Davis, C., Arnone, R., Carder, K., … Voss, K. J. (2003). Ocean Optics Protocols For Satellite Ocean Color Sensor Validation, Revision 4, Volume III: Radiometric Measurements and Data Analysis Protocols. In *NASA/TM-2003-21621*.
168. Murty, A. V. S. (1969). A Theorettcal Approach To the Attenuation Coefficient of light in water. *Indian Journal of Fisheries*, *1&2*, 151–155.
169. Naik, P., D'Sa, E. J., Goés, J. I., & Gomes, H. d. R. (2009). Particulate absorption properties from MODIS ocean color and four in-situ transects in the southeastern Bering Sea shelf during July 2008. *Remote Sensing of the Ocean, Sea Ice, and Large Water Regions*. https://doi.org/10.1117/12.831351
170. Nair, A., Sathyendranath, S., Platt, T., Morales, J., Stuart, V., Forget, M.-H., … Bouman, H. (2008). Remote sensing of phytoplankton functional types. *Remote Sensing of Environment*, *112*, 3366–3375.
171. Naqvi, S. W.A., Naik, H., Pratihary, A., D'Souza, W., Narvekar, P. V., Jayakumar, D. A., … Saino, T. (2006). Coastal versus open-ocean denitrification in the Arabian Sea. *Biogeosciences*, *3*, 621–633.
172. Naqvi, S. Wajih A., Naik, H., Jayakumar, A., Pratihary, A. K., Narvenkar, G., Kurian, S., … Narvekar, P. V. (2009). Seasonal anoxia over the Western Indian continental shelf. *Geophysical Monograph Series*, *185*, 333–345.

173. Nelson, N. B., Siegel, D. a., Carlson, C. a., & Swan, C. M. (2010). Tracing global biogeochemical cycles and meridional overturning circulation using chromophoric dissolved organic matter. *Geophysical Research Letters*, *37*, L03610. https://doi.org/10.1029/2009GL042325
174. Nelson, N. B., & Siegel, D. a. (2013). The global distribution and dynamics of chromophoric dissolved organic matter. *Annual Review of Marine Science*, *5*, 447–476.
175. Overmann, J., & Garcia-Pichel, F. (2013). The phototrophic way of life. *The Prokaryotes: Prokaryotic Communities and Ecophysiology*, *9783642301*, 203–257.
176. Padmavati G, S. C. G. (1996). Zooplankton ecology in the Mandovi-Zuari estuarine system of Goa. west coast of India. *Indian Journal of Marine Sciences*, *25*, 268–273.
177. Paerl, H. W., & Huisman, J. (2008). Bloom like it hot. *Science*, 57–58.
178. Parab, S. G., Matondkar, S. G. P., Gomes, H. do R., & Goes, J. I. (2013). Effect of Freshwater Influx on Phytoplankton in the Mandovi Estuary (Goa, India) during Monsoon Season: Chemotaxonomy. *Journal of Water Resource and Protection*, *05*, 349–361.
179. Patil, J. S., & Anil, A. C. (2015). Effect of monsoonal perturbations on the occurrence of phytoplankton blooms in a tropical bay. *Marine Ecology Progress Series*, *530*, 77–92.
180. Pednekar, Suraksha M., Bates, S. S., Kerkar, V., & Matondkar, S. G. P. (2018). Environmental Factors Affecting the Distribution of Pseudo-nitzschia in Two Monsoonal Estuaries of Western India and Effects of Salinity on Growth and Domoic Acid Production by P. pungens. *Estuaries and Coasts*, *41*, 1448–1462.
181. Pednekar, Suraksha Mohan, Kerkar, V., Ganesh, S., & Matondkar, P. (2014). *Spatiotemporal distribution in phytoplankton community with distinct salinity regimes along the Mandovi estuary , Goa , India*. 800–818.
182. Pegau, W. S., Zaneveld, J. R. V., & Voss, K. J. (1995). Toward closure of the inherent optical properties of natural waters. *Journal of Geophysical Research: Oceans*, *100*(C7), 13193-13199. https://doi.org/10.1029/95jc00457
183. Pegau, W. Scott, Zaneveld, J. R. V., Mitchell, B. G., Mueller, J. L., Kahru, M., Wieland, J., & Stramska, M. (2002). Ocean optics protocols for satellite ocean color sensor validation, Inherent Optical Properties: Instruments, Characterizations, Field Measurements and Data Analysis Protocols. *Ocean Optics Protocols For Satellite Ocean Color Sensor Validation, IV*, 83.
184. Petzold, T. J. (1972). *Volume scattering functions for selected ocean waters* (No. SIO-REF-72-78). Scripps Institution of Oceanography La Jolla Ca Visibility Lab.
185. Poole, H. H., & Atkins, W. R. G. (1929). Photo-electric measurements of submarine illumination throughout the year. *Journal of the Marine Biological Association of the United Kingdom*, *16*(1), 297-324. https://doi.org/10.1017/S0025315400029829
186. Pope, R. M., & Fry, E. S. (1997). Absorption spectrum (380–700 nm) of pure water. II. Integrating cavity measurements. *Applied optics*, *36*(33), 8710-8723.
187. Portalier, S. M. J., Cherif, M., Zhang, L., Fussmann, G. F., & Loreau, M. (2016). Size-related effects of physical factors on phytoplankton communities. *Ecological Modelling*, *323*, 41–50.
188. Pradeep Ram, A. S., Nair, S., & Chandramohan, D. (2007). Bacterial growth efficiency in a tropical estuary: Seasonal variability subsidized by allochthonous carbon. *Microbial Ecology*, *53*, 591–599.
189. Pradhan A. (2016). State of India's Rivers for India Rivers Week, Goa, 2016, (https://indiariversforum.org/publications/)

190. Prasad, R. (1952). Preliminary observations on the temperature gradients and light penetration in the upper 200 feet of water of the Bay of Bengal. In *Proceedings of the Indian Academy of Sciences* (Vol. 36, No. 1 A, pp. 60-69). Indian Academy of Sciences.
191. Preisendorfer, R. W. (1986). Secchi disk science: Visual optics of natural waters. *Limnology and Oceanography, 31*, 909–926.
192. Preisendorfer, R. W. (1976). *Hydrologic optics*. US Department of Commerce, National Oceanic and Atmospheric Administration, Environmental Research Laboratories, Pacific Marine Environmental Laboratory
193. Prieur, L., & Morel, A. (1971). Etude theorique du regime asymptotique: relations entre characteristiques optiques et coefficient d'extinction relatif a la penetration de la lumiere du jour. *Cah. Oceanogr., 23*, 35-48.
194. Purnachandra Rao, V., Shynu, R., Kessarkar, P. M., Sundar, D., Michael, G. S., Narvekar, T., … Mehra, P. (2011). Suspended sediment dynamics on a seasonal scale in the Mandovi and Zuari estuaries, central west coast of India. *Estuarine, Coastal and Shelf Science*, *91*, 78–86.
195. Qasim, S., Wafar, M., Royan, J., & Krishnakumari, L. (1978). Biological Productivity of Coastal Waters of India - From Dabhol to Tuticorin. *Indian Journal of Geo-Marine Sciences (IJMS)*, *07*, 84–93.
196. Qasim, S. Z., Bhattathiri, P. M. A., & Abidi, S. A. H. (1968). Solar radiation and its penetration in a tropical estuary. *Journal of experimental marine biology and ecology, 2(1)*, 87-103.
197. Qasim, S. Z., & Sen Gupta, R. (1981). Environmental characteristics of the Mandovi-Zuari estuarine system in Goa. *Estuarine, Coastal and Shelf Science, 13(5),* 557-578. https://doi.org/10.1016/S0302-3524(81)80058-8.
198. Qin, Y., Brando, V. E., Dekker, A. G., & Blondeau- Patissier, D. (2007). Validity of SeaDAS water constituents retrieval algorithms in Australian tropical coastal waters. *Geophysical Research Letters*, *34*(21).
199. Rajaneesh K.M., & Mitbavkar, S. (2013). Factors controlling the temporal and spatial variations in Synechococcus abundance in a monsoonal estuary. *Marine Environmental Research*, *92*, 133–143.
200. Ralston, D. K., Geyer, W. R., & Warner, J. C. (2012). Bathymetric controls on sediment transport in the Hudson River estuary: Lateral asymmetry and frontal trapping. *Journal of Geophysical Research: Oceans*, *117*, 1–21.
201. Ramakrishnan, R., Thayapurath, S., Manguesh, U. G., & Dias, A. B. (2018). Low light phytoplankton genera observed in the coastal and estuarine waters of Goa, India. *Applied Ecology and Environmental Research*, *16*, 1783–1796.
202. Rangarajan, K. (1959). Light penetration in the inshore waters of Porto Novo. *Proceedings of the Indian Academy of Sciences - Section B*. https://doi.org/10.1007/BF03052049
203. Rao, K. (1974). Ecology of Mandovi and Zuari estuaries, Goa: Distribution of foraminiferal assemblages. *Indian Journal of Geo-Marine Sciences (IJMS)*, *03*, 61–66.
204. Rao, R., Molinari, R. L., & Festa, J. F. (1989). Evolution of the climatological near-surfacer themlal structure of the tropical Indian Ocean. *Journal of Geophysical Research*, *94*, 10801–10815.
205. Rao, T. S. (1957). Studies on the penetration of light in the bay of bengal. Part-I. Transparency of the waters on the east coast of India and its significance. *Proc. natn. Inst. Sci. India*, *23*, 165-190.
206. Raven, J. A., & Geider, R. J. (1988). Temperature and algal growth. *New Phytologist*, *110*, 441–461.

207. Raven, J. A., Kübler, J. E., & Beardall, J. (2000). Put out the light, and then put out the light. *Journal of the Marine Biological Association of the United Kingdom*, *80*, 1–25.
208. Rehm, E. C., Mccormick, N. J., & Mobley, C. D. (2013). *Estimation of inherent optical properties and phytoplankton community structure from hyperspectral in-water radiometry Estimation of inherent optical properties and phytoplankton community structure from hyperspectral in-water radiometry*.
209. Reilly, E. O., Carder, L., Siegel, A., Greg, B., Garver, A., O'Reilly, J., & Maritorena, S. (1998). Ocean color chlorophyll algorithms for SeaWiFS. *Journal of Geophysical Research*, *103*, 24937–24953.
210. Roesler, C. S., Perry, M. J., & Carder, K. L. (1989). Modeling in situ phytoplankton absorption from total absorption spectra in productive inland marine waters. *Limnology and Oceanography, 34(8),* 1510-1523. https://doi.org/10.4319/lo.1989.34.8.1510
211. Sahay, A., Chauhan, P., Nagamani, P. V., Sanwalani, N., & Dwivedi, R. M. (2011). Backscattering of light by coastal waters using hyperspectral in-situ measurements: A case study off Veraval, Gujarat, India. *Indian Journal of Marine Sciences*, *40*, 762–769.
212. Sandén, P., & Håkansson, B. (1996). Long-term trends in Secchi depth in the Baltic Sea. *Limnology and Oceanography, 41(2),* 346-351. https://doi.org/10.4319/lo.1996.41.2.0346
213. Sardessai, S. (1993). Dissolved, particulate and sedimentary humic acids in the mangroves and estuarine ecosystem of Goa, west coast of India. *Indian Journal of Marine Sciences*, *22*, 54–58.
214. Sardessai, S., & Sundar, D. (2007). Variability of nitrate and phosphate. In *The Mandovi and Zuari estuaries*: *Vol. Chapter 5* (pp. 59–66). National Institute of Oceanography, India.
215. Sarma, V. V. S. S., Gupta, S. N. M., Babu, P. V. R., Acharya, T., Harikrishnachari, N., Vishnuvardhan, K., … Kumar, M. D. (2009). Influence of river discharge on plankton metabolic rates in the tropical monsoon driven Godavari estuary, India. *Estuarine, Coastal and Shelf Science, 85(4),* 515-524. https://doi.org/10.1016/j.ecss.2009.09.003
216. Sarma, V. V. S. S., Krishna, M. S., Prasad, V. R., Kumar, B. S. K., Naidu, S. A., Rao, G. D., … Reddy, N. P. C. (2014). Distribution and sources of particulate organic matter in the Indian monsoonal estuaries during monsoon. *Journal of Geophysical Research G: Biogeosciences, 119(11),* 2095-2111. https://doi.org/10.1002/2014JG002721
217. Sathyendranath, S., & Varadachari, V. V. R. (1982). Light penetration in the coastal waters off Goa. *Indian Journal of Marine Sciences*, *11*, 148–152.
218. Sathyendranath, S, Cota, G., Stuart, V., & Maass, H. (2001). *Remote sensing of phytoplankton pigments : a comparison of empirical*. *22*, 249–273.
219. Sathyendranath, Shubha, & Platt, T. (1998). Ocean-color model incorporating transspectral processes. *Applied Optics 37(12),* 2216-2227. https://doi.org/10.1364/ao.37.002216
220. Sathyendranath, Shubha, Platt, T., Caverhill, C. M., Warnock, R. E., & Lewis, M. R. (1989). Remote sensing of oceanic primary production: computations using a spectral model. *Deep Sea Research Part A, Oceanographic Research Papers, 36(3),* 431-453. https://doi.org/10.1016/0198-0149(89)90046-0
221. Sathyendranath, S., & Platt, T. (1988). The spectral irradiance field at the surface and in the interior of the ocean: a model for applications in oceanography and remote sensing. *Journal of Geophysical Research: Oceans*, *93*(C8), 9270-9280

222. Schoellhamer, D. H. (1996). Anthropogenic sediment resuspension mechanisms in a shallow microtidal estuary. *Estuarine, Coastal and Shelf Science, 43(5),* 533-548. https://doi.org/10.1006/ecss.1996.0086
223. Scully, M. E., & Friedrichs, C. T. (2007). Sediment pumping by tidal asymmetry in a partially mixed estuary. *Journal of Geophysical Research: Oceans*, *112*, 1–12.
224. Selvakumar, R., Nair, V., & Madhupratap, M. (1980). Seasonal variations in Secondary Production of the Mandovi-Zuari Estuarine System of Goa. *Indian Journal of Geo-Marine Sciences (IJMS)*, *09*, 7–9.
225. Shanmugam, P., Ahn, Y. H., Ryu, J. H., & Sundarabalan, B. (2010). An evaluation of inversion models for retrieval of inherent optical properties from ocean color in coastal and open sea waters around Korea. *Journal of Oceanography*, *66*, 815–830.
226. Shenoy, D. M., Sujith, K. B., Gauns, M. U., Patil, S., Sarkar, A., Naik, H., … Naqvi, S. W. A. (2012). Production of dimethylsulphide during the seasonal anoxia off Goa. *Biogeochemistry, 110(1-3),* 47-55. https://doi.org/10.1007/s10533-012-9720-5
227. Shetye, S. R., Kumar, M. D., & Shankar, D. (2007). *The Mandovi and Zuari Esuaries* (and D. S. Satish R. Shetye, M. Dileep Kumar, Ed.). National Institute of Oceanography, India.
228. Shi, K., Li, Y., Li, L., & Lu, H. (2013). Absorption characteristics of optically complex inland waters: Implications for water optical classification. *Journal of Geophysical Research: Biogeosciences*, *118*, 860–874.
229. Shi, K., Li, Y., Zhang, Y., Li, L., Lv, H., & Song, K. (2014). Classification of inland waters based on bio-optical properties. *IEEE Journal of Selected Topics in Applied Earth Observations and Remote Sensing*, *7*, 543–561.
230. Shynu, R., Purnachandra Rao, V., Sarma, V. V. S. S., Kessarkar, P. M., & Mani Murali, R. (2015). Sources and fate of organic matter in suspended and bottom sediments of the Mandovi and Zuari estuaries, western India. *Current Science, 108(2),* 226-238. https://doi.org/10.1159/000363218
231. Shynu, R., Rao, V. P., Parthiban, G., Balakrishnan, S., Narvekar, T., & Kessarkar, P. M. (2013). REE in suspended particulate matter and sediment of the Zuari estuary and adjacent shelf, western India: Influence of mining and estuarine turbidity. *Marine Geology*, *346*, 326–342.
232. Shanmugam, P. (2011). A new bio- optical algorithm for the remote sensing of algal blooms in complex ocean waters. *Journal of Geophysical Research: Oceans*, *116*(C4).
233. Siegel, D. a. (2002). Global distribution and dynamics of colored dissolved and detrital organic materials. *Journal of Geophysical Research*, *107*, 3228.
234. Siegel, D. a. (2005). Colored dissolved organic matter and its influence on the satellite-based characterization of the ocean biosphere. *Geophysical Research Letters*, *32*, L20605.
235. Silveira, N., Suresh, T., Talaulikar, M., Desa, E., Prabhu Matondkar, S. G., & Lotlikar, A. (2014). Sources of errors in the measurements of underwater profiling radiometer. *Indian Journal of Marine Sciences, 43,*88-95.
236. Singbal, S. Y. S. (1973). Diurnal Variations of Some Physico-chemical Factors in the Zuari Estuary of Goa. *Indian Journal of Marine Sciences*, *2*, 90–93.
237. Smith, R. C. (1981). *Remote Sensing and Depth Distribution of Ocean Chlorophyll*. *5*, 4–6.
238. Slade, W. H., & Boss, E. (2015). Spectral attenuation and backscattering as indicators of average particle size. *Applied optics*, *54*(24), 7264-7277.
239. Smith, R. C., & Baker, K. S. (1981). *Optical properties of the clearest natural waters (200-800 nm). 20*, 177–184.

240. Smyth, T. J., Moore, G. F., Hirata, T., & Aiken, J. (2006). Semianalytical model for the derivation of ocean color inherent optical properties: description, implementation, and performance assessment. *Applied Optics*, *45*, 8116–8131.
241. Sokoletsky, L. G., Kokhanovsky, A. a, & Shen, F. (2013). Comparative analysis of radiative transfer approaches for calculation of diffuse reflectance of plane-parallel light-scattering layers. *Applied Optics*, *52*, 8471–8483.
242. Sokoletsky, L. G., & Yacobi, Y. Z. (2011). Comparison of chlorophyll a concentration detected by remote sensors and other chlorophyll indices in inhomogeneous turbid waters. *Applied Optics*, *50*, 5770–5779.
243. Sprintall, J., & Roemmich, D. (1999). Characterizing the structure of the surface layer in the Pacific Ocean. *Journal of Geophysical Research: Oceans*, *104*, 23297–23311.
244. Spyrakos, E., O'Donnell, R., Hunter, P. D., Miller, C., Scott, M., Simis, S. G. H., … Tyler, A. N. (2018). Optical types of inland and coastal waters. *Limnology and Oceanography*, *63*, 846–870.
245. Stavn, R. H., & Weidemann, A. D. (1989). Shape factors, two-flow models, and the problem of irradiance inversion in estimating optical parameters. *Limnology and Oceanography*, *34*, 1426–1441.
246. Subha Anand, S., Sardessai, S., Muthukumar, C., Mangalaa, K. R., Sundar, D., Parab, S. G., & Dileep Kumar, M. (2014). Intra- and inter-seasonal variability of nutrients in a tropical monsoonal estuary (Zuari, India). *Continental Shelf Research*, *82*, 9–30.
247. Subramaniam, A., Brown, C. W., Hood, R. R., Carpenter, E. J., & Capone, D. G. (2001). Detecting Trichodesmium blooms in SeaWiFS imagery. *Deep-Sea Research Part II: Topical Studies in Oceanography*, *49*, 107–121.
248. Subramaniam, A., Carpenter, E. J., & Falkowski, P. G. (1999). Bio-optical properties of the marine diazotrophic cyanobacteria Trichodesmium spp. II. A reflectance model for remote-sensing. *Limnology and Oceanography*, *44*, 618–627.
249. Suja, S., Kessarkar, P. M., Shynu, R., Rao, V. P., & Fernandes, L. L. (2016). Spatial distribution of suspended particulate matter in the Mandovi and Zuari estuaries: Inferences on the estuarine turbidity maximum. *Current Science*, *110*, 1165–1168.
250. Sundar, D., & Shetye, S. R. (2005). Tides in the Mandovi and Zuari estuaries, Goa, west coast of India. *Journal of Earth System Science*, *114*, 493–503.
251. Sundar, D., Unnikrishnan, A. S., Michael, G. S., Kankonkar, A., Nidheesh, A. G., & Subeesh, M. P. (2015). Observed variations in stratification and currents in the Zuari estuary, west coast of India. *Environmental Earth Sciences*, *74*, 6951–6965.
252. Suresh, T., & Desa, E. (2005). Seasonal variations of aerosol over Dona Paula, a coastal site on the west coast of India. *Atmospheric Environment*, *39*, 3471–3480.
253. Suresh, T., Desa, E., Desai, R. G. P., Jayaraman, A., & Mehra, P. (1996). Photosynthetically available radiation in the central and eastern Arabian Sea. *Current Science*, *71*, 883–887.
254. Suresh, T., Desa, E. E. E., Suresh, T., Matondkar, S. S. G. P. G. P. P., Desa, E. E. E., Goes, J., … Matondkar, S. S. G. P. G. P. P. (2005). Sea truth validation of sea WiFS ocean colour sensor in the coastal waters of the eastern Arabian Sea. *Current Science*, *80*, 1–7.
255. Suresh, T., Desa, E., Kurian, J., & Mascarenhas, A. (1998). Measurement of inherent optical properties in the Arabian Sea. *Indian Journal of Marine Sciences*, *27*, 274–280.

256. Suresh, T., Desa, E., Mascaranahas, A., Matondkar, S. G. P., Naik, P., & Nayak, S. R. (2006). An empirical method to estimate bulk refractive index for ocean satellite applications. *Asia-Pacific Remote Sensing Symposium, 6406*, 64060B-64060B – 11.
257. Suresh, T., Desa, E., Matondkar, S. G. P., Mascarenhas, A., Nayak, S. R., & Naik, P. (2006). An Algorithm To Determine Backscattering Ratio And Single Scattering Albedo. *Asia-Pacific Remote Sensing Symposium*, *6404*, 64040V-64040V – 7.
258. Suresh, T., Naik, P., Bandishte, M., Desa, E., Mascaranahas, A., & Matondkar, S. G. P. (2006). *Secchi Depth Analysis Using Bio-Optical Parameters Measured In The Arabian Sea*. *6406*, 64061Q-64061Q – 10.
259. Suresh, T., Talaulikar, M., Desa, E., Mascarenhas, A., Matondkar, S. G. P., Mascaranhas, A., & Matondkar, S. G. P. (2007). Evaluation of satellite derived spectral diffuse attenuation coefficients. *Fourth Indian National Conference on Harbour and Ocean Engineering (INCHOE-2007) Held at the National Institute of Technology, Surathkal during 12-14 December 2007, Eds. by: Rao, S.; Shirlal, KG 116-123p.*, 12–14.
260. Suresh, T., Talaulikar, M., Desa, E., Prabhu Matondkar, S. G., Kumar, T. S., & Lotlikar, A. (2012). A Simple Method to Minimize Orientation Effects in a Profiling Radiometer. *Marine Geodesy*, *35*, 441–454.
261. Suresh T., Ramakrishnan, R., Dias, A., Choudhury, S. B. (2019, February).*Underestimation of chlorophyll in the estuarine waters of Goa*. Presented at WOSC, Vishakhapatnam.
262. Suresh, T., Dias, A., Desa. (2019, February). *Some factors that control the transparencies of coastal and estuarine waters of Goa*. Presented at WOSC, Vishakhapatnam.
263. Suresh, T., Dias, A., Desa, E. J.A. (2018). *Some insight into the transparencies of the coastal and estuarine waters of Goa*, Presented at ICESAL-2018.
264. Szeto, M., Werdell, P. J., Moore, T. S., & Campbell, J. W. (2011). Are the world's oceans optically different? *Journal of Geophysical Research: Oceans*, *116*, 1–14.
265. Talaulikar, M., Suresh, T., Desa, E., & Inamdar, A. (2014a). An empirical algorithm to estimate spectral average cosine of underwater light field from remote sensing data in coastal oceanic waters. *Limnology and Oceanography: Methods, 12(2)*, 74-85. https://doi.org/10.4319/lom.2014.12.74
266. Talaulikar, M., Suresh, T., Desa, E., & Inamdar, A. (2014b). Optical Closure of Apparent Optical Properties in Coastal Waters off Goa. *Journal of the Indian Society of Remote Sensing*, 1–9.
267. Talaulikar, M., Suresh, T., Silveira, N., & Matondkar, S. G. P. (2011). Spectral Variations of UV-A and PAR Solar Radiation In Estuarine Waters of Goa. *Presented at IEEE*.
268. Talaulikar, M., Thayapurath, S., Desa, E., Matondkar, S. G. P., Srinivasa Kumar, T., Lotliker, A., & Inamdar, A. (2012). Empirical algorithm to estimate the average cosine of underwater light field at 490 nm. *Remote Sensing Letters*, *3(7)*, 585-593. https://doi.org/10.1080/01431161.2011.643506
269. Thadathil, Pakajakshan, & Gosh, A. K. (1992). Surface layer temperature inversion in the Arabian Sea during winter. *Journal of Oceanography*, *48*, 293–304.
270. Thadathil, I. Suresh, S. Gautham, S. Prasanna Kumar, M. L., & R. R. Rao, S. Neetu, and A. H. (2016). Surface layer temperature inversion in the Bay of Bengal: Main characteristics and related mechanisms. *Journal of Geophysical Research: Oceans*, *121*, 3372–3380.

271. Thayapurath, S., Dias, A. B., Desa, E. J. A., & Sahay, A. (2018). An Algorithm to Determine the Slope of the Spectral Absorption of Colored Dissolved Organic Matter (CDOM) and Detritus. *Journal of the Indian Society of Remote Sensing*, *46*, 625–631.
272. Thayapurath, S., Joshi, S., Talaulikar, M., & Desa, E. J. A. (2016, May). Preliminary results of algorithms to determine horizontal and vertical underwater visibilities of coastal waters. *Remote Sensing of the Oceans and Inland Waters: Techniques, Applications, and Challenges (*Vol. 9878, p. 98781I*).* International Society for Optics and Photonics.
273. Thayapurath, S., & Talaulikar, M. (2011). Comparison of measured and satellite-derived spectral diffuse attenuation coefficients for the Arabian Sea. *International Journal of Remote Sensing*, *33*, 570–585.
274. Thayapurath, S., Talaulikar, M., Desa, E. J., & Lotliker, A. (2016, May). Preliminary results of an algorithm to determine the total absorption coefficient of water. In *Remote Sensing of the Oceans and Inland Waters: Techniques, Applications, and Challenges* (Vol. 9878, p. 98780E). International Society for Optics and Photonics.
275. Tholkapiyan, M., Shanmugam, P., & Suresh, T. (2014). Monitoring of ocean surface algal blooms in coastal and oceanic waters around India. *Environmental Monitoring and Assessment, 186(7),* 4129 - 4137. https://doi.org/10.1007/s10661-014-3685-x
276. Thomson, Richard E., I. V. F. (2003). Estimating Mixed Layer Depth from Oceanic Profile Data. *Journal of Atmospheric and Oceanic Technology*, *20*, 319–329.
277. Twardowski, M. S., Boss, E., Macdonald, J. B., Pegau, W. S., Barnard, A. H., & Zaneveld, J. R. V. (2001). A model for estimating bulk refractive index from the optical backscattering ratio and the implications for understanding particle composition in case I and case II waters. *Journal of Geophysical Research: Oceans*, *106*, 14129–14142.
278. Twardowski, M. S., Boss, E., Sullivan, J. M., & Donaghay, P. L. (2004). Modeling the spectral shape of absorption by chromophoric dissolved organic matter. *Marine Chemistry*, *89*, 69–88.
279. Tyler, J. E. (1968). The Secchi disc. *Limnology and Oceanography*, *XIII*, 1–6.
280. Uitz, J., Stramski, D., Reynolds, R. A., & Dubranna, J. (2015). Assessing phytoplankton community composition from hyperspectral measurements of phytoplankton absorption coefficient and remote-sensing reflectance in open-ocean environments. *Remote Sensing of Environment*, *171*, 58–74.
281. Uncles, R. J., Stephens, J. A., & Law, D. J. (2006). Turbidity maximum in the macrotidal, highly turbid Humber Estuary, UK: Flocs, fluid mud, stationary suspensions and tidal bores. *Estuarine, Coastal and Shelf Science*, *67*, 30–52.
282. Untawale, A. G., Wafar, S., Jagtap, T. G. (1982). Application of remote sensing techniques to study the distribution of mangroves along the estuaries of Goa. Wetlands Ecology and Management. *Proceedings of the First International Wetlands Conference*, 51-67.
283. Valente, A., Sathyendranath, S., Brotas, V., Groom, S. B., Grant, M., Taberner, M., … Zibordi, G. (2016). A compilation of global bio-optical in situ data for ocean-colour satellite applications. *Earth System Science Data Discussions*, 1–41.
284. Valenti, D., Denaro, G., Spagnolo, B., Conversano, F., & Brunet, C. (2015). How diffusivity, thermocline and incident light intensity modulate the dynamics of deep chlorophyll maximum in tyrrhenian sea. *PLoS ONE*, *10*, 1–31.
285. Vantrepotte, V., Loisel, H., Dessailly, D., & Mériaux, X. (2012). Optical classification of contrasted coastal waters. *Remote Sensing of Environment*, *123*, 306–323.

286. Varma, K., Rao, L., & Cherian, T. (1975). Temporal and Spatial variations in Hydrographic Conditions of Mandovi Estuary. *Indian Journal of Geo-Marine Sciences (IJMS)*, *04*, 11–17.
287. Vidussi, F., Claustre, H., Manca, B. B., Luchetta, A., & Jean-Claude, M. (2001). Phytoplankton pigment distribution in relation to upper thermocline circulation in the eastern Mediterranean Sea during winter. *Journal of Geophysical Research*, *106*, 939–956.
288. Vijith, V. (2014). *Physical Oceanography of the Mandovi and Zuari , two monsoonal estuaries in Goa , central west coast of India*. Goa University.
289. Vijith, V., Sundar, D., & Shetye, S. R. (2009). Time-dependence of salinity in monsoonal estuaries. *Estuarine, Coastal and Shelf Science*, *85*, 601–608.
290. Vinh, V. D., Ouillon, S., & Van Uu, D. (2018). Estuarine Turbidity Maxima and variations of aggregate parameters in the Cam-Nam Trieu Estuary, North Vietnam, in Early Wet Season. *Water*, *10(1)*, 68 *(Switzerland)*. https://doi.org/10.3390/w10010068
291. Voss, K. J. (1992). A spectral model of the beam attenuation coefficient in the ocean and coastal areas. *Limnology and Oceanography*, *37*(3), 501-509.
292. Werdell, P. J., & Bailey, S. W. (2005). An improved in-situ bio-optical data set for ocean color algorithm development and satellite data product validation. *Remote Sensing of Environment*, *98*, 122–140.
293. Wernand, M. R. (2010). On the history of the Secchi disc. *Journal of the European Optical Society*, *5*, 10014s1-7. https://doi.org/10.2971/jeos.2010.10013s
294. Westberry, T. K., Boss, E., & Lee, Z. (2013). Influence of Raman scattering on ocean color inversion models. *Applied Optics*, *52*, 5552–5561.
295. Westberry, T. K., Siegel, D. A., & Subramaniam, A. (2005). An improved bio-optical model for the remote sensing of Trichodesmium spp. blooms. *Journal of Geophysical Research: Oceans*, *110*, 1–11.
296. Winder, M., & Sommer, U. (2012). Phytoplankton response to a changing climate. *Hydrobiologia*, *698*, 5–16.
297. Zaneveld, J. R., & Pegau, W. (2003). Robust underwater visibility parameter. *Optics Express*, *11*, 2997–3009.
298. Zaneveld, J., & Twardowski, MJ, Marlon Lewis, A. B. (2005). Introduction to radiative transfer. *Remote Sensing of Environment*. Retrieved from http://link.springer.com/content/pdf/10.1007/978-1-4020-3100-7_1.pdf
299. Zhang, H., Chen, R., Li, F., & Chen, L. (2015). Effect of flow rate on environmental variables and phytoplankton dynamics: results from field enclosures. *Chinese Journal of Oceanology and Limnology*, *33*(2), 430-438.
300. Zhu, W., Yu, Q., Tian, Y. Q., Chen, R. F., & Gardner, G. B. (2011). Estimation of chromophoric dissolved organic matter in the Mississippi and Atchafalaya river plume regions using above- surface hyperspectral remote sensing. *Journal of Geophysical Research: Oceans*, *116*(C2).